ADVANCING OPTIMAL CONTROL THEORY USING TRIGONOMETRY FOR SOLVING COMPLEX AEROSPACE PROBLEMS

A Dissertation

Submitted to the Faculty

of

Purdue University

by

Kshitij Mall

In Partial Fulfillment of the

Requirements for the Degree

of

Doctor of Philosophy

December 2018

Purdue University

West Lafayette, Indiana

THE PURDUE UNIVERSITY GRADUATE SCHOOL
STATEMENT OF DISSERTATION APPROVAL

Dr. Michael J. Grant, Chair

School of Aeronautics and Astronautics

Dr. Dengfeng Sun

School of Aeronautics and Astronautics

Dr. Carolin E. Frueh

School of Aeronautics and Astronautics

Dr. Ethiraj Venkatapathy

NASA Ames Research Center

Approved by:

Dr. Wayne Chen

Head of the School Graduate Program

To my parents, Dr. Vinod Pratap Mall and Mrs. Madhubala Mall.

To my angel, Sawa Chan (紗和ちゃん).

To my sister, Dr. Sapna Mittal.

To my inspirations, Dr. A.P.J. Kalam, Neil Armstrong and Elon Musk.

To my motherland, India.

Love and inspiration are the fuel-oxidizer combination that propel aspirations of those who dream big with open eyes.

ACKNOWLEDGMENTS

There is a long list of people that I would like to thank to for making this dissertation come to life. First of all, I would like to thank my advisor, Professor Michael Grant. I would not be wrong in saying that I had the best advisor I can think of for several reasons. When I wanted to pursue my dream of being an astronaut, I applied to Space Systems Design Laboratory at Georgia Tech. I mentioned in my statement of purpose that I would like to do an awesome research work like the Smart Divert proposed for Mars missions by Grant and Braun. I didn't know then that I was writing about my future advisor. Working with Professor Grant has been a dream come true and has shaped my life immensely. He also supported me financially for my Masters studies through a research assistantship. The two most important things I learnt from him are how to stay humble after success and how to manage the competing objectives of life to make it more meaningful.

I am very thankful to Professor Longuski for teaching me the basics of optimal control theory, which led to this thesis. His recommendation made me the first student of Professor Grant and his laboratory, Rapid Design of Systems Lab. (RDSL). Professor Frueh was kind and very helpful to join my committee when Professor Longuski took sabbatical. Dr. Venkatapathy decided to fly for my preliminary Ph.D. exam and woke up very early morning to attend my Ph.D. final exam at the cost of inconvenience. He is an inspiration to all the EDLers at RDSL. It was great fun to work with Professor Sun for the general aviation based problem used in this thesis. I was very fortunate to meet some of the best talents in my field of study at RDSL. Thanks to Thomas Antony for being the co-solver of many of the problems that I faced all throughout my Ph.D. program. Thanks to Maxwell Fagin, Harish Saranathan, Joseph Williams, Justin Mansell, Zhenbo Wang, Michael Sparapany,

Shubham Singh, Chris Dapkus, Sean Nolan, and Ted Danielson. I learnt a lot from each one of you.

I would like to thank the director of Information Management and Analysis (IMA) at Purdue Graduate School, Mr. Don Brier, who hired me as a database programmer for 3 years and provided financial support for my Ph.D. studies. He is a great human being and certainly one of the best boss one can think of. I would also like to thank Ashlee Messersmith, Nicole Barr, Ayush Parolia and all my colleagues at the IMA. I am thankful to the School of Aeronautics & Astronautics for supporting one year of my Ph.D. studies through a teaching assistantship. Thanks also due to Professor Seiko Shirasaka from Keio University for allowing me to attend two graduate exchange programs during my Ph.D. program. Thanks to Japan Student Services Organization for providing me the financial support to attend these exchange programs.

Thanks to my family, who always allowed me to pursue my dreams. My dad, who saved many human lives as an orthopedic surgeon, has always been a role model to me. He wanted to see me as a medical doctor too, but I knew that my passion lies with Aerospace Engineering. My elder sister, Dr. Sapna Mittal, consistently pushed me to profess excellence. She always reminded me that with hard work and passion anything can be made possible. My mom, Mrs. Madhubala Mall, always asked me to relax when life got turbulent during my Ph.D. program. My extended Mall family has been very supportive as well. I have been fortunate to be loved unconditionally by a sweet and a beautiful lady from Japan, Miss Sawako, who patiently listened to my words about Mars missions and about my research work, even when being from the music field and being a genius pianist. She also helped me with each and every presentation event that I delivered either in public or for an exam related to this thesis. My Japanese family: Sawako, Mom Chan Keiko, Sakiko, Grandma Hiroko, and Ram Chan have been very supportive to me, especially during the final phase of my doctoral thesis.

I am thankful to my American host family, The Schwartz, from Milwaukee, Wisconsin: Mary, John, TJ, Marli, Amy, Joe, Grandma Betty, Grace, and the list goes

on. Several individuals from India are responsible for supporting me in reaching the US to pursue my dreams: Professor A. K. Ghosh, Professor C. V. Chandrashekhar, Mr. V. K. Bansal, Dr. Sonal Rajora, Mr. Pranjal Chaubey, Mr. Anand Kumar, Mr. Sanampreet Singh Sarabha, and Mr. Shreyas Gore.

Lastly, I am thankful to Purdue University, for making my dreams come true and for accepting me as another boilermaker. I got to meet several students at Purdue University who shaped my life positively and who helped with this thesis work in one way or the other. Thanks due to Parthsarathi Trivedi, Ashwati Das-Stuart, Jeff Stuart, William O'Neill, Shreyas Vathul Subramanian, Shanmukesh Vankayala, Samarth Jain, Raja Manish, Goutham Reddy, Cesare Guariniello, Melanie Grande, Samuel Alberts, Mark Gee, Krishna Singhal and the long friend list goes on. Thanks due to Purdue University Cricket Club and Stallions cricket team for helping me play my favorite game as a break from my Ph.D. work. Thanks to the Eskimo dog at my residence, Lucy, for being a great stress buster.

TABLE OF CONTENTS

Page

LIST OF TABLES

Table Page

LIST OF FIGURES

Figure Page

Figure Page

Figure Page

ABBREVIATIONS

BVP	Boundary value problem
CDA	Continuous descent approach
CMT	Covector Mapping Theorem
DOF	Degree-of-freedom
EDL	Entry, descent, and landing
EPNL	Effective perceived noise level
EOM	Equation of motion
EU	European Union
GLCC	Generalized Legendre Clebsch condition
GPOPS	General Purpose OPtimal control Software
GPU	Graphics processing unit
ICRM	Integrated Control Regularization Method
IEPNL	Integral effective perceived noise level
KKT	Karush-Kuhn-Tucker
LG	Legendre-Gauss
LGL	Legendre-Gauss-Lobatto
LGR	Legendre-Gauss-Radau
MPBVP	Multi-point boundary value problem
NLP	Non-linear programming
OCP	Optimal control problem
OCT	Optimal control theory
PDF	Population distribution function
PGS	Prompt Global Strike
PMP	Pontryagin's minimum principle
RDSL	Rapid Design of Systems Laboratory

RK4	Runge-Kutta 4^{th} order
SEV	Slender entry vehicle
SRP	Supersonic retropropulsion
TPBVP	Two-point boundary value problem
TPS	Thermal protection system
US	United States

SYMBOLS

A	Vehicle reference area, m^2
C	Aerodynamic coefficient
D	Drag force magnitude, N
ΔC_{LH}	Parameter to shift heating constraint
$F/\dot{m}_0$	Specific thrust, m/s
G	Terminal cost
H	Hamiltonian or scale height, m
I_{sp}	Specific impulse, s
J	Cost functional
L	Path cost or lift force magnitude, N
M	Mach number
$\boldsymbol{N}$	Tangency conditions
$\boldsymbol{S}$	Path constraint
T	Thrust or temperature, N or K
T_λ	Burner exit to free stream temperature ratio
T_{MAX}	Static temperature at combustor exit, K
T'_{MAX}	Total temperature at combustor exit, K
T_r	Inlet temperature ratio
V	Speed, m/s
W	Weight, N
f	Fuel-to-air ratio
g	Earth's gravitational acceleration, m/s^2
h	Altitude, m
h_{pr}	Fuel heating value, J/kg
m	Vehicle mass, kg

q	Order of path constraint or dynamic pressure, nd or Pa
r	Radial magnitude, m
t	Time, s
$\mathbf{u}$	Control vector
v	Velocity magnitude, m/s
$\mathbf{x}$	State vector
x	Downrange, m
y	Crossrange, m
z	Altitude, m
α	Angle of attack or turn angle, rad
ϵ	Error parameter
γ	Flight path angle, rad
γ_r	Ratio of specific heats
$\boldsymbol{\lambda}$	Costate vector
μ	Gravitational parameter, $\mathrm{m}^3/\mathrm{s}^2$
Φ	Terminal constraints
ϕ	Terminal cost or crossrange angle, rad
$\boldsymbol{\Pi}$	Tangency constraint multipliers
Ψ	Initial constraints
ψ	Heading angle, rad
ρ	Atmospheric density, kg/m^3
σ	Bank angle, rad

Superscripts

-	Before
+	After

Subscripts

0	Initial, surface, or free-stream

1	Switching
C	Combustion
D	Drag
E	Earth
ENTRY	At entry point
EXIT	At exit point
L	Lift
LH	Heat constraint based
MAX	Maximum value
MIN	Minimum value
REF	Reference
TRIG	Trigonometric
e	Exhaust
f	Final
h, z	Altitude
m	Mass
n	Nose
p	Planet
v	Velocity
x	Downrange
y	Crossrange
ϵ	Error
γ	Flight path angle
ϕ	Latitude angle
ψ	Heading angle
θ	Latitude angle

ABSTRACT

Mall, Kshitij PhD, Purdue University, December 2018. **Advancing Optimal Control Theory Using Trigonometry For Solving Complex Aerospace Problems.** Major Professor: Michael James Grant.

Optimal control theory (OCT) exists since the 1950s. However, with the advent of modern computers, the design community delegated the task of solving the optimal control problems (OCPs) largely to computationally intensive direct methods instead of methods that use OCT. Some recent work showed that solvers using OCT could leverage parallel computing resources for faster execution. The need for near real-time, high quality solutions for OCPs has therefore renewed interest in OCT in the design community. However, certain challenges still exist that prohibits its use for solving complex practical aerospace problems, such as landing human-class payloads safely on Mars.

In order to advance OCT, this thesis introduces Epsilon-Trig regularization method to simply and efficiently solve bang-bang and singular control problems. The Epsilon-Trig method resolves the issues pertaining to the traditional smoothing regularization method. Some benchmark problems from the literature including the Van Der Pol oscillator, the boat problem, and the Goddard rocket problem verified and validated the Epsilon-Trig regularization method using GPOPS-II.

This study also presents and develops the usage of trigonometry for incorporating control bounds and mixed state-control constraints into OCPs and terms it as Trigonometrization. Results from literature and GPOPS-II verified and validated the Trigonometrization technique using certain benchmark OCPs. Unlike traditional OCT, Trigonometrization converts the constrained OCP into a two-point boundary value problem rather than a multi-point boundary value problem, significantly reducing the computational effort required to formulate and solve it. This work

uses Trigonometrization to solve some complex aerospace problems including prompt global strike, noise-minimization for general aviation, shuttle re-entry problem, and the g-load constraint problem for an impactor. Future work for this thesis includes the development of the Trigonometrization technique for OCPs with pure state constraints.

1. Motivation and Background

1.1 Motivation

Optimization is a very broad field of study and an integral part of many real-world engineering problems. It is a branch of pure mathematics but has applications in every major branch of science and engineering. [1] The field of aerospace engineering contains many complex trajectory optimization problems. [2, 3] To solve such complicated optimal control problems (OCPs), researchers developed and used two major optimization methods to date: direct and indirect methods. [2, 4]

Since the dawn of modern computing, academia and industry have preferred direct methods of optimization over indirect methods. [5–10] General purpose optimal control software (GPOPS-II) [11] and DIDO [12–14], based on pseudospectral methods, are the current state-of-the-art optimization software. Pseudospectral methods are a class of direct methods, where the optimization tool transcribes the OCP to a nonlinear programming (NLP) problem by parameterizing the state and control using global polynomials. These methods perform the collocation of differential–algebraic equations using nodes obtained from a Gaussian quadrature. [15–21] Since these methods ignore the necessary conditions of optimality, they do not guarantee high quality and optimal solutions. [4, 5] Moreover, tools like GPOPS-II require designer to know some "tricks" a priori in problem formulation to avoid jittery control solutions.

OCT is the other major branch of optimization based on calculus of variations, where the problem parameters are functions of time. [22–24] This theory has been extensively used in the aerospace engineering field to solve a wide variety of problems. Shooting methods, based on OCT and having inherent parallelism, can extensively use parallel computing. [25–28] Graphical processing units (GPUs) were originally designed for use in 3D graphics on computers. [29] Since the early 2000's, the scien-

tific community exploited GPUs for general purpose computing applications including scientific research. [30–33] GPUs significantly reduce computation time, thereby enabling indirect methods for use as an on-board, real-time trajectory optimization tool. [34] Several real-world applications desire high quality optimal solutions for real-time trajectory planning. [35–44] One of these applications require unmanned aerial vehicles to reconstruct optimal trajectories when encountering an obstacle in their original proposed path as shown in the animated Fig. 1.1. [36] Indirect methods could be game changers for such real-world applications, prompting further research and advancements in OCT. Furthermore, this thesis reduces the complexity of the tricks associated with the usage of GPOPS-II for OCPs by offering less complex and advanced indirect methods.

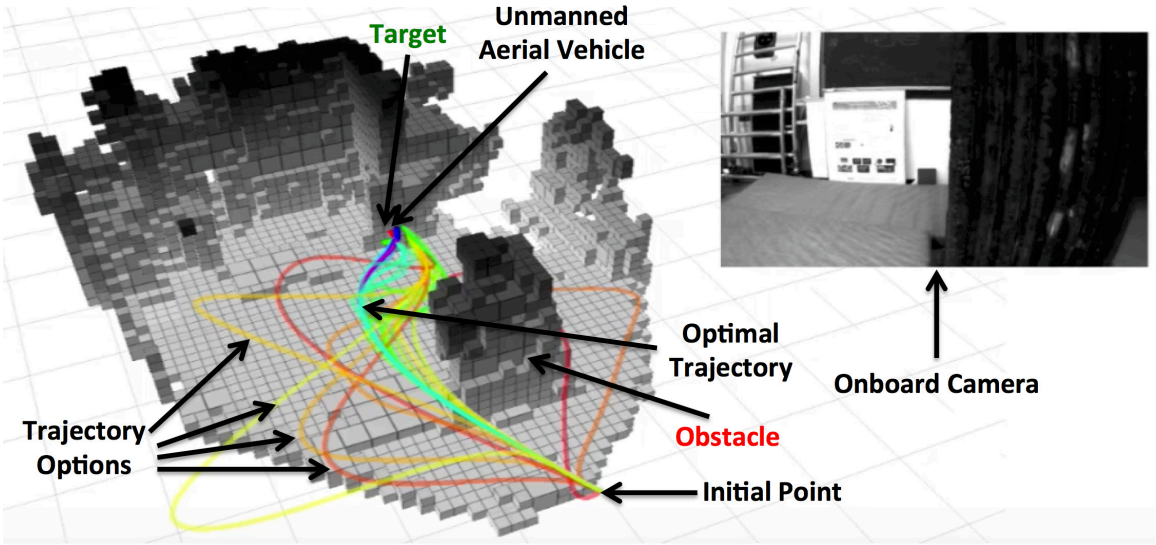

Figure 1.1.: An example of real-time trajectory optimization for an unmanned aerial vehicle to avoid obstacles. [36]

This study discovered many areas in OCT that require improvements. One such area consists of bang-bang and singular control problems, where the control appears in a linear form in the Hamiltonian. The optimal control for such problems stays at extremal values. [24, 45, 46] When the control switches between these values, the boundary value problem (BVP) solver such as MATLAB's bvp4c encounters numerical issues. The trajectory becomes discontinuous and the solver is unable to evaluate the state equations at the switch points. [47, 48] A regularization technique can resolve these issues by introducing error controls and error parameters to solve for a very close approximate problem. [48] This traditional regularization technique also suffers from certain fundamental drawbacks that require improvement to support practical aerospace problems. The first contribution of this thesis is an improved regularization technique that resolves the issues with the traditional regularization technique.

Real-world complex OCPs also involve constraints on the controls and states of the trajectory. [49] The traditional way of treating OCPs with pure control constraints is to introduce and solve for extra parameters. [5, 24] The problem thus converts from a two-point boundary value problem (TPBVP) to a multi-point boundary value problem (MPBVP). Hence, the problem formulation and problem solving process become more complicated and time intensive. On the other hand, for pure state or mixed state-control inequality constraints, the design community follows the theory described by Bryson et al. [50] in practice. However, the study by Jacobson et al. [51] found this theory to be underspecified. OCT requires certain additional necessary conditions to avoid spurious results, which make the problem formulation and solving process even more difficult. This thesis aims at resolving all such issues.

Once the improvements introduced and suggested in this thesis are made to the existing OCT, it would be possible to quickly formulate and solve many challenging and complicated aerospace problems like landing human-class payloads on the surface of Mars. The following section provides an overview of theory, concepts, and underlying principles used in this thesis for verification, validation, and advancement of OCT.

1.2 Overview

Literature often cites the following three reasons that prevent the usage of indirect optimization methods in a practical manner to perform trajectory optimization. [25]

- **Issue 1:** The use of indirect methods requires knowledge of OCT, which is quite complicated.
- **Issue 2:** It is necessary to make a priori estimate of the sequence and number of constrained and unconstrained trajectory segments for an OCP with path inequality constraints.
- **Issue 3:** It is difficult to provide a good initial guess for the mathematical and non-intuitive costates of the OCP.

The research work performed at the Rapid Design of Systems Laboratory (RDSL), including this thesis, primarily aim at addressing these issues with indirect methods of optimization. The following is a brief overview of direct and indirect methods of optimization, which form the basis for optimization solvers used in this thesis.

1.2.1 Direct Methods

The direct methods address the OCPs directly by utilizing Karush-Kuhn-Tucker (KKT) conditions. [3, 52] The optimization tool converts the OCP into an NLP problem by the discretization of both the states and controls. [4, 53] The objective function and the constraints upon the problem in the NLP are non-linear functions. NLP solvers like SNOPT [54] or IPOPT [55–58] then aim at finding values for many different user-specified variables that can optimize the objective function for the given constraints from initial and terminal points of the trajectory. SNOPT employs sequential quadratic programming based on a sparse matrix structure [59–61], which finds locally optimal solutions.

Since it is impossible to perform infinite function evaluations, the trajectory is divided into a finite number of points, also known as nodes. The placement of these nodes is not arbitrary and the equations of motion (EOMs) should be satisfied at these nodes. The direct methods employ collocation for this purpose.

The optimization research community developed collocation as an alternative to explicit integration. [6] Only the controls are discretized while using the explicit integration methods with the aim of finding the optimal control through corrections. On the other hand, both the controls and the states of the OCP are discretized while using the collocation methods. [62] Due to the discretization of states, the OCP grows larger in size, which appears to be a disadvantage at first. However, the inclusion of states helps in developing quadrature rules and in enforcing EOMs at the discretized locations. The collocation method devised in Ref. 6 uses cubic and linear polynomials to interpolate the states and the control, respectively. The solution obtained using the collocation method is identical to an explicit Runge-Kutta 4^{th} order (RK4) integration scheme with an adequate accuracy level. [63] Thus, collocation methods serve as implicit integration methods. [7]

The direct methods employing collocation are unable to estimate the costates of indirect solutions. To resolve this issue, the optimization research community introduced and developed advanced direct methods known as pseudospectral methods.

1.2.1.1 Pseudospectral Methods

Before the inception of pseudospectral methods, the design community often unwillingly chose between direct and indirect methods of optimization. Direct methods have been a popular choice due to ease of implementation for a wide variety of OCPs. However, the design studies desire rapid convergence of indirect methods. [5] Pseudospectral methods aim at bridging the gap existing between direct and indirect methods while capitalizing on the strengths of these two methods. [7, 15, 64]

There are two ways to solve a general trajectory optimization problem, represented as Problem B shown in Fig. 1.2. [65, 66] The first approach is to apply the optimality conditions using an indirect method and then to discretize it. Another approach is to discretize Problem B first by using a direct method and then to apply optimality conditions upon the discretized problem. N represents the discretization process and λ represents the application of optimality conditions.

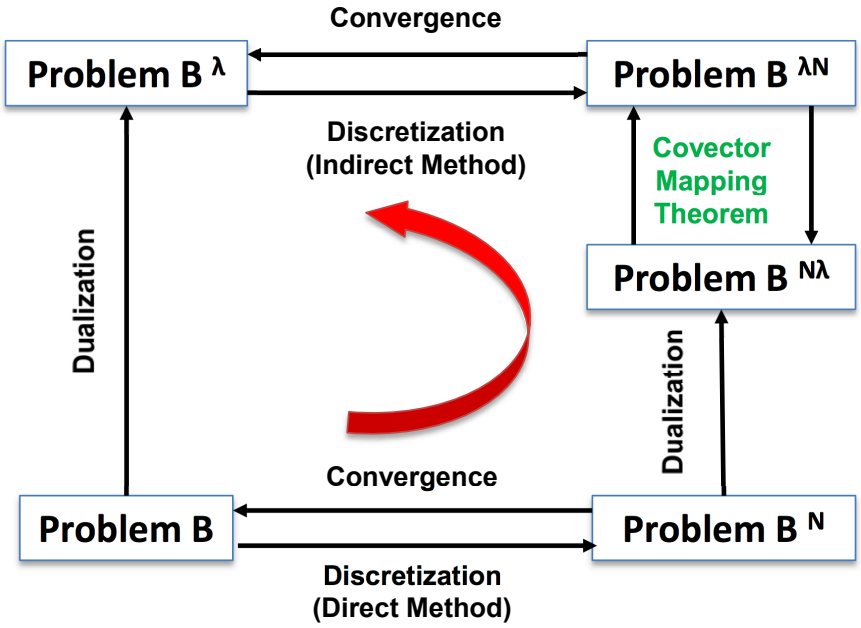

Figure 1.2.: Schematic of the Covector Mapping Theorem. [65, 66]

Discretization is a common step during the conceptual design phase while solving for optimal trajectories. As the number of discretized points increases to infinity, the discrete solution is assumed to converge to the continuous solution. Since it is impossible to perform infinite calculations during the optimization process, the number of discretized points is kept large enough for practical engineering applications. However, the assumption that the discretized solutions approach continuous solutions for a large number of discretized points is not necessarily true. [67] Many direct methods were actually developed without knowing how to fix this assumption.

As illustrated in Fig. 1.2, the direct and indirect methods approach problem B in an inverted manner. Direct methods first discretize the problem B to obtain the problem B^N. These methods then apply KKT optimality conditions to dualize B^N and obtain $B^{N\lambda}$. On the other hand, indirect methods dualize the continuous problem through the adjoint of costates. Indirect methods then discretize the resulting augmented problem, B^λ, for a computer-based solution. Thus, there seems to be a similarity between the discrete costates of indirect methods and the KKT multipliers of direct methods. However, even when these two methods obtained similar results for controls and states, the KKT multipliers of direct methods and the discrete costates of indirect methods were not necessarily consistent. [66] The discretization and dualization processes thus seemed to be immutable.

For certain OCPs, the KKT multipliers were found to be non-unique, resulting in this discrepancy. [66] To resolve this issue, researchers developed the Covector Mapping Theorem (CMT) [18] using pseudospectral methods. The CMT provides a set of closure conditions that enforce unique, properly scaled KKT multipliers, consistent with the discrete costates of indirect methods. Pseudospectral methods enable computation of costates using the CMT, as suggested by prior work in collocation methods. [7] These costates validate the necessary conditions of optimality provided by indirect methods. [68] Pseudospectral methods enable the designer to use intuitive direct methods and still obtain a converged indirect solution, which is otherwise difficult to obtain. The initial converged solution helps to perform rapid trade studies on different parameters of the OCP using the indirect methods.

Pseudospectral methods use global polynomial approximations for the state functions with Gaussian quadrature collocation points. [15, 20] Legendre–Gauss (LG), Legendre–Gauss–Radau (LGR), and Legendre–Gauss–Lobatto (LGL) points are the three most commonly used sets of collocation points. [20] Linear combinations of a Legendre polynomial and its derivatives help in obtaining these three sets of collocation points. LGL [18, 69] and LGR pseudospectral methods [70], based on these sets of collocation points, are most well documented in literature. The LG and LGR

methods have different convergence properties from the LGL method as they use a distinct mathematical form. The optimal control software used for validation of the OCPs in this thesis, GPOPS-II, employs LGR collocation points. [11]

Unlike traditional collocation methods, the global polynomials enable high-order LGR quadrature rules. The LGR points have a non-uniform distribution along the trajectory. The distribution of LGR nodes near the endpoints is dense, which helps in avoiding large interpolation errors resulting from the Runge phenomenon. [68] The KKT multipliers are appropriately scaled with the LGR weights to obtain the costates. [70] Thus, the solutions for OCPs obtained using pseudospectral methods like LGR method could be checked through the Hamiltonian obtained using the estimated costates. The Hamiltonian for the OCPs usually has a constant value and is not a function of time. The Hamiltonian time-history can then be compared between pseudospectral and indirect methods to check the quality of solutions obtained using the former. Although pseudospectral methods are able to estimate the costates well for most OCPs, but they do not guarantee high quality solutions. Indirect methods, on the other hand, guarantee high quality solutions.

1.2.1.2 Optimization Tool

For verification and validation purposes, this thesis uses a popular optimal control software called GPOPS-II, which is based on pseudospectral methods and is used to solve a wide variety of OCPs. [11] It implements LGR quadrature orthogonal collocation method to convert a continuous OCP into a sparse NLP. It uses collocation at LGR points and approximates the states as Lagrange polynomials by using the values at the initial point and at the N LGR points. The LGR method approximates costates as Lagrange polynomials by using the value at the terminal point and at the N LGR points. GPOPS-II utilizes LGR collocation method because it provides highly accurate state, control, and costate approximations while maintaining a relatively low-dimensional approximation of the continuous-time problem. An adaptive

mesh refinement method determines the number of mesh intervals and the degree of the approximating polynomial within each mesh interval for achieving a specified accuracy. GPOPS-II interfaces with NLP solvers like SNOPT or IPOPT, where sparse finite-differencing of the OCP functions approximates all derivatives required by the solver. [11]

Although GPOPS-II is a powerful software to solve a wide variety of OCPs, it suffers from few drawbacks as described below.

1. GPOPS-II is a proprietary optimization tool.

2. Solvers can parallelize GPOPS-II only to a certain extent.

3. GPOPS-II obtains jittery control solutions for many OCPs, which are unrealistic to implement in real-world scenarios. Fig. 1.3 shows one such example of a jittery angle of attack control time-history for a Mars aerocapture problem.

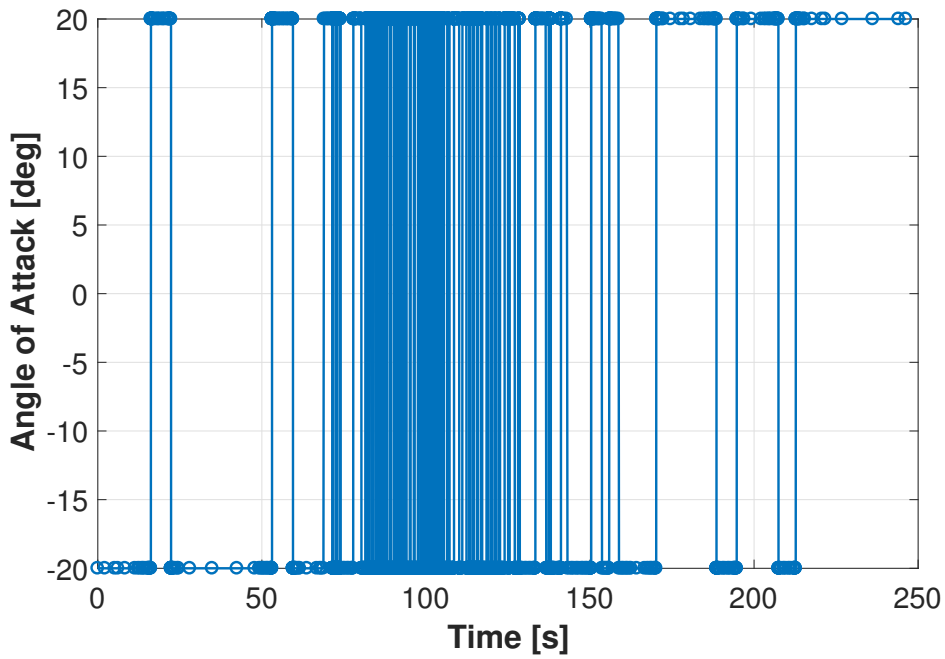

Figure 1.3.: An example of jitters in control solutions obtained using GPOPS-II.

GPOPS-II does not satisfy the necessary and sufficient conditions of optimality stated in OCT, leading to jitters in the solutions. The trajectory designer needs to express non-linear path constraints in a logarithmic form in order to avoid such jittery control solutions.

4. LGR method needs more computationally efficient, numerical linear algebra techniques [71] to identify LGR node locations.

The following subsection discusses indirect methods, which can resolve issues with direct methods including pseudospectral methods.

1.2.2 Indirect Methods

OCPs involve the calculation of the time-history of the control variable(s), associated with a system that optimizes a given performance index, while satisfying problem-specific constraints at the initial point, terminal point, and interior points as well as path constraints. An OCP generally attains the form given in Eq. (1.1). J is the cost functional, with ϕ being the terminal cost and $\int_{t_0}^{t_f} L(\boldsymbol{x}, \boldsymbol{u}, t)\,\mathrm{d}t$ being the path cost, where t_0 is chosen to be 0 s. Eq. (1.2) specify the EOMs for the OCP. Indirect methods also need to simultaneously satisfy initial and terminal constraints, $\boldsymbol{\Psi}$ and $\boldsymbol{\Phi}$, shown in Eq. (1.3) and Eq. (1.4), respectively.

$$\text{Minimize: } J = \phi(\boldsymbol{x}(t_f), t_f) + \int_{t_0}^{t_f} L(\boldsymbol{x}, \boldsymbol{u}, t)\mathrm{d}t \tag{1.1}$$

$$\text{Subject to: } \dot{\boldsymbol{x}} = \boldsymbol{f}(\boldsymbol{x}, \boldsymbol{u}, t) \tag{1.2}$$

$$\boldsymbol{\Psi}(\boldsymbol{x}(t_0), t_0) = 0 \tag{1.3}$$

$$\boldsymbol{\Phi}(\boldsymbol{x}(t_f), t_f) = 0 \tag{1.4}$$

Indirect methods optimize the cost functional, J, shown in Eq. (1.1) by formulating a MPBVP that represents the necessary conditions of optimality. If indirect

methods satisfy these boundary conditions, the solution will be locally optimal in the design space. To accomplish this, indirect methods augment the dynamic equations of the system with a set of costates. Euler-Lagrange equations then help with formulation of the necessary conditions of optimality described as follows. [24]

1.2.2.1 Necessary Conditions of Optimality using Calculus of Variations

A mathematical quantity called the Hamiltonian generates the necessary conditions of optimality. Eq. (1.5) defines the Hamiltonian, where $\boldsymbol{\lambda}$ is the costate vector with its corresponding dynamic equations defined in Eq. (1.6). Eq. (1.7) shows the optimal control law, $\boldsymbol{u}(t)$, as a function of the states and costates. Eq. (1.8) and Eq. (1.9) specify the initial and terminal boundary conditions on the costates, where $\boldsymbol{\nu_0}$ and $\boldsymbol{\nu_f}$ are sets of undetermined parameters, which are used to adjoin these boundary conditions to the cost functional. The free final time condition, shown by Eq. (1.10), determines the time of flight of the trajectory. Eqs. (1.6)–(1.10) define the necessary conditions of optimality, and they form a well-defined TPBVP. BVP solvers can solve such TPBVP.

$$H = L(\boldsymbol{x}, \boldsymbol{u}, t) + \boldsymbol{\lambda}^T(t)\boldsymbol{f}(\boldsymbol{x}, \boldsymbol{u}, t) \tag{1.5}$$

$$\dot{\boldsymbol{\lambda}} = -\frac{\partial H}{\partial \boldsymbol{x}} \tag{1.6}$$

$$\frac{\partial H}{\partial \boldsymbol{u}} = 0 \tag{1.7}$$

$$\boldsymbol{\lambda}(t_0) = \boldsymbol{\nu}_\mathbf{0}^T \frac{\partial \boldsymbol{\Psi}}{\partial \boldsymbol{x}(t_0)} \tag{1.8}$$

$$\boldsymbol{\lambda}(t_f) = \frac{\partial \phi}{\partial \boldsymbol{x}(t_f)} + \boldsymbol{\nu}_\boldsymbol{f}^T \frac{\partial \boldsymbol{\Phi}}{\partial \boldsymbol{x}(t_f)} \tag{1.9}$$

$$\left(H + \frac{\partial \phi}{\partial t} + \boldsymbol{\nu}_\boldsymbol{f}^T \frac{\partial \boldsymbol{\Phi}}{\partial t} \right)_{t=t_f} = 0 \tag{1.10}$$

When more than one option exists after solving Eq. (1.7), Pontryagin's Minimum Principle (PMP) helps select the optimal control as shown in Eq. (1.11), where * refers to the optimal value. [24] It states that the optimal control will minimize the Hamiltonian, H, for all admissible values of control. [24]

$$H(t, \boldsymbol{x}^*(t), \boldsymbol{u}^*(t), \boldsymbol{\lambda}^*(t)) \leq H(t, \boldsymbol{x}^*(t), \boldsymbol{u}(t), \boldsymbol{\lambda}^*(t)) \tag{1.11}$$

Please note that Eq. (1.12), popularly known as the transversality condition [24] in the literature, is also used in this thesis to validate that the results obtained are optimal based on the time-history of the Hamiltonian. Usually, the Hamiltonian is not an explicit function of time and is a constant function. The value of the Hamiltonian obtained at the terminal point should thus be a constant over the entire time interval of the trajectory. The first part of Eq. (1.12), $H(t_f) + \phi_{t_f} dt_f$, is used to determine the constant value of the Hamiltonian. This terminal value of the Hamiltonian can then be matched with the Hamiltonian time-history plot to further verify and validate whether the results obtained are optimal. In Eq. (1.12), ϕ is the terminal cost, which is a function of the final time, t_f, and the final states, $\boldsymbol{x}_f$.

$$\left[H(t_f) + \frac{\partial \boldsymbol{\phi}}{\partial t_f}\right] dt_f + \left[\boldsymbol{\lambda}(t_f)^T + \frac{\partial \boldsymbol{\phi}}{\partial \boldsymbol{x}_f}\right] dx_f = 0 \tag{1.12}$$

1.2.2.2 Control Constraints

Control constraints are usually of the form shown in Eq. (1.13). The traditional approach augments the Hamiltonian as shown by Eq. (1.14) and obtains the control law for the constraint boundary by solving $\boldsymbol{C} = 0$.

$$\boldsymbol{C}(\boldsymbol{u}, t) \leq 0 \tag{1.13}$$

$$H = L + \boldsymbol{\lambda}^T \boldsymbol{f} + \boldsymbol{\mu}^T \boldsymbol{C} \tag{1.14}$$

The modified dynamic EOM for the costates along the constraint arcs is shown in Eq. (1.15), where Eq. (1.16) calculates the multipliers $\boldsymbol{\mu}$.

$$\dot{\boldsymbol{\lambda}} = -\frac{\partial H}{\partial \boldsymbol{x}} = -\boldsymbol{L}_{\boldsymbol{x}} - \boldsymbol{\lambda}^T \boldsymbol{f}_x - \boldsymbol{\mu}^T \boldsymbol{C}_{\boldsymbol{x}} \tag{1.15}$$

$$\frac{\partial H}{\partial \boldsymbol{u}} = \boldsymbol{L}_{\boldsymbol{u}} + \boldsymbol{\lambda}^T \boldsymbol{f}_u + \boldsymbol{\mu}^T \boldsymbol{C}_{\boldsymbol{u}} = 0 \tag{1.16}$$

The traditional approach pieces the constrained and the unconstrained arcs together. If the Hamiltonian is regular (i.e., the optimal control law for the OCP is unique), then the control stays continuous across the unconstrained and constrained arcs. [51, 72, 73]

1.2.2.3 Path Constraints

The presence of path constraints further complicates the boundary conditions by introducing corner conditions in certain costates and effectively splitting the trajectory into multiple arcs. Path constraints are usually of the form shown in Eq. (1.17). To obtain the control history for the constrained arc, the solution process takes time derivatives of the path constraints until a control variable appears explicitly. If this happens with the q^{th} derivative, the solution process augments the Hamiltonian as shown in Eq. (1.18), and obtains the control law for the constraint boundary by solving $\boldsymbol{S}^{(q)} = 0$. [24, 50]

$$\boldsymbol{S}(\boldsymbol{x}, t) \leq 0 \tag{1.17}$$

$$H = L + \boldsymbol{\lambda}^T \boldsymbol{f} + \boldsymbol{\mu}^T \boldsymbol{S}^q \tag{1.18}$$

The addition of path constraints also modifies the dynamic equations of the costates along the constrained arcs as shown in Eq. (1.19), where Eq. (1.20) determines the multipliers $\boldsymbol{\mu}$.

$$\dot{\boldsymbol{\lambda}} = -\frac{\partial H}{\partial \boldsymbol{x}} = -\boldsymbol{L}_{\boldsymbol{x}} - \boldsymbol{\lambda}^T \boldsymbol{f}_x - \boldsymbol{\mu}^T \boldsymbol{S}^q_{\boldsymbol{x}} \tag{1.19}$$

$$\frac{\partial H}{\partial \boldsymbol{u}} = \boldsymbol{L_u} + \boldsymbol{\lambda}^T \boldsymbol{f}_u + \boldsymbol{\mu}^T \boldsymbol{S}_{\boldsymbol{u}}^q = 0 \tag{1.20}$$

The states are continuous at the entry (t_1) and exit (t_2) of the constrained arc as shown in Eq. (1.21). The solution process chooses corner conditions on costates such that the costates are continuous at the exit of the constrained arc as shown in Eq. (1.22). The tangency conditions described in Eq. (1.23) and corner conditions in Eq. (1.24) and Eq. (1.25) apply at the entry point of the constrained arc, where $\boldsymbol{\Pi}$ are the multipliers corresponding to the tangency constraint conditions.

$$\begin{aligned} \boldsymbol{x}(t_1{}^+) &= \boldsymbol{x}(t_1{}^-) \\ \boldsymbol{x}(t_2{}^+) &= \boldsymbol{x}(t_2{}^-) \end{aligned} \tag{1.21}$$

$$\begin{aligned} \boldsymbol{\lambda}(t_2{}^+) &= \boldsymbol{\lambda}(t_2{}^-) \\ H(t_2{}^+) &= H(t_2{}^-) \end{aligned} \tag{1.22}$$

$$\boldsymbol{N}(\boldsymbol{x}, t) = \left[S(\boldsymbol{x}, t) \;\; S^1(\boldsymbol{x}, t), ..., \;\; S^{q-1}(\boldsymbol{x}, t) \right]^T \tag{1.23}$$

$$\boldsymbol{\lambda}(t_1{}^+) = \boldsymbol{\lambda}(t_1{}^-) + \boldsymbol{\Pi}^T \boldsymbol{N}_x \tag{1.24}$$

$$H(t_1{}^+) = H(t_1{}^-) + \boldsymbol{\Pi}^T \boldsymbol{N}_t \tag{1.25}$$

1.2.2.4 Additional Necessary Conditions

Eq. (1.26) states the additional necessary conditions needed for OCPs with path constraints in a general form, where q is the order of the path constraint. [50, 51, 73] Note that the superscript for μ represent the order of its time-derivative.

$$\pi_{k-1} - (-1)^{q-k}\mu^{q-k}(t^{+}_{\text{ENTRY}}) \begin{cases} \geq 0 & \text{if} \quad \text{k} = 1 \\ = 0 & \text{if} \quad \text{k} = 2, ..., \text{q}, \text{q} > 1 \end{cases} \tag{1.26a}$$

$$(-1)^{q-k}\mu^{q-k}(t^{-}_{\text{EXIT}}) \begin{cases} \geq 0 & \text{if} \quad \text{k} = 1, \\ = 0 & \text{if} \quad \text{k} = 2, ..., \text{q}, \text{q} > 1 \end{cases} \tag{1.26b}$$

$$(-1)^{q}\mu^{q}(t) \geq 0 \quad \text{if} \quad \text{t} \in [\text{t}_{\text{ENTRY}}, \text{t}_{\text{EXIT}}] \tag{1.26c}$$

1.2.2.5 Bang-Bang Control and Singular Arcs

Suppose a bounded OCP with a scalar control, u, has a Hamiltonian, H, as shown in Eq. (1.27). [24] The control stays bounded between -k and +k. Since H is linear in u, Eq. (1.7) results in Eq. (1.28).

$$H = H_0(t, \boldsymbol{x}(t), \boldsymbol{\lambda}(t)) + H_1(t, \boldsymbol{x}(t), \boldsymbol{\lambda}(t))u \tag{1.27}$$

$$\frac{\partial H}{\partial u} = H_1 \tag{1.28}$$

The choice of u cannot influence $H_0(t, \boldsymbol{x}^*(t), \boldsymbol{\lambda}(t))$, so the solution process ignores this term. If H_1 is a positive number, then the solution process picks the lowest value of u to minimize H. Similarly, if H_1 is less than 0, the process picks the maximum value of u. In summary, the PMP gives the control law shown in Eq. (1.29).

$$u = \begin{cases} -k & \text{if } H_1 > 0 \\ \text{unknown} & \text{if } H_1 = 0 \\ k & \text{if } H_1 < 0 \end{cases} \tag{1.29}$$

OCT defines the coefficient $H_1(t, \boldsymbol{x}^*(t), \boldsymbol{\lambda}(t))$ as the switching function. When H_1 oscillates through positive and negative values, the control law switches back and forth between its lower and upper bounds, attaining a "bang-bang" form. When H_1

$\equiv 0$ units on some non-zero time interval, say $[t_1,t_2] \leq [t_0,t_f]$, then the subarc $[t_1,t_2]$ becomes a singular subarc and the control no longer influences H, leading to non-uniqueness issues. To determine unique candidate singular controls, the traditional approach differentiates Eq. (1.7) with respect to time as shown in Eq. (1.30). The last term in Eq. (1.30) vanishes because the derivative of Hamiltonian with respect to the control, H_u, is a constant and $\frac{\partial H_u}{\partial u}$ becomes 0 units as a result.

$$\frac{d}{dt}(H_u) = 0 = \frac{\partial H_u}{\partial t} + \frac{\partial H_u}{\partial x}\dot{x} + \frac{\partial H_u}{\partial \lambda}\dot{\lambda} + \frac{\partial H_u}{\partial u}\dot{u} \tag{1.30}$$

The solution process forms $\frac{d^2}{dt^2}H_u \equiv 0$, and if u appears explicitly, the process uses the condition specified in Eq. (1.30) along with the Generalized Legendre-Clebsch Condition (GLCC) as shown in Eq. (1.31) to determine the singular control law. If u does not appear explicitly, the solution process takes even time derivatives of H_u until the process satisfies GLCC along with the conditions specified by odd time-derivatives of H_u [24] to obtain the singular control law.

$$(-1)^q \frac{\partial}{\partial u}\left(\frac{d^{2q}H_u^*}{dt^{2q}}\right) \geq 0 \tag{1.31}$$

1.2.2.6 Optimization Tool

This thesis uses MATLAB's BVP solver, bvp4c [74,75], to implement the indirect method of optimization. This solver is a finite difference code that implements the three-stage Lobatto IIIa formula. This is a collocation formula through which the collocation polynomial provides a C^1 continuous solution that is fourth-order accurate. The residual of the continuous solution forms the basis for mesh selection and error control.

The solver bvp4c aims at solving BVPs of the form shown in Eq. (1.32a) subjected to non-linear boundary conditions shown in Eq. (1.32b). Please note that x here

ranges between the values a and b. Also, $\boldsymbol{p}$ is the vector of unknown parameters and n is the number of mesh points for the BVP.

$$\boldsymbol{y}' = \boldsymbol{f}(x_n, \boldsymbol{S}(x_n)) \tag{1.32a}$$

$$\boldsymbol{g}(\boldsymbol{y}(a), \boldsymbol{y}(b), \boldsymbol{p}) = 0 \tag{1.32b}$$

The approximate solution to this BVP, $\mathbf{S}(x)$, is a cubic polynomial on each mesh subinterval, which satisfies the boundary conditions specified in Eq. (1.33a). $\mathbf{S}(x)$ also satisfies the differential equations specified by the collocation at both end points and the mid-point of each mesh subinterval as shown in Eqs. (1.33b)–(1.33d).

$$\boldsymbol{g}(\boldsymbol{S}(a), \boldsymbol{S}(b)) = 0 \tag{1.33a}$$

$$\boldsymbol{S}'(x_n) = \boldsymbol{f}(x_n, \boldsymbol{S}(x_n)) \tag{1.33b}$$

$$\boldsymbol{S}'((x_n + x_{n+1})/2) = \boldsymbol{f}((x_n + x_{n+1})/2, \boldsymbol{S}((x_n + x_{n+1})/2)) \tag{1.33c}$$

$$\boldsymbol{S}'(x_{n+1}) = \boldsymbol{f}(x_{n+1}, \boldsymbol{S}(x_{n+1})) \tag{1.33d}$$

The solver bvp4c employs some interesting properties of the Simpson method for solving BVPs with poor initial guesses. [76] Ultimately, bvp4c calculates the residual $r(x)$ given by Eq. (1.34) and the residual in the boundary conditions, $\boldsymbol{g}(\boldsymbol{S}(a), \boldsymbol{S}(b))$. Here $\boldsymbol{S}'(x)$ is the exact solution for the BVP. For a low enough value of these residuals, bvp4c converges to a good solution, very close to $\boldsymbol{S}'(x)$.

$$\boldsymbol{r}(x) = \boldsymbol{S}'(x) - \boldsymbol{f}(x, \boldsymbol{S}(x)) \tag{1.34}$$

1.2.2.7 Advantages and Disadvantages of Direct and Indirect Methods of Optimization

Table 1.1 summarizes the major advantages and disadvantages of direct and indirect methods. [5, 53, 77, 78] The problem formulation for OCPs with path constraints using indirect methods becomes difficult as it requires a priori knowledge of the sequence and number of constrained and unconstrained arcs. [5, 79] Moreover, the trajectory designer faces difficulty while selecting an initial guess for the non-intuitive

costates. However, the advantages of indirect methods prompt further development of OCT. The research community working on OCT decreased massively since 1970's due to the difficulties presented by indirect methods in solving OCPs. Recently, this small community, including researchers at RDSL, addressed the issues with indirect methods to an extent.

Table 1.1.: Comparison between direct and indirect methods of optimization.

Feature	**Direct Methods**	**Indirect Methods**
Problem formulation	Fast	Slow
Sensitivity to an initial guess	Low	High
Handling path constraints	Easy	Difficult
Convergence accuracy	Can be inaccurate	Accurate
Parallel computing	Difficult	Easy
Developer and user community	Very large	Very small
Available solvers	Many	Few

1.2.2.8 Resolution of Issues for Indirect Methods

The research work done at RDSL has successfully addressed the three issues regarding use of indirect methods as mentioned previously.

- **Resolution of Issue 1 (Concerning Problem Formulation):** Advancements in modern symbolic computation enable the automated derivation of the necessary conditions of optimality.

- **Resolution of Issue 2 (Concerning Path Constraints):** Continuation of indirect methods enables real-time assessment of the constrained-arc sequence and the automated inclusion of appropriate constraints.

- **Resolution of Issue 3 (Concerning Initial Guess):** Continuation of indirect methods enables rapid evolution to complex optimal solutions without a good initial guess.

The MATLAB-Mathematica based framework developed at RDSL and used in this study is shown in Fig. 1.4. [5] This framework is the culmination of the Ph.D. research work carried out by Grant.

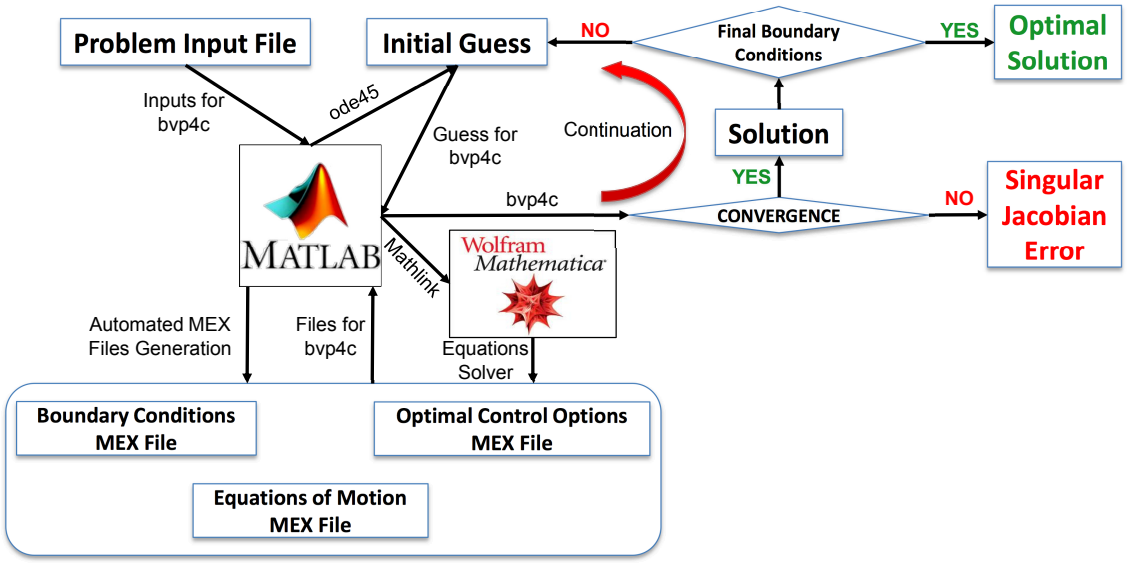

Figure 1.4.: MATLAB and Mathematica based rapid optimization framework developed at RDSL.

Mathematica is a state-of-the-art symbolic computation toolbox, which Grant used to resolve issue 1 with the indirect methods. [5, 80] An input MATLAB file includes the problem statement and constants used to generate the boundary conditions and EOM files. In order to generate the optimal control law, MATLAB links with Mathematica to generate a MATLAB file listing all the optimal control options. PMP then selects the best control combination at each node of the trajectory. Thus, the necessary conditions for optimality are automatically generated in this framework.

This framework can use an initial guess file. A simpler and faster option is to obtain the initial guess using auto-generation, where MATLAB's ODE45 propagates

initial (or terminal) values of the states with an EOM file for a small, predetermined time. MATLAB's codegen then generates MEX files corresponding to the boundary conditions, EOMs, and optimal control options.

A simpler problem is thus solved for the initial guess provided to MATLAB's bvp4c, increasing the likelihood of obtaining convergence. By marching the values of the states to terminal (or initial) values, the complexity of the problem increases. The converged solution for the simpler problem serves as a guess for the subsequent complex problem. This process is popularly known as continuation. [81] The continuation process can break during an intermediate step if the BVP is very difficult (or impossible) to solve, thereby generating an error message: a singular Jacobian encountered. To resolve this issue, the solution process requires changing the number of steps or the order of continuation sets. For example, running a continuation first on altitude and then on velocity can result in a faster convergence as against running continuation on altitude and velocity simultaneously.

Mansell and Singh made further improvements to the RDSL's optimization framework for addressing issue 3 with indirect methods. Mansell developed a heuristic analytical method to control the order and selection of continuation sets for the OCP. [82] On the other hand, Singh used homotopy based approximation methods to obtain a good initial guess for complex OCPs that guarantee convergence. [83,84] The order of continuation is an ongoing work at RDSL and can substantially help in rapidly solving complex OCPs. Researchers at RDSL have also been developing a Python based, open-source and more efficient optimization framework named Beluga. However, this thesis has used the MATLAB based framework in entirety.

At RDSL, Grant and Mall devised a new innovative way of landing human class payloads on the surface of Mars, which sets motivation for this thesis. The following discussion includes the issues with solving this high mass Mars landing problem using traditional OCT.

1.2.2.9 Spurious Results for the High Mass Mars Problem

To date, Mars exploration and human spaceflight used blunt bodies, such as sphere-cones and capsules. The research community views entry, descent, and landing (EDL) at Mars as a deceleration challenge within a finite time-line. Braun and Manning outlined that without some combination of the following: 1) decreasing the hypersonic ballistic coefficient, 2) extending the established supersonic parachute deployment region, 3) moving to a more effective supersonic decelerator, or 4) increasing the vertical lift of the entry vehicle, landing a mass as low as 2 mT on the Martian surface may be infeasible. [85] Christian et al. concluded that the extension of traditional EDL technologies may be insufficient for human Mars exploration. [86] Steinfeldt et al. made comparisons between different technologies for a human-class payload mission to Mars. These comparisons concluded that as the required payload mass increases, the severity of the deviation from traditional Mars EDL technologies also increases. [87]

Hypersonic Inflatable Aerodynamic Decelerators (HIADs) have been predominantly identified as a key enabler for Mars missions based on points 1) and 3) of Braun and Manning, and testing of these systems is underway. [85] The current research estimates the diameter of HIADs necessary for human-class payloads between 20 and 40 m, which is very large. [88] This results in a low ballistic coefficient, low L/D, and supersonic terminal velocities at Mars. Inflating large inflatables is also a cause of concern and involves risk. Moreover, it is hard to control and guide such blunt and voluminous inflated systems. Supersonic retropropulsion was found to deliver even lower payloads than HIAD-based architectures by EDL systems analysis conducted at NASA. [89, 90]

At NASA Ames, Venkatapathy et al. carried out a feasibility study of an umbrella-based EDL system, popularly called as Adaptable, Deployable Entry Placement Technology (ADEPT). [91] Both HIAD and ADEPT configurations do not offer protection for payload. [92, 93] There are concerns about heating on the payload during aero-

capture and entry for an exposed payload. These drag based technologies require a significant amount of additional mass to mitigate this risk. SpaceX has initially been a proponent of propulsion based EDL systems such as supersonic retropropulsion (SRP) for high mass Mars exploration. [94, 95] However, SRP requires carrying a large amount of rocket propellant, leading to higher mission costs. [90, 96] A part of the EDL community thus started investigating lift-based architectures to explore and provide more EDL options for high mass Mars missions.

Many studies looked into using bank angle modulation to impact vertical lift of the entry vehicle. [97, 98] In 2009, Lafleur and Cerimele proposed augmenting angle of attack modulation with bank angle modulation to maximize the terminal altitude for a Mach 3.5 terminal velocity at Mars and to utilize the lifting properties of the vehicle for deceleration. [99] Recently, Cerimele et al. proposed a rigid mid L/D approach to human-class EDL. [100] In 2012, Cruz-Ayoroa and Braun investigated high lift and drag properties of slender entry vehicles (SEVs) with deployable aerosurfaces and performed an in-depth systems study including aerodynamics and aerothermodynamics. [101] The major focus of their study was to decrease the ballistic coefficient of such SEVs by increasing drag. These lift-based EDL technologies jettison the deployable aerosurfaces at the supersonic phase and do not fully utilize the aerosurfaces to decrease the energy further. Thus, these prior studies did not explore the true potential of the lift of SEV. Grant and Mall developed a new innovative way of flying and landing human class payloads to the surface of Mars using SEVs with high lift. [102] At the International Astronautical Congress in 2017, Elon Musk shared his approach to make life interplanetary by landing on Mars using a similar flying technique, highlighting its importance. [103]

The objective for the lift-based high mass Mars problem is to maximize the terminal altitude for a safe terminal descent phase. The trajectory includes three phases: dive, cruise, and loft. The dive phase implements the heat-rate and g-load constraints. During the cruise phase, the SEV maintains a constant safe altitude. Finally, the SEV

lofts to a higher altitude from where it initiates the terminal descent phase. Fig. 1.5 illustrates this EDL technique.

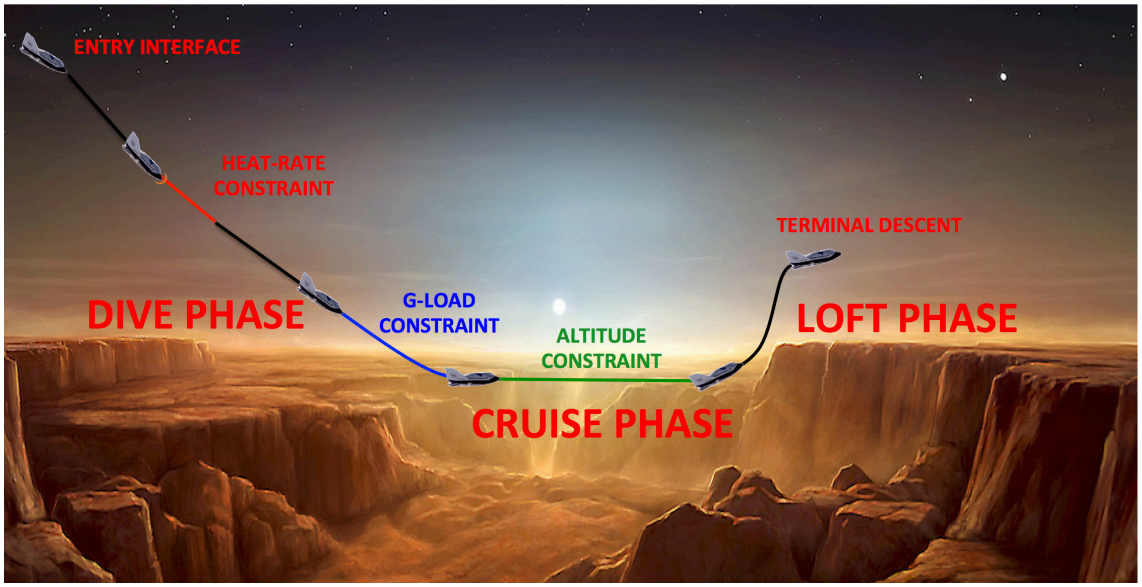

Figure 1.5.: The lift-based EDL architecture developed at RDSL. [102]

This study encountered an issue while using traditional indirect methods to solve this problem. The trajectory plot, shown in Fig. 1.6, gives an impression that the solution is correct. However, the flight path angle time-history plot indicates otherwise. For the SEV to fly at a constant altitude, the flight path angle, γ, should be 0^0. But as shown in Fig. 1.7, γ ranges between -60^0 and 0^0.

Upon further investigation, it was found that the traditional smoothing regularization method employed in traditional indirect methods, is unable to bound the error controls used in this problem. The smoothing method, discussed in Sec. 2.2, uses Eq. (1.35) to solve this problem, where the error control appears explicitly after taking the first derivative of the constraint, S. This method introduces a small error into the EOM corresponding to the altitude, $\dot{h}$, to regularize the problem. Although the error term, ϵu_{ϵ_1}, usually remains small in Eq. (1.35a); it has the potential to blow up while staying unbounded.

$$S^1 = \dot{h} = v \sin\gamma + \epsilon u_{\epsilon_1} = 0 \tag{1.35a}$$

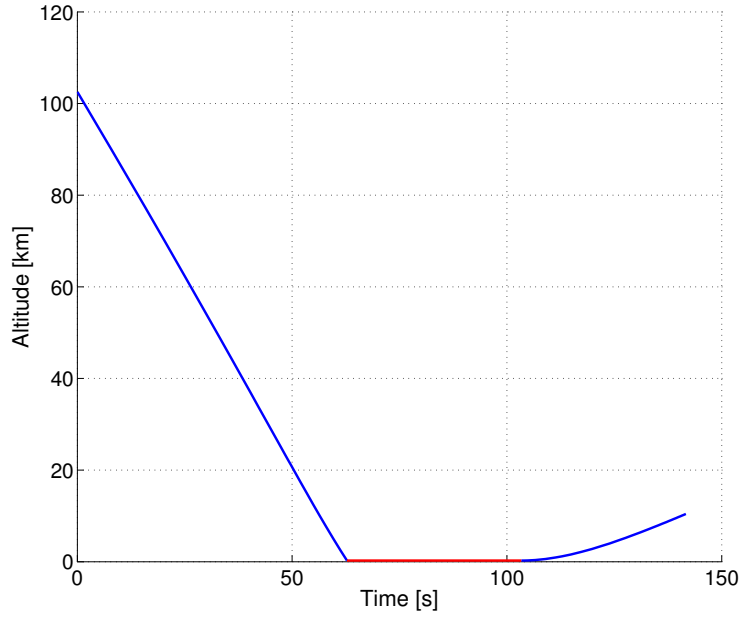

Figure 1.6.: The altitude time-history plot for the high mass Mars problem.

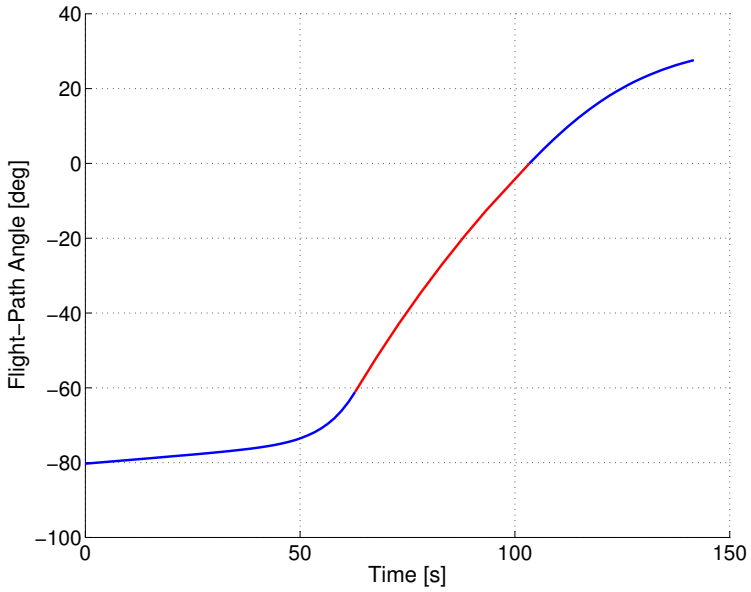

Figure 1.7.: The flight path time-history plot for the high mass Mars problem.

$$u_{\epsilon_1} = -\frac{v \sin\gamma}{\epsilon} \tag{1.35b}$$

Eq. (1.35b) shows the unbounded form of the error control, u_{ϵ_1}. Thus, it blows up for a large value of velocity, v, coupled with a very low value of error parameter, ϵ, and a non-zero flight path angle, γ, as shown in Fig. 1.8. This leads to unrealistic results, which give a false impression of obtaining correct solutions for the OCP. Realistically, error controls of traditional smoothing technique should be close to 0 units.

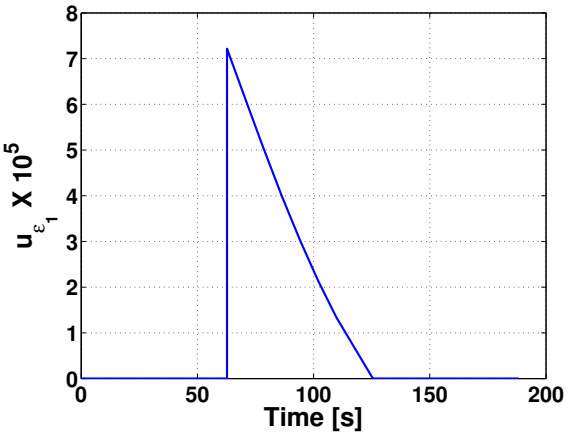

Figure 1.8.: An Unrealistically large error control for the high mass Mars problem.

The spurious result for the high mass Mars problem paved the way for the development of two new regularization methods at RDSL. These new methods simplify and advance OCT for better resolution of issue 2 with indirect methods. The following discussion includes an overview of regularization methods developed at RDSL.

1.2.2.10 Regularization Methods

Regularization, in mathematics and statistics, refers to a process of introducing additional information to solve an ill-posed problem. [104–114] Regularization methods developed at RDSL aim at reducing the problem formulation time and to handle the path constraints with ease. The core idea of these methods is to remove possible discontinuities in the state EOMs of the OCPs with control and path constraints by

modifying controls using smoothing functions. Saturation functions are a class of smoothing functions used for path constraint regularization. Some of the common examples of saturation functions are the sigmoid, arc-tangent, and hyperbolic tangent functions. Antony developed a regularization method based on these saturation functions at RDSL called Integrated Control Regularization Method (ICRM). [79,115]

Ref. 116 forms the basis for ICRM in which the path constraints of the OCP, $c_{\mathrm{i}}(\mathbf{x})$, are shown in Eq. (1.36). A suitable saturation function, ψ, replaces these constraints as shown in Eq. (1.37).

$$c_{\mathrm{i}}(\mathbf{x}) \in [{c_{\mathrm{i}}}^{-}, {c_{\mathrm{i}}}^{+}], \quad \mathrm{i} = 1...\mathrm{p} \tag{1.36}$$

$$c_{\mathrm{i}}(\mathbf{x}) = \psi(\xi_{i,1}), \quad \mathrm{i} = 1...\mathrm{p} \tag{1.37}$$

The solution process then successively differentiates $c_{\mathrm{i}}(\mathbf{x})$ with respect to time until the control variable appears. For example, if $c_{\mathrm{i}}(\mathbf{x})$ is of the order 2, the control appears by differentiating the constraint equation twice as shown in Eq. (1.38a) and Eq. (1.38b). The solution process introduces new state variables, $\xi_{\mathrm{i,j}}$, and new control variable, u_{ϵ_1}, with EOMs as shown in Eq. (1.38c) and Eq. (1.38d).

$$c^{(1)}(\mathbf{x}) = \psi' \dot{\xi}_{\mathrm{i},1} := h_1 \tag{1.38a}$$

$$c^{(2)}(\mathbf{x}) = \psi'' {\xi^2}_{\mathrm{i},2} + \psi' \dot{\xi}_{\mathrm{i},2} := h_2 \tag{1.38b}$$

$$\dot{\xi}_{\mathrm{i},1} = \xi_{\mathrm{i},2} \tag{1.38c}$$

$$\dot{\xi}_{\mathrm{i},2} = u_{\epsilon_1} \tag{1.38d}$$

The objective functional, J, has an added term to the path cost with respect to Eq. (1.1) as shown in Eq. (1.39a), where ϵ is a regularization parameter. Finally, an equality constraint, is also added to the problem as shown in Eq. (1.39b), where q is the order of the constraint. A suitable numerical method then solves the resulting extended OCP with path constraints.

$$\text{Minimize: } J = \phi(\boldsymbol{x}(t_f), t_f) + \int_{t_0}^{t_f} (L(\boldsymbol{x}, \boldsymbol{u}, t) + \epsilon u_{\epsilon_1}) \mathrm{d}t \tag{1.39a}$$

$${c_{\mathrm{i}}}^{(\mathrm{q})}(\mathbf{x}) - h_{\mathrm{q}} = 0 \tag{1.39b}$$

Ref. 116 recommends a sigmoid function for two-sided functions. The method formulates Eq. (1.40a) so that the resulting function has a slope of 1 at $\xi = 0$. Eq. (1.40b) shows the scaling of the exponential term, s, in this resulting function.

$$\psi(\xi) = c^+ - \frac{c^+ - c^-}{1 + \exp(s\xi)} \tag{1.40a}$$

$$s = \frac{4}{c^+ - c^-} \tag{1.40b}$$

ICRM adds the EOM for the control variable, u, to the OCP, and obtains the control numerically. ICRM is a well-developed regularization technique to solve OCPs with control and path constraints. However, there are three issues with ICRM.

- **Issue 1:** The constraint is never active in this method, which might affect the overall result for the OCP. Moreover, ICRM cannot solve OCPs with boundary points on the constraint.

- **Issue 2:** The use of extra variables and equations significantly increases the amount of mathematics involved in ICRM, thereby affecting the problem solving process.

- **Issue 3:** ICRM cannot obtain the control law analytically, thereby affecting the quality of solutions to the OCPs.

This thesis provides a complimentary solution to ICRM by investigating the usage of periodic trigonometric functions instead of saturation functions for regularization of OCPs with control and path constraints. The following section describes the contributions and outline of this thesis.

1.3 Contributions and Outline of Thesis

To improve and advance the current literature on OCT, this study has the following three major research objectives.

1. Devise a new regularization technique for bang-bang and singular control problems that can overcome the drawbacks suffered by the traditional smoothing method.

2. Develop a simplified, complete and improved methodology for solving OCPs with pure control constraints and non-linear controls in the Hamiltonian.

3. Develop a simplified and improved methodology for solving OCPs with mixed state-control constraints and pure state constraints.

This thesis also comprises of the following four chapters. Chapter 2 introduces a new regularization method to solve bang-bang and singular control problems. Chapter 3 extends the idea proposed in chapter 2 to OCPs with control constraints where controls appear in a non-linear form in the Hamiltonian using a method called Trigonometrization. Chapter 4 extends the Trigonometrization technique to OCPs with mixed state-control constraints and pure state constraints. Chapter 5 summarizes this thesis and lists the future work needed to further advance OCT using Trigonometrization. Fig. 1.9 shows the class of OCPs solved in the different chapters and the overall flow of this thesis.

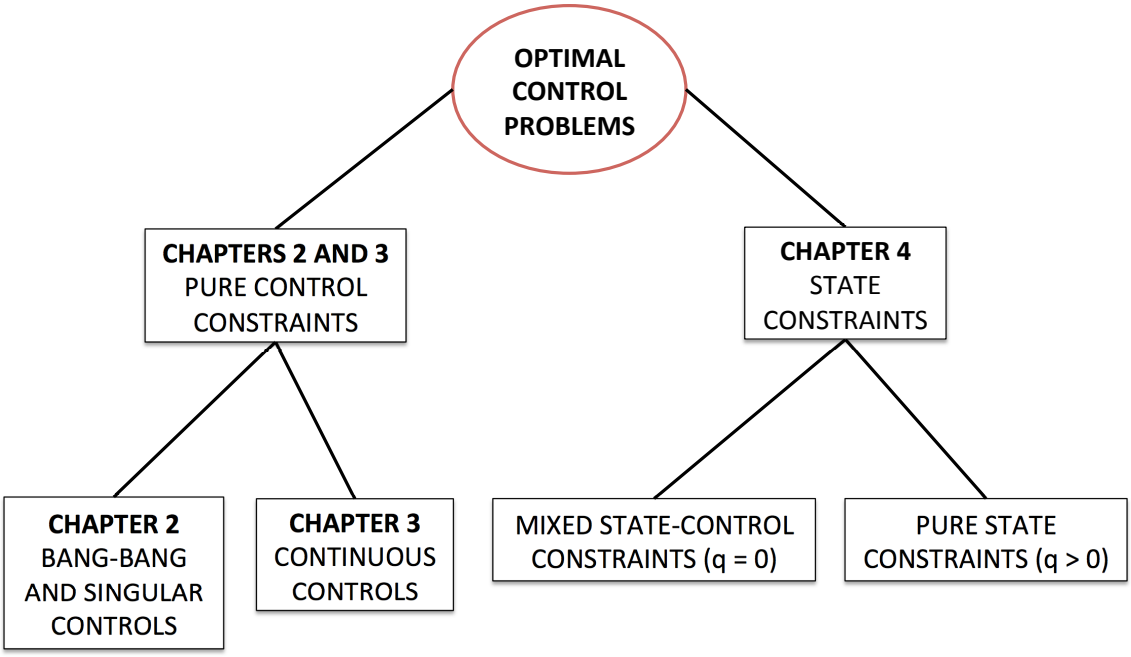

Figure 1.9.: Flow of this thesis.

2. Advancements in Solving Bang-Bang and Singular Control Problems

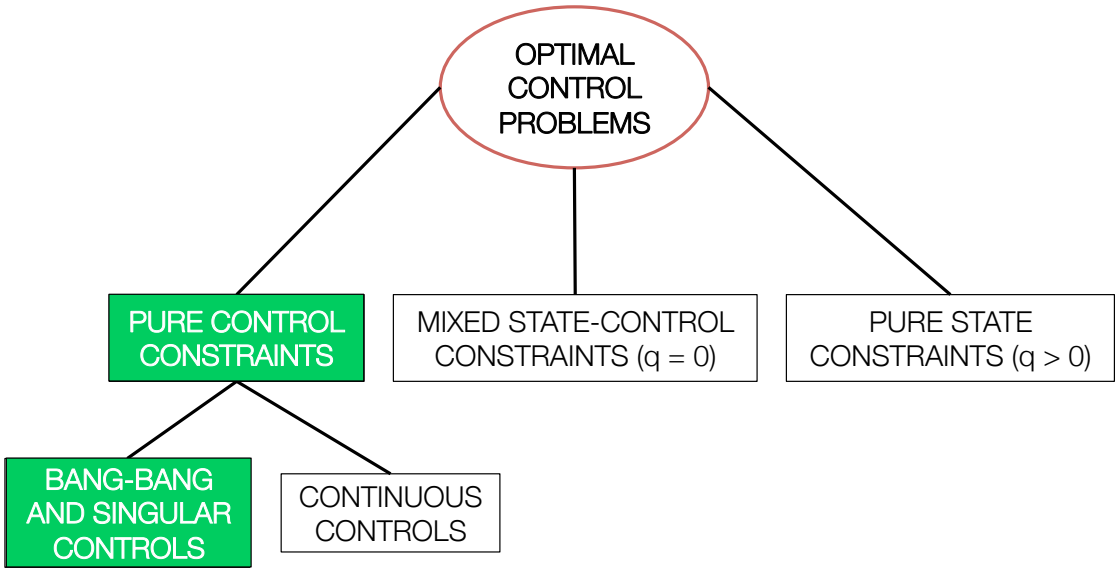

2.1 Introduction

Bang-bang control problems are a class of OCPs where the control appears in a linear form in the Hamiltonian. The optimal control for such problems often stays at extremum values. When switches in control between these values occur, the optimization solver encounters numerical issues when using OCT that relies on derivatives.

A common approach to solving these numerical issues is to regularize the OCP by adding a perturbed energy term in the cost functional. [47, 117–121] The focus of this chapter is the class of regularization methods that perturb the dynamics of the system. Silva and Trélat [48] developed one such smooth regularization technique

(Sec. 2.2) that uses the concept of error controls and an error parameter, ϵ, to obtain a smooth control structure. This smoothing method provides a relation between the error controls and the smooth control, using a particular condition, which is discussed in Sec. 2.2.

However, this chapter uncovers some issues with the traditional smooth regularization method. This chapter introduces a new method termed as Epsilon-Trig regularization (Sec. 2.3), which addresses the issues encountered by the traditional smooth regularization approach using trigonometric functions.

2.2 Traditional Smooth Regularization Method

Bang-bang control problems have numerical issues, when there are discontinuities in the control structure, while using OCT that relies on derivatives. Researchers developed various types of regularization methods to resolve these numerical issues by solving for an auxiliary problem instead of the original problem. The first smoothing regularization method is energy-based, where the cost functional is perturbed. Some of the penalty functions used in this approach are the quadratic penalty, extended logarithmic penalty, and logarithmic barrier. [47] There are also piecewise-linear methods in the energy-based approach, commonly known as simplicial methods that build a piecewise linear approximation of homotopy to solve the auxiliary problem. [122] An important aerospace problem on low thrust trajectory optimization has been solved using various forms of energy-based homotopic regularization methods. [123–126]

This study focuses on another class of regularization methods, in which the solution process introduces perturbation in the dynamics of the state system. [127] Silva and Trélat [48] devised one such method to pose the bang-bang control problem as shown in Eq. (2.1). The smoothing method introduces a small error into k state equations, where the control is absent, using the combination of an error parameter, ϵ, and error controls, u_{ϵ_n}. Graphically, this is shown in Fig. 2.1, where the error controls (shown in blue) solve for a smooth optimal control (shown in green) instead of the

original discontinuous control structure (shown in red). Please note that the error controls happen to be orthogonal to the smooth control, which was not explained in the traditional regularization method. The general form of the state equations with error parameter and error controls is shown in Eq. (2.1b), where n ranges between 1 and k. For simplicity, only one state equation has the original control as shown in Eq. (2.1c).

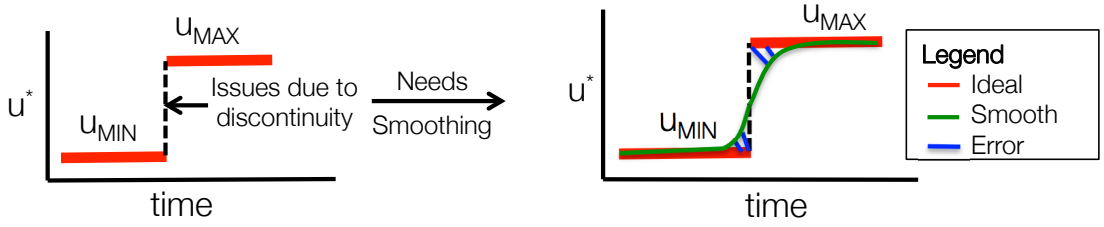

Figure 2.1.: Resolving discontinuity issues with bang-bang control by smoothing it.

$$\text{Minimize: } J = J(t_f, \boldsymbol{x}(t_f)) \tag{2.1a}$$

$$\text{Subject to: } \dot{x}_{\epsilon_n} = f_n(t, \boldsymbol{x}(t)) + \epsilon u_{\epsilon_n} \tag{2.1b}$$

$$\dot{x}_{k+1} = f_{k+1}(t, \boldsymbol{x}(t)) + u \tag{2.1c}$$

$$u^2 + \sum_{n=1}^{k} u_{\epsilon_n}^2 = 1 \tag{2.1d}$$

PMP requires Eq. (2.1d) to hold along non-singular sub arcs and obtains u at the boundary of the control constraint. Upon calculations using Eq. (1.7) and Eq. (2.1d), the values of controls, u and u_ϵ, are found as shown in Eq. (2.2).

$$u^* = \frac{-\lambda_{x_{k+1}}}{\sqrt{\epsilon^2 \sum_{n=1}^{k} \lambda_{x_n}^2 + \lambda_{x_{k+1}}^2}} \tag{2.2a}$$

$$u_{\epsilon_n}^* = \frac{-\epsilon \lambda_{x_n}}{\sqrt{\epsilon^2 \sum_{n=1}^{k} \lambda_{x_n}^2 + \lambda_{x_{k+1}}^2}} \tag{2.2b}$$

It becomes possible to solve a problem very close to the original OCP that has a bang-bang control solution, where ϵ determines the amount of smoothing of the bang-bang control. Usually, the value of ϵ is small (e.g., 0.01 units).

2.2.1 Existing Issues

Although the traditional smooth regularization method resolves issues related to switches in control, it fails to address the following issues.

1. Introducing too many error controls complicates the problem formulation and solution process.

2. For OCPs with path constraints, the resulting control law for the constraint arc violates an important condition on controls as specified in Eq. (2.1d). The resulting error controls grow very large in magnitude and become unrealistic.

3. The error parameter, ϵ, becomes dimensionally inconsistent when used in more than one state equation, which introduces numerical issues while scaling the original problem. Scaling the OCP can convert it from an ill-conditioned to a well-conditioned form.

Eq. (2.3) determines the unit of ϵ. Since the state equations generally have different units, the unit of ϵ for the same control will also be different. Thus, ϵ becomes dimensionally inconsistent. For e.g., if angle of attack is the control measured in radians and if ϵ is present in two state equations, one corresponding to altitude, h, and other corresponding to velocity, v, then the same ϵ has two different units of m/(s rad) and m/(s^{2}rad), respectively.

$$\text{Unit of } \epsilon = \frac{\text{The unit of state equation}}{\text{The unit of control}} \tag{2.3}$$

2.2.2 Solving a Bounded Control Oscillator Problem using Traditional Smoothing Method

A minimal time oscillator problem [24] is shown in Eq. (2.4), where the traditional smooth regularization method is used. Table 2.1 contains the constants used in this problem.

$$\text{Minimize: } J = t_f \tag{2.4a}$$

$$\text{Subject to: } \dot{x}_1 = x_2 + \epsilon u_\epsilon \tag{2.4b}$$

$$\dot{x}_2 = -x_1 + u \tag{2.4c}$$

Table 2.1.: Constants for the oscillator problem.

Parameter	x_{1_0}	x_{2_0}	x_{1_f}	x_{2_f}	ϵ
Value	1	1	0	0	0.001

The Hamiltonian, H, for the above problem, is shown in Eq. (2.5). Eq. (1.7) helps in generating the optimal control law shown in Eq. (2.6). The Hamiltonian also helps in generating the EOMs for the costates as shown in Eq. (2.7).

$$H = \lambda_{x_1}(x_2 + \epsilon u_\epsilon) + \lambda_{x_2}(-x_1 + u) \tag{2.5}$$

$$u^* = \frac{-\lambda_{x_2}}{\sqrt{\epsilon^2\lambda_{x_1}^2 + \lambda_{x_2}^2}} \tag{2.6a}$$

$$u_\epsilon^* = \frac{-\epsilon\lambda_{x_1}}{\sqrt{\epsilon^2\lambda_{x_1}^2 + \lambda_{x_2}^2}} \tag{2.6b}$$

$$\dot{\lambda_{x_1}} = \lambda_{x_2} \tag{2.7a}$$

$$\dot{\lambda_{x_2}} = -\lambda_{x_1} \tag{2.7b}$$

2.3 Epsilon-Trig Regularization Method

Trigonometry is one of the most basic elements of mathematics, used in problems involving measurements, number theory, Fourier series and Fourier transforms. [128] The controls need to be bounded in bang-bang control problems. When the controls assume a trigonometric form, they gain implicit bounds. This study developed a new regularization method to bound controls using trigonometry, named as the Epsilon-Trig regularization method, where epsilon stands for the parameter introducing a small disturbance in the state equations and trig stands for the error control expressed in a trigonometric form.

This method is very similar to the traditional approach except for one major addition. Instead of posing the OCP with different controls, this method reformulates the problem to have only one control, u_{TRIG}. Trigonometric functions can then help in forming two orthogonal control components, one is the smooth control and the other is the error control. This method uses the concept of projection. [129]

The projection and error for $\boldsymbol{b}$ (represented by $\boldsymbol{OB}$) at an angle θ on $\boldsymbol{a}$ (represented by $\boldsymbol{OA}$) is shown in Fig. 2.2. $\boldsymbol{OP}$ represents the projection, p, and calculates the dot product of $\boldsymbol{a}$ and $\boldsymbol{b}$. It shows how much $\boldsymbol{b}$ is in the direction of $\boldsymbol{a}$. On the other hand, the error, $\boldsymbol{e}$ (represented by $\boldsymbol{PB}$) shows how much $\boldsymbol{b}$ is away from $\boldsymbol{a}$. Please note that $\boldsymbol{e}$ is orthogonal to the projection, $\boldsymbol{p}$.

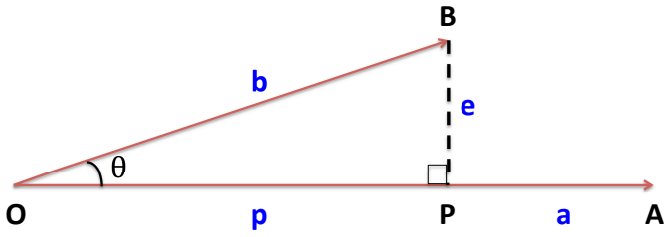

Figure 2.2.: Projection and error of $\boldsymbol{b}$ on $\boldsymbol{a}$.

As shown in Fig. 2.3, the control can attain a maximum value of $\boldsymbol{OB}$ for the original normalized bang-bang control problem indicated in red. $\boldsymbol{OA}$ represents the smoothed bang-bang control (indicated in green) and $\boldsymbol{BA}$ represents the error control.

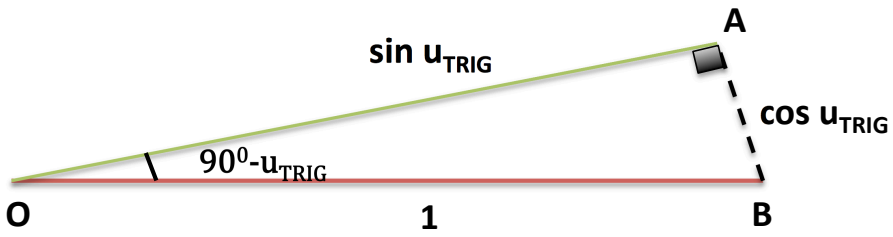

Figure 2.3.: Smoothing of control using Trigonometrization.

The error control is orthogonal to the smooth control such that a triangle is formed with sides measuring sin u_{TRIG}, cos u_{TRIG} and 1. Eq. (2.1) reformulates into Eq. (2.8), where the value of n varies from 2 to k.

$$\text{Minimize: } J = J(t_f, \boldsymbol{x}(t_f)) \tag{2.8a}$$

$$\text{Subject to: } \dot{x}_\epsilon = f_1(t, \boldsymbol{x}(t)) + \epsilon \cos u_{\text{TRIG}} \tag{2.8b}$$

$$\dot{x}_n = f_n(t, \boldsymbol{x}(t)) \tag{2.8c}$$

$$\dot{x}_{k+1} = f_{k+1}(t, \boldsymbol{x}(t)) + \sin u_{\text{TRIG}} \tag{2.8d}$$

Please note that the control, sin u_{TRIG}, and the error control, cos u_{TRIG}, are present only in one state equation, respectively. This makes the entire system very simple to solve and ensures that the new system of equations is very close to the original system. Thus, the Epsilon-Trig method greatly simplifies the problem formulation and solution process as compared to the traditional regularization method. Also, note that this method introduces the error control into any state equation to solve the OCP, including a state equation that contains the control. Moreover, the error parameter, ϵ, helps in smoothing the bang-bang control structure indirectly by determining the magnitude of error control needed to solve the problem.

Eq. (1.7) determines the optimal control options shown in Eq. (2.9) and PMP helps in choosing the optimal control from these options. The smooth control is sin u_{TRIG} and the error control is cos u_{TRIG}. Thus, based on the choice of the placement of error into the state equations system, only one EOM is perturbed in the Epsilon-Trig method. In the traditional smoothing method nearly all the EOMs are perturbed, which makes the problem formulation and solving process more complicated and less efficient.

$$u_{\text{TRIG}}{}^{*} = \begin{cases} \arctan\left(\dfrac{\lambda_{x_{k+1}}}{\epsilon\lambda_{x_1}}\right) \\ \\ \arctan\left(\dfrac{\lambda_{x_{k+1}}}{\epsilon\lambda_{x_1}}\right) + \pi \end{cases} \tag{2.9}$$

The Epsilon-Trig method generates a unique control law even when $\lambda_{x_{k+1}}$, which happens to be the switching function for the original bang-bang problem, becomes 0 units. Usually, the switching function does not become exactly 0 units while using the Epsilon-Trig method due to the errors introduced into the state equations, thereby obtaining a near-singular control law. It might happen that the costates λ_{x_1} and $\lambda_{x_{k+1}}$ in Eq. (2.9) simultaneously vanish, which can lead to numerical issues. It is a very rare situation that has not been encountered in this study. Nolan from RDSL suggested addition of the error control and error parameter in the objective function. This step eliminates the presence of a costate in the denominator of the control law, thereby avoiding singularity issues when that costate vanished.

2.3.1 Applicability Range

The Epsilon-Trig method can be used for OCPs for which the following hold.

1. The controls appear in a linear form in the Hamiltonian.

2. The controls have constant upper and/or lower bounds upon them.

3. This method can be combined with the Trigonometrization technique described later in this thesis.

2.3.2 Assumptions

Following are the assumptions used in the Epsilon-Trig method.

1. PMP suffices for the sufficient condition of optimality.
2. All costates do not vanish simultaneously.

2.3.3 Solving the Bounded Control Oscillator Problem using the Epsilon-Trig Regularization Method

When using the Epsilon-Trig regularization method for this problem, the state equations in Eq. (2.4) change to Eq. (2.10).

$$\dot{x_1} = x_2 + \epsilon \cos u_{\text{TRIG}} \tag{2.10a}$$

$$\dot{x_2} = -x_1 + \sin u_{\text{TRIG}} \tag{2.10b}$$

Eq. (2.11) and Eq. (2.12) describe the Hamiltonian, H and the optimal control options, respectively. PMP then selects the optimal control option from among these options.

$$H = \lambda_{x_1}(x_2 + \epsilon \cos u_{\text{TRIG}}) + \lambda_{x_2}(-x_1 + \sin u_{\text{TRIG}}) \tag{2.11}$$

$$u^*_{TRIG} = \begin{cases} \arctan\left(\dfrac{\lambda_{x_2}}{\epsilon\lambda_{x_1}}\right) \\ \\ \arctan\left(\dfrac{\lambda_{x_2}}{\epsilon\lambda_{x_1}}\right) + \pi \end{cases} \tag{2.12}$$

A comparison was drawn between the two regularization methods. The phase and the control time-history plots are shown in Fig. 2.4. There is one switch involved in the control time-history plot. The costates time-history plots are shown in Fig. 2.5, where λ_{x_2} is the switching function.

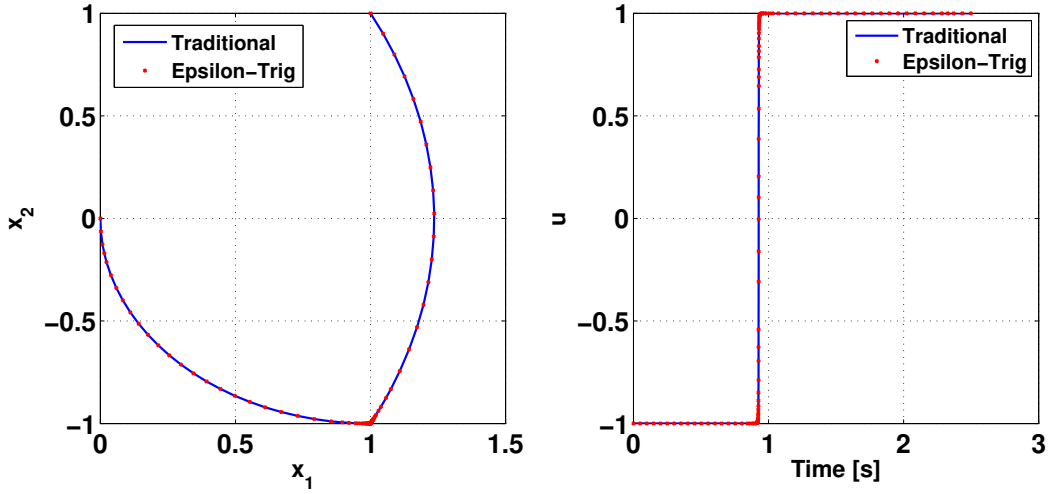

Figure 2.4.: Phase and control time-history plots for the oscillator problem.

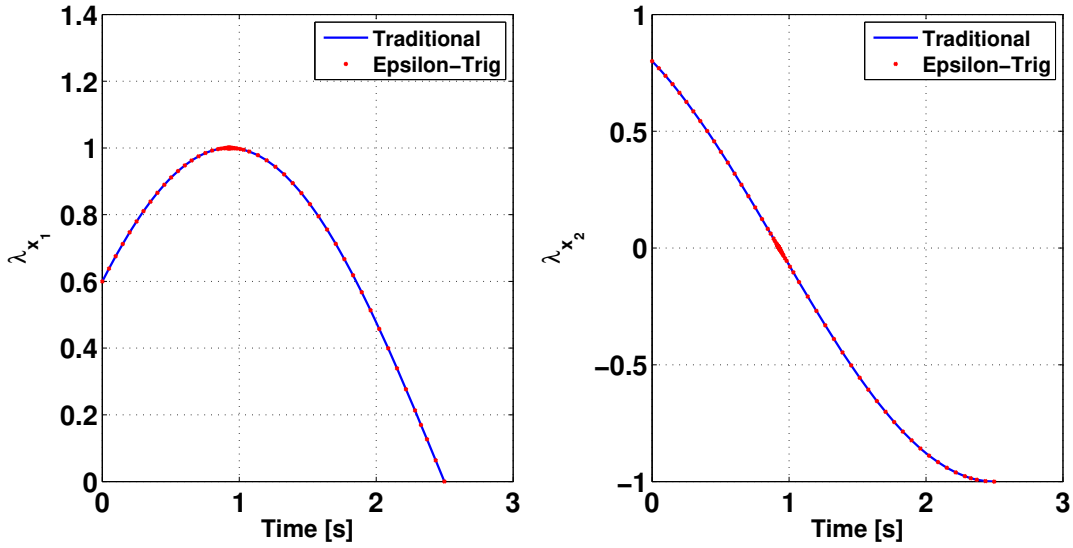

Figure 2.5.: Costates time-history plots for different regularization techniques.

The value of $\frac{\partial \phi}{\partial t_f}$ is 1 unit for this problem since the objective is to minimize the final time. According to Eq. (1.12), the terminal value of Hamiltonian, $H(t_f)$, is found to be -1 unit. Moreover, the Hamiltonian is a constant because it is not an explicit function of time. The Hamiltonian time-history plot, shown in Fig. 2.6, is in excellent agreement with the result obtained using the transversality condition and has an accuracy of 10^{-7}. Please note that the Hamiltonian is non-dimensional for this problem.

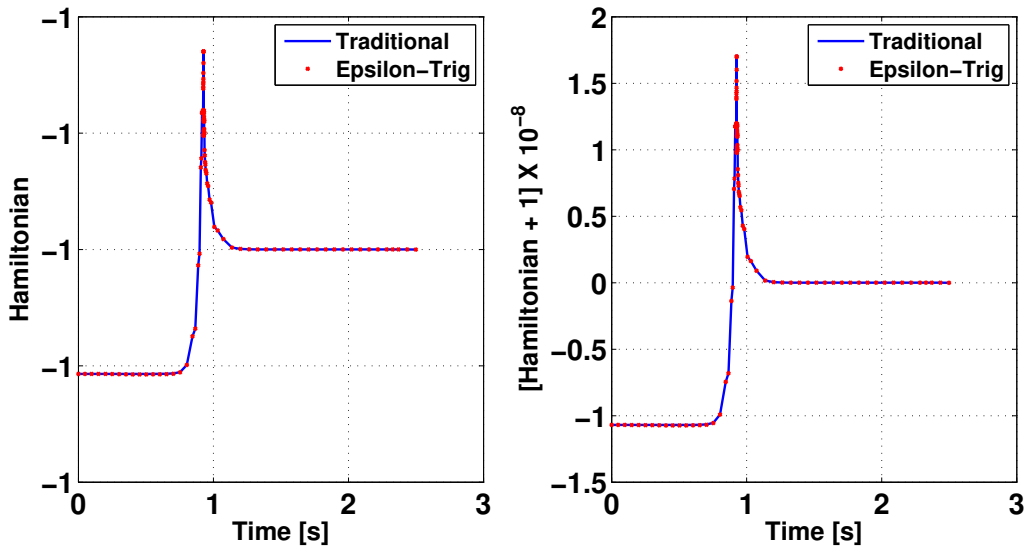

Figure 2.6.: Hamiltonian time-history plots for different regularization techniques.

The two methods are in excellent agreement with each other. When using the traditional regularization method, the solution satisfies Eq. (2.1d). But, the next example shows that the solution can easily violate this equation when the same problem includes a path constraint.

2.4 Motivation for Development of Epsilon-Trig Method through Oscillator Problem with a Bounded Control and a Path Constraint

The Epsilon-trig regularization method proves useful for OCPs with path constraints. To demonstrate this point, the previous problem includes a path constraint on the state variable x_1 as shown in Eq. (2.13).

$$S = x_1 - x_{1_{\text{MAX}}} \leqslant 0 \tag{2.13}$$

In addition to Eq. (2.4), the solution must satisfy a tangency constraint, N. Eqs. (2.14a)–(2.14c) show N, its state derivative, N_x, and its time derivative, N_t, respectively. Since N does not contain the time, t, explicitly, its time derivative, N_t, vanishes and there is no discontinuity in the Hamiltonian at the entry point of the constraint boundary.

$$N = x_1 - x_{1_{\text{MAX}}} \tag{2.14a}$$

$$N_x = \begin{bmatrix} 1, & 0 \end{bmatrix}^T \tag{2.14b}$$

$$N_t = 0 \tag{2.14c}$$

Eq. (2.15) describes the augmented Hamiltonian for this problem, which results in a modified costate EOM, $\dot{\lambda_{x_1}}$, as shown in Eq. (2.16). Eq. (2.17) determines the value of the multiplier for the path constraint, μ. Using the traditional regularization method, the state equation corresponding to x_1 should vanish as shown by Eq. (2.18a) and Eq. (2.18b) calculates the value of u_ϵ for the constraint boundary. ϵ has a value of 0.1 units in this problem.

$$H = \lambda_{x_1}(x_2 + \epsilon u_\epsilon) + \lambda_{x_2}(-x_1 + u) + \mu(x_1 - x_{1_{\text{MAX}}}) \tag{2.15}$$

$$\dot{\lambda_{x_1}} = \lambda_{x_2} - \mu \tag{2.16}$$

$$\mu = \begin{cases} 0 & \text{if} \quad \mathrm{x}_1 < \mathrm{x}_{1_{\mathrm{MAX}}} \\ \pi & \text{if} \quad \mathrm{x}_1 = \mathrm{x}_{1_{\mathrm{MAX}}} \end{cases} \tag{2.17}$$

$$S^1 = \dot{x}_1 = x_2 + \epsilon u_\epsilon = 0 \tag{2.18a}$$

$$u_\epsilon = -\frac{x_2}{\epsilon} \tag{2.18b}$$

Eq. (2.14) and Eq. (2.18) along with Eqs. (1.18)–(1.25), as mentioned in Sec. 1.2.2.3, were used to solve this problem. The value of control, u, and the other error controls were calculated using Eq. (2.2).

The Epsilon-Trig method follows on similar lines except that the control is expressed in a trigonometric form. The Hamiltonian for this problem then assumes the form as shown in Eq. (2.19).

$$H = \lambda_{x_1}(x_2 + \epsilon \cos u_{\mathrm{TRIG}}) + \lambda_{x_2}(-x_1 + \sin u_{\mathrm{TRIG}}) + \mu_{\mathrm{TRIG}}(x_1 - x_{1_{\mathrm{MAX}}}) \tag{2.19}$$

Eq. (2.20) evaluates the Lagrange multiplier, μ_{TRIG}, corresponding to the path constraint. The traditional approach using OCT requires taking derivatives of the constraint, S, until the control appears in an explicit form. The first derivative of the constraint, S^1, contains the control in an explicit form as shown in Eq. (2.21a). The value of the control at the constraint boundary in this method is then found using Eq. (2.21b), which is obtained after rearranging Eq. (2.21a) and is a slight modification to Eq. (2.18b).

$$\mu_{TRIG} = \begin{cases} 0 & \text{if} \quad \mathrm{x}_1 < \mathrm{x}_{1_{\mathrm{MAX}}} \\ \pi & \text{if} \quad \mathrm{x}_1 = \mathrm{x}_{1_{\mathrm{MAX}}} \end{cases} \tag{2.20}$$

$$S^1 = \dot{x}_1 = x_2 + \epsilon \cos u_{\mathrm{TRIG}} = 0 \tag{2.21a}$$

$$u_{\mathrm{TRIG}} = \arccos\left(\frac{-x_2}{\epsilon}\right) \tag{2.21b}$$

This section analyzes two cases based on the constraint on the state variable x_1: a realistic case and an unrealistic case. The traditional regularization and the Epsilon-Trig methods solved both these cases as discussed in the following subsections.

2.4.1 A Realistic Case

The maximum value of x_1 was found to be 1.231 units in the state unconstrained problem. In the realistic case, the maximum value of x_1 was reduced by 0.008 units. The time-history plot of x_1 is shown in Fig. 2.7, where the black line shows its maximum original value and red line signifies its new allowable maximum value. The smoothed and the error control history plots using both methods are shown in Fig. 2.8. It is clear that both methods lead to the same results. As seen in Fig. 2.8, the controls are already reaching bounds in this case.

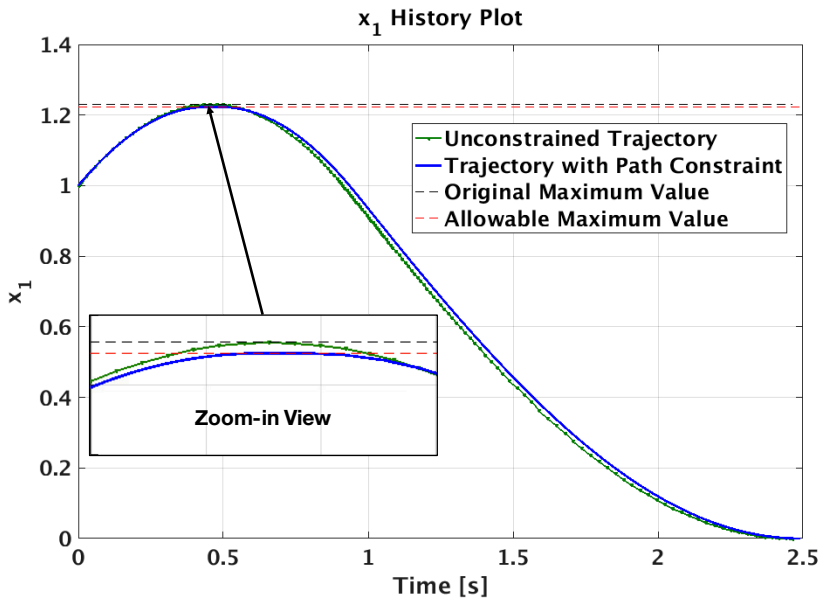

Figure 2.7.: x_1 time-history plot for unconstrained and path constraint cases.

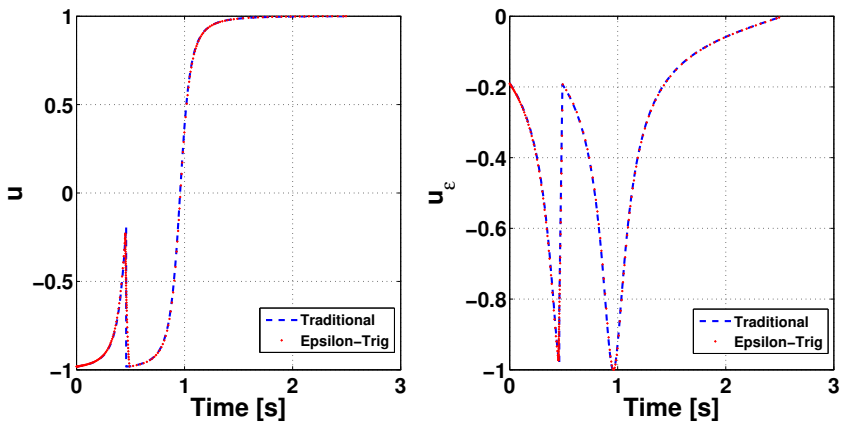

Figure 2.8.: Controls time-history plots for different regularization methods.

2.4.2 An Unrealistic Case

The issue with the traditional method is that it cannot impose bounds on the error control, u_ϵ, while using Eq. (2.18b). This enables unrealistic solutions such as trying to decrease the maximum allowable value for x_1 by 0.01 units. Thus, by using the traditional approach, one can solve even for a reduction of 0.01 units in the maximum value of x_1 as shown in Fig. 2.9.

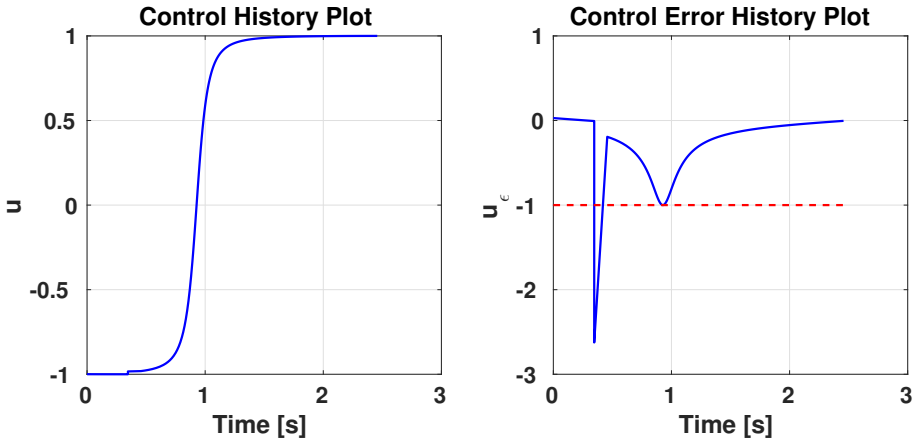

Figure 2.9.: Unrealistic controls time-history plots using the traditional smoothing method.

It can be seen that u_ϵ attains a value of -2.624 units, which is less than the minimum possible value of -1 unit, needed to satisfy Eq. (2.1d). Thus, the Epsilon-Trig method proves to be superior to the existing traditional approach because in the latter it is possible to make ϵ close to zero and get an illusion that the solution obtained is realistic. In such cases, u_ϵ can grow to very large magnitudes instead of remaining bounded between -1 and 1. Trajectories with singular arcs involve issues of obtaining a singular control, which can also be addressed very simply by the Epsilon-Trig method as shown in the examples that follow in the next section.

2.5 Verification and Validation of Epsilon-Trig Regularization Method using Popular Bang-Bang and Singular Control Problems from Literature

The Epsilon-Trig method is applicable to a wide variety of problems including bang-bang control, bang-singular-bang control, bang-bang-singular control, and so on. The following subsections contain solutions to some example problems using Epsilon-Trig method. GPOPS-II is used to verify and validate the Epsilon-Trig method for these problems.

2.5.1 Boat Problem

This subsection demonstrates the ability of the Epsilon-Trig regularization method to accommodate bang-singular control problems. It also shows that only one error control is sufficient for a system with more than two state equations. Consider the case of a boat moving at constant speed, V, traveling from the origin to (x_f, y_f) in a minimum time as shown in Eq. (2.22). Thus, the objective is to minimize the time for the boat to travel from the origin to the terminal point as shown in Eq. (2.22a). Using the Epsilon-Trig method, the error is introduced in the EOM corresponding to x as shown in Eq. (2.22b). The remaining EOMs for this problem are shown in

Eq. (2.22c) and Eq. (2.22d). The control for this OCP is $\dot{\alpha}$, which is written in a trigonometric form using the Epsilon-Trig method and is shown in Eq. (2.22d).

$$\text{Minimize: } J = t_f \tag{2.22a}$$

$$\text{Subject to: } \dot{x} = V\cos\alpha + \epsilon\cos u_{\text{TRIG}} \tag{2.22b}$$

$$\dot{y} = V\sin\alpha \tag{2.22c}$$

$$\dot{\alpha} = \sin u_{\text{TRIG}} \tag{2.22d}$$

This problem was solved in Ref. [24] by using GLCC. Please note that the error control can be introduced in any one of the state equations, $\dot{x}$ or $\dot{y}$. Table 2.2 includes the constants and boundary conditions used for the boat problem.

Table 2.2.: Constants for the boat problem.

Parameter	$x(0)$	$y(0)$	$\alpha(0)$	$x(t_\text{f})$	$y(t_\text{f})$	V	ϵ
Value	0	0	0	2.05	2	1	0.01

Eq. (2.23) describes the Hamiltonian for the boat problem. The Euler-Lagrange necessary conditions then use this Hamiltonian to obtain the EOMs for the costates as shown in Eq. (2.24).

$$H = \lambda_x(V\cos\alpha + \epsilon\cos u_{\text{TRIG}}) + \lambda_y V\sin\alpha + \lambda_\alpha \sin u_{\text{TRIG}} \tag{2.23}$$

$$\dot{\lambda_x} = 0 \tag{2.24a}$$

$$\dot{\lambda_y} = 0 \tag{2.24b}$$

$$\dot{\lambda_\alpha} = V(\lambda_x\sin\alpha - \lambda_y\cos\alpha) \tag{2.24c}$$

The Euler-Lagrange necessary conditions also generate the optimal control law, shown in Eq. (2.25). PMP performs the sufficiency check and selects the optimal control from among the control law options.

$$u_{\text{TRIG}} = \begin{cases} \arctan\left(\dfrac{\lambda_\alpha}{\epsilon\lambda_x}\right) & \text{if} \quad \lambda_\alpha < 0 \\ \arctan\left(\dfrac{\lambda_\alpha}{\epsilon\lambda_x}\right) + \pi & \text{if} \quad \lambda_\alpha > 0 \end{cases} \tag{2.25}$$

2.5.1.1 Analytical Solution

This problem can be solved analytically and a comparison can be drawn between the analytical and Epsilon-Trig regularization methods. The boat is expected to utilize maximum control initially to align itself toward the terminal point, (x_f, y_f). Thus, the value of control is 1 unit until the time becomes t_1 and then the control stays at 0 units until the terminal time, t_f. At t_1, the switching function, λ_α, too becomes 0 units, leading to a singular arc from t_1 to t_f. It should be noted that when OCT utilizes analytical method in solving this problem, it considers the entire trajectory to be broken into two arcs. Thus, OCT uses multiple arcs because certain derivatives corresponding to the costates become infinite at the points where the control jumps from the minimum value to the maximum value and vice versa. The analytical method just combines the two arcs in the form of a single solution.

The following is a brief discussion about GLCC used in the analytical method, which would validate that the control attains a 0 value for the singular arc. GLCC thus obtains a unique control law for a singular arc. The first time derivative of Hamiltonian, calculated in Eq. (2.26), generates options for α as shown in Eq. (2.27).

$$\dot{H}_u = \dot{\lambda_\alpha} = -H_\alpha = \lambda_x V \sin\alpha - \lambda_y V \cos\alpha = 0 \tag{2.26}$$

$$\tan\alpha = \frac{\lambda_y}{\lambda_x} = \frac{-\lambda_y}{-\lambda_x} \tag{2.27}$$

The solution process then calculates the second time derivative of H_u to obtain control in an explicit form as shown in Eq. (2.28). The control for the singular part of the trajectory turns out to be 0 units based on Eq. (2.28). The derivative of $\ddot{H}_u$ with respect to u obtains GLCC as shown in Eq. (2.29), which then selects the negative option for $\tan\alpha$ given in Eq. (2.27). The control law is summarized in Eq. (2.30).

$$\ddot{H}_u = (\lambda_x V\cos\alpha + \lambda_y V\sin\alpha)u = 0 \tag{2.28}$$

$$-\frac{\partial}{\partial u}(\ddot{H}_u) = -(\lambda_x V\cos\alpha + \lambda_y V\sin\alpha) \geq 0 \tag{2.29}$$

$$u = \dot{\alpha} = \begin{cases} 1 & \text{for} \quad 0 \leq t \leq t_1 \\ 0 & \text{for} \quad t_1 \leq t \leq t_f \end{cases} \tag{2.30}$$

Upon integration, Eq. (2.30) results in Eq. (2.31). The expression for α is used to perform integration upon and obtain expressions for the states, x and y, as shown in Eq. (2.32a) and Eq. (2.32b), respectively.

$$\alpha = \begin{cases} t & \text{for} \quad 0 \leq t \leq t_1 \\ t_1 & \text{for} \quad t_1 \leq t \leq t_f \end{cases} \tag{2.31}$$

$$x = \begin{cases} V\sin t & \text{for} \quad 0 \leq t \leq t_1 \\ V\sin t_1 + V\sin t_1(t - t_1) & \text{for} \quad t_1 \leq t \leq t_f \end{cases} \tag{2.32a}$$

$$y = \begin{cases} 1 - V\cos t & \text{for} \quad 0 \leq t \leq t_1 \\ 1 - V\cos t_1 + V\cos t_1(t - t_1) & \text{for} \quad t_1 \leq t \leq t_f \end{cases} \tag{2.32b}$$

The terminal values of x and y are substituted in Eq. (2.32). After rearrangement, these two equations are found to be related to each other through the expression, $t_f - t_1$, as shown in Eq. (2.33).

$$t_f - t_1 = \frac{x_f - \sin t_1}{\cos t_1} = \frac{y_f - (1 - \cos t_1)}{\sin t_1} \tag{2.33}$$

A trigonometric equation in t_1 can be formed using Eq. (2.33), which can then be used to obtain expressions for $\sin t_1$, $\cos t_1$, and t_1. Upon cross multiplication, Eq. (2.33) transforms into Eq. (2.34a). Both the sides of Eq. (2.34a) are then squared to obtain a quadratic equation for $\sin t_1$ as shown in Eq. (2.34b).

$$x_f \sin t_1 = 1 + y_f \cos t_1 - \cos t_1 \tag{2.34a}$$

$$[x_f^2 + (y_f - 1)^2] \sin^2 t_1 - 2x_f \sin t_1 + [1 - (y_f - 1)^2] = 0 \tag{2.34b}$$

Eq. (2.34b) results in two solutions for t_1 as shown in Eq. (2.35). The solution for t_1 is chosen from Eq. (2.35) after checking for the consistency of this solution between Eq. (2.32) and the given terminal values. The value of t_f is then obtained using Eq. (2.33).

$$\sin t_1 = \frac{x_f \pm \sqrt{x_f^2 - [x_f^2 + (y_f - 1)^2][1 - (y_f - 1)^2]}}{x_f^2 + (y_f - 1)^2} \tag{2.35}$$

The values of $\sin \alpha$ and $\cos \alpha$ obtained using GLCC for time between t_1 and t_f are shown in Eq. (2.36a) and Eq. (2.36b), respectively. It should be noted that α has a constant value, t_1, for Eq. (2.36a) and Eq. (2.36b).

$$\sin \alpha = \sin t_1 = \frac{-\lambda_y}{\sqrt{\lambda_x^2 + \lambda_y^2}} \tag{2.36a}$$

$$\cos \alpha = \cos t_1 = \frac{-\lambda_x}{\sqrt{\lambda_x^2 + \lambda_y^2}} \tag{2.36b}$$

Since $\dot{\lambda_x}$ and $\dot{\lambda_y}$ are 0 units based on Eq. (2.24a) and Eq. (2.24b), λ_x and λ_y are constants. Using Eq. (2.36a) and Eq. (2.36b), the values of λ_x and λ_y are obtained as shown in Eq. (2.37a) and Eq. (2.37b), respectively, where k is a constant. Finally, Eq. (2.38) specifies the expressions for λ_α based on time.

$$\lambda_x = k \cos t_1 \tag{2.37a}$$

$$\lambda_y = k \sin t_1 \tag{2.37b}$$

$$\lambda_\alpha = \begin{cases} 1 - \cos t & \text{for} \quad 0 \leq t \leq t_1 \\ 1 - \cos t_1 & \text{for} \quad t_1 \leq t \leq t_f \end{cases} \tag{2.38}$$

Although GLCC is able to generate a control law when the switching function vanishes, it is a complicated and lengthy process. This could be easily avoided by using the Epsilon-Trig regularization method.

2.5.1.2 Results Comparison

The results for the boat problem are shown in Fig. 2.10 and Fig. 2.11. The boat turns at the maximum rate until the turn angle aligns with the terminal point, (x_f, y_f), at time $t_1 = 0.9078$ seconds. The turn angle remains constant for the remainder of the trajectory, which is a singular arc.

The smoothed and error control histories are shown in Fig. 2.11. The results using the analytical approach and the Epsilon-Trig method were found to be in excellent agreement with each other. According to the Epsilon-Trig method, if the switching function, $\lambda_{x_{k+1}}$, becomes exactly 0 units, the singular control will also become 0 units and the error control will become 1 unit. The boat problem is a specific problem where both the analytical and the Epsilon-Trig methods lead to the same singular control law. In general, the singular control can be different from 0 units, but one can still solve for a near-singular control using the Epsilon-Trig method.

For this time-minimization problem, the value of $\frac{\partial \phi}{\partial t_f}$ is 1 unit. The terminal value of Hamiltonian, $H(t_f)$, is found to be -1 unit according to Eq. (1.12). Moreover, the Hamiltonian is not an explicit function of time and hence has a constant value. The Hamiltonian time-history plot, shown in Fig. 2.12, is in excellent agreement with the result obtained using the transversality condition and has an accuracy of 10^{-9}. Please note that the Hamiltonian is non-dimensional for this problem.

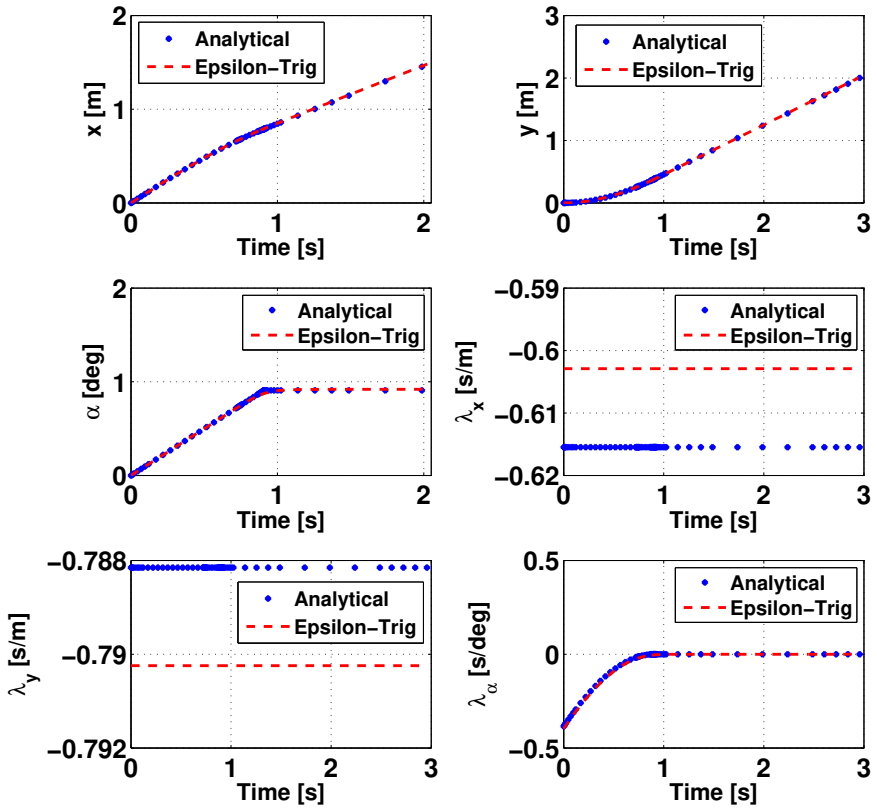

Figure 2.10.: States and costates time-history comparison plots.

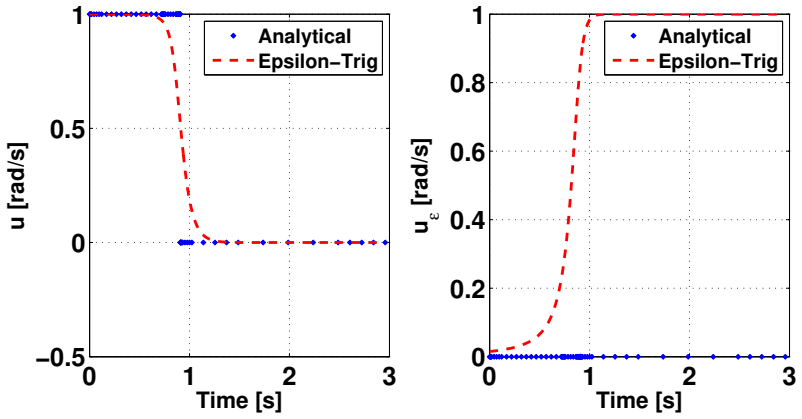

Figure 2.11.: Controls time-history comparison plots for the boat problem.

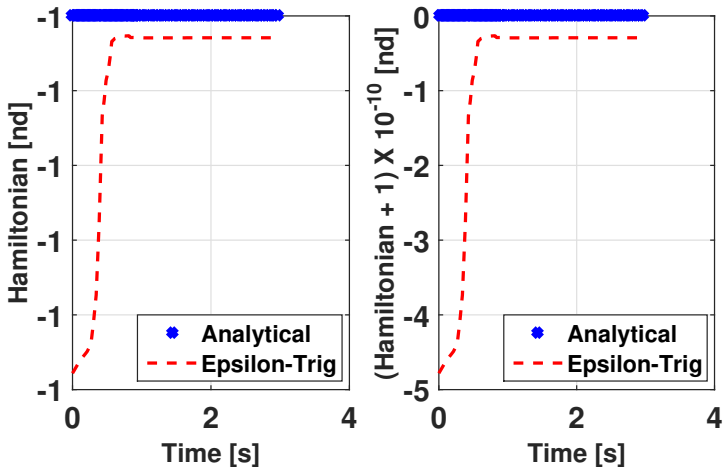

Figure 2.12.: Hamiltonian time-history comparison plots for the boat problem.

2.5.2 Van Der Pol Oscillator Problem

This subsection demonstrates the ability of the Epsilon-Trig regularization method to solve bang-bang-singular control problems. Eq. (2.39) expresses the Van Der Pol oscillator problem. Table 2.3 shows the constants for this problem.

$$\text{Minimize: } J = x_3(t_f) \tag{2.39a}$$

$$\text{Subject to: } \dot{x}_1 = x_2 + \epsilon \cos u_{\text{TRIG}} \tag{2.39b}$$

$$\dot{x}_2 = -x_1 + x_2(1 - x_1^2) + \sin u_{\text{TRIG}} \tag{2.39c}$$

$$\dot{x}_3 = \frac{1}{2}(x_1^2 + x_2^2) \tag{2.39d}$$

Table 2.3.: Constants for the Van der Pol oscillator problem.

Parameter	$x_1(0)$	$x_2(0)$	$x_3(0)$	t_f	ϵ
Value	0	1	0	4	0.001

Eq. (2.40) describes the Hamiltonian for this problem. Eq. (2.41) shows the EOMs for the costates obtained using this Hamiltonian.

$$H = \lambda_{x_1}(x_2 + \epsilon \cos u_{\text{TRIG}}) + \lambda_{x_2}[-x_1 + x_2(1 - x_1^2) + \sin u_{\text{TRIG}}] + \frac{\lambda_{x_3}(x_1^2 + x_2^2)}{2} \tag{2.40}$$

$$\dot{\lambda_{x_1}} = \lambda_{x_2}(1 + 2x_1x_2) - \lambda_{x_3}x_1 \tag{2.41a}$$

$$\dot{\lambda_{x_2}} = \lambda_{x_2}(x_1^2 - 1) - \lambda_{x_1} - \lambda_{x_3}x_2 \tag{2.41b}$$

$$\dot{\lambda_{x_3}} = 0 \tag{2.41c}$$

The optimal control law is the same as that in Eq. (2.9). The time-history plots for the states are shown in Fig. 2.13.

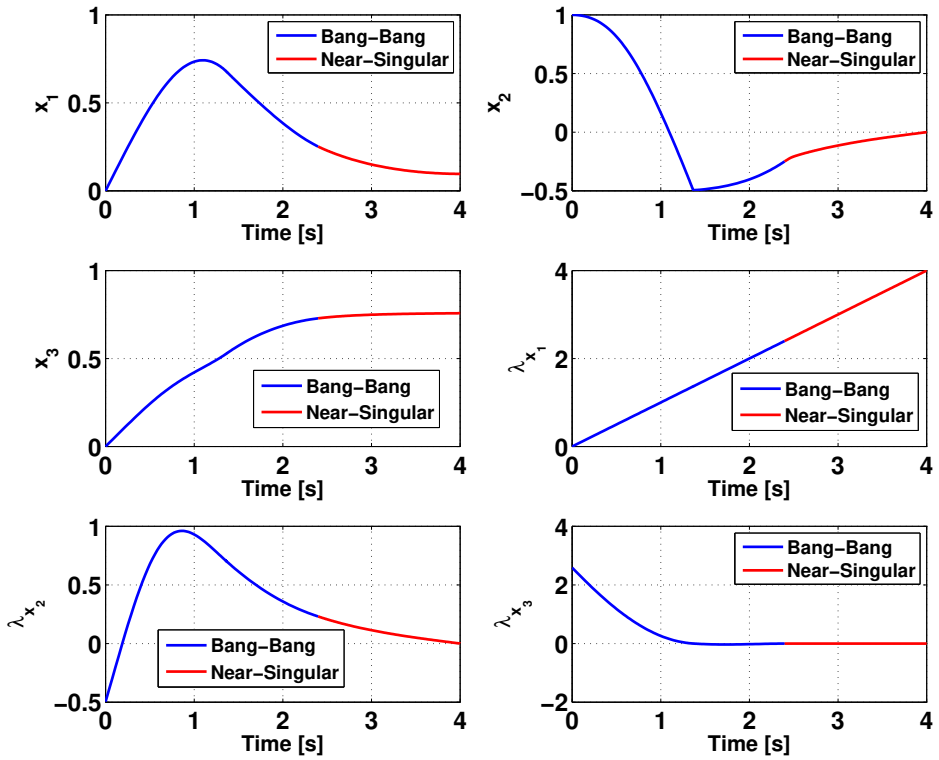

Figure 2.13.: States time-history plots for the Van Der Pol oscillator problem.

The smoothed and error control history plots are shown in Fig. 2.14. The blue color indicates the arc corresponding to the bang-bang control and red color indicates the near-singular arc at the end of the trajectory, where the control is not at the extremal values and the switching function, λ_{x_2}, is close to 0 units.

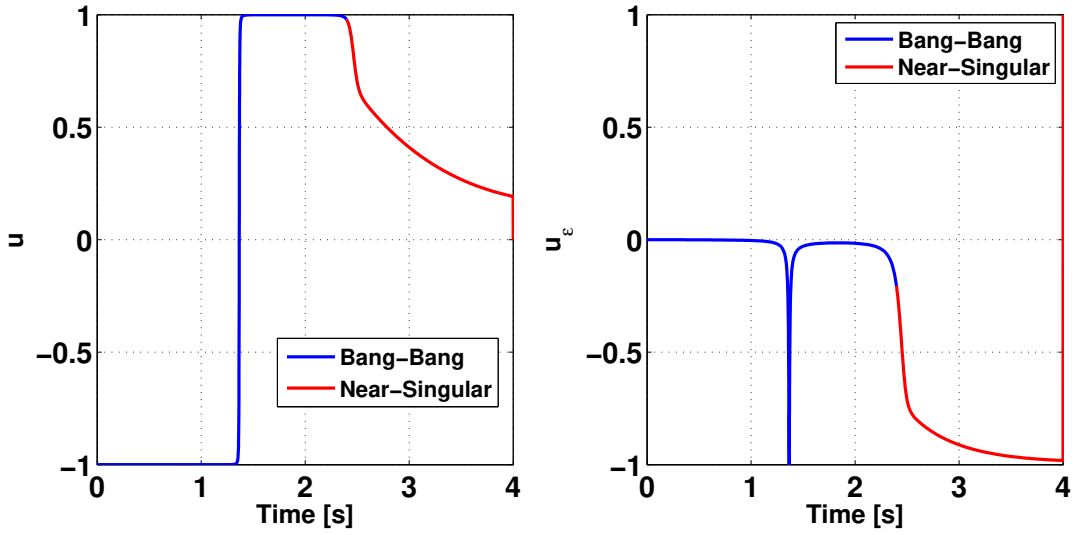

Figure 2.14.: Controls time-history plots for the Van Der Pol problem.

Fig. 2.14 shows that a unique control exists for the near-singular arc, since the switching function is not exactly 0 units. The optimal value of the objective function is found to be 0.7575 units, which matches very closely with Ref. [130] where its value is 0.7585 units. Thus, the Epsilon-Trig method greatly simplifies solving OCPs involving singular arcs. In this problem the switching function, λ_{x_2} becomes exactly 0 units at the terminal point of the trajectory and the control history plot matches with Ref. [130] except at this point. It is not a concern because any change in control at the terminal point does not influence the trajectory.

2.5.2.1 A Note on the Control Options of the Epsilon-Trig Method

The traditional smoothing technique for bang-bang and singular control problems specify the smooth control and the error controls with a negative sign in the numerator as shown in Eq. (2.2). This corresponds to the second control option obtained using the Epsilon-Trig method, where both the smooth and error controls are in the third quadrant. This choice of controls is made to minimize the Hamiltonian. Since the costates are usually related to each other and are not always positive valued, such a choice of controls in the traditional method may lead to spurious results. This chapter utilizes three different control laws for the Van Der Pol oscillator problem to demonstrate this issue.

The first case involves only the first control option of the Epsilon-Trig method corresponding to the first quadrant as shown in Eq. (2.9). The second case involves both the control options specified in the Epsilon Trig method that covered the first and the third quadrants of Eq. (2.9). The final case involves only the control option corresponding to the traditional method that covers the third quadrant of Eq. (2.9). All three cases converged to yield the same solution for the states but with different optimal control histories. Since the Hamiltonian is not an explicit function of time, it must remain constant for this problem. Furthermore, the value of Hamiltonian must be zero based on Eq. (1.12). Only case 2 corresponding to the Epsilon-Trig method was found to obtain the expected results. The spurious results obtained by using the traditional smoothing method and the correct result found using Epsilon-Trig method are both shown in Fig. 2.15. The Hamiltonian was found to be non-zero for the traditional smoothing technique. Thus, the Epsilon-Trig method ensures capturing all possible control options and obtaining the correct optimal control solutions.

This section used GPOPS-II to validate the Epsilon-Trig method regarding the correct solution for the Van Der Pol oscillator problem. The results obtained from GPOPS-II were found to be very noisy for the singular part of the solution as shown

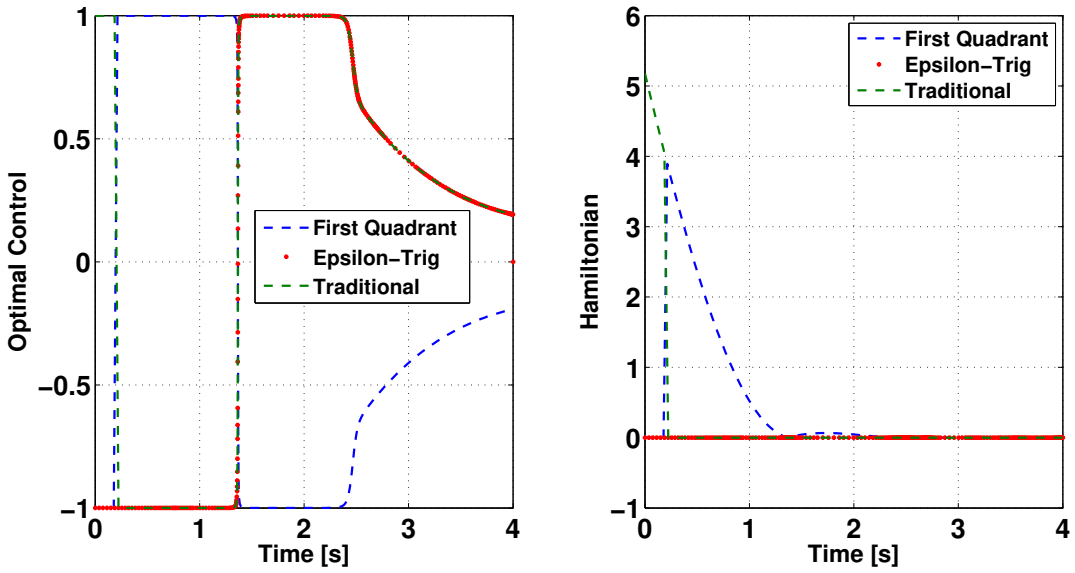

Figure 2.15.: Optimal control and Hamiltonian time-history comparison plots between the traditional and Epsilon-Trig methods.

in Fig. 2.16. Thus, the solutions obtained by using the Epsilon-Trig method were found to be of higher quality than GPOPS-II.

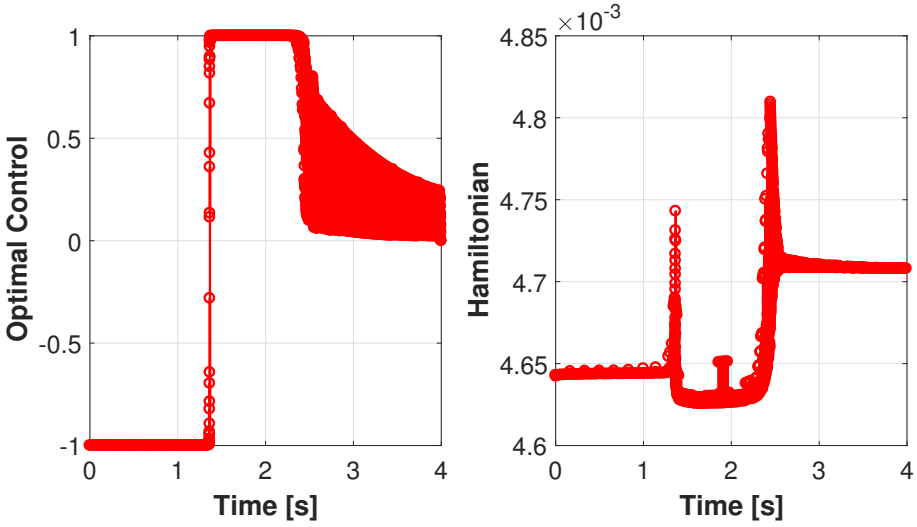

Figure 2.16.: Optimal control and Hamiltonian time-history plots obtained using GPOPS-II.

2.5.3 Goddard Rocket Maximum Ascent Problem

This subsection demonstrates the ability of the Epsilon-Trig regularization method to solve bang-singular-bang control problems. Consider the well-known OCP shown in Eq. (2.42).

$$\text{Minimize: } J = -h_f \tag{2.42a}$$

$$\text{Subject to: } \dot{h} = v + \epsilon \cos T_{\text{TRIG}} \tag{2.42b}$$

$$\dot{v} = \frac{T - D}{m} - g \tag{2.42c}$$

$$\dot{m} = -\frac{T}{V_{\text{e}}} \tag{2.42d}$$

$$T = \frac{T_{\text{MAX}}(\sin T_{\text{TRIG}} + 1)}{2} \tag{2.42e}$$

$$D = D_0 v^2 e^{\frac{-h}{H}} \tag{2.42f}$$

In Eq. (2.42) h is the altitude, v is the velocity, m is the mass, T is the thrust, D is the drag, g is the acceleration due to gravity, ρ_0 is the air density at sea-level, H is the scale height of Earth's atmosphere, and V_{e} is the exhaust velocity.

The Epsilon-Trig method introduces the smoothed control for the thrust, T, present in two state equations. This method also introduces the error control in the remaining state equation. This problem is one of the benchmark problems in GPOPS-II [11] and has been modified only by including the error in the state equation, $\dot{h}$, and by using Trigonometrization of the controls. This study then verifies and validates the Epsilon-Trig method using GPOPS-II. This problem uses English units for consistency with literature. [11] The boundary conditions for this problem are shown in Table 2.4.

Table 2.4.: Boundary conditions for the Goddard rocket problem.

Parameter	h_0 (ft)	v_0 (ft/s)	m_0 (lbm)	m_{t_f} (lbm)
Value	0	0	3	1

The constants used in this problem are shown in Table 2.5. Please note that the error parameter has a unit of ft/s.

Table 2.5.: Constants for Goddard rocket problem.

Parameter	ρ_0	H	V_e	g	D_0	T_{Max}	ϵ
Value	0.002378	23800	1580.9425	32.174	5.49153485e-5	193	0.5
Unit	slugs/ft^3	ft	ft/s	ft/s^2	slugs/ft	lbf	s/slug

Eq. (2.43) shows the Hamiltonian for the Goddard rocket problem. Eq. (2.44) shows the EOMs for the costates obtained using this Hamiltonian.

$$H = \lambda_h(v + \epsilon \cos T_{\text{TRIG}}) + \lambda_v \left(\frac{T - D}{m} - g\right) - \frac{\lambda_m T}{V_e} \tag{2.43}$$

$$\dot{\lambda_h} = -\frac{\lambda_v D}{mH} \tag{2.44a}$$

$$\dot{\lambda_v} = \frac{2\lambda_v D}{mv} - \lambda_h \tag{2.44b}$$

$$\dot{\lambda_m} = \frac{\lambda_v (T - D)}{m^2} \tag{2.44c}$$

Eq. (1.7) obtains the control law as shown in Eq. (2.45). Since the control is present in two state equations, the costates corresponding to both of them are present in the control law. PMP then chooses the optimal control from the control law options.

$$T_{\text{TRIG}}{}^* = \begin{cases} \arctan\left[\dfrac{T_{\text{Max}}}{2\epsilon\lambda_h}\left(\dfrac{\lambda_v}{m} - \dfrac{\lambda_m}{V_e}\right)\right] \\ \\ \arctan\left[\dfrac{T_{\text{Max}}}{2\epsilon\lambda_h}\left(\dfrac{\lambda_v}{m} - \dfrac{\lambda_m}{V_e}\right)\right] + \pi \end{cases} \tag{2.45}$$

The results are in excellent agreement with GPOPS-II as shown in Fig. 2.17. This shows that Epsilon-Trig method is extremely useful for conceptual design and can solve non-uniqueness issues related to the singular arc, by solving a problem very

similar to the original problem. It gives the designer a good estimate of the singular control law and expedites the design process. Choosing a good value for ϵ is a part of the design process and involves experimentation on the part of the designer. The author advises to start with a slightly large value of ϵ, say 0.5 units, and then to use a numerical continuation [49] to reduce it to a smaller value (e.g., 0.001 units). Fig. 2.18 shows an excellent agreement between the Epsilon-Trig method and GPOPS-II for the costate time-history plots.

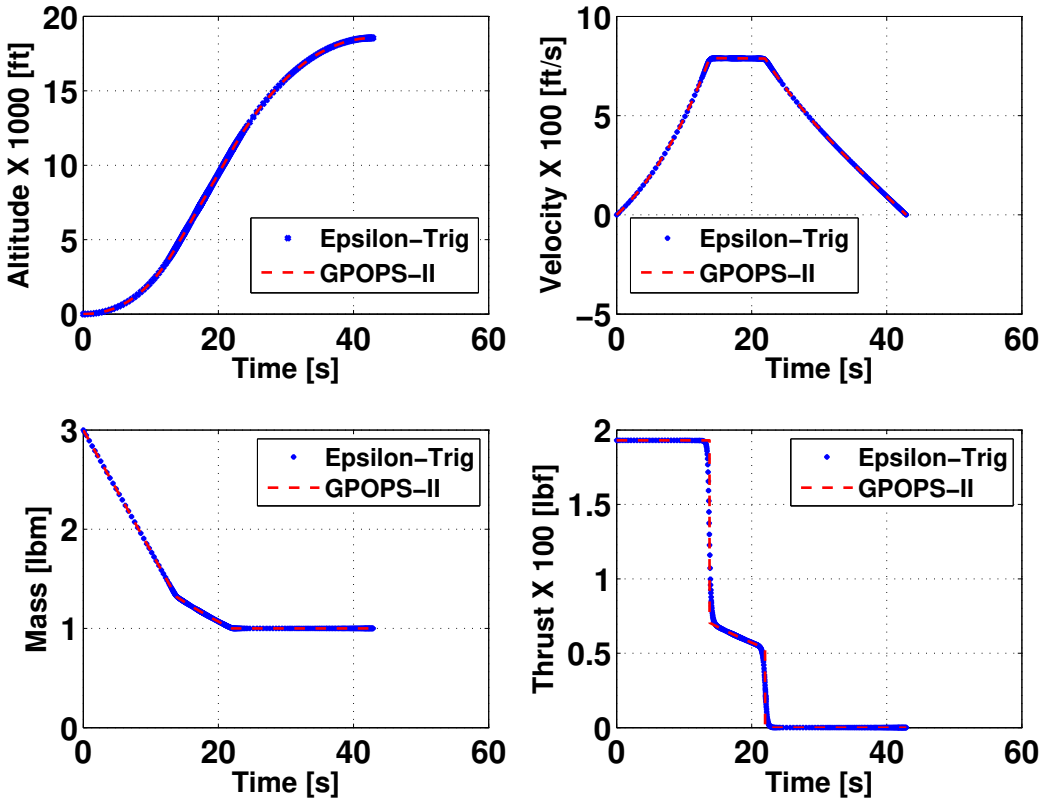

Figure 2.17.: Results comparison for the states and control of the Goddard rocket problem.

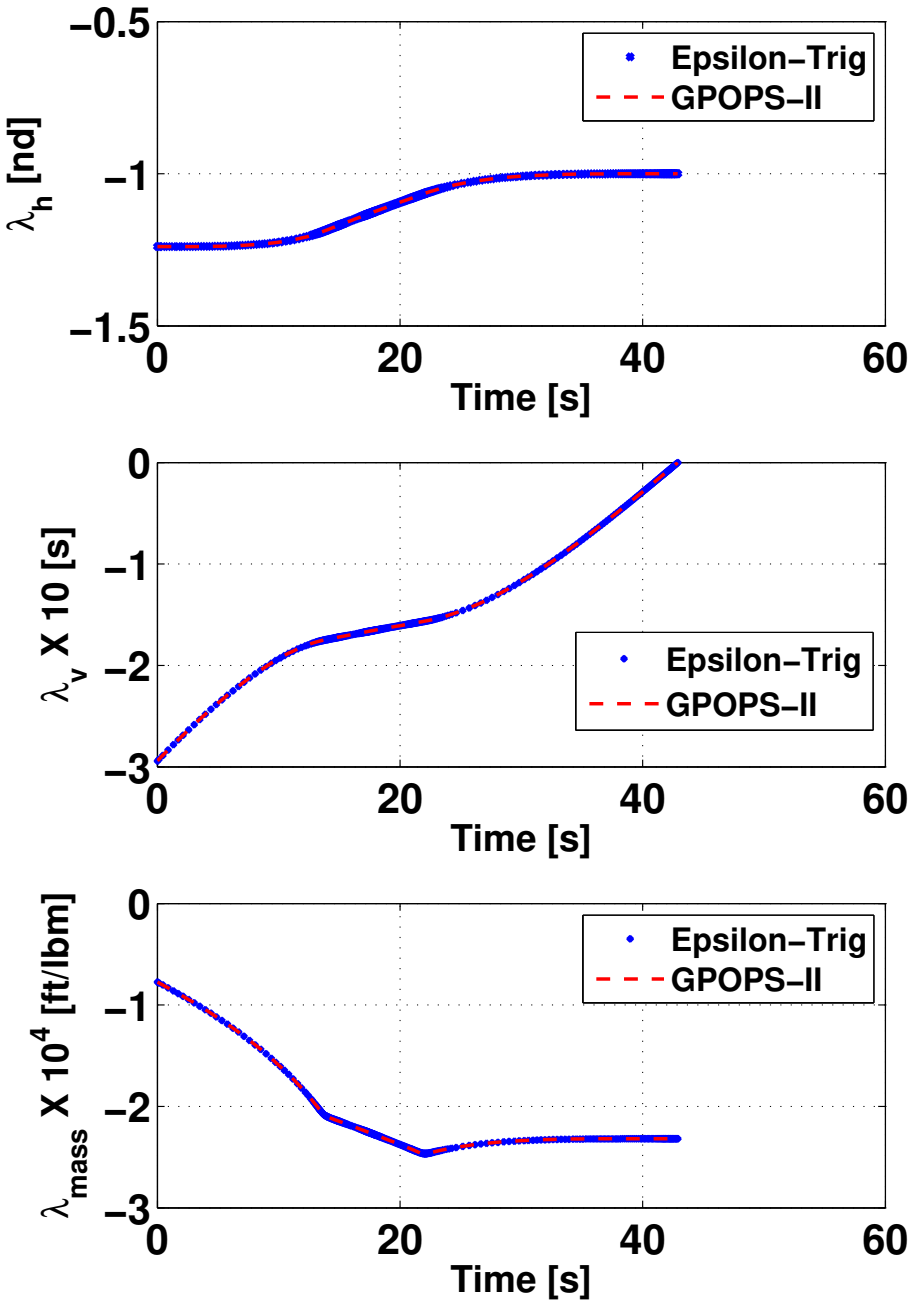

Figure 2.18.: Results comparison for the costates of the Goddard rocket problem.

For this problem, the value of $\frac{\partial \phi}{\partial t_f}$ is 0 ft/s. Hence, the terminal value of Hamiltonian, $H(t_f)$, is also 0 ft/s according to Eq. (1.12). Since the Hamiltonian is not an explicit function of time, it has a constant value. The Hamiltonian time-history plot, shown in Fig. 2.19, matches well with the result obtained using the transversality condition and has an accuracy of 10^{-2}. Please note that the results for the Hamiltonian obtained using GPOPS-II are not as accurate as the Epsilon-Trig regularization method.

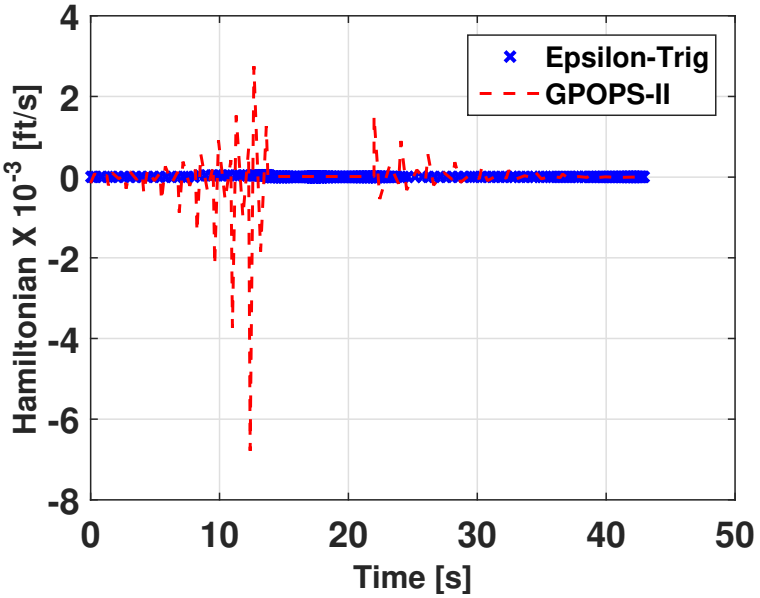

Figure 2.19.: Results comparison for the Hamiltonian of the Goddard rocket problem.

2.6 A Complex Aerospace Problem: Scramjet Based Prompt Global Strike

Earlier, the United States (US) used to have military bases around the world to deter any conflict with the Soviet Union and its allies, especially at unstable regions. With the demise of the Soviet Union, the US has restructured its army deployment and in many cases reduced its overseas military presence. [131] To deter and con-

tain unexpected threats from unexpected regions of the world, the US developed the Prompt Global Strike (PGS) program. This program enables the US to maintain and enhance its long-range strike capability from military bases in or near the US. [131, 132]

The focus of the Joint Technology Office on Hypersonics road maps has been on developing hypersonic PGS weapons with a nominal range of 600-1000 nautical miles. These weapons should enable and improve time-sensitive regional strike missions with precision engagement of high payoff, fixed or relocatable, moving, and deeply buried targets. [133,134] An expendable, fuel-cooled scramjet engine, capable of an extended flight at Mach 6 or above, is a prime candidate to fulfill this requirement. It is important to understand the optimal trajectories of hypersonic systems based on such an engine in order to further improve and develop such systems. [134]

Certain assumptions or simplifications forms the basis for the traditional approaches of solving hypersonic thrusting problems. Please note that the air-breathing thrusting model used in these approaches has been curve-fitted from a tabulated data of a specific mission. [134, 135]

1. **Issue with assumptions:** Ref. 136 used GPOPS-II to maximize the downrange of an aircraft-dropped, rocket-boosted scramjet missile. The trajectory comprises of three predetermined phases: ascent, cruise, and descent. The cruise phase had a fixed altitude of 20 km and a fixed velocity of 2 km/s. Similarly, in Ref. 137, a fuel-optimal trajectory is split into two sub-problems: ascent and maximum glide. The solutions to these sub-problems then reconstruct the optimal flight. These assumptions constrain the optimal search region and might overlook more optimal solutions.

2. **Issue with simplifications:** Refs. 49 and 138 employed indirect methods to solve trajectory optimization problems similar to the scramjet problem. While using OCT, the optimal control law for the angle of attack control in these problems, α, assumed a transcendental form for which there was no closed form

solution. Therefore, a small angle approximation of α removes the trigonometric terms in α from the problem statement. Thus, the resulting optimal trajectories can potentially have a large error corresponding to a large value of α.

Moreover, Ref. [139] solved a minimum fuel orbital ascent by a hypersonic air-breathing vehicle using OCT. Numerical methods obtain the control laws for the angle of attack and throttle instead of finding a closed-form, higher quality analytical solution. The scramjet PGS problem solved in this study is devoid of such assumptions and approximations. Sec. 3.4 includes a detailed discussion on the approach adopted here to avoid the transcendental control equations. Additionally, this section uses a scramjet thrusting model based on a parametric, ideal, thermodynamic cycle analysis. The inlet area control, A, of the engine, which has a simulated, variable inlet geometry achieved by adjusting wedge angles, forms the basis for its thrust control. This chapter further assumes the inlet to be in the optimal position for the entire trajectory.

Eq. (2.46) describes the scramjet PGS problem, where the objective is to minimize the time of flight of the missile as shown in Eq. (2.46a). The EOMs are shown in Eqs. (2.46b)–(2.46f) with important expressions included in Eqs. (2.46g)–(2.46q). Please note that the expression for thrust in this problem contains more variables due to coupling of the propulsion system with Earth's atmosphere. Additionally, this problem is planar and excludes bank angle control.

$$\text{Minimize: } J = t_{\text{f}} \tag{2.46a}$$

$$\text{Subject to: } \dot{h} = v \sin\gamma \tag{2.46b}$$

$$\dot{\theta} = \frac{v\cos\gamma}{r} \tag{2.46c}$$

$$\dot{v} = \frac{T\cos\alpha - D}{m} - \frac{\mu\sin\gamma}{r^2} \tag{2.46d}$$

$$\dot{\gamma} = \frac{L + T\sin\alpha}{mv} + \left(\frac{v}{r} - \frac{\mu}{vr^2}\right)\cos\gamma \tag{2.46e}$$

$$\dot{m} = -\dot{m}_0 f + \epsilon_1 \cos\dot{\alpha}_{\text{TRIG}} + \epsilon_2 \cos A_{\text{TRIG}} \tag{2.46f}$$

$$\text{Where: } \rho = \rho_0 e^{\frac{-h}{H}} \tag{2.46g}$$

$$C_{\mathrm{L}} = C_{L_1}\alpha + C_{L_0} \tag{2.46h}$$

$$C_{\mathrm{D}} = C_{\mathrm{D}_2}\alpha^2 + C_{\mathrm{D}_1}\alpha + C_{\mathrm{D}_0} \tag{2.46i}$$

$$D = \frac{1}{2}\rho v^2 C_{\mathrm{D}} A \tag{2.46j}$$

$$L = \frac{1}{2}\rho v^2 C_{\mathrm{L}} A \tag{2.46k}$$

$$\dot{m}_0 = \rho A v \tag{2.46l}$$

$$f = \frac{c_p T_0}{h_{pr}}\left[\frac{T_{\mathrm{MAX}}}{T_0}\left(1 + \frac{\gamma - 1}{2}M_c^2\right) - \left(1 + \frac{\gamma - 1}{2}M_0^2\right)\right] \tag{2.46m}$$

$$T = \rho A v^2 \sqrt{\frac{\frac{T_{\mathrm{MAX}}}{T_0}\left(1 + \frac{\gamma - 1}{2}M_c^2\right)}{1 + \frac{\gamma - 1}{2}M_0^2} - 1} \tag{2.46n}$$

$$M_0 = \frac{v}{\sqrt{\gamma R T_0}} \tag{2.46o}$$

$$r = r_{\mathrm{E}} + h \tag{2.46p}$$

$$A = A_{\mathrm{MAX}}\left(\frac{1 + \sin A_{\mathrm{TRIG}}}{2}\right) \tag{2.46q}$$

In the Eq. (2.46), h is the altitude, r is the radial magnitude, θ is the downrange, v is the velocity magnitude, γ is the flight path angle, m is the mass of the vehicle, T is the thrust force magnitude, D is the drag force magnitude, L is the lift force magnitude, and α is the angle of attack. C_{L_0}, C_{L_1}, C_{D_0}, C_{D_1}, and C_{D_2} are constants related to the coefficients of lift and drag. A is the reference area of the vehicle, μ is the gravitational parameter of the planet, r_{E} is the radius of the Earth, ρ_0 is the Earth's surface atmospheric density, and H is the Earth's atmospheric scale height. Ref. [134] and Appendix A outline a more detailed discussion of this engine model, where f is the ratio of mass flow rates of fuel injected into the burner to that of the air passing through the engine, M_0 is the free-stream Mach number, and M_c is the combustion chamber Mach number.

Table 2.6 includes the constants required for this OCP [140], where parameters like the specific heat ratio, γ, the Earth's atmospheric gas constant, R, and the heat capacity at a constant pressure, c_{p}, have values corresponding to a perfect gas. The

free-stream temperature, T_0, remains constant assuming an exponential atmosphere. The fuel heating value, h_{pr}, corresponds to JP-7 used in the SR-71 Blackbird. [141–144] The endothermic properties of JP-7 allow for active cooling while cracking the fuel before combustion, making JP-7 a popular fuel choice. [145–148]

Table 2.6.: Constants for the scramjet PGS problem.

Parameter	**Value**
r_{E} (km)	6378
μ (km^3/s^2)	398600
ρ_0 (kg/m^3)	1.2
H (km)	7.5
C_{L_1} (1/rad)	10.305
C_{L_0}	0.1758
C_{D_2} (1/rad^2)	18.231
C_{D_1} (1/rad)	-0.4113
C_{D_0}	0.26943
γ (nd)	1.4
R (m^2/s^{2}K)	287.058
c_{p} (m^2/s^{2}K)	1004
h_{pr} (m^2/s^2)	43903250
M_{c} (nd)	3
T_{MAX} (K)	1600
T_0 (K)	230
A_{REF} (m^2)	0.35
A_{MAX} (m^2)	0.3
ϵ_1 (kg/rad)	0.5
ϵ_2 (kg/(m^{2}s))	10^{-13}

Table 2.7 specifies the boundary conditions for the scramjet PGS problem. The initial conditions are set to values that are obtainable by a booster and conducive to scramjet operations. The terminal boundary conditions specify both the target's location and the missile's dry weight.

Table 2.7.: Initial and final conditions for the scramjet PGS problem.

Attribute	**Initial Value**	**Final Value**
Time (s)	0	free
Altitude (km)	20	0
Downrange (km)	0	1700
Velocity (km/s)	1.3	free
Flight Path Angle (deg)	free	free
Mass (kg)	1300	600
Angle of Attack (deg)	free	free

The Hamiltonian for this problem is shown in Eq. (2.47). The Euler-Lagrange necessary conditions of optimality use this Hamiltonian to generate the EOMs for the costates as shown in Eq. (2.48).

$$\begin{aligned} H = {} & \lambda_h v \sin\gamma + \frac{\lambda_\theta v \cos\gamma}{r} + \lambda_v \left(\frac{T\cos\alpha - D}{m} - \frac{\mu \sin\gamma}{r^2} \right) \\ & + \lambda_\gamma \left[\frac{(L + T\sin\alpha)}{mv} + \left(\frac{v}{r} - \frac{\mu}{vr^2} \right) \cos\gamma \right] \\ & + \lambda_m \left(-\dot{m}_0 f + \epsilon_1 \cos\dot{\alpha}_{\mathrm{TRIG}} + \epsilon_2 \cos A_{\mathrm{TRIG}} \right) \end{aligned} \tag{2.47}$$

$$\begin{aligned} \dot{\lambda}_h = {} & \lambda_\gamma \left[\frac{T\sin\alpha + L}{mvH} + \left(\frac{v}{r^2} - \frac{2\mu}{vr^3} \right) \cos\gamma \right] - \frac{\lambda_m \dot{m}_0 f}{H} \\ & + \lambda_v \left(\frac{T\cos\alpha + D}{mH} - \frac{2\mu\sin\gamma}{r^3} \right) + \frac{\lambda_\theta v \cos\gamma}{r^2} \end{aligned} \tag{2.48a}$$

$$\dot{\lambda}_\theta = 0 \tag{2.48b}$$

$$\dot{\lambda}_v = -\lambda_h \sin\gamma - \frac{\lambda_\theta \cos\gamma}{r} + \lambda_v \left[\rho A v \sqrt{\frac{\mathrm{P}_1}{1 + \mathrm{P}_2 \mathrm{v}^2}} \left(\frac{v^2}{1 + \mathrm{P}_2 \mathrm{v}^2} - 2 \right) - \frac{2D}{v} \right]$$

$$- \lambda_\gamma \left\{ \left[\rho A v \sqrt{\frac{\mathrm{P}_1}{1 + \mathrm{P}_2 \mathrm{v}^2}} \left(\frac{v^2}{1 + \mathrm{P}_2 \mathrm{v}^2 - 1} \right) + \frac{L}{mv^2} \right] \right\} \tag{2.48c}$$

$$\dot{\lambda_\gamma} = -\lambda_h \sin\gamma + \frac{\lambda_\theta v \sin\gamma}{r} + \frac{\lambda_v \mu \cos\gamma}{r^2} + \lambda_\gamma \sin\gamma \left(\frac{v}{r} - \frac{\mu}{v r^2} \right) \tag{2.48d}$$

$$\dot{\lambda_m} = \frac{\lambda_v (T\cos\alpha - D)}{m^2} + \frac{\lambda_\gamma (L + T\sin\alpha)}{m^2 v} \tag{2.48e}$$

$$\mathrm{P}_1 = \frac{T_{\mathrm{MAX}}}{T_0} \left(1 + \frac{\gamma - 1}{2} M_c^2 \right) \tag{2.48f}$$

$$\mathrm{P}_2 = \frac{(\gamma - 1) v^2}{2\gamma R T_0} \tag{2.48g}$$

The necessary conditions of optimality also help in obtaining the optimal control law for the two controls involved as shown in Eq. (2.49a) and Eq. (2.49b). A_{TRIG} shows the increased complexity of the control law, which requires expressions defined in Eqs. (2.48f), (2.48g), (2.49c), and (2.49d).

$$A_{\mathrm{TRIG}} = \begin{cases} \arctan \left[\dfrac{\dfrac{\mathrm{P}_3}{m} \left(\sqrt{\dfrac{\mathrm{P}_1}{\mathrm{P}_2}} - 1 \right) (\lambda_v v \cos\alpha + \lambda_\gamma \sin\alpha) - \lambda_{\mathrm{m}} \mathrm{P}_3 \mathrm{P}_4 (\mathrm{P}_1 - \mathrm{P}_2)}{\epsilon_2 \lambda_m} \right] \\ \arctan \left[\dfrac{\dfrac{\mathrm{P}_3}{m} \left(\sqrt{\dfrac{\mathrm{P}_1}{\mathrm{P}_2}} - 1 \right) (\lambda_v v \cos\alpha + \lambda_\gamma \sin\alpha) - \lambda_{\mathrm{m}} \mathrm{P}_3 \mathrm{P}_4 (\mathrm{P}_1 - \mathrm{P}_2)}{\epsilon_2 \lambda_m} \right] + \pi \end{cases} \tag{2.49a}$$

$$\dot{\alpha}_{\mathrm{TRIG}} = \begin{cases} \arctan \left(\dfrac{\alpha_{\mathrm{RATE}} \lambda_\alpha}{\epsilon_1 \lambda_m} \right) \\ \arctan \left(\dfrac{\alpha_{\mathrm{RATE}} \lambda_\alpha}{\epsilon_1 \lambda_m} \right) + \pi \end{cases} \tag{2.49b}$$

$$\mathrm{P}_3 = \frac{\rho v A_{\mathrm{MAX}}}{2} \tag{2.49c}$$

$$\mathrm{P}_4 = \frac{c_{\mathrm{p}} T_0}{h_{pr}} \tag{2.49d}$$

The results obtained for this problem using indirect methods employing the Epsilon-Trig technique are in excellent agreement with GPOPS-II. The scramjet missile im-

mediately dives into a thicker portion of the atmosphere contrary to avoiding atmospheric drag for a rocket-type missile. This maneuver, as shown in the trajectory plot of Fig. 2.20, leads to larger dynamic pressures, thereby generating higher thrust. The scramjet missile climbs to a higher altitude with lower drag after burning a significant amount of fuel to gain a higher velocity initially. [134]

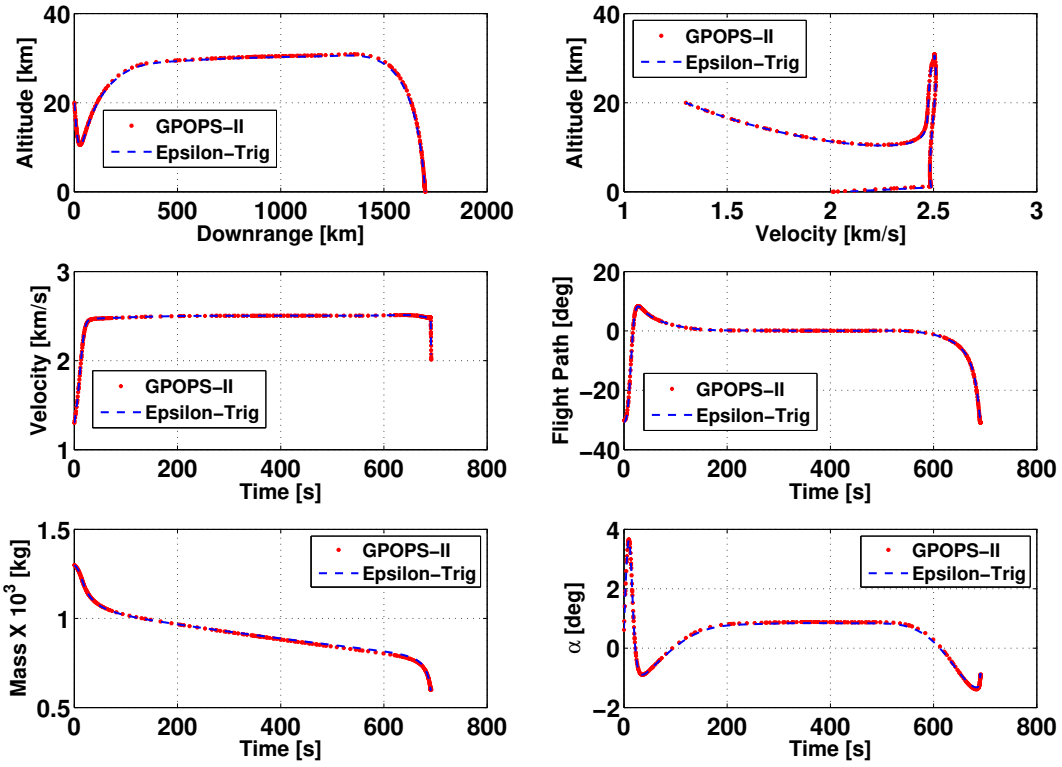

Figure 2.20.: Comparison plots between GPOPS-II and Epsilon-Trig method for the states of the scramjet PGS problem.

The mass time-history plot shown in Fig. 2.20 indicates that most of missile's fuel burn is at the initial and final segments of the trajectory. Both these segments occur at lower parts of the atmosphere, where oxygen is available aplenty. The first major fuel burn occurs to provide maximum acceleration to the missile. The second major fuel burn compensates for the deceleration during the near-cruise descent phase, which occurs in between these two major fuel burn segments. As a result, the missile nearly reaches the terminal downrange at the near-cruise altitude and then performs a steep dive to the target. The optimal solution includes these rapid fuel burn and near-cruise phases as expected. [134] The dynamic pressure is found to be within the realistic range for a sustainable engine operation as given in Ref. [149]. For high dynamic pressures, the missile would have to either reduce velocity or climb to higher altitudes without enough oxygen for sustainable combustion. Both these options would result in a longer time to the target and are therefore not optimal. [134]

The optimal controls are shown in Fig. 2.21. The throttle control time-history shows that the missile burns all its fuel for the mass flow rate of air that passes into its inlet until the missile depletes all its fuel. The control results are in agreement with the literature and are optimal. [134]

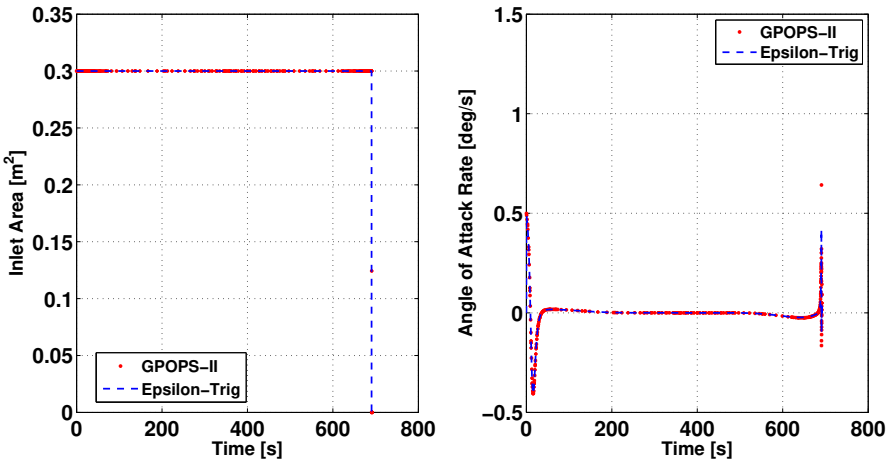

Figure 2.21.: Comparison plots between GPOPS-II and Epsilon-Trig method for the controls of the scramjet PGS problem.

The solution process of this complicated scramjet PGS problem includes a prudent choice in introducing error into the EOMs. If the Epsilon-Trig method introduces error into the EOM corresponding to the altitude, the computation time to obtain the optimal solution increased significantly. The resulting optimal control law amounts to an increase in the computation time, which has λ_h in its denominator. As seen in Fig. 2.22, λ_h crosses the zero value at two places. These lead to singularity issues and consequently require placement of more number of nodes around the singularity regions. The solution process resolves this issue by placing an error in EOM corresponding to mass as λ_m never crosses zero value throughout the trajectory. [134]

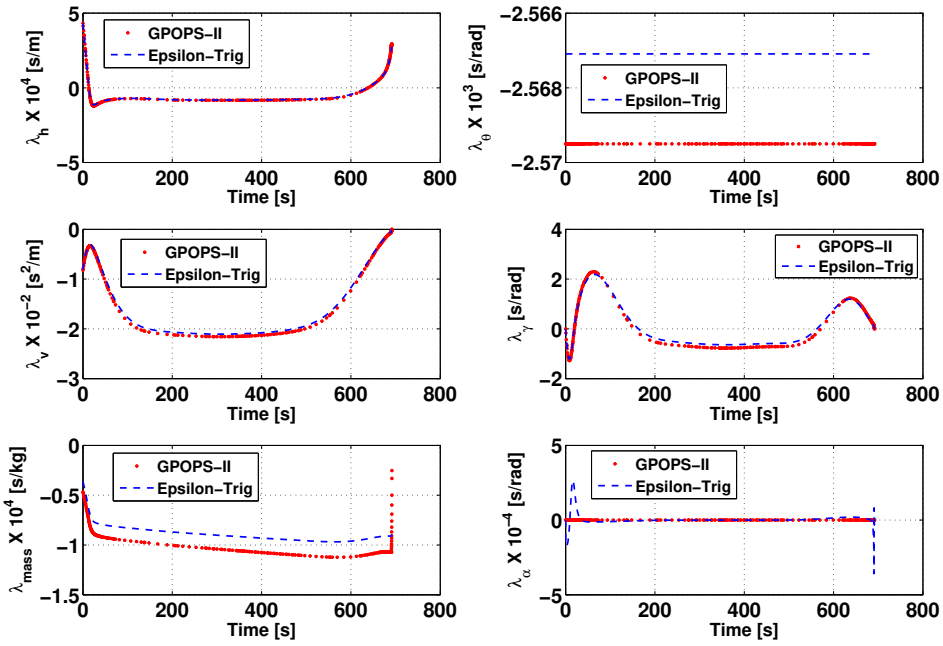

Figure 2.22.: Comparison plots between GPOPS-II and Epsilon-Trig method for the costates of the scramjet PGS problem.

Table 2.8 summarizes the complexity of the scramjet PGS problem. The major complexity in this problem is to derive and to solve for a very complicated control law corresponding to the missile's thrust.

Table 2.8.: Complexities of the scramjet PGS problem.

Parameter	**Complexity**
States	Five states
Controls	Bounded and complicated functions dependent on the states and costates
Control law	Initially transcendental
State equations	Highly non-linear and coupled
Costate equations	Highly non-linear, lengthy, and coupled

2.7 Conclusions

Bang-bang control problems have numerical issues due to discontinuities in the control structure, when using OCT that relies on derivatives. The smooth regularization method developed by Silva and Trélat resolved these issues, but was found to have the following three limitations.

1. Traditional smoothing method introduces too many error controls into the state equations system, which complicates the problem formulation and solution process.

2. When OCP includes path constraints, the resulting control law for the constraint arc violates an important condition on controls. As a result, the error controls grow very large in magnitude and become unrealistic.

3. The error parameter, ϵ, become dimensionally inconsistent when used in more than one state equation.

To overcome these limitations, this chapter proposed and developed a new method using the concept of Trigonometrization, named the Epsilon-Trig method. This method introduces the error parameter, ϵ, and the error control only into one state equation, which greatly simplifies the problem formulation and solution process. Trigonometry proves that the smooth control and error control are orthogonal to each other. This study used the traditional and Epsilon-Trig methods to solve a bounded oscillator problem with path constraints. For an unrealistic case of this problem, the traditional method was able to generate results by using very large unrealistic values of one error control. Thus, the traditional regularization method was shown to generate spurious results, whereas the Epsilon-Trig method was able to solve only realistic cases. Moreover, since this method has ϵ in only one state equation, it has dimensional consistency using the Epsilon-Trig method. This study solved some benchmark examples, including the Goddard rocket problem, to show that the Epsilon-Trig method can generate near-singular controls in case of singular arcs.

This chapter includes solutions to a very complicated aerospace problem using the Epsilon-Trig method. This OCP requires minimizing the time of flight of a scramjet based PGS missile. The Epsilon-Trig method solved this problem in a simple manner while generating high quality solutions. These solutions matched well with the results obtained using GPOPS-II, thereby verifying and validating the Epsilon-Trig method. A class of OCPs comprises of pure control constraints, where the controls appear in non-linear forms in the Hamiltonian. The next chapter introduces a unique technique inspired from the Epsilon-Trig method to solve this class of OCPs.

3. Advancements in Optimal Control Theory for Problems with Pure Control Constraints and Non-Linear Controls

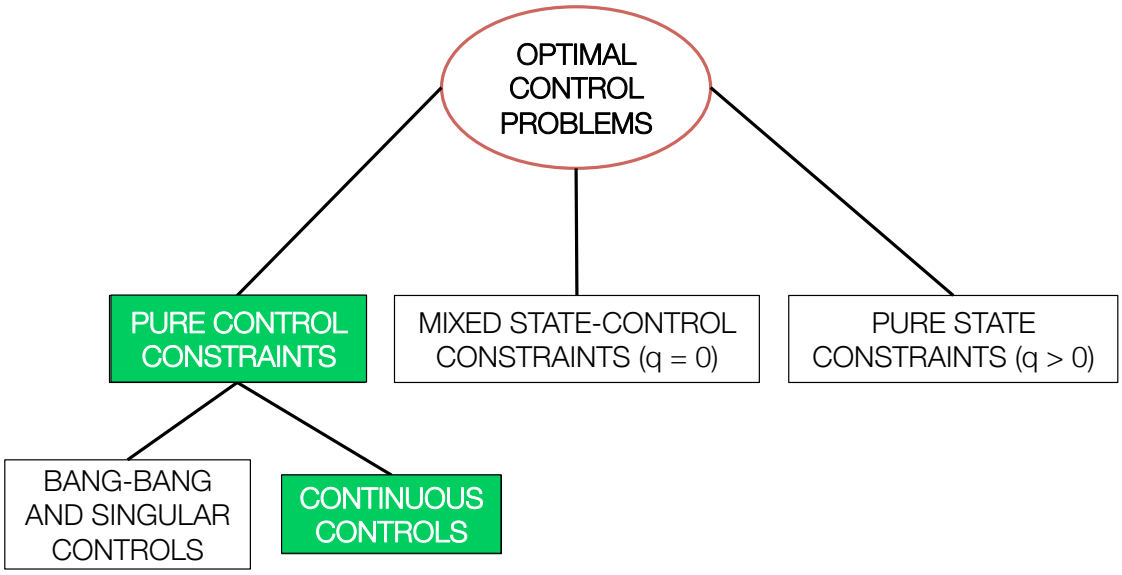

3.1 Introduction

The use of trigonometry in solving bounded control problems was first applied by using the Epsilon-Trig regularization method [150], as discussed in the previous chapter. In the Epsilon-Trig regularization method the control appears in a linear form in the Hamiltonian of the OCP. This study extends the use of the bounding property of trigonometric functions to OCPs with control constraints, where the control appears in a non-linear form in the Hamiltonian. This chapter identified three issues with such OCPs having control constraints.

1. The traditional application of control constraints requires the solution to a MP-BVP, which is very complicated and difficult to solve for practical aerospace

problems. [50, 51] An example of the control structure for such a complicated MPBVP is shown in Fig. 3.1, where arcs 1 and 3 correspond to control constraints and arcs 2 and 4 correspond to unconstrained trajectory arcs.

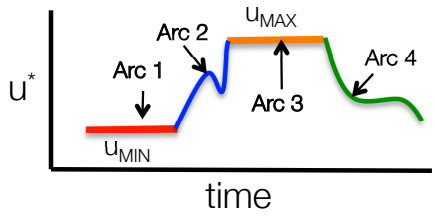

Figure 3.1.: A complicated control solution for an OCP with control constraints.

2. An issue arises when the problem contains both polynomial and trigonometric terms of control, often resulting in a transcendental equation when solving for the optimal control law. Since such transcendental equations are devoid of closed-form solutions, the EOMs are traditionally rewritten based on certain approximations (e.g., small angle approximations) that convert trigonometric terms to polynomial terms. [49, 151, 152] The polynomial-based, closed-form optimal solution is thus obtained only for specific applications where the approximations are valid.

3. Since the solver usually employs only the necessary conditions of optimality when solving OCPs, the results obtained may correspond to the wrong extremum. To avoid such wrong results, the solver needs to have additional control options.

Posing the control in a trigonometric form, defined as Trigonometrization, addresses the aforementioned issues and greatly simplifies the problem formulation and solution process. Secs. 3.3, 3.4, and 3.5 describe the benefits of using Trigonometrization with an example problem. Sec. 3.6 includes the solutions to a very complicated general aviation based trajectory optimization problem using Trigonometrization. Sec. 3.7 concludes this chapter.

3.2 Trigonometrization of OCPs with Pure Control Constraints and Non-Linear Controls

Chapter 2 described a class of OCPs that can utilize the Epsilon-Trig method, where the Hamiltonian, H, has the control in a linear form. In order to solve a wider set of OCPs with control constraints, this chapter introduces the Trigonometrization approach. [153] In this second set of OCPs, the control appears in the Hamiltonian in a polynomial form, $f(u)$, with order more than 1, as shown in Eq. (3.1).

$$H = H_0(t, x, \lambda) + H_1(t, x, \lambda) f(u) \tag{3.1}$$

The control in real world OCPs is usually constrained between an upper limit and a lower limit as shown in the inequality Eq. (3.2). Eq. (3.3a) shows a trigonometric form of this bounded control. The values of constants c_1 and c_0 are shown in Eq. (3.3b) and Eq. (3.3c), respectively.

$$u_{\text{LB}} \leq u \leq u_{\text{UB}} \tag{3.2}$$

$$u = c_1 \sin u_{\text{TRIG}} + c_0 \tag{3.3a}$$

$$\text{Where : } c_1 = \frac{u_{\text{UB}} - u_{\text{LB}}}{2} \tag{3.3b}$$

$$c_0 = \frac{u_{\text{UB}} + u_{\text{LB}}}{2} \tag{3.3c}$$

Using Eq. (1.7), the optimal control options are shown in Eq. (3.4). The values $\pm\pi/2$ for u_{TRIG} restrict control, u, between u_{LB} and u_{UB}. The control, u, can attain unbounded values when u_{TRIG} is $\arcsin(f(t, x, \lambda))$. It may happen that $f(t, x, \lambda)$ becomes less than -1 unit or more than unit 1, leading to imaginary values for $\arcsin(f(t, x, \lambda))$. In such cases, PMP determines the control, u, from only two options for u_{TRIG}, $\pm\pi/2$.

$${u_{\text{TRIG}}}^* = \begin{cases} \dfrac{-\pi}{2} \\ \arcsin(f(t, x, \lambda)) \\ \dfrac{\pi}{2} \end{cases} \tag{3.4}$$

3.2.1 Applicability Range

The Trigonometrization technique developed in this chapter is applicable to the OCPs for which the following hold.

1. The controls appear in a non-linear form in the Hamiltonian.
2. The controls have constant lower and/or upper bounds upon them.
3. This technique can be combined with the Epsilon-Trig method.

3.2.2 Assumptions

Following are the assumptions used in the Trigonometrization technique for this chapter.

1. PMP suffices for the sufficiency condition of optimality.
2. The states are unconstrained.

Please note that the Epsilon-Trig method can be coupled with the Trigonometrization technique to solve OCPs in which certain controls appear in a linear form and rest of the controls appear in a non-linear form in the Hamiltonian. There are three benefits of using Trigonometrization for OCPs with non-linear control expressions in the Hamiltonian, which are discussed in the following sections.

3.3 Benefit 1: Avoid Solving a Multi-Point Boundary Value Problem

Traditionally, the design community uses the methodology described in Sec. 1.2.2.2 to solve OCPs with constraints on control, where the control may appear in a non-linear form in the Hamiltonian. This section chose the Rayleigh problem, as specified in Eq. (3.5), to illustrate this traditional approach. [72, 154] Table 3.1 contains the constants used in this problem.

$$\text{Minimize: } J = \int_{t_0}^{t_f} (u^2 + x_1^2)\mathrm{d}t \tag{3.5a}$$

$$\text{Subject to: } \dot{x_1} = x_2 \tag{3.5b}$$

$$\dot{x_2} = -x_1 + x_2(1.4 - 0.14{x_2}^2) + 4u \tag{3.5c}$$

$$|u| \leq 1 \tag{3.5d}$$

Table 3.1.: Constants for the Rayleigh problem.

Parameter	x_{1_0}	x_{2_0}	t_0	t_f
Value	-5	-5	0	4.5

Eq. (3.6) gives the Hamiltonian for this problem. The Hamiltonian then helps generate the EOMs for the costates as shown in Eq. (3.7). The expressions for μ_1 and μ_2 are shown in Eq. (3.8a) and Eq. (3.8b), respectively.

$$H = \lambda_{x_1}\dot{x_1} + \lambda_{x_2}\dot{x_2} + \mu_1(-u - 1) + \mu_2(u - 1) + u^2 + x_1^2 \tag{3.6}$$

$$\dot{\lambda_{x_1}} = -2x_1 + \lambda_{x_2} \tag{3.7a}$$

$$\dot{\lambda_{x_2}} = -\lambda_{x_1} - \lambda_{x_2}(1.4 - 0.42x_2^2) \tag{3.7b}$$

$$\mu_1 = \begin{cases} 0 \quad \text{if} \quad \text{u} > -1 \\ 4\lambda_{x_2} - 2 \quad \text{if} \quad \text{u} = -1 \end{cases} \tag{3.8a}$$

$$\mu_2 = \begin{cases} 0 \quad \text{if} \quad \text{u} < 1 \\ -4\lambda_{x_2} - 2 \quad \text{if} \quad \text{u} = 1 \end{cases} \tag{3.8b}$$

Ref. 72 gives the control structure of the solution. This control structure is shown in Eq. (3.9), where the optimal control, u^*, first stays at the upper bound until time t_1, followed by an unconstrained arc until time t_2, a lower bound constrained arc until time t_3, and finally an unconstrained arc for the remaining time.

$$u^* = \begin{cases} 1 \quad \text{if} \quad 0 \leq \mathrm{t} \leq \mathrm{t}_1 \\ -2\lambda_{x_2}(t) \quad \text{if} \quad \mathrm{t}_1 \leq \mathrm{t} \leq \mathrm{t}_2 \\ -1 \quad \text{if} \quad \mathrm{t}_2 \leq \mathrm{t} \leq \mathrm{t}_3 \\ -2\lambda_{x_2}(t) \quad \text{if} \quad \mathrm{t}_3 \leq \mathrm{t} \leq \mathrm{t}_\mathrm{f} \end{cases} \tag{3.9}$$

Since the Hamiltonian is regular, the control should be continuous across the unconstrained and constrained arcs. [72] An additional set of boundary conditions is thus obtained as shown in Eq. (3.10).

$$u(t_1) = -2\lambda_{x_2}(t_1) = 1 \tag{3.10a}$$

$$u(t_2) = -2\lambda_{x_2}(t_2) = -1 \tag{3.10b}$$

$$u(t_3) = -2\lambda_{x_2}(t_3) = -1 \tag{3.10c}$$

The traditional approach results in a five-point BVP and becomes much more difficult to solve as compared to a TPBVP. This study reformulates the Rayleigh problem by substituting a trigonometric form of u into Eq. (3.5), as shown in Eq. (3.11), which ensures u stays bounded between the values ± 1, and the problem remains a TPBVP.

$$u = \sin u_{\mathrm{TRIG}} \tag{3.11}$$

Using the Euler-Lagrange necessary conditions, the optimal control law obtained for this reformulated Rayleigh problem is shown in Eq. (3.12).

$${u_{\mathrm{TRIG}}}^* = \begin{cases} -\pi/2 \\ \arcsin(-2\lambda_{\mathrm{x}_2}) \\ \pi/2 \end{cases} \tag{3.12}$$

PMP forms the basis for the control selection and imposes implicit constraints on the control. The selection process discards large positive or negative values of λ_{x_2} that violate the bounds of arcsin. Trigonometrization retains a TPBVP form and obtains the same solution as the traditional method without segmenting the problem explicitly into multiple constrained and unconstrained arcs. To justify this point, a comparison was made between the traditional and Trigonometrization approaches, and the results match as expected. The phase and control time-history comparison plots are shown in Fig. 3.2.

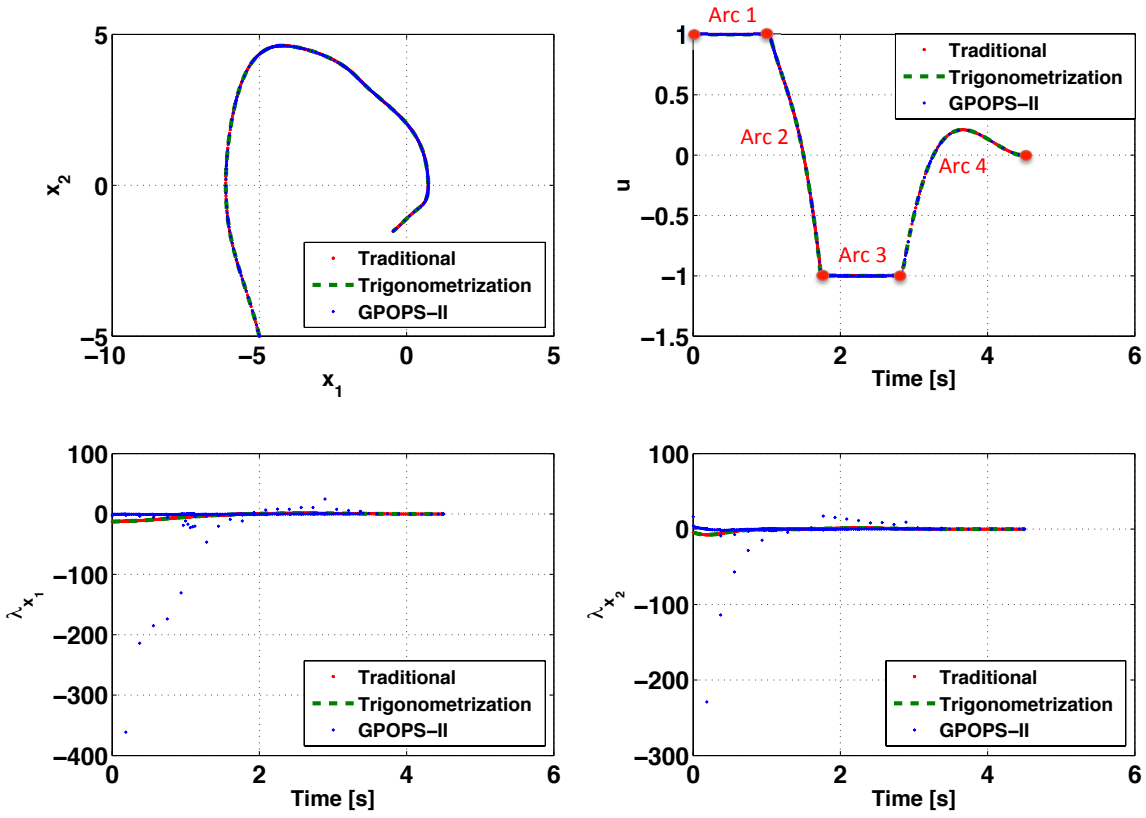

Figure 3.2.: Comparison plots between the traditional and Trigonometrization methods for the Rayleigh problem.

For this problem, the value of $\frac{\partial \phi}{\partial t_f}$ is 0 units. Hence, the terminal value of Hamiltonian, $H(t_f)$, is also 0 units according to Eq. (1.12). Since the Hamiltonian is not an explicit function of time, it has a constant value. The Hamiltonian time-history

plot, shown in Fig. 3.3, matches well with the result obtained using the transversality condition. Please note that the results for the Hamiltonian obtained using GPOPS-II are not as accurate as the Epsilon-Trig regularization method.

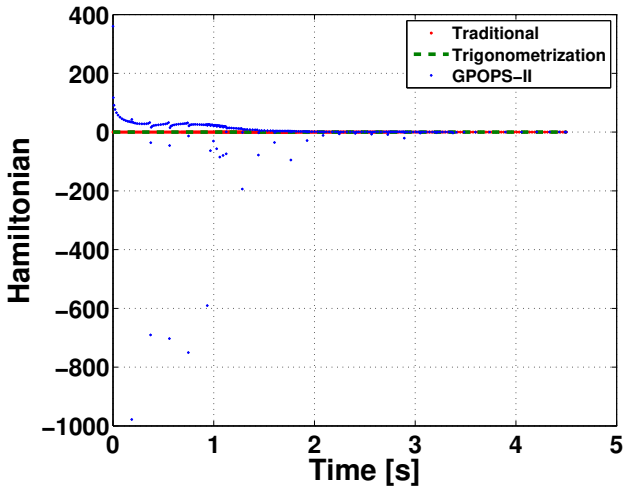

Figure 3.3.: Comparison plots between the traditional and Trigonometrization methods for the Rayleigh problem.

A comparison between various features of the traditional and Trigonometrization approaches is presented in Table 3.2, which demonstrates that Trigonometrization is an effective means to solve OCPs with constraints on control. Please note that a built-in BVP solver, bvp4c, in MATLAB 2014b performed all computations on a 2.5-GHz Intel i5 processor.

Table 3.2.: Comparison between the traditional and Trigonometrization methods for the Rayleigh problem.

Attribute	**Traditional Method**	**Trigonometrization**
Type	Five-Point BVP	TPBVP
Number of Trajectory Arcs	4	1
Number of Boundary Conditions	34	13
Computation Time (s)	5	3.5

3.4 Benefit 2: Avoiding Transcendental Equations of Optimality

For certain OCPs, the optimal control law assumes a transcendental form such that the solver cannot obtain a closed-form solution for the control. In practice, a Taylor series expansion enables a closed-form solution for the control at the cost of loss in accuracy. This study chose to solve an impactor problem to illustrate this issue and aimed at minimizing its time of flight. For simplicity, the analysis considers only planar motion as shown in Eq. (3.13), and assumes that the thrust magnitude is constant.

$$\text{Minimize: } J = t_{\mathrm{f}} \tag{3.13a}$$

$$\text{Subject to: } \dot{h} = v\sin\gamma \tag{3.13b}$$

$$\dot{\theta} = \frac{v\cos\gamma}{r} \tag{3.13c}$$

$$\dot{v} = \frac{T\cos\alpha - D}{m} - \frac{\mu\sin\gamma}{r^2} \tag{3.13d}$$

$$\dot{\gamma} = \frac{L + T\sin\alpha}{mv} + \left(\frac{v}{r} - \frac{\mu}{vr^2}\right)\cos\gamma \tag{3.13e}$$

$$\dot{m} = -\frac{T}{g_0 I_{\mathrm{sp}}} \tag{3.13f}$$

$$\rho = \rho_0 e^{\frac{-h}{H}} \tag{3.13g}$$

$$C_{\mathrm{L}} = C_{L_1}\alpha + C_{L_0} \tag{3.13h}$$

$$C_{\mathrm{D}} = C_{\mathrm{D}_2}\alpha^2 + C_{\mathrm{D}_1}\alpha + C_{\mathrm{D}_0} \tag{3.13i}$$

$$D = \frac{1}{2}\rho v^2 C_{\mathrm{D}} A \tag{3.13j}$$

$$L = \frac{1}{2}\rho v^2 C_{\mathrm{L}} A \tag{3.13k}$$

$$r = r_{\mathrm{p}} + h \tag{3.13l}$$

In the above equations, r is the radial magnitude, h is the altitude, θ is the downrange, v is the velocity magnitude, γ is the flight path angle, m is the mass of the vehicle, A is the reference area of the vehicle, μ is the gravitational parameter of the planet, r_{p} is the radius of the planet, ρ_0 is the surface atmospheric density of the planet, D is

the drag force magnitude, L is the lift force magnitude, and α is the angle of attack. C_{L_0}, C_{L_1}, C_{D_0}, C_{D_1}, and C_{D_2} are constants related to the coefficients of lift and drag.

The only control is the angle of attack, α, bounded between $\pm 20°$, and the bank angle is fixed at 0°. This section used Ref. 155 to select an impactor. Table 3.3 shows the constants used in this problem with Earth as the planet.

Table 3.3.: Constants for the impactor problem.

Parameter	**Value**
r_p (km)	6378
μ (km^3/s^2)	398600
ρ_0 (kg/m^3)	1.2
H (km)	7.5
g_0 (m/s^2)	9.80665
A (m^2)	557.4
C_{L_1} (1/rad)	0.4639
C_{L_0}	-0.0278
C_{D_2} (1/rad^2)	0.3216
C_{D_1} (1/rad)	-0.0305
C_{D_0}	0.03
T (kN)	2000
Isp (s)	400

Eq. (3.14) shows the Hamiltonian for this problem. The Euler-Lagrange necessary conditions then utilize this Hamiltonian to obtain the costate EOMs as shown in Eq. (3.15).

$$\begin{aligned} H = \lambda_h v \sin\gamma + \frac{\lambda_\theta v \cos\gamma}{r} + \lambda_v \left(\frac{T\cos\alpha - D}{m} - \frac{\mu \sin\gamma}{r^2} \right) \\ + \lambda_\gamma \left[\frac{(L + T\sin\alpha)}{mv} + \left(\frac{v}{r} - \frac{\mu}{vr^2} \right) \cos\gamma \right] - \frac{\lambda_m T}{g_0 Isp} \end{aligned} \tag{3.14}$$

$$\dot{\lambda_h} = -\frac{\lambda_v D}{mH} \tag{3.15a}$$

$$\dot{\lambda_v} = \frac{2\lambda_v D}{mv} - \lambda_h \tag{3.15b}$$

$$\dot{\lambda_m} = \frac{\lambda_v (T - D)}{m^2} \tag{3.15c}$$

The optimal control law for the unbounded control problem is shown by Eq. (3.16). The control law becomes transcendental because of the presence of polynomial and trigonometric expressions of control, α.

$$\frac{\partial H}{\partial \alpha^*} = \frac{\lambda_v[\rho v^2 A(-2C_{\mathrm{D}_2}\alpha^* - C_{\mathrm{D}_1}) - T\sin\alpha^*]}{2m} + \frac{\lambda_\gamma(\rho v^2 A C_{\mathrm{L}_1} + T\cos\alpha^*)}{2mv} = 0 \tag{3.16}$$

Traditionally, the small angle approximation reduces the trigonometric expressions of α to a polynomial form, which enables the construction of a closed-form but approximate optimal control expression. [49, 138, 151, 152] As an example, Eq. (3.17a) and Eq. (3.17b) represent a small angle approximation that enables a closed-form solution of the optimal control as shown in Eq. (3.17c). [49, 138, 151, 152]

$$\sin\alpha = \alpha \tag{3.17a}$$

$$\cos\alpha = 1 \tag{3.17b}$$

$$\alpha^* = \frac{\lambda_\gamma(A\rho v^2 C_{\mathrm{L}_1} + 2T) - \lambda_v A\rho v^3 C_{\mathrm{D}_1}}{2\lambda_v A\rho v^3 C_{\mathrm{D}_2}} \tag{3.17c}$$

This scenario can be altogether avoided by converting the controls to trigonometric forms. The original control, α, could be made a state variable and its time-derivative could be made the new control, u, as shown in Eq. (3.18).

$$\dot{\alpha} = u \tag{3.18}$$

The reformulated OCP utilizes the Epsilon-Trig regularization method, which happens to be a specific case of the Trigonometrization technique applicable only to bang-bang and singular control problems. [150] A trigonometric form then describes the control as shown in Eq. (3.19a). The state equation corresponding to v now includes an error parameter, ϵ, and an error control, $\cos u_{\text{TRIG}}$, as shown in Eq. (3.19b). This choice of error placement into the dynamics of the problem is purely based on the observation that such a choice resulted in faster convergence. The value of α_{RATE} used in this problem is 5 deg/s. ϵ is kept to a small value of 0.001 m/(rad s) for more accurate results.

$$\dot{\alpha} = \alpha_{\text{RATE}} \sin u_{\text{TRIG}} \tag{3.19a}$$

$$\dot{v} = \frac{T\cos\alpha - D}{m} - \frac{\mu \sin\gamma}{r^2} + \epsilon \cos u_{\text{TRIG}} \tag{3.19b}$$

The optimal control law becomes very simple as compared to the previous scenario and is shown in Eq. (3.20). PMP then selects the optimal control.

$${u_{\text{TRIG}}}^* = \begin{cases} \arctan\left(\dfrac{\lambda_{\alpha_{\text{TRIG}}}}{\epsilon\lambda_v}\right) \\ \\ \arctan\left(\dfrac{\lambda_{\alpha_{\text{TRIG}}}}{\epsilon\lambda_v}\right) + \pi \end{cases} \tag{3.20}$$

The boundary conditions for the problem are shown in Table 3.4. This study draws a comparison between the features of the typical approximation and Trigonometrization methods. Using $\dot{\alpha}$ as the control is valid for realistic aerospace problems as $\dot{\alpha}$ specifies a definite realistic rate at which the angle of attack, α, can change.

Table 3.4.: Initial and final conditions for the impactor problem.

Attribute	Initial Value	Final Value
Time (s)	0	free
Altitude (km)	26	0
Downrange (km)	0	340
Velocity (km/s)	1.5	free
Flight Path Angle (deg)	free	free
Mass (kg)	136000	free
Angle of Attack (deg)	free	free

Comparisons between the typical approximation and Trigonometrization methods for the impactor problem are shown in Fig. 3.4 and Fig. 3.5. Although the results match closely for this problem, there might be situations where the control is too large and small angle approximation is not valid, leading to large errors. This impactor problem demonstrates how to avoid a transcendental control law scenario.

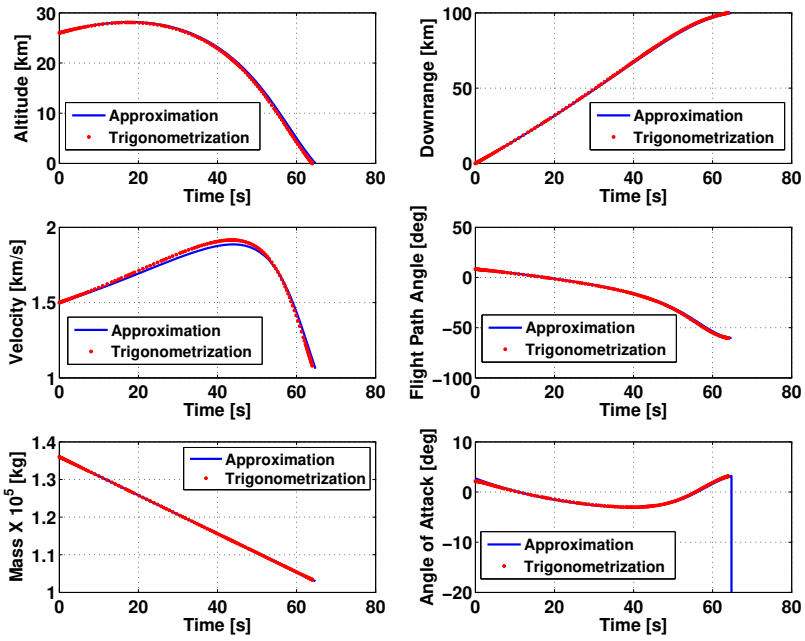

Figure 3.4.: States time-history comparison plots for the impactor problem.

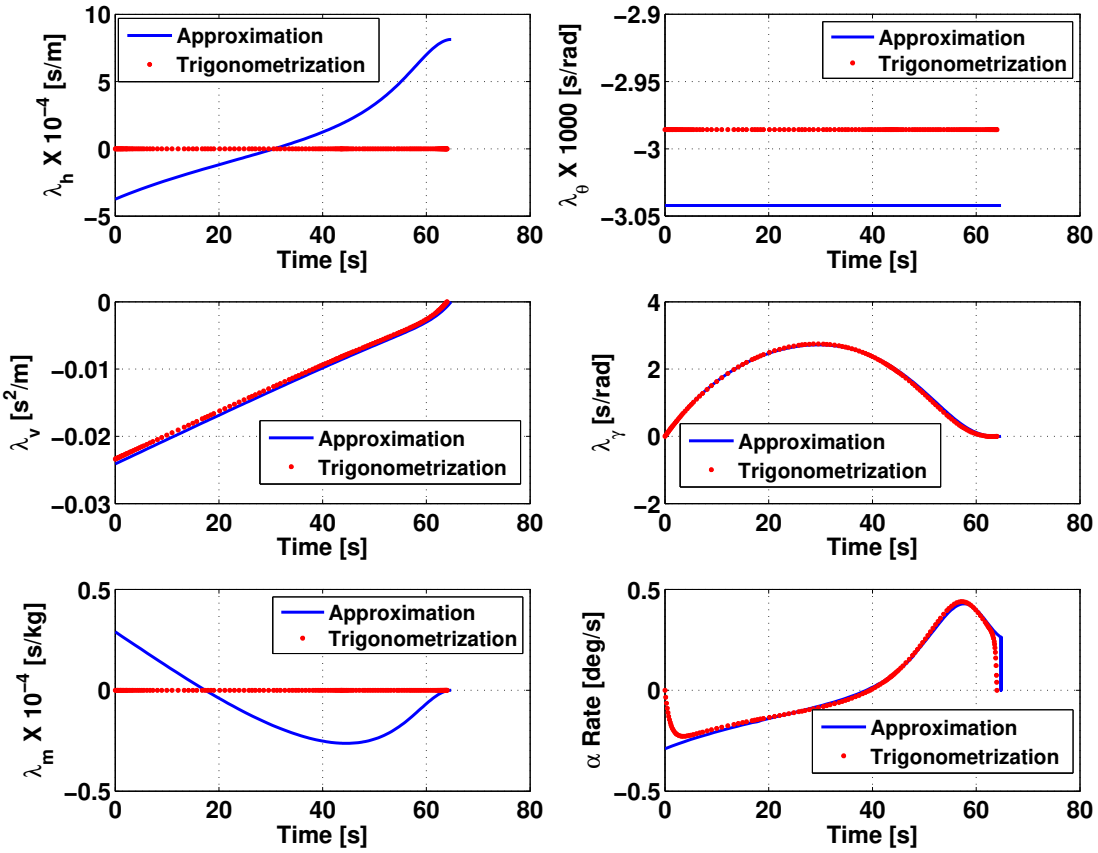

Figure 3.5.: Costates and control time-history comparison plots between the typical approximation and Trigonometrization methods.

According to Eq. (1.12), the terminal value of Hamiltonian, $H(t_f)$, is -1 unit for this time-minimization problem. Since the Hamiltonian is not an explicit function of time, it has a constant value. The Hamiltonian time-history plot, shown in Fig. 3.6, matches well with the result obtained using the transversality condition and has an accuracy of 10^{-7}.

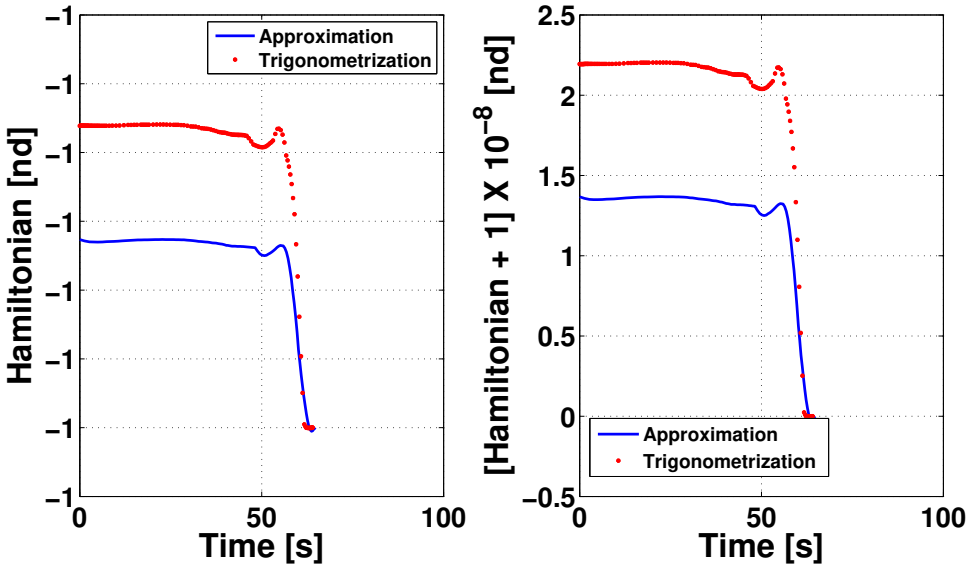

Figure 3.6.: Hamiltonian time-history comparison plots between the typical approximation and Trigonometrization methods.

3.5 Benefit 3: Avoiding Convergence to a Wrong Extremal

Consider a Mars aerocapture problem with an entry vehicle as specified in Ref. 11. The vehicle enters at a very high speed and eliminates a desired amount of kinetic energy before exiting the Martian atmosphere. Eq. (3.13) (discussed in the last section) describes this problem except it has a constant mass and no thrust. The constants related to the vehicle and Mars are shown in Table 3.5. Please note that real-world aerocapture problems have different objectives as compared to this problem. This particular aerocapture problem is chosen to illustrate an advantage of using Trigonometrization.

This section analyzes two test cases, first with an unbounded control and the second with a bounded control using Trigonometrization. The optimal control law for the unbounded control problem is shown by Eq. (3.21). There is only one control option in this case.

$$\alpha^* = \frac{1}{2C_{\mathrm{D}_1}} \left(\frac{\lambda_\gamma C_{\mathrm{L}_1}}{\lambda_v v} - C_{\mathrm{D}_2} \right) \tag{3.21}$$

Table 3.5.: Constants for the Mars aerocapture problem.

Parameter	**Value**
r_p (km)	3397
μ (km^3/s^2)	42828.37
ρ_0 (kg/m^3)	0.02
H (km)	11.1
mass (kg)	92080
A (m^2)	250
C_{L_1} (1/rad)	1.6756
C_{L_0}	-0.2070
C_{D_2} ($1/rad^2$)	2.04
C_{D_1} (1/rad)	-0.3529
C_{D_0}	0.0785

For the latter case, Eq. (3.22) describes the control, where α_{TRIG} becomes the control instead of α. The values of the lower bound, α_{LB}, and the upper bound, α_{UB}, are -16^0 and 16^0, respectively.

$$\alpha = \alpha_1 \sin \alpha_{\text{TRIG}} + \alpha_0 \tag{3.22a}$$

$$\alpha_1 = \frac{\alpha_{\text{UB}} - \alpha_{\text{LB}}}{2} \tag{3.22b}$$

$$\alpha_0 = \frac{\alpha_{\text{UB}} + \alpha_{\text{LB}}}{2} \tag{3.22c}$$

By using Trigonometrization, the optimal control law gains more than one option to choose from, and PMP can then select the optimal control. Eq. (1.7) for this problem reduces to the expression shown in Eq. (3.23) and the control law for the bounded problem is shown by Eq. (3.24).

$$\frac{\partial H}{\partial u^*} = [-2v\lambda_v C_{D_1}(\alpha_1 \sin \alpha_{\text{TRIG}} + \alpha_0) - v\lambda_v C_{D_2} + \lambda_\gamma C_{L_1}] \cos \alpha_{\text{TRIG}} = 0 \tag{3.23}$$

$$\alpha_{\text{TRIG}}{}^{*} = \begin{cases} \dfrac{-\pi}{2} \\ \dfrac{\pi}{2} \\ \arcsin\left[\dfrac{1}{2C_{\text{D}_1}\alpha_1}\left(\dfrac{\lambda_\gamma C_{\text{L}_1}}{\lambda_v v} - C_{\text{D}_2}\right) - \dfrac{\alpha_0}{\alpha_1}\right] \end{cases} \tag{3.24}$$

The conditions on the initial and final states of the TPBVP for both the cases are shown in Table 3.6. A comparison of the results obtained for the two cases is shown in Table 3.7. The minimum time for the unbounded case is more than 2000 s, and the angle of attack remains small even without imposing constraints upon it. The bounded control case, on the other hand, has an optimal time of flight of around 100 s, which matches with intuitive expectations.

Table 3.6.: Initial and final conditions for the Mars aerocapture problem.

Attribute	**Initial State**	**Final State**
Time (s)	0	free
Altitude (km)	80	80
Downrange (km)	0	free
Velocity (km/s)	6	4
Flight Path Angle (deg)	free	free

Table 3.7.: Results comparison for the Mars aerocapture problem.

Attribute	**Unbounded Control**	**Bounded Control**
Time of Flight (s)	2192.54	96.56
Downrange (km)	19178.16	828.05
Initial Flight Path Angle (deg)	-6.13	-22.06
Terminal Flight Path Angle (deg)	3.02	23.47

The states and control time-history plots comparison between the unbounded and bounded control cases are shown in Fig. 3.7. Since the solver minimizes the

time of flight, the control attains very large positive values, and the vehicle dives deep into the atmosphere using a steep initial flight path angle, thereby removing a large amount of kinetic energy in a short amount of time. However, the results for the unbounded case are opposite from this expectation, indicating that the control should maintain a low negative value and fly with a shallow flight path angle to stay longer in the atmosphere. This should actually happen when maximizing the time of flight. The solution process often finds it challenging to construct solutions that satisfy the necessary conditions of optimality, and it omits a sufficiency check to avoid a further increase in complexity.

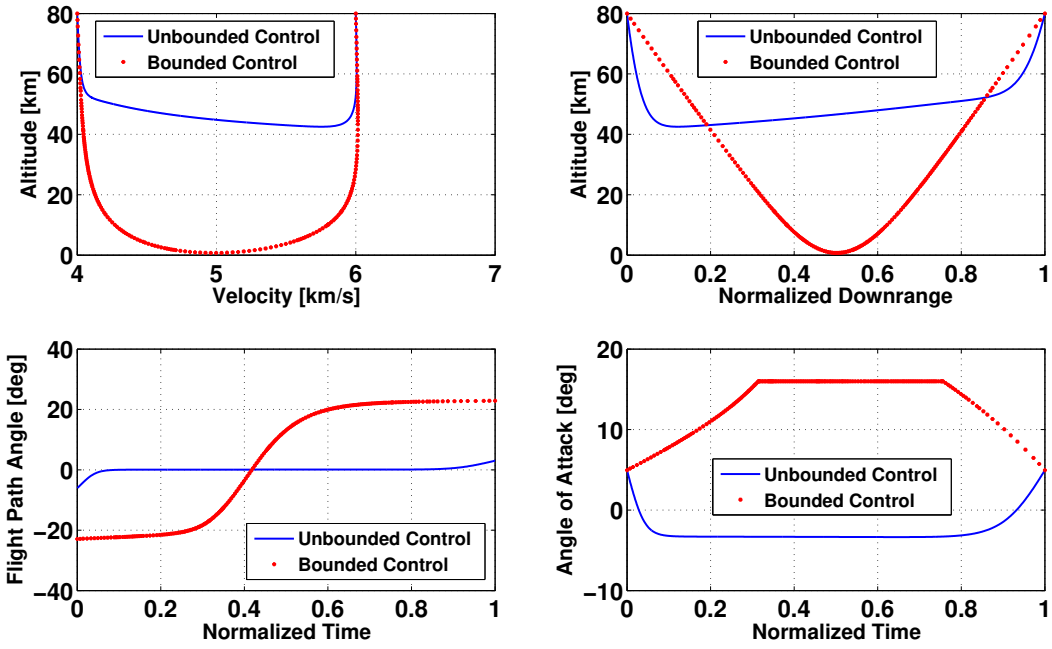

Figure 3.7.: States and control time-histories for the Mars aerocapture problem.

In the case of a bounded control, the control law has the options listed in Eq. (3.24), and PMP leads to a simple sufficiency check for each option. This process easily guarantees that the solution will be a local minimum and not a maximum. When the unbounded case used the Trigonometrization solution as a guess, it still resulted in a

local maximum, proving that there is no way the unbounded formulation can output a minimum time solution.

Since the optimal control law and the boundary condition on the Hamiltonian depend on costates, a particular combination of them can lead to a local maximum even when the problem is to find the local minimum. Fig. 3.8 shows such a combination of costates for the unbounded control case and draws a comparison with the costates obtained for the trigonometrized problem. Thus, Trigonometrization avoids such wrong extremals while simultaneously making the OCP more realistic by imposing practical bounds on the control.

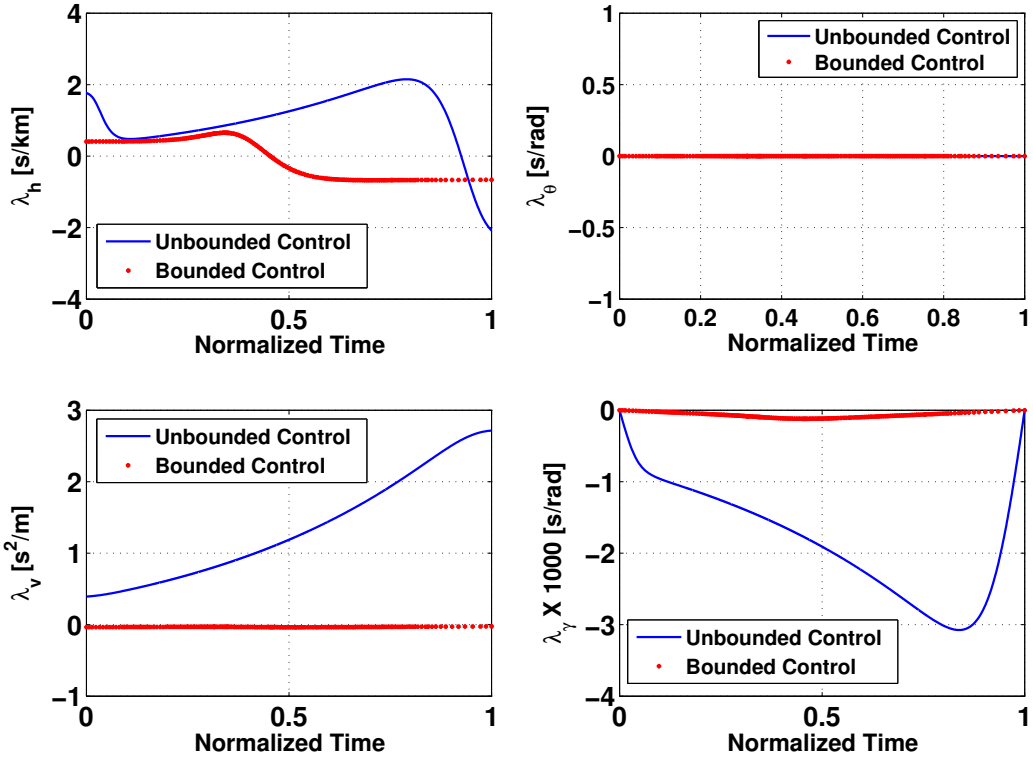

Figure 3.8.: Costates time-history plots for the Mars aerocapture problem.

The terminal value of Hamiltonian, $H(t_f)$, is -1 unit according to Eq. (1.12) for this time-minimization problem. The Hamiltonian is not an explicit function of time

and has a constant value. The Hamiltonian time-history plot, shown in Fig. 3.9, matches well with the result obtained using the transversality condition and has an accuracy of 10^{-7}.

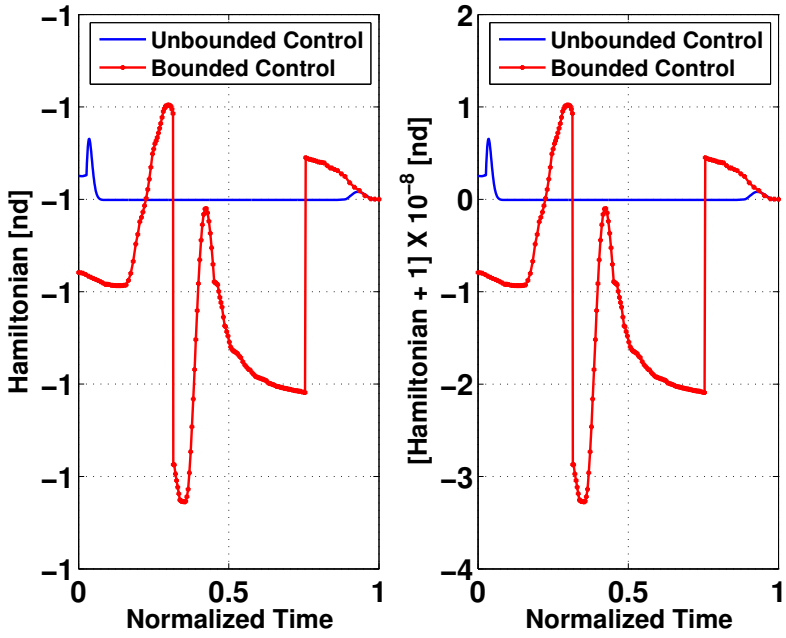

Figure 3.9.: Hamiltonian time-history plots for the Mars aerocapture problem.

The Trigonometrization technique resolved the three issues pertaining to OCPs with pure control constraints containing non-linear controls. This technique can be used to solve very complicated aerospace OCPs as shown in the following section.

3.6 A Complex Aerospace Problem: Noise-Minimal Trajectories For Enabling Night Flights

Optimization of flight trajectories is an area of vital importance in air traffic management from the operations point of view. Generally, studies under this topic aim to define optimal flight paths that ultimately lead to energy-efficient flights. [156] Noise of commercial aircraft has been a cause of serious concern for the population around airports. [157] This problem manifests during night-time operations when an

aircraft significantly disturbs the surrounding area. While constant descent approach (CDA) is a possible solution [158], many countries impose night flying restrictions wherein the airport is closed and no aircraft operations can take place. Hence, flight authorities can cancel the flight at the airport of origin if they scheduled an aircraft to land at a particular airport. Alternatively, flight authorities can divert the aircraft to the nearest airport open for night-time operations. Such laws become a serious impediment, especially in the European Union (EU) where almost all airports do not permit night-time operations. [159] The cost incurred due to these impediments is likely to be high.

Improvement of engine characteristics as well as development of new flight paths are two solutions that reduce aircraft noise. [156, 160] The goal of the investigation in this section is to maintain the high safety standards of flight operations when designing new flight paths that minimize noise. [157] This study formulates an OCP and solves to minimize the noise of an aircraft during landing. The flight dynamics of an aircraft represent a system of ordinary differential equations along with some safety and comfort constraints used in general practice to satisfy public transport requirements. [161, 162] Trigonometrization imposes realistic bounds on the controls to simulate and solve a real-world, noise minimal aircraft landing problem, which has not been done before. [153] Previously, researchers conducted a 2-DOF study on noise minimization aircraft trajectories whereas this section focuses on a more complicated and realistic 3-DOF case. [163] Subsequently, this section defines a cost functional that aims to minimize the noise index of an aircraft landing event. [157, 160, 164]

To design minimal noise trajectories, the OCP should consist of a suitable noise index. The general aircraft noise indices, which effectively describe the noise during an aircraft landing event, are Sound Exposure Level, Overall Sound Pressure Level [165], Effective Perceived Noise Level (EPNL), and Equivalent Noise Level. [157] This chapter selects minimization of the EPNL (i.e., the noise level that a person standing at a fixed distance perceives from the aircraft). In any aircraft landing event [160], it is necessary to consider the person who is nearest to the aircraft and who is affected

the most by the aircraft's noise. Hence, the noise index is a function of the altitude, z. This function represents the zoning-plan of the community surrounding the airport and approximates the altitude as (z+50) to avoid issues related to singularity when the altitude, z, becomes 0 units. [160]

It is also necessary to consider the duration for which the noise lasts. Hence, this study choses minimization of the EPNL. [160] Thus, the cost functional is to minimize the EPNL over the entire trajectory, termed as Integral Effective Perceived Noise Level (IEPNL). Eq. (3.25a) [160] shows IEPNL while Appendix B contains the mathematical background about it. This problem uses EOMs describing a 3-DOF trajectory of an aircraft as shown in Eqs. (3.25b)-(3.25g) [161]. Eq. (3.25h) and Eq. (3.25i) approximate the lift force, L, and the drag force, D, respectively. [156,160]

$$\text{Minimize: } J = \int_0^{t_f} \frac{18.73\ T^{5.2}}{v(z+50)^{2.5}} \cos\gamma \, \mathrm{d}t \tag{3.25a}$$

$$\text{Subject to: } \dot{x} = v\cos\gamma\cos\psi \tag{3.25b}$$

$$\dot{y} = v\cos\gamma\sin\psi \tag{3.25c}$$

$$\dot{z} = v\sin\gamma \tag{3.25d}$$

$$\dot{v} = \frac{T\cos\alpha - D}{m} - g\sin\gamma \tag{3.25e}$$

$$\dot{\psi} = \frac{(T\sin\alpha + L)\sin\phi}{mv\cos\gamma} \tag{3.25f}$$

$$\dot{\gamma} = \frac{(T\sin\alpha + L)\cos\phi}{mv} - \frac{g\cos\gamma}{v} \tag{3.25g}$$

$$L = W = mg \tag{3.25h}$$

$$D = c_1 v^2 + \frac{c_2}{v^2} \tag{3.25i}$$

In the above equation, J is the noise minimization cost functional, x is the down-range, y is the crossrange, z is the altitude, v is the velocity, ψ is the heading angle, γ is the flight path angle, m is the mass of the vehicle, D is the drag force magnitude, L is the lift force magnitude, ϕ is the bank angle, α is the angle of attack, and T is the thrust force magnitude. The constants used in this problem, as shown in

Table 3.8, are the weight of the aircraft, W, the acceleration due to Earth's gravity, g, and constants related to the drag force, c_1 and c_2. The literature studies used these constants for this problem, which correspond to a light fighter aircraft. This problem is particularly difficult to solve because the general tendency to minimize noise based on the cost functional (as shown in Eq. (3.25a)) would be to fly at high altitudes with low thrust and high velocity. While considering a landing event, not only the altitude but also the velocity must decrease to satisfy operational constraints, which would inevitably lead to an increase in the noise level. [164]

Table 3.8.: Parameters for the aircraft noise minimization trajectory problem.

Parameter	c_1	c_2	W	g
Value	0.226	5.2e6	7.18	9.81
Unit	kg/m	kg m^3/s^4	kN	m/s^2

Trigonometrization converts the bank angle and the angle of attack to the form shown in Eq. (3.26a) and Eq. (3.26b), respectively. The bounds on the bank angle and angle of attack are $\pm 60°$ ($\pm\pi/3$) and $\pm 15°$ ($\pm\pi/12$), respectively. Thrust is similarly trigonometrized as shown in (3.26c) with a lower bound of 300 N and an upper bound of 3420 N. [160]

$$\phi = \frac{\pi}{3} \sin \phi_{\text{TRIG}} \tag{3.26a}$$

$$\alpha = \frac{\pi}{12} \sin \alpha_{\text{TRIG}} \tag{3.26b}$$

$$T = 1560 \sin T_{\text{TRIG}} + 1860 \tag{3.26c}$$

The Hamiltonian for this problem is shown in Eq. (3.27). Eq. (1.6) evaluate the EOMs corresponding to the costates as shown in Eq. (3.28).

$$\begin{aligned} H = {} & \frac{18.73\ T^{5.2}}{v(z+50)^{2.5}} \cos\gamma + \lambda_x v \cos\gamma \cos\psi + \lambda_y v \cos\gamma \sin\psi + \lambda_z v \sin\gamma \\ & + \lambda_v \left(\frac{T\cos\alpha - D}{m} - g\sin\gamma \right) + \frac{\lambda_\psi (T\sin\alpha + L)\sin\phi}{mv\cos\gamma} \\ & + \lambda_\gamma \left[\frac{(T\sin\alpha + L)\cos\phi}{mv} - \frac{g\cos\gamma}{v} \right] \end{aligned} \tag{3.27}$$

$$\dot{\lambda_x} = 0 \tag{3.28a}$$

$$\dot{\lambda_y} = 0 \tag{3.28b}$$

$$\dot{\lambda_z} = \frac{46.825\ T^{5.2}}{v(z+50)^{3.5}} \cos\gamma \tag{3.28c}$$

$$\begin{aligned} \dot{\lambda_v} = {} & \frac{18.73\ T^{5.2}}{v^2(z+50)^{2.5}} \cos\gamma - \lambda_x \cos\gamma\cos\psi - \lambda_y \cos\gamma \sin\psi - \lambda_z \sin\gamma \\ & + \frac{2\lambda_v (c_1 v^4 - c_2)}{mv^3} + \frac{\lambda_\psi (T\sin\alpha + L)\sin\phi}{mv^2\cos\gamma} \\ & + \lambda_\gamma \left[\frac{(T\sin\alpha + L)\cos\phi}{mv^2} - \frac{g\cos\gamma}{v^2} \right] \end{aligned} \tag{3.28d}$$

$$\dot{\lambda_\psi} = \lambda_x v \cos\gamma \sin\psi - \lambda_y v \cos\gamma \cos\psi \tag{3.28e}$$

$$\begin{aligned} \dot{\lambda_\gamma} = {} & \frac{18.73\ T^{5.2}}{v(z+50)^{2.5}} \sin\gamma + \lambda_x v \sin\gamma \cos\psi + \lambda_y v \sin\gamma \sin\psi \\ & - \lambda_z v \cos\gamma + \lambda_v g \cos\gamma - \frac{\lambda_\psi (T\sin\alpha + L)\sin\phi\sin\gamma}{mv\cos^2\gamma} - \frac{\lambda_\gamma g \sin\gamma}{v} \end{aligned} \tag{3.28f}$$

Using OCT, the optimal control options obtained for this problem are shown in Eqs. (3.29)–(3.31) for bank angle, angle of attack, and thrust control, respectively.

PMP, described in Eq. (1.11), then selects the optimal combination of controls from among these options.

$$\phi^*_{TRIG} = \begin{cases} -\dfrac{\pi}{2} \\ \arcsin\left[\dfrac{\arctan\left(\dfrac{\lambda_\psi}{\lambda_\gamma \cos\gamma}\right)}{\frac{\pi}{3}}\right] \\ \arcsin\left[\dfrac{\arctan\left(\dfrac{\lambda_\psi}{\lambda_\gamma \cos\gamma}\right) + \pi}{\frac{\pi}{3}}\right] \\ \dfrac{\pi}{2} \end{cases} \tag{3.29}$$

$$\alpha^*_{TRIG} = \begin{cases} -\dfrac{\pi}{2} \\ \arcsin\left[\dfrac{\arctan\left(\dfrac{\lambda_\psi \sin\phi}{v\lambda_v \cos\gamma} + \dfrac{\lambda_\gamma \cos\phi}{v\lambda_v}\right)}{\frac{\pi}{12}}\right] \\ \arcsin\left[\dfrac{\arctan\left(\dfrac{\lambda_\psi \sin\phi}{v\lambda_v \cos\gamma} + \dfrac{\lambda_\gamma \cos\phi}{v\lambda_v}\right) + \pi}{\frac{\pi}{12}}\right] \\ \dfrac{\pi}{2} \end{cases} \tag{3.30}$$

$$T^*_{TRIG} = \begin{cases} -\dfrac{\pi}{2} \\ \arcsin\left[\dfrac{1}{1560}\left(\dfrac{v(z+50)^{2.5}}{97.396\cos\gamma}\right)^{\frac{1}{4.2}}\right. \\ \left.\left(-\dfrac{\lambda_v \cos\alpha}{m} - \dfrac{\lambda_\psi \sin\alpha \sin\phi}{mv\cos\gamma} - \dfrac{\lambda_\gamma \sin\alpha\cos\phi}{mv}\right)^{\frac{1}{4.2}} - \dfrac{1860}{1560}\right] \\ \dfrac{\pi}{2} \end{cases} \tag{3.31}$$

Eq. (3.30) shows that the calculation of the angle of attack, α^*_{TRIG}, requires optimal values of bank angle, ϕ^*_{TRIG}. Similarly, ϕ^*_{TRIG} and α^*_{TRIG} are necessary to evaluate optimal thrust control, T^*_{TRIG}, as shown in Eq. (3.31). Thus, it is mandatory

to evaluate the optimal bank angle first, followed by the optimal angle of attack and lastly the optimal value of thrust. There are four options for optimal bank angle, four options for optimal angle of attack and three options for optimal thrust, resulting in a total of 48 optimal control options to select by using PMP.

3.6.1 Results

This subsection presents and solves an example scenario for the initial and final conditions enforced upon the aircraft trajectory as shown in Table 3.9. A 3-DOF problem described in Ref. 160 defines the values in this table.

Table 3.9.: Initial and final conditions for the aircraft noise minimization problem.

Attribute	**Initial Value**	**Final Value**
Time (s)	0	free
Downrange (km)	0	5.4
Crossrange (km)	0	4.6
Altitude (km)	1.197	0
Velocity (m/s)	124	77.5
Heading Angle (deg)	0	45
Flight Path Angle (deg)	0	0

The results obtained by satisfying necessary conditions of optimality in OCT for this OCP were matched with the results obtained using GPOPS-II. The 3D trajectory plot and the noise generated by the aircraft are shown in Fig. 3.10. The IEPNL generated by the aircraft is found to be 6395 dB-s. [156, 160] The time-histories of the states are shown in Fig. 3.11. The velocity along the trajectory is within the acceptable range for comfort and safety of the passengers.

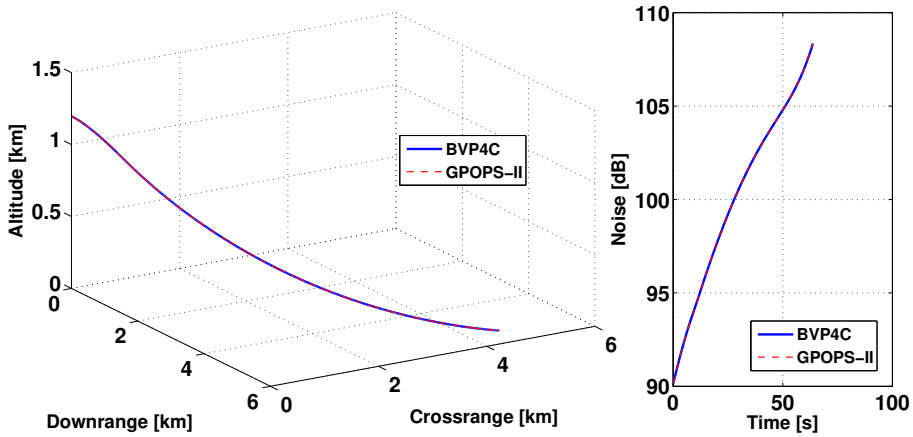

Figure 3.10.: 3D trajectory and objective plots for the noise minimization problem.

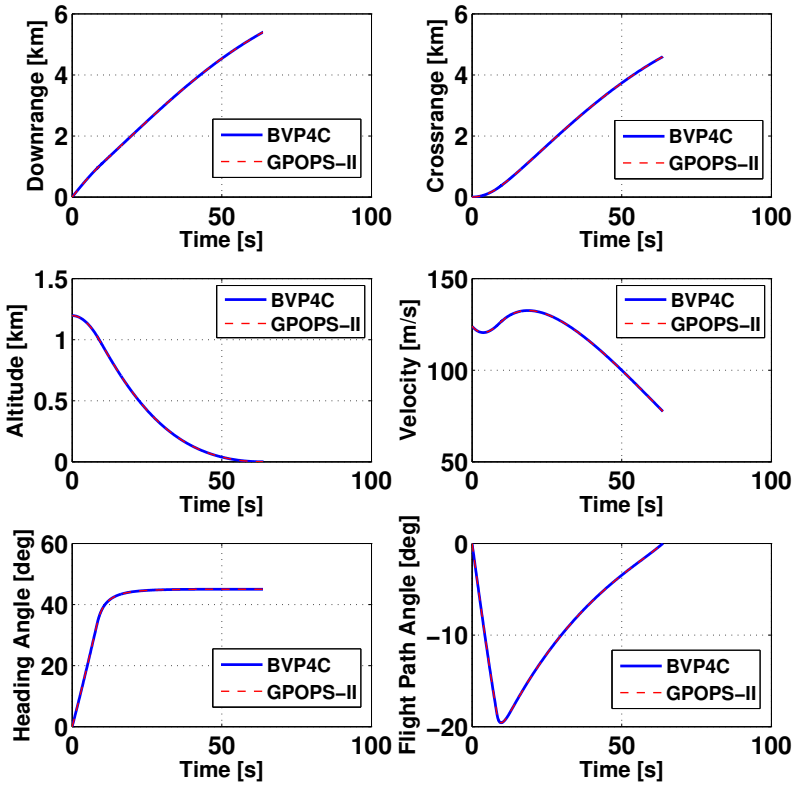

s

Figure 3.11.: State time-history plots for the aircraft noise minimization problem.

The control time-history plots for the bank angle, the angle of attack, and the thrust are shown in Fig. 3.12. These controls stay within the required bounds.

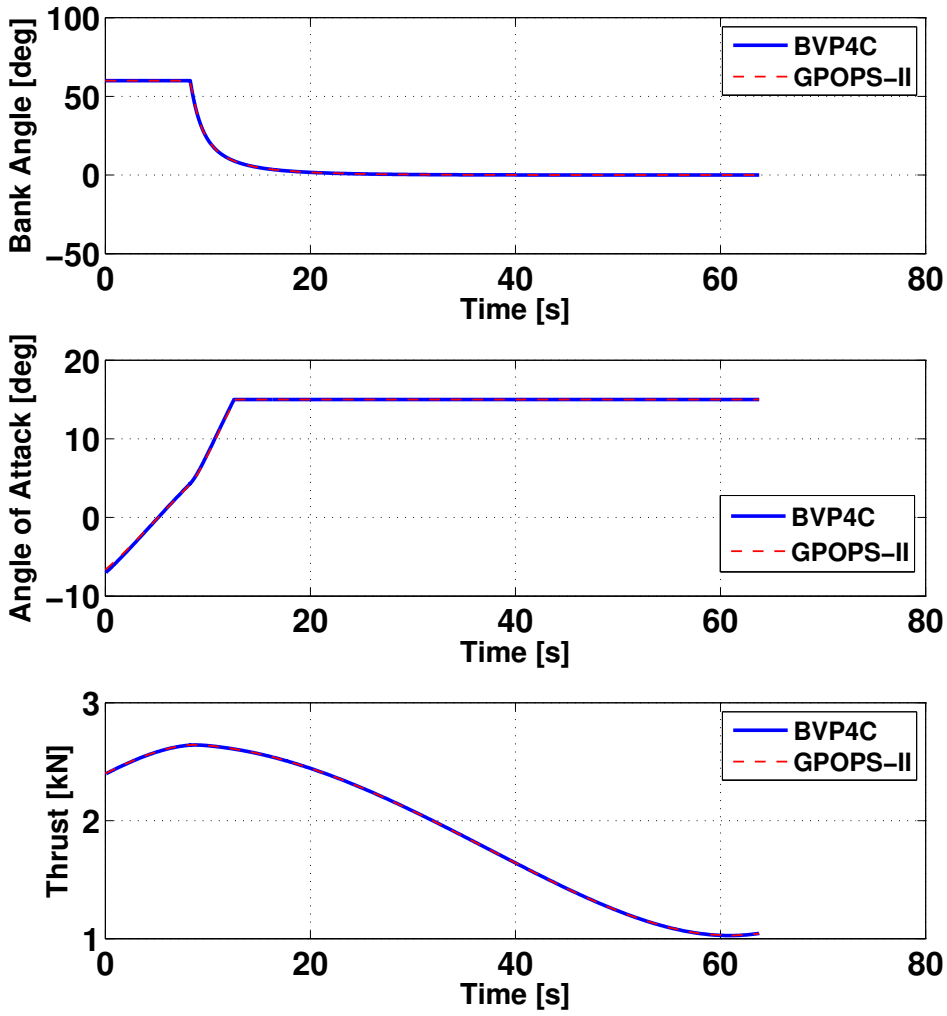

Figure 3.12.: Controls time-history plots for the aircraft noise minimization problem.

Fig. 3.13 shows that the magnitudes of the costates are extremely high, thus highlighting the need to scale the problem under consideration. However, no scaling has been employed to solve this problem in its current form, which goes to show the robustness of the solver employed. Please note that a different combination of

costates from GPOPS-II results in the same optimal controls, and, hence, there is a difference in the costates between OCT and GPOPS-II as shown in Fig. 3.13.

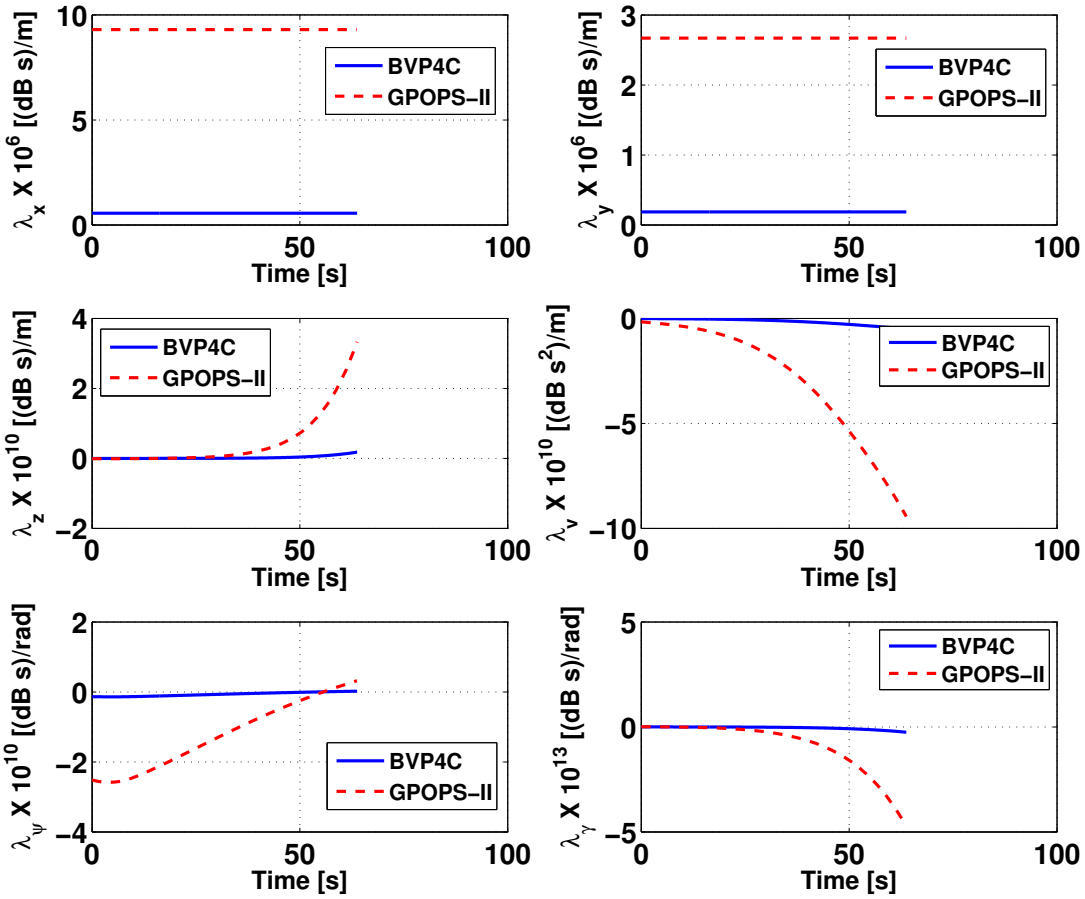

Figure 3.13.: Costates time-history plots for the aircraft noise minimization problem.

The value of $\frac{\partial \phi}{\partial t_f}$ for this problem is 0 dB. Hence, the terminal value of Hamiltonian is also 0 dB according to Eq. (1.12). The Hamiltonian also has a constant value since it is not an explicit function of time. The Hamiltonian time-history plot is shown in Fig. 3.14, which matches very well with the result obtained using the transversality condition. Please note in Fig. 3.14 that the results for the Hamiltonian obtained using GPOPS-II are inaccurate.

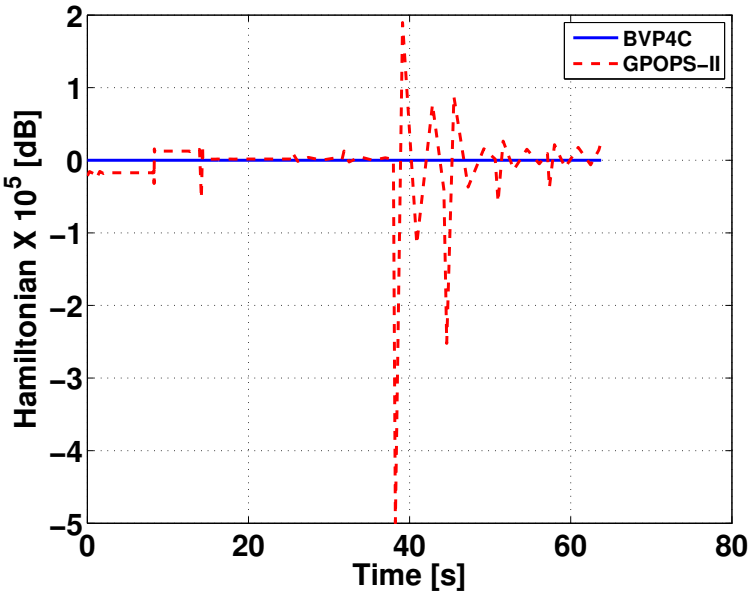

Figure 3.14.: Results comparison for the Hamiltonian of the aircraft noise minimization problem.

This is the first instance when an aerospace problem with six states and three bounded controls, as presented in this chapter, has been solved using Trigonometrization. This sets the confidence to increase the fidelity of the noise minimization functional by incorporating a population model, thus accounting for a more realistic perceived noise, as described in the next subsection.

3.6.2 Higher Fidelity Population Model

In the prior example, the cost functional minimized is the IEPNL as perceived by the person nearest to the aircraft. In order to model and simulate a realistic scenario, it is important to incorporate the population distribution around the airport. If the latitudinal and the longitudinal coordinate data corresponding to the area around the airport is available, a polynomial function can model the population data. This equation, when multiplied with the noise model, yields a weighted cost functional

that is representative of the noise perceived by the total number of people in an area rather than the noise perceived when considering a unit population distribution. Such a weighted cost functional will ensure that the aircraft's noise affects a minimum number of people during its terminal descent. Eq. (3.32) shows the modified cost functional, which is essentially the product of Eq. (3.25a) and the PDF.

$$J = \int_0^{t_f} (\text{PDF}) \frac{18.73\ T^{5.2}}{v(z+50)^{2.5}} \cos\gamma \, \mathrm{d}t \tag{3.32}$$

Due to unavailability of the aforementioned coordinate data for the population model, this study employed a general polynomial function as shown in Eq. (3.33), which is representative of a population change as the aircraft flies towards the airport. This non-linear function models the population variation based on the changes in the crossrange as shown in Fig. 3.15.

$$\text{PDF} = \frac{4600}{y+1} \tag{3.33}$$

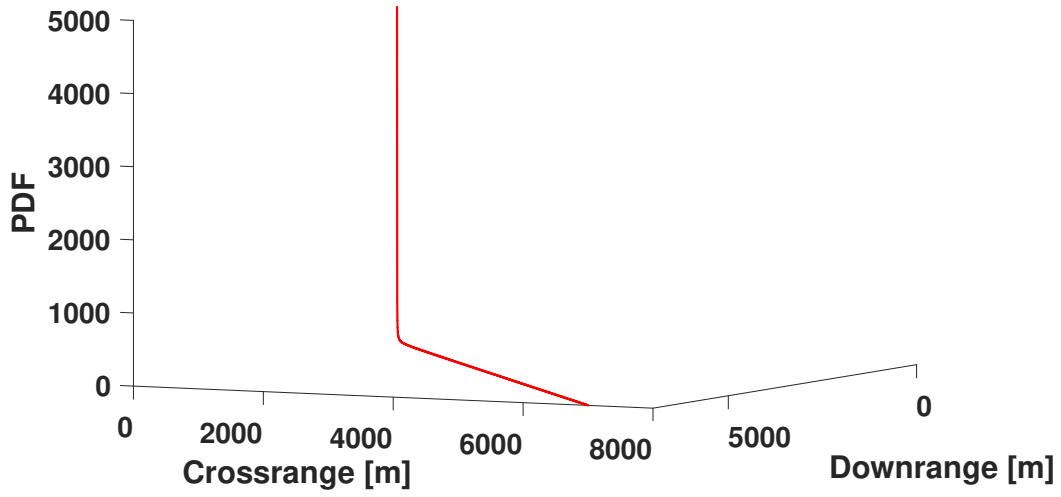

Figure 3.15.: The chosen PDF.

The problem formulation is similar to Sec. 3.6 except that Eq. (3.32) describes the objective functional, where the PDF is as shown in Eq. (3.33). Eq. (3.34) shows the optimal control law for thrust. The optimal control law for the angle of attack and bank angle controls remain unchanged from the previous example. Also, the modified EOMs for the costates are shown in Eqs. (3.35a)–(3.35d). The costates for the downrange, x, and the heading angle, ψ, remain unmodified.

$$T^*_{TRIG} = \begin{cases} -\dfrac{\pi}{2} \\ \arcsin\left[\dfrac{1}{1560}\left(\dfrac{v(1+y)(z+50)^{2.5}}{448021.6\cos\gamma}\right)^{\frac{1}{4.2}}\right. \\ \left.\left(-\dfrac{\lambda_v\cos\alpha}{m} - \dfrac{\lambda_\psi\sin\alpha\sin\phi}{mv\cos\gamma} - \dfrac{\lambda_\gamma\sin\alpha\cos\phi}{mv}\right)^{\frac{1}{4.2}} - \dfrac{1860}{1560}\right] \\ \dfrac{\pi}{2} \end{cases} \tag{3.34}$$

$$\dot{\lambda}_y = \frac{86158\ T^{5.2}\cos\gamma}{v(1+y)^2(z+50)^{2.5}} \tag{3.35a}$$

$$\dot{\lambda}_z = \frac{215395\ T^{5.2}\cos\gamma}{v(1+y)(z+50)^{3.5}} \tag{3.35b}$$

$$\begin{aligned}\dot{\lambda}_v = {} & \frac{86158\ T^{5.2}\cos\gamma}{v^2(1+y)(z+50)^{2.5}} - \lambda_x\cos\gamma\cos\psi - \lambda_y\cos\gamma\sin\psi \\ & - \lambda_z\sin\gamma + \frac{2\lambda_v(c_1v^4 - c_2)}{mv^3} + \frac{\lambda_\psi(T\sin\alpha + L)\sin\phi}{mv^2\cos\gamma} \\ & + \lambda_\gamma\left[\frac{(T\sin\alpha + L)\cos\phi}{mv^2} - \frac{g\cos\gamma}{v^2}\right]\end{aligned} \tag{3.35c}$$

$$\begin{aligned}\dot{\lambda}_\gamma = {} & \frac{86158\ T^{5.2}\sin\gamma}{v(1+y)(z+50)^{2.5}} + \lambda_x v\sin\gamma\cos\psi + \lambda_y v\sin\gamma\sin\psi \\ & - \lambda_z v\cos\gamma + \lambda_v g\cos\gamma - \frac{\lambda_\psi(T\sin\alpha + L)\sin\phi\sin\gamma}{mv\cos^2\gamma} - \lambda_\gamma\frac{g\sin\gamma}{v}\end{aligned} \tag{3.35d}$$

This section draws a comparison between the results obtained while considering the effect of the PDF given by Eq. (3.33) and the results obtained in Sec. 3.6. The 3D trajectory and noise time-history plots, as shown in Fig. 3.16, indicate a different flight path adopted by the aircraft resulting in a higher noise. The IEPNL obtained is 6860 dB-s. As expected, the PDF in this scenario has significantly higher magnitudes than the uniform population distribution investigated previously.

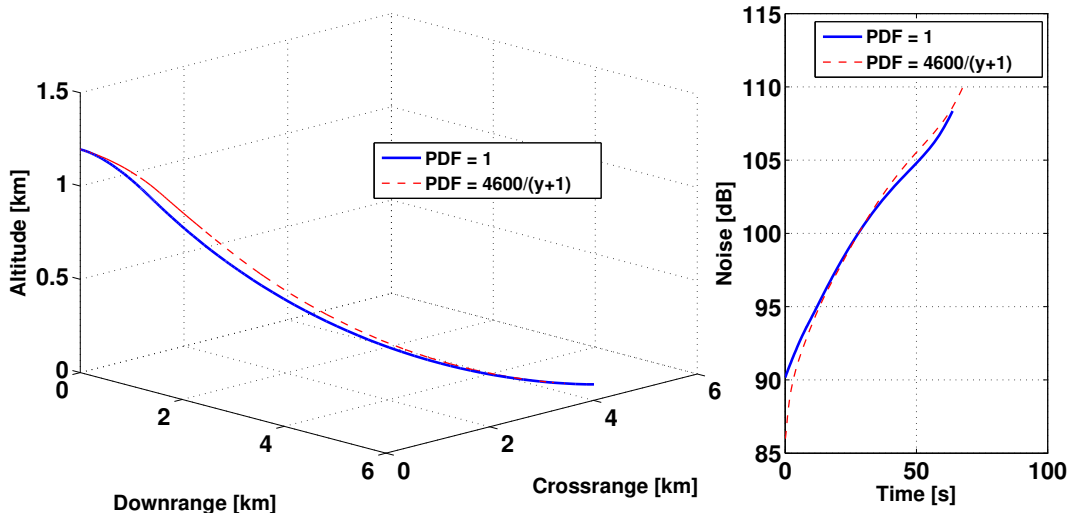

Figure 3.16.: 3D trajectory and noise time-history comparison plots between two population models for aircraft noise minimization problem.

Since the population is very high initially in the crossrange direction, the aircraft flies at a higher altitude to minimize the total perceived noise. The state time-history plots as shown in Fig. 3.17 illustrate this finding.

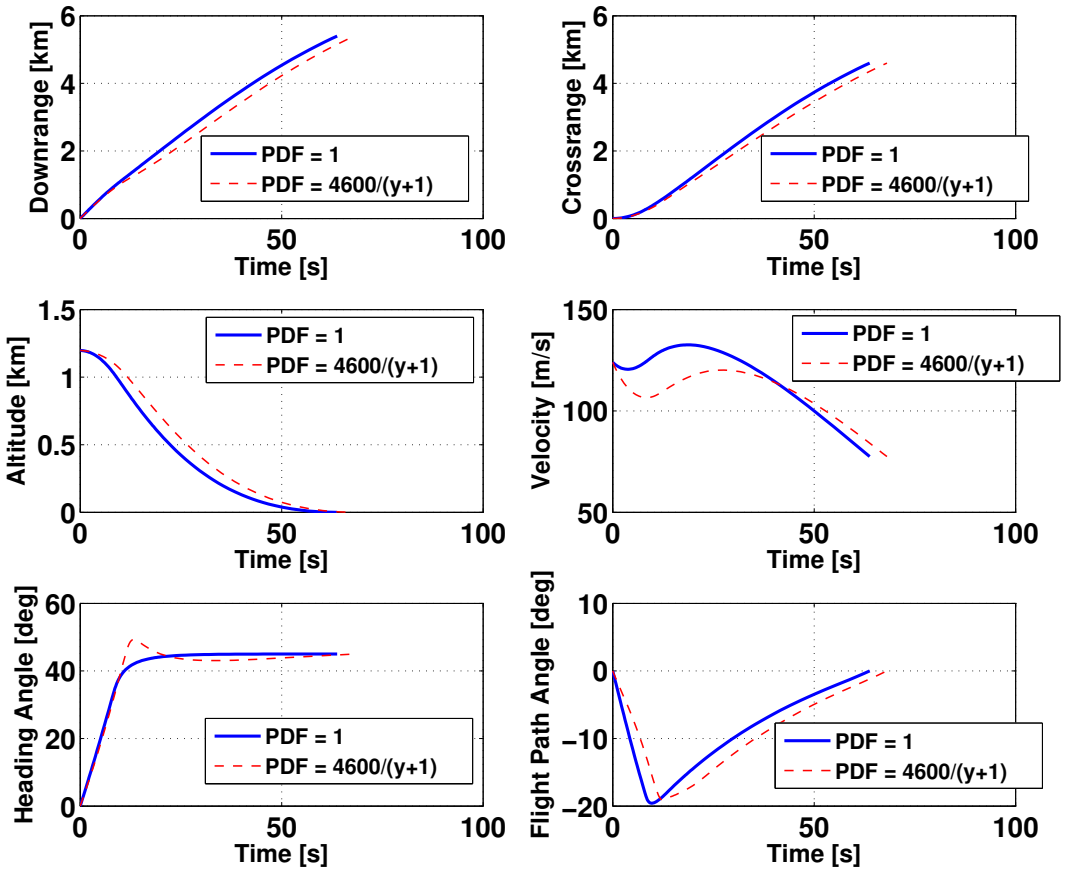

Figure 3.17.: States time-history comparison between two population models.

Given the final state constraints, the aircraft utilizes extremal controls and follow the optimal trajectory as seen in Fig. 3.18. OCT requires the costates to be of high magnitudes in order to obtain such extremal controls. The costates time-history plots as shown in Fig. 3.19, are consistent with the expected results.

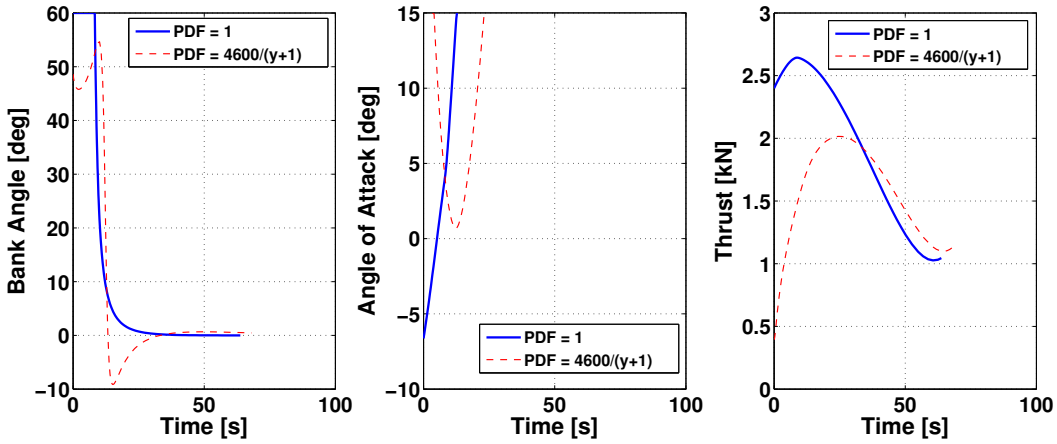

Figure 3.18.: Controls time-history comparison between two population models.

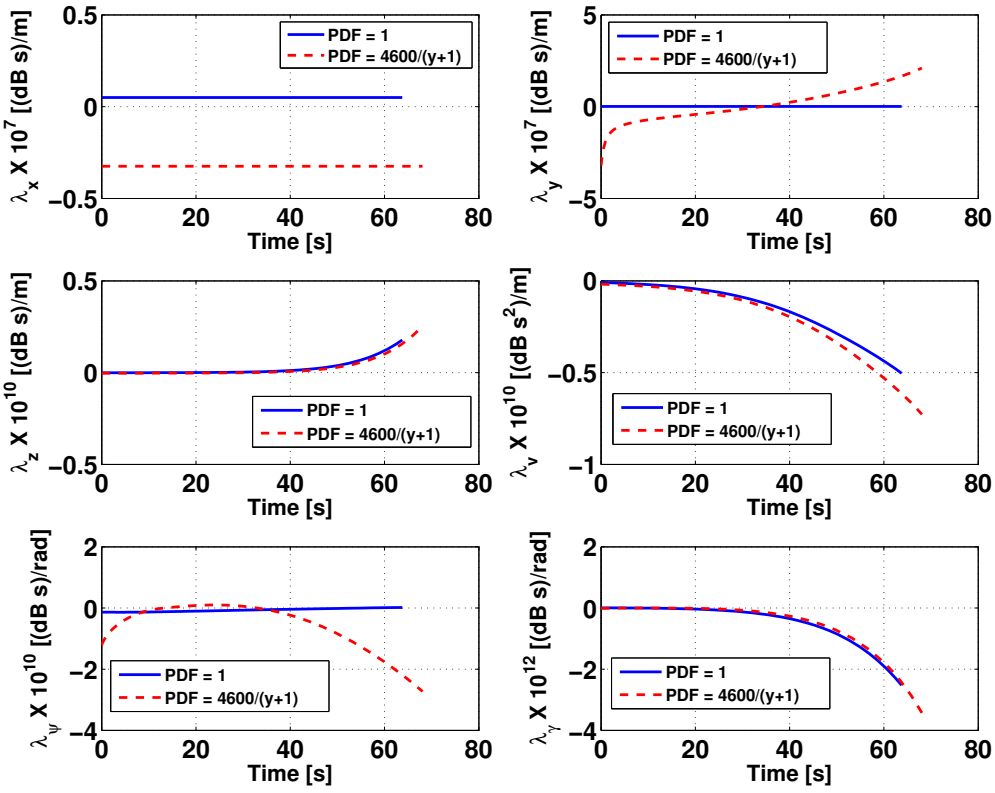

Figure 3.19.: Costates time-history comparison between two population models.

Additionally, to study the practicability of the proposed method, it is interesting to draw comparisons with the currently accepted CDA. The flight trajectory employing CDA has been simulated using the EOMs as described in Eqs. (3.25b)–(3.25f) and the constant parameters as described in Table 3.10.

Table 3.10.: Constant parameters for CDA.

Parameter	**Value**
Angle of attack (deg)	10
Bank angle (deg)	12.5
Thrust (N)	1700
Flight path angle (deg)	-8.5

The optimal noise trajectory reduces the IEPNL by approximately 7% over CDA. This analysis compares the simulated CDA trajectory and corresponding noise time-history with the optimal results in Fig. 3.20.

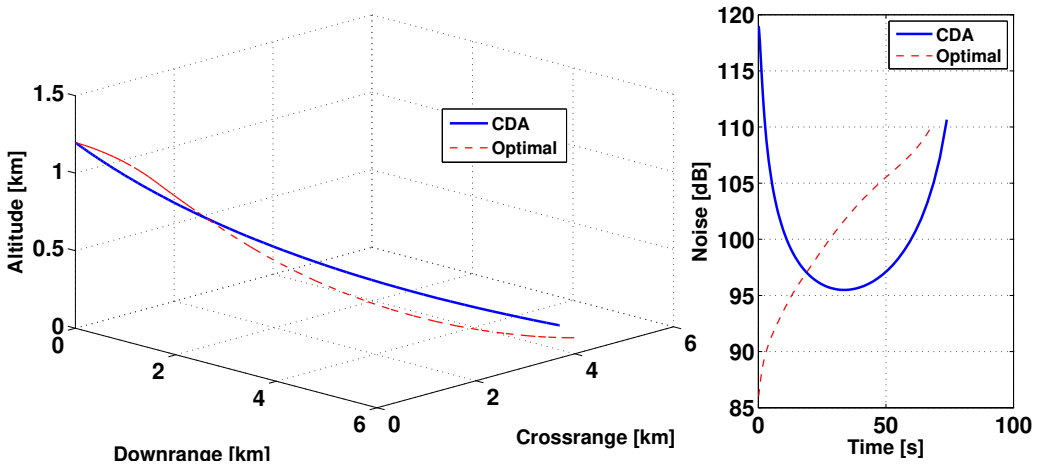

Figure 3.20.: Comparison of 3D trajectory and noise time-history of the aircraft between optimal approach and CDA.

Table 3.11 summarizes the complexity of the noise minimization problem. The major complexities of this problem is the complicated objective function, a large number of optimal control options, and very complicated EOMs for costates.

Table 3.11.: Complexities of the aircraft noise minimization problem.

Parameter	**Complexity**
States	Six states
Controls	Three bounded controls
State equations	Highly non-linear and coupled
Costate equations	Highly non-linear, lengthy, and coupled
Objective functional	Highly non-linear and complex

3.7 Conclusions

This chapter proposed and tested the use of trigonometry in reformulating control expressions in an OCP. It identified three major issues concerning OCPs with constraints upon control, which appear in a non-linear form in the Hamiltonian.

1. Solving a MPBVP using the traditional approach when solving OCPs with control constraints is very complicated.

2. When the necessary conditions for optimality became transcendental, traditional methods cannot guarantee obtaining analytic control solutions.

3. Some unconstrained OCPs may converge to the wrong extremum as they satisfy only the necessary conditions of optimality.

For issue 1, trigonometrizing the controls ensured the OCP remained a TPBVP, which is much simpler to solve and leads to faster computation of results. This study used the Rayleigh problem to validate this point. For issue 2, it was shown through an

impactor problem that the use of Trigonometrization avoids transcendental control laws and employs more realistic controls. Moreover, Trigonometrization of OCPs described in issue 3 generates additional control options corresponding to the limits of control, thereby permitting the usage of PMP to check for the sufficiency of solutions to identify the correct extremum. This benefit of Trigonometrization was shown using the Mars aerocapture problem with a SEV, where the objective was to minimize the time of flight. When the OCP was left unbounded, the vehicle followed the maximum time of flight trajectory whereas for the bounded case, the vehicle followed the minimum time of flight trajectory. Verification and validation in this chapter utilized GPOPS-II, and the results obtained from the two solvers match well.

After verification and validation of Trigonometrization, this chapter involved solving a 3-DOF flight trajectory problem to find noise-minimal trajectories for an aircraft during its terminal descent phase. OCT requires satisfying necessary conditions of optimality, thus guaranteeing a high-quality solution. This chapter, therefore, uses OCT along with Trigonometrization to find the optimal solution. To demonstrate the effect of variable population on the noise optimal trajectories of the aircraft, an example scenario has been presented with a simplistic PDF. OCT solves the considered scenario and yields a relatively different 3D trajectory to the original problem that does not take population into account while calculating total perceived noise. Comparisons drawn with the CDA trajectory reveal that the solvers indeed minimize IEPNL. Thus, this chapter lays the foundation for assessing the practicability of constrained night time operations, especially cargo operations. This chapter gains high relevance in the current scenario where the flight authorities plan on using the NextGen air transportation system, part of which aims to reduce noise pollution.

The successful application of the Trigonometrization technique to OCPs containing pure control constraints prompted further development of this technique for two other big classes of OCPs: first with mixed state-control constraints and second with pure state constraints. The next chapter includes the development and usage of the Trigonometrization technique for these classes of OCPs.

4. Advancements in Optimal Control Theory for Problems with Mixed State-Control and Pure State Constraints

4.1 Introduction

TRIGONOMETRY can successfully solve OCPs with pure control constraints as shown in Chapters 2 and 3 of this thesis. This chapter extends the use of the bounding property of trigonometric functions to OCPs with mixed state control constraints, where the bounds on control are variable and dependent on the state.

The traditional approach for OCPs with mixed constraints requires formulating and solving a MPBVP, which is very complicated and difficult for practical aerospace problems. Sec. 1.2.2.3 contains a brief discussion about this traditional approach. Fig. 4.1 shows an example of the constraint structure for such a complicated MPBVP, where arcs 1 and 3 correspond to mixed state-control and arcs 2 and 4 correspond to unconstrained trajectory. Here, $f(u, x)$ is the mixed state-control constraint with S_{MIN} and S_{MAX} as its extremal values. Posing the control in a trigonometric form greatly simplifies the problem formulation and solution processes by keeping the problem as a TPBVP.

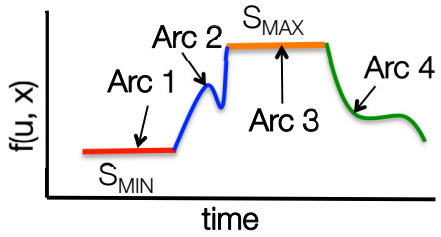

Figure 4.1.: A complicated constraint history for an OCP with mixed constraints.

This chapter comprises of the following four sections. Sec. 4.2 introduces and describes the concept of Trigonometrization for mixed constraint problems. Sec. 4.3 verifies and validates Trigonometrization using Rayleigh mixed constraint problem. Sec. 4.4 shows a complex aerospace application of the Trigonometrization approach developed for mixed constraint OCPs through a space shuttle reentry problem with a complicated heating constraint. Sec. 4.5 and Sec. 4.6 describe the development and application of the Trigonometrization technique to OCPs with mixed constraints containing non-linear controls and OCPs with pure state constraints, respectively. Sec. 4.7 forms the conclusion of this chapter.

4.2 Trigonometrization of Mixed Constraint Optimal Control Problems

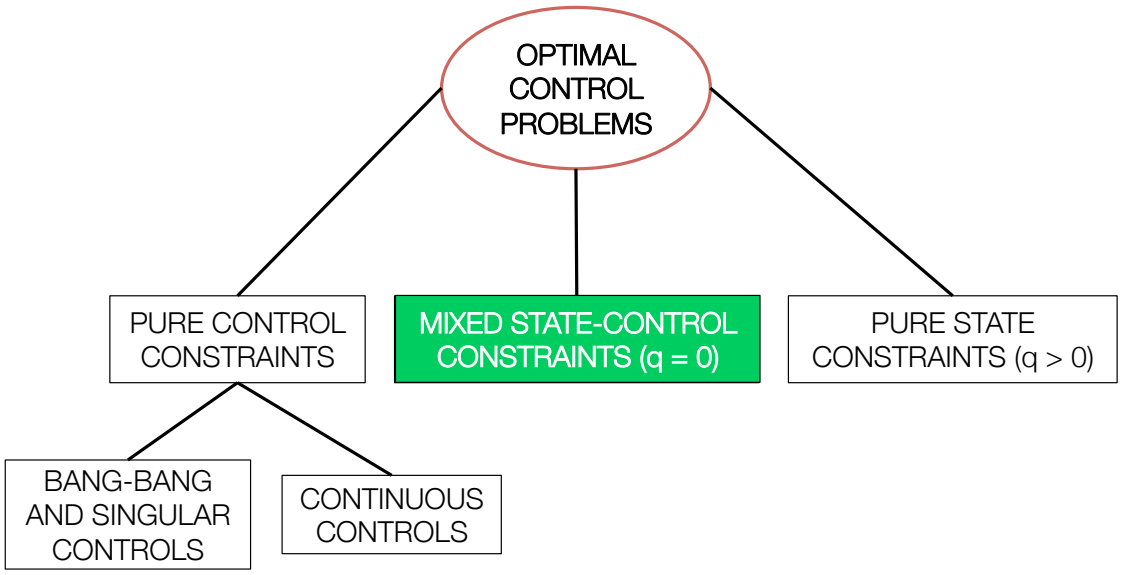

A set of OCPs has constraints on the states and controls as shown in the inequality Eq. (4.1), where S_{LB} and S_{UB} are constant lower and upper bounds on the constraint, respectively. The constraint on state is dependent on the control. Another way to look at it is that the constraint on control is dependent on the state. This set of OCPs has the order of path constraint (described in Sec. 1.2.2.3), q, as 0. As a result, this set does not require the additional necessary conditions described in Sec. 1.2.2.4.

Literature calls the constraint for such OCPs as mixed state control constraint or in short, mixed constraint. For simplicity, this section assumes that u appears linearly in the mixed constraint.

$$S_{\text{LB}} \leq f(x) + g(x)\ u \leq S_{\text{UB}} \tag{4.1}$$

Eq. (4.1) gains the form of inequality constraint on the control as shown in Eq. (4.2a). Eq. (4.2a) can be further simplified to show lower and upper limits on control, u, given by Eq. (4.2b). The Hamiltonian remains the same as Eq. (3.1) discussed in previous chapter. The major difference here is that the control has variable bounds on it based on the state of the system, thereby increasing the complexity in solving the OCP.

$$\frac{S_{\text{LB}} - f(x)}{g(x)} \leq u \leq \frac{S_{\text{UB}} - f(x)}{g(x)} \tag{4.2a}$$

$$u_{\text{LB}}(x) \leq u \leq u_{\text{UB}}(x) \tag{4.2b}$$

Trigonometrization poses the control, u, in a trigonometric form, u_{TRIG}, as shown in Eq. (4.3a). The values of variables c_1 and c_0, used in Eq. (4.3a), are shown in Eq. (4.3b) and Eq. (4.3c), respectively.

$$u = c_1 \sin u_{\text{TRIG}} + c_0 \tag{4.3a}$$

$$c_1 = \frac{u_{\text{UB}}(x) - u_{\text{LB}}(x)}{2} \tag{4.3b}$$

$$c_0 = \frac{u_{\text{UB}}(x) + u_{\text{LB}}(x)}{2} \tag{4.3c}$$

Using Eq. (1.7), the optimal control options are obtained as shown in Eq. (4.4), which is similar to Eq. (3.4). It may happen that $h(t, x, \lambda)$ becomes less than -1 unit or more than 1 unit, leading to imaginary values for $\arcsin(h(t, x, \lambda))$. In such cases, PMP chooses the control, u, from among two options for u_{TRIG}, $\pm\pi/2$.

$${u_{\text{TRIG}}}^* = \begin{cases} \dfrac{-\pi}{2} \\ \arcsin(h(t, x, \lambda)) \\ \dfrac{\pi}{2} \end{cases} \tag{4.4}$$

4.2.1 Applicability Range

The Trigonometrization technique developed in this chapter is valid for the following.

1. The controls have lower and/or upper bounds depending upon the states of the OCP.
2. Many mixed constraints are present in the OCP.
3. Pure control constraints are present for certain controls along with mixed constraints upon rest of the controls in the OCP.

4.2.2 Assumptions

Following are the assumptions used in this method.

1. PMP suffices for the sufficiency condition of optimality.
2. Pure and mixed constraints are not present simultaneously for a control.
3. Pure state constraints are absent.

Please note that $g(u, x)$ in Eq. (4.1) can have higher powers of the control, u. However, the procedure to obtain trigonometric bounds on u becomes very complicated for mixed constraint expressions where u appears in a non-linear form. Sec. 4.4 showcases a complex aerospace problem involving such complicated mixed constraints with a non-linear control. For simplicity, the following section discusses only one mixed constraint with one control.

4.3 Verification and Validation

Traditionally, the design community applies the methodology described in Sec. 1.2.2.3 to solve OCPs with mixed constraints, where the order of path constraint,

q, is 0. This chapter uses the Rayleigh mixed constraint problem, as specified in Eq. (4.5), to illustrate this traditional approach. [72, 166] Table 4.1 describes the constants used in this problem.

$$\text{Minimize: } J = \int_{t_0}^{t_f} (u^2 + x_1^2)\mathrm{d}t \tag{4.5a}$$

$$\text{Subject to: } \dot{x_1} = x_2 \tag{4.5b}$$

$$\dot{x_2} = -x_1 + x_2(1.4 - 0.14{x_2}^2) + 4u \tag{4.5c}$$

$$-1 \leq u + \frac{x_1}{6} \leq 0 \tag{4.5d}$$

Table 4.1.: Constants for the Rayleigh mixed constraint problem.

Parameter	x_{1_0}	x_{2_0}	t_0	t_f
Value	-5	-5	0	4.5

Eq. (4.6) expresses the Hamiltonian for this problem. The EOM for the costate λ_{x_1} is shown in Eq. (4.7). The EOM for the costate λ_{x_2} is the same as shown in Eq. (3.7b) in Sec. 3.3. The expressions for μ_1 and μ_2 used in the Hamiltonian are shown in Eq. (4.8a) and Eq. (4.8b), respectively.

$$H = \lambda_{x_1}\dot{x_1} + \lambda_{x_2}\dot{x_2} + \mu_1\left(-1 - u - \frac{x_1}{6}\right) + \mu_2\left(u + \frac{x_1}{6}\right) + u^2 + x_1^2 \tag{4.6}$$

$$\dot{\lambda_{x_1}} = -2x_1 + \lambda_{x_2} + \frac{\mu_1 - \mu_2}{6} \tag{4.7}$$

$$\mu_1 = \begin{cases} 0 \quad \text{if} \quad \mathrm{u} + \mathrm{x_1}/6 > -1 \\ 4\lambda_{x_2} + 2u \quad \text{if} \quad \mathrm{u} = -1 - \mathrm{x_1}/6 \end{cases} \tag{4.8a}$$

$$\mu_2 = \begin{cases} 0 \quad \text{if} \quad \mathrm{u} + \mathrm{x_1}/6 < 0 \\ -4\lambda_{x_2} - 2u \quad \text{if} \quad \mathrm{u} = -\mathrm{x_1}/6 \end{cases} \tag{4.8b}$$

Ref. [72] helps in obtaining the control structure of the traditional solution as shown in Eq. (4.9). The optimal control, u^*, first stays at the upper variable bound until time t_1, followed by an unconstrained arc until time t_2, a lower variable bound constrained arc until time t_3, followed by an unconstrained arc until time t_4, an upper variable bound constrained arc until time t_5, and finally, an unconstrained arc for the remaining time.

$$u^* = \begin{cases} \dfrac{-x_1(t)}{6} & \text{if} \quad 0 \leq \mathrm{t} \leq \mathrm{t}_1 \\ -2\lambda_{x_2}(t) & \text{if} \quad \mathrm{t}_1 \leq \mathrm{t} \leq \mathrm{t}_2 \\ -1 - \dfrac{x_1(t)}{6} & \text{if} \quad \mathrm{t}_2 \leq \mathrm{t} \leq \mathrm{t}_3 \\ -2\lambda_{x_2}(t) & \text{if} \quad \mathrm{t}_3 \leq \mathrm{t} \leq \mathrm{t}_4 \\ \dfrac{-x_1(t)}{6} & \text{if} \quad \mathrm{t}_4 \leq \mathrm{t} \leq \mathrm{t}_5 \\ -2\lambda_{x_2}(t) & \text{if} \quad \mathrm{t}_5 \leq \mathrm{t} \leq \mathrm{t}_\mathrm{f} \end{cases} \tag{4.9}$$

The traditional approach results in a seven-point BVP and becomes significantly more difficult to formulate and solve as compared to a TPBVP. The Rayleigh mixed constraint problem becomes a TPBVP using Trigonometrization such that u stays bounded between -1 - $x_1/6$ and -$x_1/6$ as described in Eq. (4.10a). Thus, Eq. (4.5) uses a trigonometric form of u as shown in Eq. (4.10b).

$$-1 - \frac{x_1}{6} \leq u \leq -\frac{x_1}{6} \tag{4.10a}$$

$$u = \frac{\sin u_{\mathrm{TRIG}}}{2} - \frac{1}{2} - \frac{x_1}{6} \tag{4.10b}$$

Using the Euler-Lagrange necessary conditions, the optimal control law obtained for this reformulated Rayleigh mixed constraint problem is shown in Eq. (4.11).

$$u_{\mathrm{TRIG}}{}^* = \begin{cases} -\pi/2 \\ \arcsin\left(1 - 4\lambda_{\mathrm{x}_2} + \dfrac{\mathrm{x}_1}{3}\right) \\ \pi/2 \end{cases} \tag{4.11}$$

PMP forms the basis for the control selection, and constraints are implicitly placed on the control. The selection process discards imaginary values of arcsin. Trigonometrization retains a TPBVP form and obtains the same solution as the traditional method without segmenting the problem explicitly into multiple constrained and unconstrained arcs. To justify this point, this study compares the traditional approach with the Trigonometrization approach, and the results match as expected. The states, control, and constraint time-history comparison plots are shown in Fig. 4.2. The constraint time-history sub-plot shows the seven points of the MPBVP as red circular dots, which divide the optimal trajectory into six arcs. Fig. 4.3 shows the costate time-history plots, in which the costates are not well estimated by GPOPS-II.

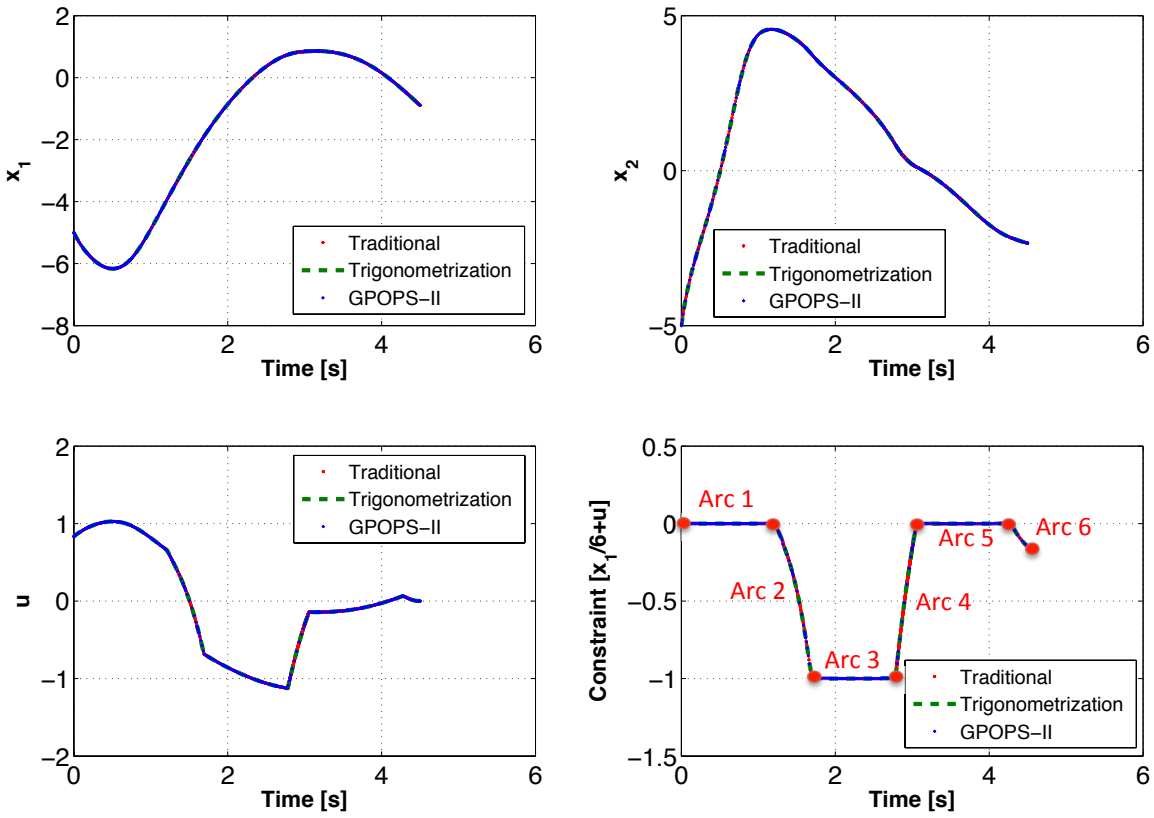

Figure 4.2.: States, control, and constraint time-history comparison plots for the Rayleigh mixed problem.

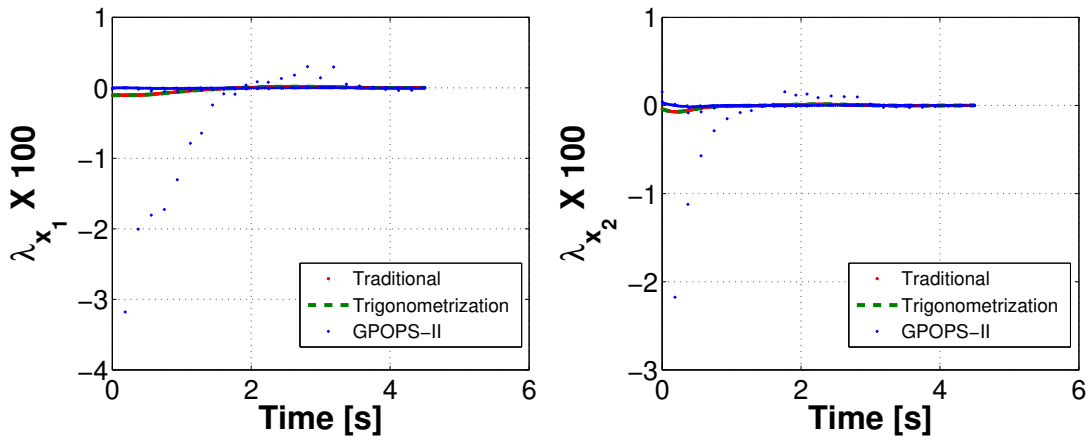

Figure 4.3.: Costates time-history comparison for the Rayleigh mixed problem.

The value of $\frac{\partial \phi}{\partial t_f}$ is 0 units for this OCP and hence the terminal value of the Hamiltonian, $H(t_f)$, is also 0 units based on Eq. (1.12). Since the Hamiltonian is not an explicit function of time, its value is constant. The Hamiltonian time-history plots for the traditional and Trigonometrization methods for this OCP, shown in Fig. 4.4, are in excellent agreement with the result obtained using the transversality condition. However, the results for the Hamiltonian obtained using GPOPS-II are not accurate as shown in Fig. 4.4.

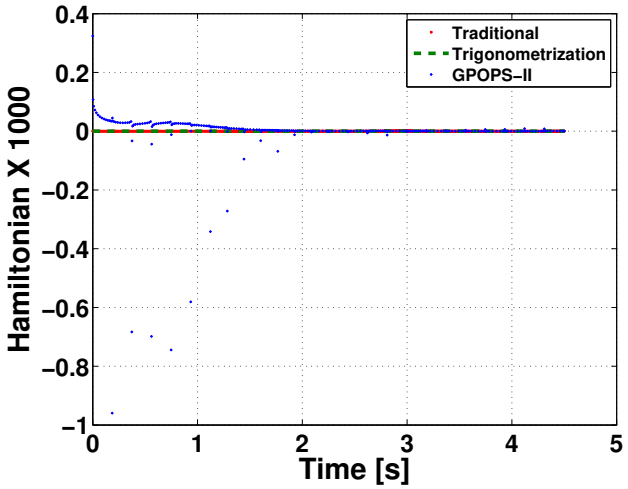

Figure 4.4.: The Hamiltonian comparison for the Rayleigh mixed problem.

A comparison between the various features of the traditional and Trigonometrization approaches is presented in Table 4.2, which demonstrates that Trigonometrization is an effective means to solve OCPs with mixed constraints. Trigonometrization reduced the computation time by about 66% and significantly reduced the problem formulation time. Please note that all computations performed in this study utilized a 2.5-GHz Intel i5 processor using a built-in BVP solver, bvp4c, in MATLAB 2014b. The results have also been compared to and are in excellent agreement with the results from GPOPS-II.

Table 4.2.: Results comparison for the Rayleigh mixed constraint problem.

Attribute	**Traditional Method**	**Trigonometrization**
Type	Seven-Point BVP	TPBVP
Number of Trajectory Arcs	6	1
Number of Boundary Conditions	48	13
Computation Time (s)	9.5	3.5

4.4 A Complex Aerospace Problem: Space Shuttle Reentry with a Re-radiative Heating Constraint

This section includes solution to a complicated OCP in which a space shuttle type vehicle reenters the Earth's atmosphere with a re-radiative heating constraint. [28, 167–171] For many years, the research community considered this OCP as one of the most demanding real-life applications during the development of the multiple shooting code. [169, 170] The objective is to increase the crossrange capacity for a space shuttle orbiter-type vehicle to allow for more frequent return opportunities from the orbit. This analysis ignores the EOM corresponding to the latitude and formulates this OCP as shown in Eq. (4.12) because the latitude is not coupled with

other states in the EOMs and can be calculated independently. Additionally, there are no boundary conditions on latitude.

$$\text{Minimize: } J = -\phi_f \tag{4.12a}$$

$$\text{Subject to: } \dot{h} = v \sin\gamma \tag{4.12b}$$

$$\dot{\phi} = \frac{v \cos\gamma \sin\psi}{r} \tag{4.12c}$$

$$\dot{v} = -\frac{D}{m} - \frac{\mu \sin\gamma}{r^2} \tag{4.12d}$$

$$\dot{\gamma} = \frac{L \cos\sigma}{mv} + \left(\frac{v}{r} - \frac{\mu}{vr^2}\right) \cos\gamma \tag{4.12e}$$

$$\dot{\psi} = \frac{L \sin\sigma}{mv \cos\gamma} - \frac{v \cos\gamma \cos\psi \tan\phi}{r} \tag{4.12f}$$

$$\rho = \rho_0 e^{\frac{-h}{H}} \tag{4.12g}$$

$$C_D = C_L^{1.86} + C_{D_0} \tag{4.12h}$$

$$D = \frac{1}{2}\rho v^2 C_D A \tag{4.12i}$$

$$L = \frac{1}{2}\rho v^2 C_L A \tag{4.12j}$$

$$r = r_E + h \tag{4.12k}$$

In the above equation, r is the radial magnitude, h is the altitude, ϕ is the crossrange angle, v is the velocity magnitude, γ is the flight path angle, ψ is the heading angle, A is the reference area of the vehicle, μ is the gravitational parameter of Earth, r_E is the radius of Earth, ρ_0 is the surface atmospheric density of Earth, D is the drag force magnitude, L is the lift force magnitude, and σ is the bank angle. C_L is the coefficient of lift and C_{D_0} is a constant related to the coefficient of drag, C_D. Table 4.3 includes the constants used in this problem. [169, 170]

Table 4.3.: Constants for the space shuttle reentry problem.

Parameter	r_E (km)	μ (km^3/s^2)	$\rho_0 A/2m$ (1/m)	H (km)	C_{D_0}
Value	6371.2	398600	3.33e-3	6.897	0.04

Using Trigonometrization, the bank angle, σ, is implicitly bounded between -90° and 90° as shown in Eq. (4.13).

$$\sigma = \frac{\pi \sin \sigma_{\text{TRIG}}}{2} \tag{4.13}$$

The lift coefficient of the space shuttle depends on the re-radiative heating constraint as shown in Eq. (4.14). $C_{\text{LH}}(h, v)$ comprises of 20 terms based on Eqs. (4.14b)–(4.14i). [169, 170, 172, 173] The skin temperature of the space shuttle forms the basis for $\Delta \text{C}_{\text{LH}}$, which helps with tightening the heating constraint. The lower the value of $\Delta \text{C}_{\text{LH}}$, the tighter the heating constraint is. The non-linear nature of C_{LH} coupled with the large number of terms in it immensely complicates the problem formulation and solution process. The OCP becomes very ill-conditioned and very sensitive to the initial guess. Please note that the value of b in Eq. (4.14) is 0.095 and its unit is 1/s. Ref. 174 and Appendix C contain a detailed description about Eq. (4.14).

$$C_{\text{L}} - C_{\text{LH}}(h, v) - \Delta C_{\text{LH}} \leq 0 \tag{4.14a}$$

$$C_{LH}(h, v) = \sum_{i=1}^{5} B_{\text{i}} H_{\text{i}} \tag{4.14b}$$

$$B_{\text{i}} = \sum_{j=1}^{4} g_{\text{ij}} \left(\frac{h}{50000} - 1 \right)^{j-1} \tag{4.14c}$$

$$H_1 = \left(\frac{bh}{v} \right)^2 \tag{4.14d}$$

$$H_2 = \frac{bh}{v} - H_1 \tag{4.14e}$$

$$H_3 = 1 - \frac{bh}{v} - H_2 \tag{4.14f}$$

$$H_4 = \frac{v}{bh} - 2 + \frac{bh}{v} - H_3 \tag{4.14g}$$

$$H_5 = \left(\frac{v}{bh} \right)^2 - \frac{3v}{bh} + 3 - \frac{bh}{v} - H_4 \tag{4.14h}$$

$$g_{\mathrm{ij}} = \begin{bmatrix} 0.110717 & 0.834519 & 1.213679 & -1.060833 \\ -0.672677 & 2.734170 & -0.864369 & -12.1 \\ 0.812241 & 2.337815 & 10.31628 & 22.97486 \\ -3.151267 & -13.62131 & -40.4855 & -57.83333 \\ 2.368095 & 19.0734 & 69.86905 & 127.777778 \end{bmatrix} \tag{4.14i}$$

This analysis utilizes a weighted approach along with Trigonometrization and scaling in order to remedy the sensitivity issue. A weighting factor, w, converts the OCP from an unconstrained form to the one with a heating constraint. [175] Trigonometrization transcribes the lift coefficient, C_{L}, into Eq. (4.15). C_{L} has a fixed lower bound, C_{LLB}, and initially a fixed upper bound, C_{LUB} when w is 0. The upper bound for C_{L} changes to a variable value based on C_{LH} when the value of w changes to 1. In short, C_{L} has a weighted upper bound, C_{LWUB}, as shown in Eq. (4.16). The solution to the unconstrained OCP serves as an initial guess for the OCP with the heat constraint. The continuation approach has small changes first in the values of w and then in the values of $\Delta \mathrm{C}_{\mathrm{LH}}$. [49, 175]

$$C_{\mathrm{L}} = \frac{(C_{\mathrm{LWUB}} - C_{\mathrm{LLB}}) \sin C_{\mathrm{LTRIG}} + C_{\mathrm{LWUB}} + C_{\mathrm{LLB}}}{2} \tag{4.15}$$

$$C_{\mathrm{LWUB}} = (1 - w) C_{\mathrm{LUB}} + w(C_{\mathrm{LH}} + \Delta C_{\mathrm{LH}}) \tag{4.16}$$

The Hamiltonian is shown in Eq. (4.17). Appendix C includes the extremely lengthy and complicated costates.

$$\begin{aligned} H = {} & \lambda_h v \sin\gamma + \lambda_\phi \frac{v \cos\gamma \sin\psi}{r} + \lambda_v \left(-\frac{D}{m} - \frac{\mu \sin\gamma}{r^2} \right) \\ & + \lambda_\gamma \left[\frac{L \cos\sigma}{mv} + \left(\frac{v}{r} - \frac{\mu}{vr^2} \right) \cos\gamma \right] + \lambda_\psi \left[\frac{L \sin\sigma}{mv \cos\gamma} - \frac{v \cos\gamma \cos\psi \tan\phi}{r} \right] \end{aligned} \tag{4.17}$$

Eq. (1.7) obtains the optimal control laws for C_{LTRIG} and σ_{TRIG} as shown in Eq. (4.18a) and Eq. (4.18b), respectively. Trigonometrization obtains 12 possible

optimal combinations between the lift coefficient and bank angle. PMP then selects the most optimal combination from them.

$$C_{\text{LTRIG}}{}^{*} = \begin{cases} \dfrac{-\pi}{2} \\ \arcsin\left[\dfrac{2}{C_{\text{LWUB}} - C_{\text{LLB}}}\left(\dfrac{\lambda_\gamma \cos\sigma + \dfrac{\lambda_\psi \sin\sigma}{\cos\gamma}}{1.86 v \lambda_v}\right)^{\frac{1}{0.86}} - \dfrac{C_{\text{LWUB}} + C_{\text{LLB}}}{C_{\text{LWUB}} - C_{\text{LLB}}}\right] \\ \dfrac{\pi}{2} \end{cases} \tag{4.18a}$$

$$\sigma_{\text{TRIG}}{}^{*} = \begin{cases} \dfrac{-\pi}{2} \\ \arcsin\left[\dfrac{4}{\pi}\arctan\left(\dfrac{\lambda_\psi}{\lambda_\gamma \cos\gamma}\right)\right] \\ \arcsin\left[\dfrac{4}{\pi}\left(\arctan\left(\dfrac{\lambda_\psi}{\lambda_\gamma \cos\gamma}\right) + \pi\right)\right] \\ \dfrac{\pi}{2} \end{cases} \tag{4.18b}$$

Trigonometrization upon the lift coefficient and bank angle controls results in solving for a TPBVP. The boundary conditions for this problem are shown in Table 4.4.

Table 4.4.: Initial and final conditions for the space shuttle reentry problem.

Attribute	**Initial Value**	**Final Value**
Time (s)	0	free
Altitude (km)	95	30
Crossrange Angle (deg)	0	free
Velocity (km/s)	7.85	1.116
Flight Path Angle (deg)	-1.25	-2.7
Heading (deg)	0	free

The time-history plots of the states of the space shuttle for three different values of ΔC_{LH} are shown in Fig. 4.5. When the value of ΔC_{LH} is 0.12 units, the OCP remains as an unconstrained problem and the constraint is inactive for the entire duration of flight.

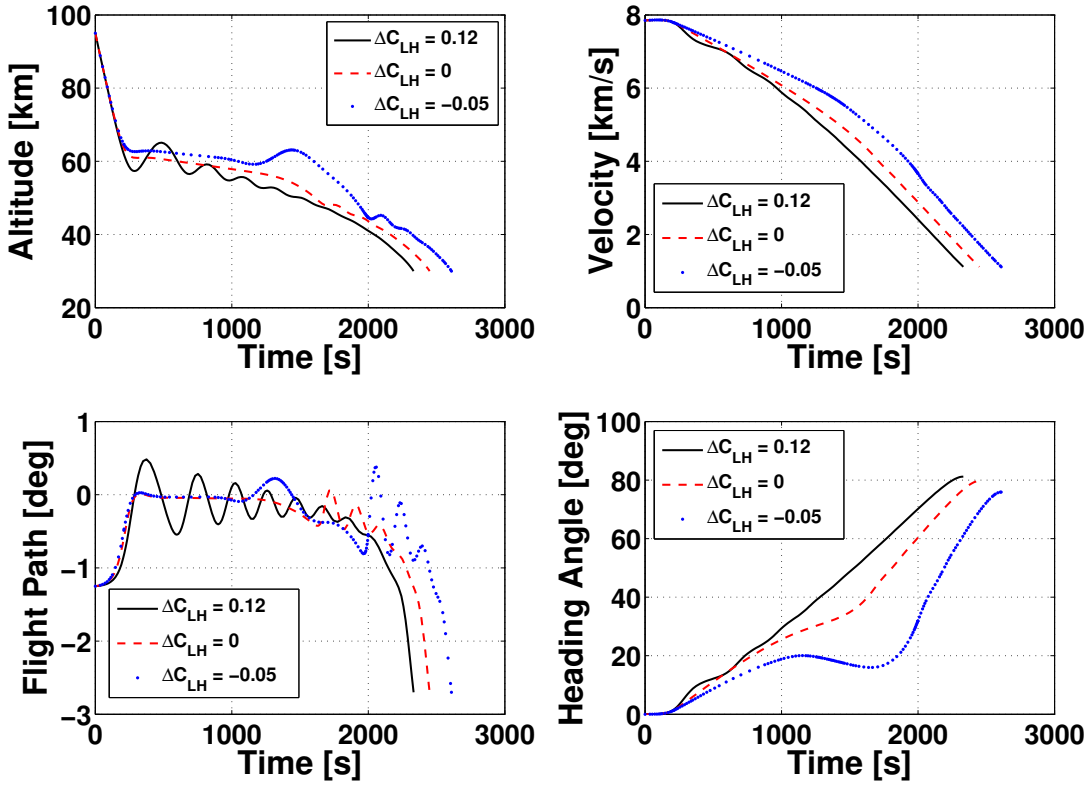

Figure 4.5.: States time-history plots for the space shuttle reentry problem.

The result from the unconstrained problem then serves as a good initial guess for the mixed constraint version of the problem. As the value of ΔC_{LH} decreases to 0 units, the flight becomes safer as the heating constraint tightens and the space shuttle avoids denser regimes of the atmosphere at higher velocities. Additionally, the trajectory becomes more stable and less oscillatory in nature. The flight path angle time-history plot is a testimonial to this phenomenon. This section uses a plot for ΔC_{LH} with a value of -0.05 units for comparison with existing literature on this

problem. The results obtained in this section are in excellent agreement with the results obtained in previous studies from the literature.

The crossrange capability of the space shuttle and the time-history for three different heating constraints are shown in Fig. 4.6. It can be clearly seen that the constraint becomes active for a significant amount of time for ΔC_{LH} as 0 units and -0.05 units.

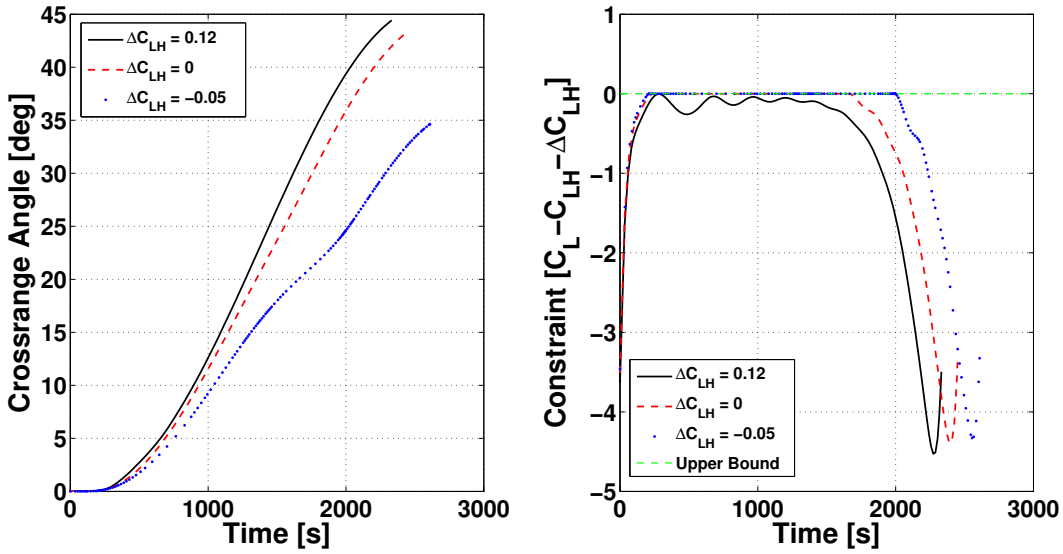

Figure 4.6.: Crossrange capability and constraint time-history plots for the space shuttle reentry problem.

The comparison results of the three different heating scenarios for the space shuttle are shown in Table 4.5. As the heating constraint tightens, the maximum crossrange capability of the space shuttle decreases and the time of flight increases.

Table 4.5.: Results for different heat constraint scenarios for space shuttle's reentry.

Attribute	**ΔC_{LH}=0.12**	**ΔC_{LH}=0**	**ΔC_{LH}=-0.05**
Time of Flight (s)	2332	2449	2609
Crossrange Angle (deg)	44.42	43.36	34.63
Heading Angle (deg)	81.19	79.68	75.91

The optimal control time-history plots for the lift coefficient and the bank angle are shown in Fig. 4.7. The bank angle primarily aims at maximizing the crossrange while the lift coefficient enables flying higher in the atmosphere at lower speeds. Thus, the lift coefficient enables the space shuttle to follow a tighter heating constraint and a safer trajectory. Fig. 4.8 depicts the costate time-history plots for this problem.

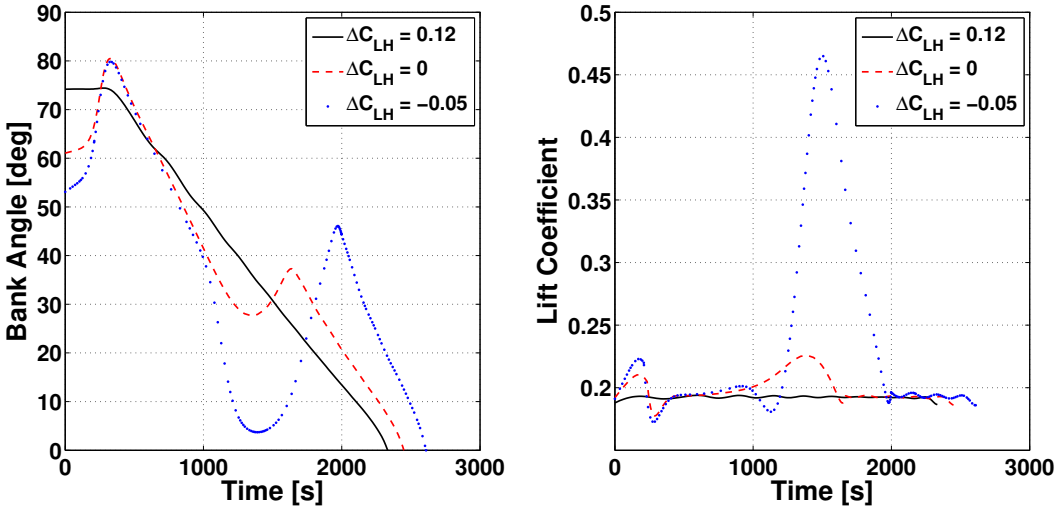

Figure 4.7.: Control time-history plots for the space shuttle reentry problem.

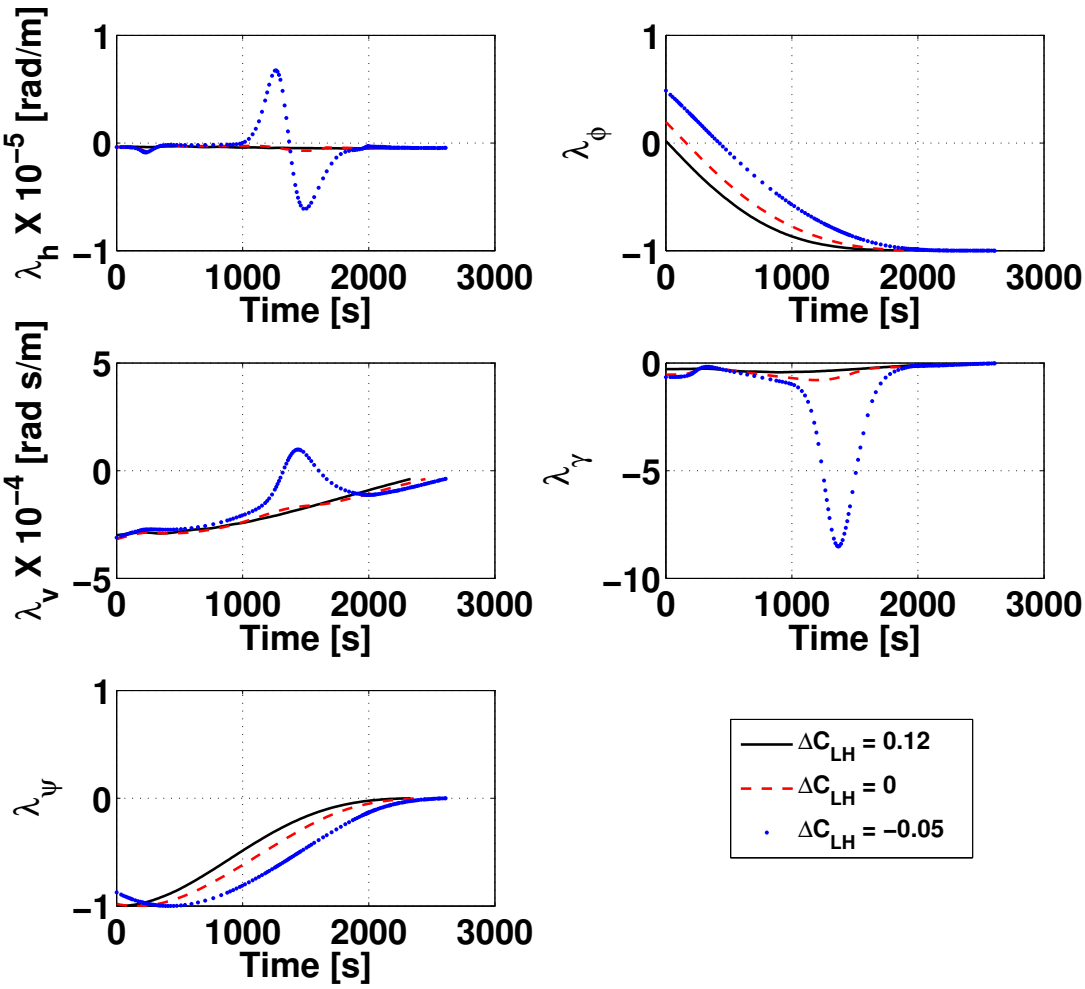

Figure 4.8.: Costates plots for the space shuttle reentry problem.

The value of $\frac{\partial \phi}{\partial t_f}$ is 0 rad/s for this problem. Hence the terminal value of the Hamiltonian, $H(t_f)$, is also 0 rad/s based on Eq. (1.12). The Hamiltonian is not an explicit function of time and therefore has a constant value. The Hamiltonian time-history plot for this OCP, shown in Fig. 4.9, is in excellent agreement with the result obtained using the transversality condition and has an accuracy of 10^{-3}.

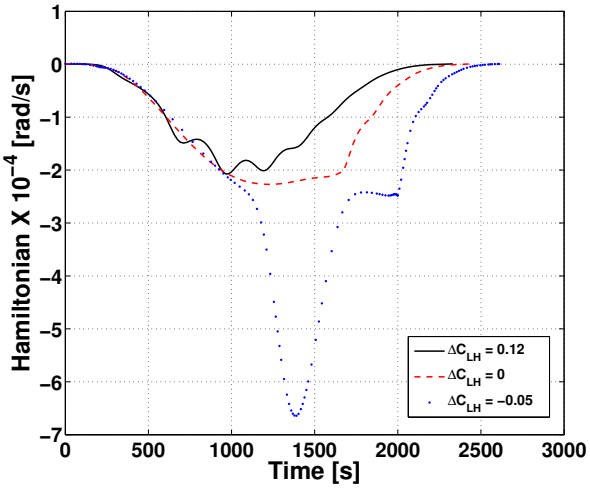

Figure 4.9.: The Hamiltonian plot for the space shuttle reentry problem.

This section proves that Trigonometrization can solve very complicated OCPs with multiple states and controls while maintaining the problem as a TPBVP. The complicated control law for the Trigonometrization approach can be quite easily generated using state-of-the-art symbolic computation software, Mathematica.

Table 4.6 summarizes the complexity of the space shuttle reentry mixed constraint problem. The main complexities in this problem are the extremely lengthy EOMs for the costates, some of which are five pages long as shown in appendix C. The control law for the coefficient of lift, C_{L}, is also very complicated. All previous studies on this problem avoided writing the EOMs for the costates for this reason.

Table 4.6.: Complexities of the space shuttle reentry mixed constraint problem.

Parameter	**Complexity**
States	Five states
Controls	Complicated bounded functions of states and costates
State equations	Highly non-linear and coupled
Costate equations	Highly non-linear, extremely lengthy, and coupled
Mixed heating constraint	21-term long, highly non-linear, and coupled

4.5 Trigonometrization of Optimal Control Problems with Mixed State-Control Constraints containing Non-Linear Controls

A complicated subset of OCPs with mixed constraints exist, where the control appears in a high order polynomial form in the state-control constraint inequality. Developing a control law for such OCPs is quite challenging. Eq. (4.19) describes one such OCP with a g-load constraint on an impactor, where the problem is planar. As a result, this problem has only one control, angle of attack, α. Table 4.7 includes the aerodynamic coefficients required for the impactor. [49]

$$\text{Minimize: } J = -v_f^2 \tag{4.19a}$$

$$\text{Subject to: } \dot{h} = v\sin\gamma \tag{4.19b}$$

$$\dot{\theta} = \frac{v\cos\gamma}{r} \tag{4.19c}$$

$$\dot{v} = -\frac{D}{m} - \frac{\mu\sin\gamma}{r^2} \tag{4.19d}$$

$$\dot{\gamma} = \frac{L}{mv} + \left(\frac{v}{r} - \frac{\mu}{vr^2}\right)\cos\gamma \tag{4.19e}$$

$$\rho = \rho_0 e^{\frac{-h}{H}} \tag{4.19f}$$

$$C_L = C_{L_1}\alpha \tag{4.19g}$$

$$C_D = C_{D_2}\alpha^2 + C_{D_0} \tag{4.19h}$$

$$D = \frac{1}{2}\rho v^2 C_D A \tag{4.19i}$$

$$L = \frac{1}{2}\rho v^2 C_L A \tag{4.19j}$$

$$r = r_E + h \tag{4.19k}$$

Table 4.7.: Aerodynamic constants for the impactor problem with a g-load constraint.

Parameter	C_{L_1}	C_{D_0}	C_{D_2}
Value	1.5658	0.0612	1.6537

G-load is the ratio of the aerodynamic (or contact) forces upon the impactor to its inertial force. [5, 176–178] This is shown in the inequality Eq. (4.20), where its lower and upper limits are 0 and g_{MAX}, respectively. The value of g is 9.80665 as g-loads are always measured in Earth gs. [5]

$$0 \leq g_{\text{LOAD}} := \frac{\sqrt{L^2 + D^2}}{mg} \leq g_{\text{MAX}} \tag{4.20}$$

Since g-loads are always positive for the impactor in the atmospheric regime considered, inequality Eq. (4.20) reduces to inequality Eq. (4.21).

$$\frac{\sqrt{L^2 + D^2}}{mg} \leq g_{\text{MAX}} \tag{4.21}$$

Rearrangement of Eq. (4.21) leads to Eq. (4.22a), which then uses Eq. (4.19i) and Eq. (4.19j) to obtain Eq. (4.22b). Inequality Eq. (4.22b) can be further expanded to inequality Eq. (4.22c) using Eq. (4.19g) and Eq. (4.19h).

$$L^2 + D^2 \leq (mgg_{\text{MAX}})^2 \tag{4.22a}$$

$$C_{\text{L}}{}^2 + C_{\text{D}}{}^2 \leq \left(\frac{2mgg_{\text{MAX}}}{\rho v^2 A}\right)^2 \tag{4.22b}$$

$$(C_{\text{L}_1}\alpha)^2 + C_{\text{D}_2}{}^2\alpha^4 + 2C_{\text{D}_2}C_{\text{D}_0}\alpha^2 + C_{\text{D}_0}{}^2 \leq \left(\frac{2mgg_{\text{MAX}}}{\rho v^2 A}\right)^2 \tag{4.22c}$$

The bi-quadratic inequality in α converts into a quadratic inequality in α_{NEW} as shown in Eq. (4.23a). Eq. (4.23b)–(4.23d) show the coefficients of this quadratic inequality.

$$a\alpha_{\text{NEW}}{}^2 + b\alpha_{\text{NEW}} + c \leq 0 \tag{4.23a}$$

$$a = C_{\text{D}_2}{}^2 \tag{4.23b}$$

$$b = C_{\text{L}_1}{}^2 + 2C_{\text{D}_2}C_{\text{D}_0} \tag{4.23c}$$

$$c = C_{\text{D}_0}{}^2 - \left(\frac{2mgg_{\text{MAX}}}{\rho v^2 A}\right)^2 \tag{4.23d}$$

The inequality constraints upon the new control, α_{NEW}, are shown in Eq. (4.24). The left hand side of this inequality is always negative and thus discarded from further discussion. Eq. (4.25) shows the final set of constraints on angle of attack, α.

$$\frac{-b - \sqrt{b^2 - 4ac}}{2a} \leq \alpha_{\text{NEW}} \leq \frac{-b + \sqrt{b^2 - 4ac}}{2a} \tag{4.24}$$

$$-\sqrt{\frac{-b+\sqrt{b^2-4ac}}{2a}} \leq \alpha \leq \sqrt{\frac{-b+\sqrt{b^2-4ac}}{2a}} \tag{4.25}$$

Trigonometrization can then place variable bounds on α, where the bounds are dependent on the altitude, velocity, and other parameters of the impactor. Eq. (4.26) describes the control, α. Please note that these equations will hold only for $C_{\mathrm{D}_0} \leq \frac{2mgg_{\mathrm{MAX}}}{\rho v^2 A}$.

$$\alpha = \sqrt{\frac{-b+\sqrt{b^2-4ac}}{2a}} \sin\alpha_{\mathrm{TRIG}} \tag{4.26}$$

The Hamiltonian for this problem is shown in Eq. (4.27). Eq. (1.7) obtains the optimal control law as shown in Eq. (4.28). The following subsections discuss about two types of g-load constraint impactor problem.

$$\begin{aligned} H = {} & \lambda_h v \sin\gamma + \frac{\lambda_\theta v \cos\gamma}{r} + \lambda_v \left(\frac{-D}{m} - \frac{\mu \sin\gamma}{r^2}\right) \\ & - \lambda_\gamma \left[\frac{L}{mv} + \cos\gamma \left(\frac{v}{r} - \frac{\mu}{vr^2}\right)\right] \end{aligned} \tag{4.27}$$

$$\alpha_{\mathrm{TRIG}}{}^* = \begin{cases} \dfrac{-\pi}{2} \\ \arcsin\left[\sqrt{\dfrac{2a}{-b+\sqrt{b^2-4ac}}}\left(\dfrac{\lambda_\gamma C_{\mathrm{L}_1}}{C_{\mathrm{D}_2} v \lambda_v}\right)\right] \\ \dfrac{\pi}{2} \end{cases} \tag{4.28}$$

4.5.1 Case 1: The G-Load Constraint Active Between the Boundary Points of the Trajectory

In this scenario, the maximum g-load value on the impactor is chosen as 25 Earth gs. The boundary value conditions for this problem are shown in Table 4.8. The state plots for this case obtained using the Trigonometrization technique and GPOPS-II are shown in Fig. 4.10, where a zoom-in view of the active constraint part of the trajectory is also shown. Thus, the trajectory comprises of three parts: unconstrained, constrained, and unconstrained, respectively.

Table 4.8.: Initial and final conditions for case 1 of the impactor g-load problem.

Attribute	Initial Value	Final Value
Time (s)	0	free
Altitude (km)	50	0
Downrange (km)	0	300
Velocity (km/s)	4	free
Flight Path Angle (deg)	free	free

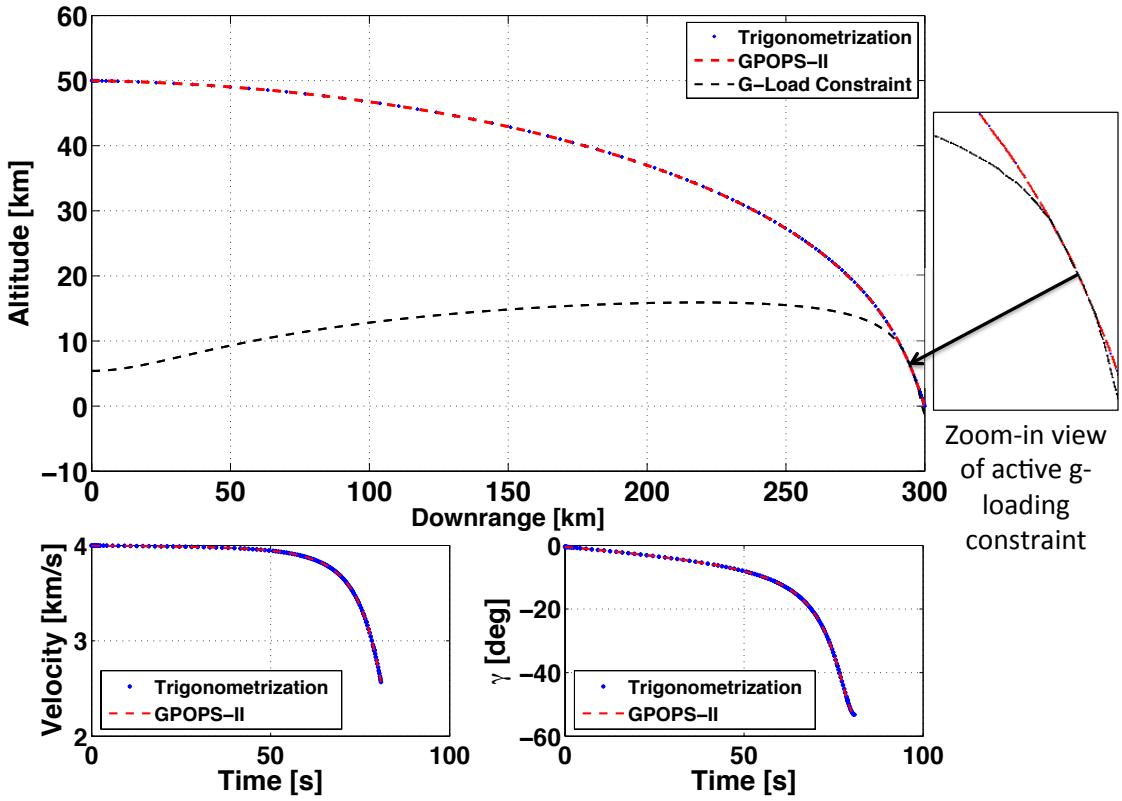

Figure 4.10.: States time-history plots for case 1 of the g-load constraint problem.

The control plots obtained for this case using the Trigonometrization technique and GPOPS-II are shown in Fig. 4.11. A zoom-in view of the control touching its lower bounds based on the g-load constraint is also included in Fig. 4.11. Please note that the upper and lower bounds on the control based on the g-load constraint are shown in magneta and black colors, respectively. The costate plots for this case are shown in Fig. 4.12. The results obtained using the Trigonometrization technique are in excellent agreement with GPOPS-II results.

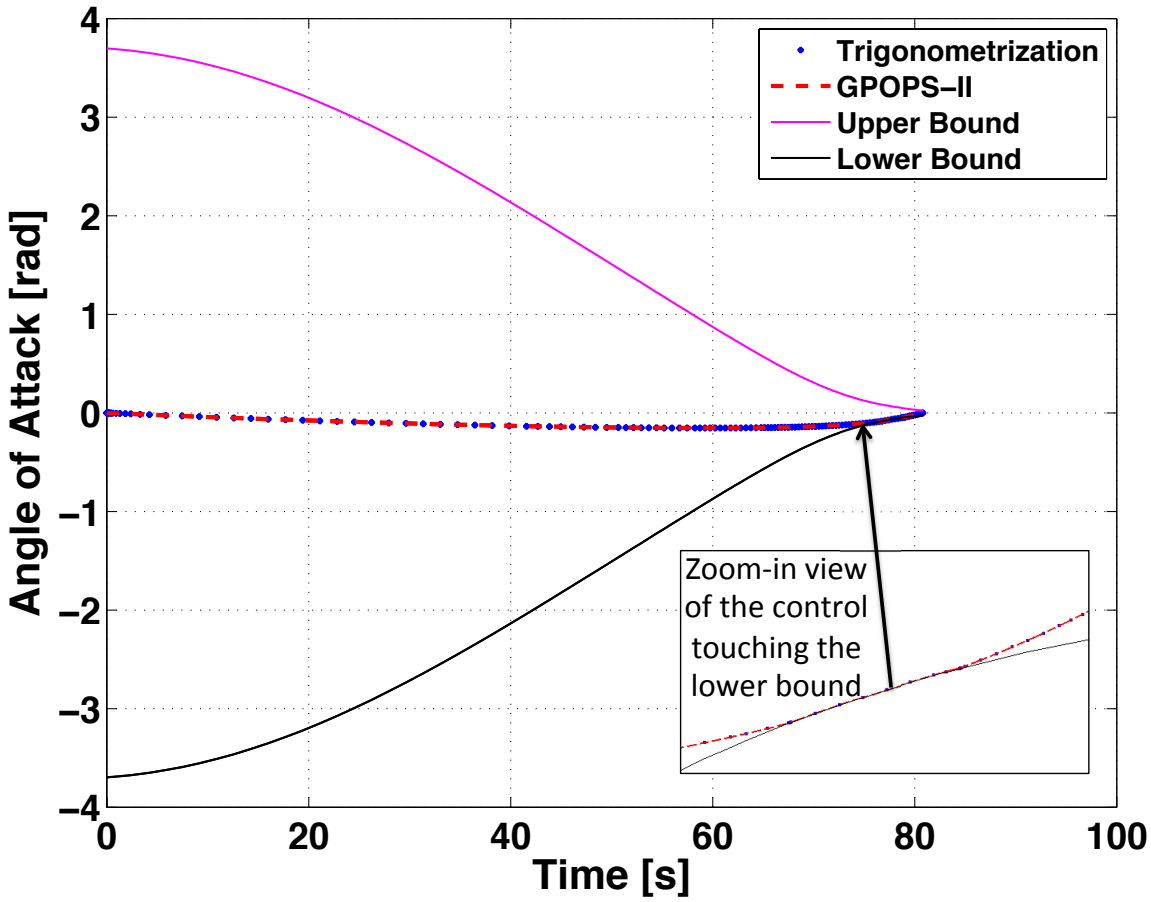

Figure 4.11.: The control time-history for case 1 of the g-load constraint problem.

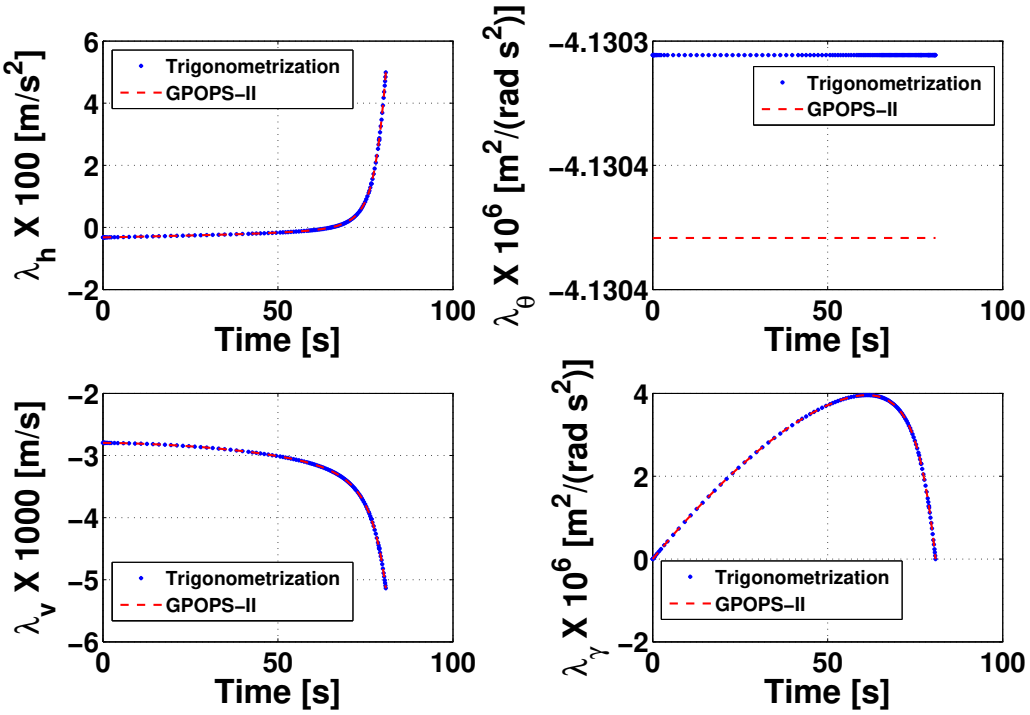

Figure 4.12.: Costates time-history plots for case 1 of the g-load constraint problem.

The g-load constraint history for this case is shown in Fig. 4.13. This figure depicts that the constraint is active for a short duration in between the boundary points of the trajectory. For this OCP, the value of $\frac{\partial \phi}{\partial t_f}$ and the terminal value of the Hamiltonian, $H(t_f)$, are found to be 0 m^2/s^3 based on Eq. (1.12). The Hamiltonian has a constant value for the entire trajectory as it is not an explicit function of time. The Hamiltonian time-history plot for the Trigonometrization method, shown in Fig. 4.13, is in excellent agreement with the result obtained using the transversality condition. However, the results for the Hamiltonian obtained using GPOPS-II are not accurate as shown in Fig. 4.13.

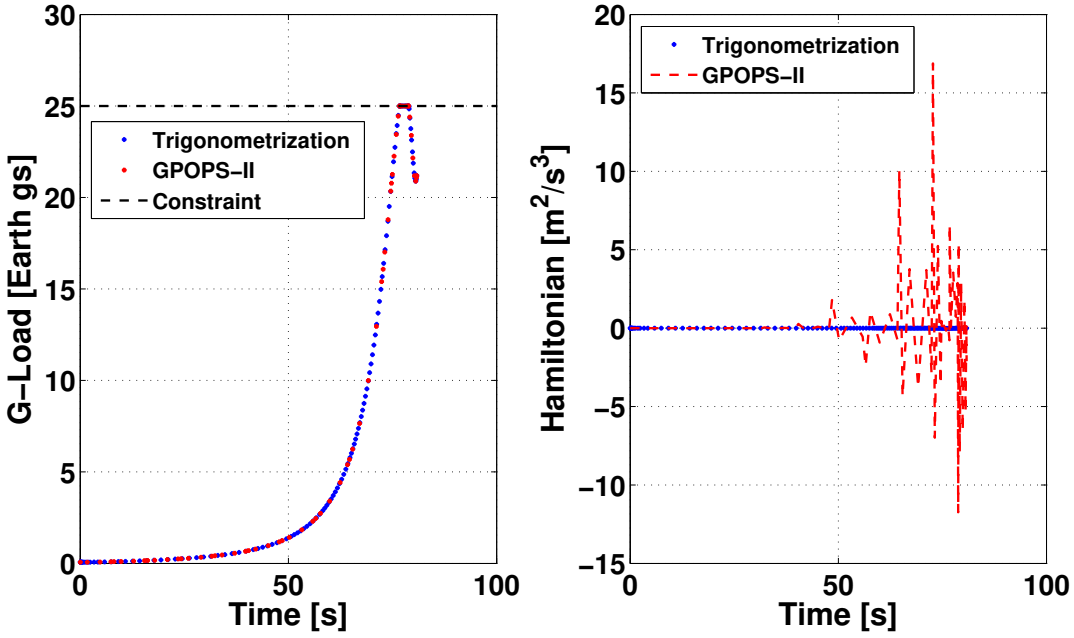

Figure 4.13.: G-load and Hamiltonian time-history plots for case 1 of the g-load constraint problem.

4.5.2 Case 2: G-Load Constraint Active at the Terminal Point of the Trajectory

In this scenario, the maximum g-load value on the impactor is chosen as 21 Earth gs. The boundary value conditions for this case of the impactor g-load problem are kept the same as shown in Table 4.8. However, the objective of the impactor problem for this case is changed to minimize the time of flight. ICRM (discussed in Sec. 1.2.2.10) is unable to handle this case because ICRM utilizes saturation functions and error parameters, which approach closely but never actually touch such terminal constraints. Since the terminal point is on the constraint arc, ICRM cannot solve this OCP. ICRM needs to change this OCP using an error parameter and error controls such that the terminal point is not on the constraint arc.

The state plots for this case obtained using the Trigonometrization technique and GPOPS-II are shown in Fig. 4.14. These plots show that the trajectory comprises of an unconstrained part followed by a constrained part. Thus, the terminal point of this BVP lies on the constrained part.

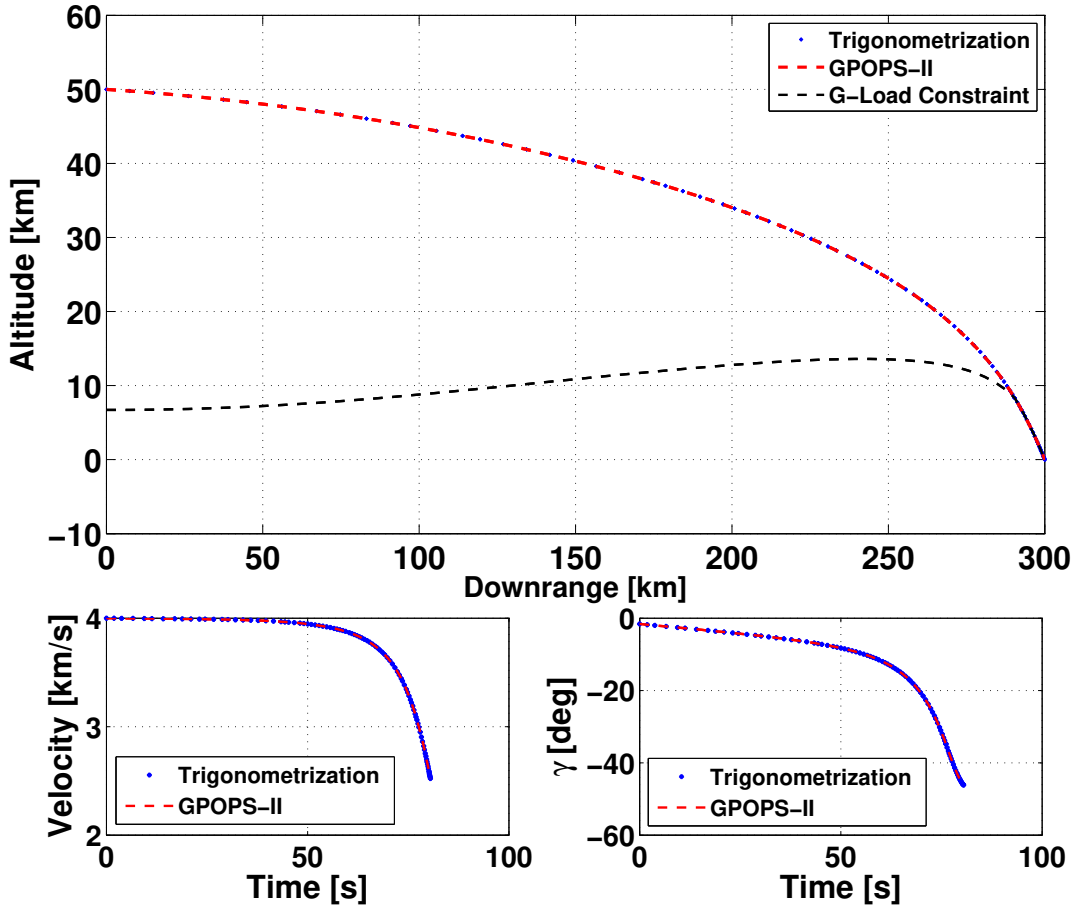

Figure 4.14.: States time-history plots for case 2 of the g-load constraint problem.

The control plot for this case obtained using the Trigonometrization technique is shown in Fig. 4.15 and the results match well with GPOPS-II. The control touches its g-load constraint based lower bound for the terminal part of the trajectory. Please note that the g-load constraint based upper and lower bounds on the control are shown in magneta and black colors, respectively.

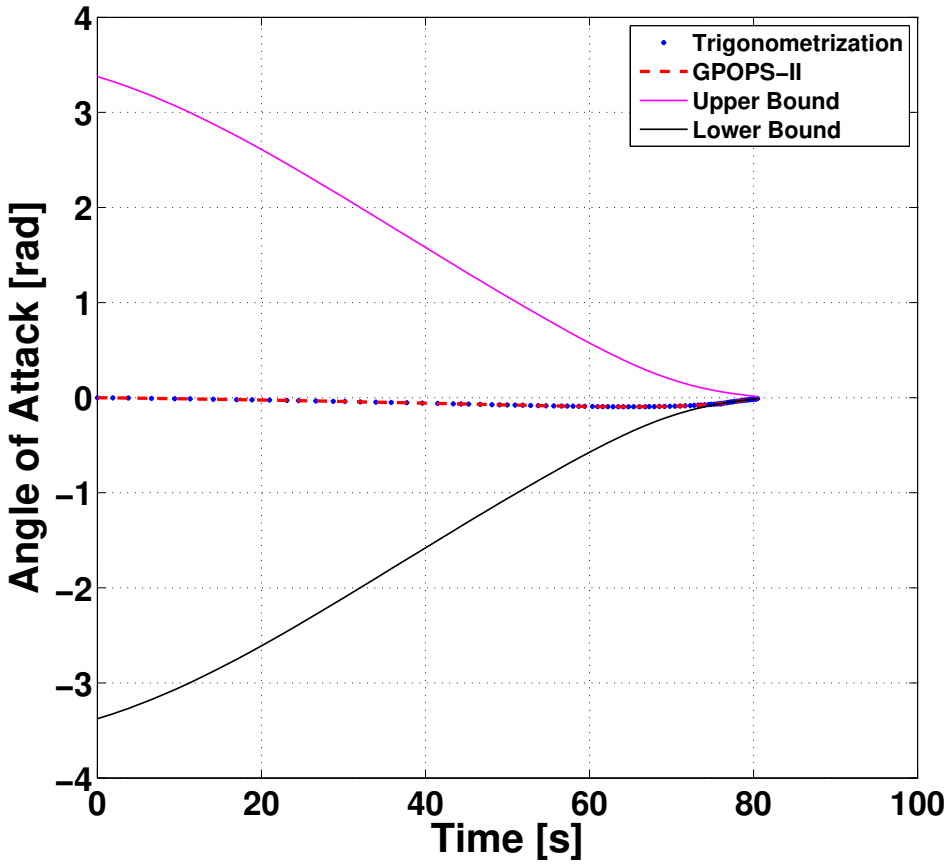

Figure 4.15.: The control time-history for case 2 of the g-load constraint problem.

The costate plots obtained for this case using the Trigonometrization technique are shown in Fig. 4.16. These results are in excellent agreement with GPOPS-II. The g-load constraint history for this case is shown in Fig. 4.17, where the g-load stays at the maximum value during the terminal part of the trajectory. For this OCP, the terminal value of the Hamiltonian, $H(t_f)$, is found to be -1 unit based on Eq. (1.12) for the minimum time impactor OCP. The Hamiltonian has a constant value for the entire trajectory as it is not an explicit function of time. The Hamiltonian time-history plots for the Trigonometrization and GPOPS-II methods, shown in Fig. 4.17, are in excellent agreement with the result obtained using the transversality condition with an accuracy of 10^{-7}.

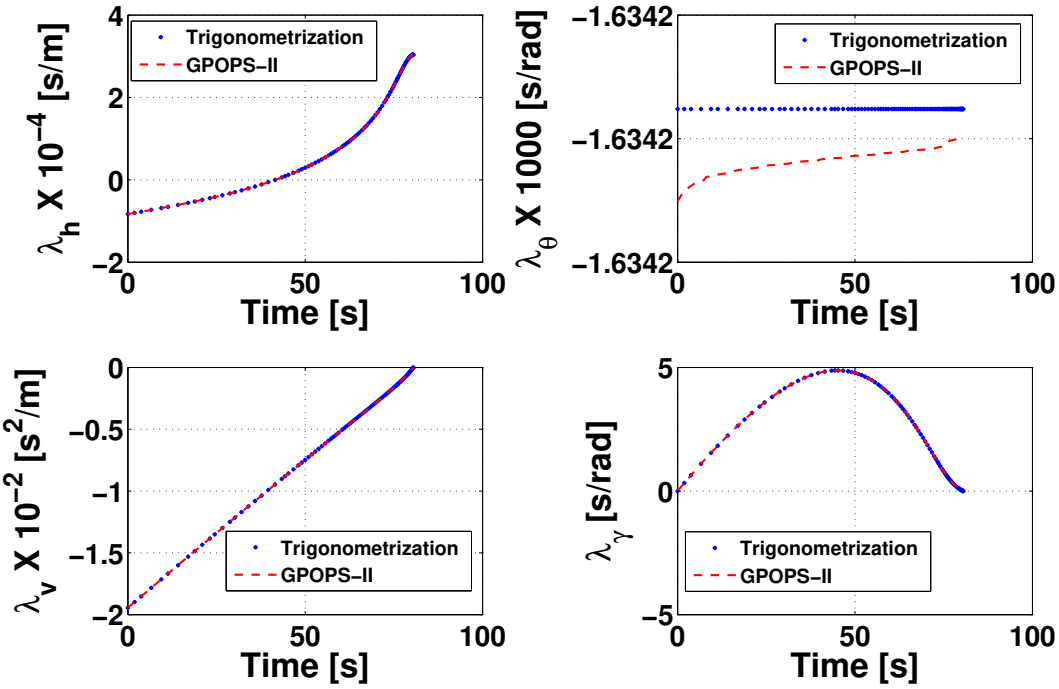

Figure 4.16.: Costates time-history plots for case 2 of the g-load constraint problem.

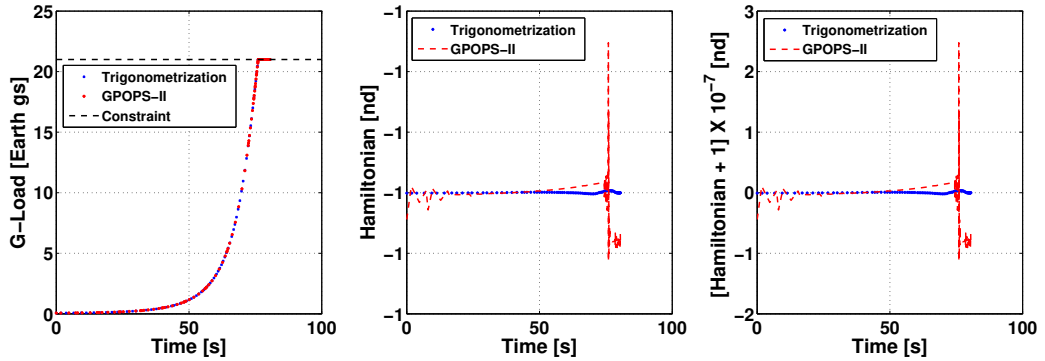

Figure 4.17.: G-load and Hamiltonian time-history plots for case 2 of the g-load constraint problem.

4.6 Extending Trigonometrization to Optimal Control Problems with Pure State Constraints

Periodic trigonometric functions can possibly bound OCPs in which constraints are purely imposed upon states. The traditional approach obtains the control law by taking time derivatives of such pure state constraints until the control appears explicitly. Trigonometrization can address two issues regarding such OCPs.

1. Some OCPs with state constraints may converge to a wrong solution using the classical indirect methods.

2. The traditional approach requires solving for a MPBVP, which is very complicated. [179]

OCPs described in issue 1 converge to the correct solution by using the additional necessary conditions devised by Jacobson et al. These additional conditions further complicate the problem formulation and problem solving processes. This prompted the author to investigate the use of Trigonometrization for solving such OCPs. The future work thus includes completion of the unified Trigonometrization approach for all classes of OCPs as shown in Fig. 4.18. The following subsections discuss the advantages of using Trigonometrization for solving OCPs with pure state constraints.

4.6.1 Benefit 1: Avoiding Convergence to a Wrong Solution

For certain OCPs with state constraints, Jacobson et al. demonstrated that certain additional necessary conditions were missing in the approach devised by Bryson et al. that led to erroneous results [50, 51, 73]. Jacobson et al. posed a fourth order problem to demonstrate this issue. The following discussion includes the traditional approach, its erroneous result and the benefit of using Trigononomerization for solving such OCPs.

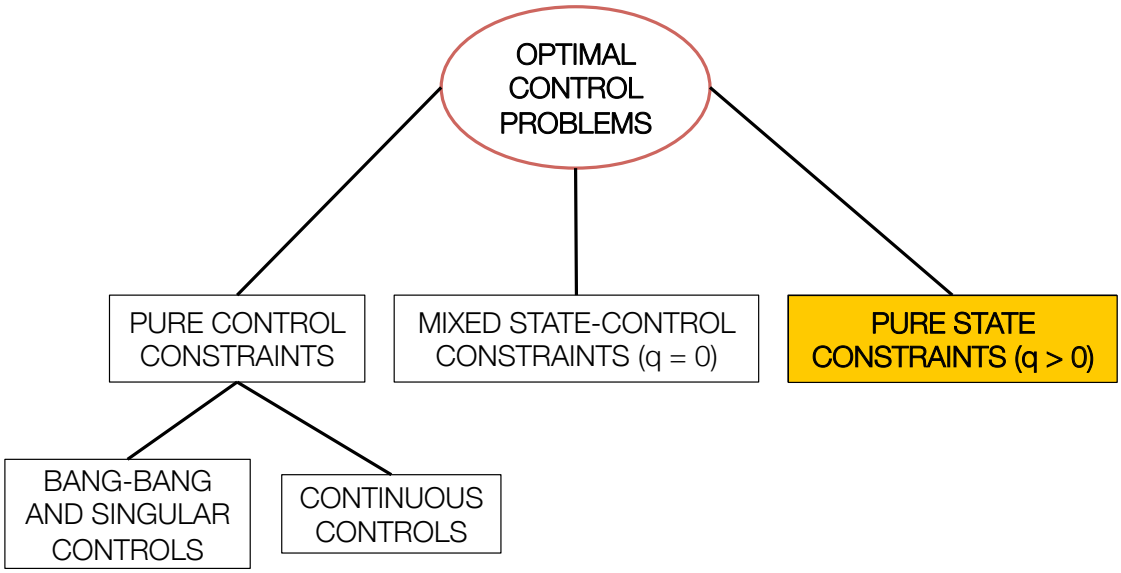

Figure 4.18.: The class of OCPs yet to successfully employ Trigonometrization.

4.6.1.1 Traditional Approach for a Fourth Order Problem

Jacobson et al. posed a fourth order path constraint problem as shown in Eq. (4.29). The objective functional for this problem is shown in Eq. (4.29a). Eqs. (4.29b)–(4.29e) describe EOMs for the states and Eqs. (4.29f)–(4.29i) show the boundary conditions on these states. Eq. (4.29j) shows the constraint on the state x_1.

$$\text{Minimize: } J = \int_0^{10} \frac{u^2}{2} \mathrm{d}t \tag{4.29a}$$

$$\text{Subject to: } \dot{x_1} = x_2 \tag{4.29b}$$

$$\dot{x_2} = x_3 \tag{4.29c}$$

$$\dot{x_3} = x_4 \tag{4.29d}$$

$$\dot{x_4} = u \tag{4.29e}$$

$$x_1(0) = 0 = x_1(10) \tag{4.29f}$$

$$x_2(0) = \frac{15}{12} = -x_2(10) \tag{4.29g}$$

$$x_3(0) = -\frac{15}{12} = x_3(10) \tag{4.29h}$$

$$x_4(0) = \frac{15}{16} = -x_4(10) \tag{4.29i}$$

$$S = x_1(t) - x_{1_{\text{MAX}}} \leq 0 \quad \text{for t} \in [0, 10] \tag{4.29j}$$

The Hamiltonian for this problem is shown in Eq. (4.30). Eq. (1.19) then uses this Hamiltonian to determine the EOMs for the costates as shown in Eq. (4.31).

$$H = \frac{u^2}{2} + \lambda_{x_1} x_2 + \lambda_{x_2} x_3 + \lambda_{x_3} x_4 + \lambda_{x_4} u + \mu u \tag{4.30}$$

$$\dot{\lambda_{x_1}} = 0 \tag{4.31a}$$

$$\dot{\lambda_{x_2}} = -\lambda_{x_1} \tag{4.31b}$$

$$\dot{\lambda_{x_3}} = -\lambda_{x_2} \tag{4.31c}$$

$$\dot{\lambda_{x_4}} = -\lambda_{x_3} \tag{4.31d}$$

Eq. (1.7) uses the Hamiltonian to calculate the optimal control for the unconstrained arcs of the solution as shown in Eq. (4.32a). The Lagrange parameter corresponding to the constraint on state x_1, μ, is shown in Eq. (4.32b).

$$u^* = -\lambda_{x_4} \tag{4.32a}$$

$$\mu = 0 \tag{4.32b}$$

When the path constraint is active, the EOMs for the states vanish as shown in Eqs. (4.33a)–(4.33d). The control and the Lagrange parameter, μ, are shown in Eq. (4.33e) and Eq. (4.33f), respectively.

$$\dot{x_1} = 0 \tag{4.33a}$$

$$\dot{x_2} = 0 \tag{4.33b}$$

$$\dot{x_3} = 0 \tag{4.33c}$$

$$\dot{x_4} = 0 \tag{4.33d}$$

$$u = 0 \tag{4.33e}$$

$$\mu = -\lambda_{x_4} - u \tag{4.33f}$$

On the other hand, when the state constraint is active, the EOMs for the costates happen to be independent of the Lagrange parameter, μ, and hence remain unmodified using Eq. (1.19). Eq. (4.34) shows the tangency constraint matrix, N. Eq. (4.35) determines the jumps in the costates at the entry to the constraint.

$$\boldsymbol{N}(\boldsymbol{x},t) = \begin{bmatrix} x_1 - x_{1_{\text{MAX}}} \\ x_2 \\ x_3 \\ x_4 \end{bmatrix} \tag{4.34}$$

$$\pi_1 = \lambda_{x_1}({t_{\text{ENTRY}}}^+) - \lambda_{x_1}({t_{\text{ENTRY}}}^-) \tag{4.35a}$$

$$\pi_2 = \lambda_{x_2}({t_{\text{ENTRY}}}^+) - \lambda_{x_2}({t_{\text{ENTRY}}}^-) \tag{4.35b}$$

$$\pi_3 = \lambda_{x_3}({t_{\text{ENTRY}}}^+) - \lambda_{x_3}({t_{\text{ENTRY}}}^-) \tag{4.35c}$$

$$\pi_4 = \lambda_{x_4}({t_{\text{ENTRY}}}^+) - \lambda_{x_4}({t_{\text{ENTRY}}}^-) \tag{4.35d}$$

The complete solution to this problem can be found in Ref. 51. A non-extremal solution that satisfies all the necessary conditions specified by Bryson et al. was obtained, which violated some of the necessary conditions specified by Jacobson et al. corresponding to the jump at the junction of unconstrained and constraint arcs. The unconstrained optimal trajectory for state x_1, which stays well within the bounds, gives a cost of 0.2897 units. On the other hand, the path constraint imposed on the trajectory using the necessary conditions specified by Bryson et al. yields a cost of 0.293 units. Thus, the cost for an active path constraint solution is higher and hence non-extremal as compared to the unconstrained case. The Trigonometrization approach is able to impose the additional necessary conditions implicitly as shown below.

4.6.1.2 Trigonometrization Approach for the Fourth Order Problem

To avoid spurious results generated by the traditional approach, the simpler and efficient technique of Trigonometrization converts the state, x_1, into a trigonometric form as shown in Eq. (4.36a). The modified EOM and boundary conditions for this state are represented by Eq. (4.36b) and Eq. (4.36c), respectively.

$$x_1 = x_{1_{\text{MAX}}} \sin x_{1_{\text{TRIG}}} \tag{4.36a}$$

$$\dot{x}_{1_{\text{TRIG}}} = \frac{x_2}{x_{1_{\text{MAX}}} \cos x_{1_{\text{TRIG}}}} \tag{4.36b}$$

$$x_{1_{\text{TRIG}}}(0) = 0 = x_{1_{\text{TRIG}}}(10) \tag{4.36c}$$

The Hamiltonian for the trigonometrized problem is shown in Eq. (4.37). Eq. (1.19) uses this Hamiltonian to obtain the EOMs for costates as shown in Eq. (4.38).

$$H = \frac{u^2}{2} + \frac{\lambda_{x_{1_{\text{TRIG}}}} x_2}{x_{1_{\text{MAX}}} \cos x_{1_{\text{TRIG}}}} + \lambda_{x_{2_{\text{TRIG}}}} x_3 + \lambda_{x_{3_{\text{TRIG}}}} x_4 + \lambda_{x_{4_{\text{TRIG}}}} u \tag{4.37}$$

$$\dot{\lambda}_{x_{1_{\text{TRIG}}}} = \frac{-\lambda_{x_{1_{\text{TRIG}}}} \sin x_{1_{\text{TRIG}}} x_2}{x_{1_{\text{MAX}}} \cos x_{1_{\text{TRIG}}}^2} \tag{4.38a}$$

$$\dot{\lambda}_{x_{2_{\text{TRIG}}}} = \frac{-\lambda_{x_{1_{\text{TRIG}}}}}{x_{1_{\text{MAX}}} \cos x_{1_{\text{TRIG}}}} \tag{4.38b}$$

$$\dot{\lambda}_{x_{3_{\text{TRIG}}}} = -\lambda_{x_{2_{\text{TRIG}}}} \tag{4.38c}$$

$$\dot{\lambda}_{x_{4_{\text{TRIG}}}} = -\lambda_{x_{3_{\text{TRIG}}}} \tag{4.38d}$$

The results between unconstrained, traditional path constraint and Trigonometrization approaches were compared as shown in Figs. 4.19, 4.20 and 4.21. The unconstrained solution remains within the limits of the constraint. Additionally, the results from Trigonometrization are in excellent agreement with the more optimal unconstrained solution. Thus, the Trigonometrization technique can simply and effectively avoid the spurious results obtained using the traditional approach.

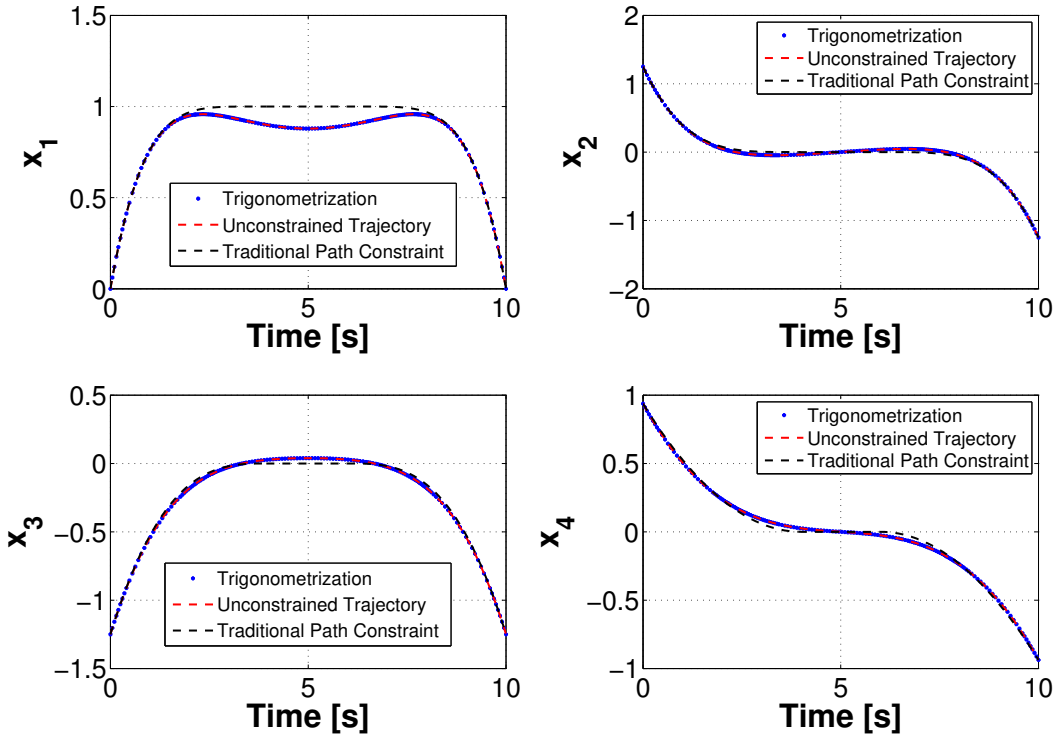

Figure 4.19.: States time-history comparison plots for the fourth order problem.

For this OCP, the value of $\frac{\partial \phi}{\partial t_f}$ and the terminal value of the Hamiltonian, $H(t_f)$, are found to be 0 units based on Eq. (1.12). The Hamiltonian has a constant value for the entire trajectory as it is not an explicit function of time. The Hamiltonian time-history plot for the three different methods, shown in Fig. 4.20, is in excellent agreement with the result obtained using the transversality condition and has an accuracy of 10^{-2}. Fig. 4.21 shows the jumps in the costates while using the traditional approach, which are absent in the costate plots of the unconstrained and Trigonomerization methods.

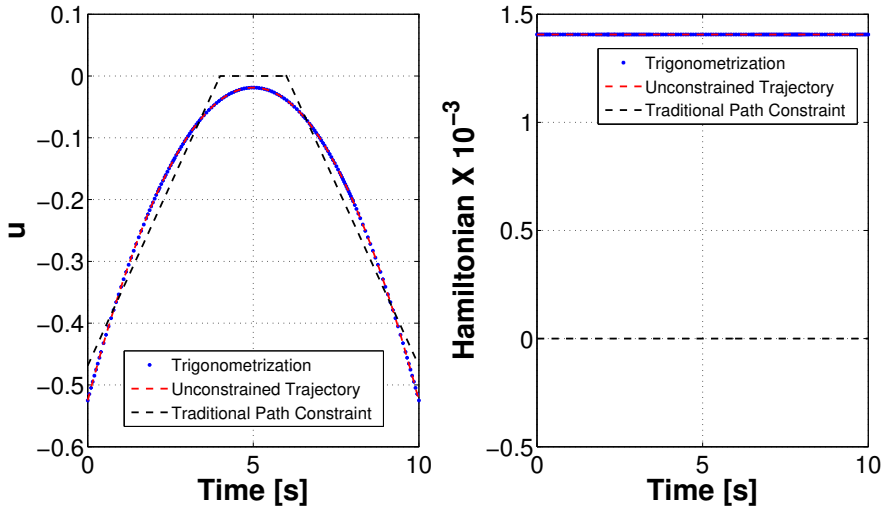

Figure 4.20.: Control and Hamiltonian time-history comparison plots for the fourth order problem.

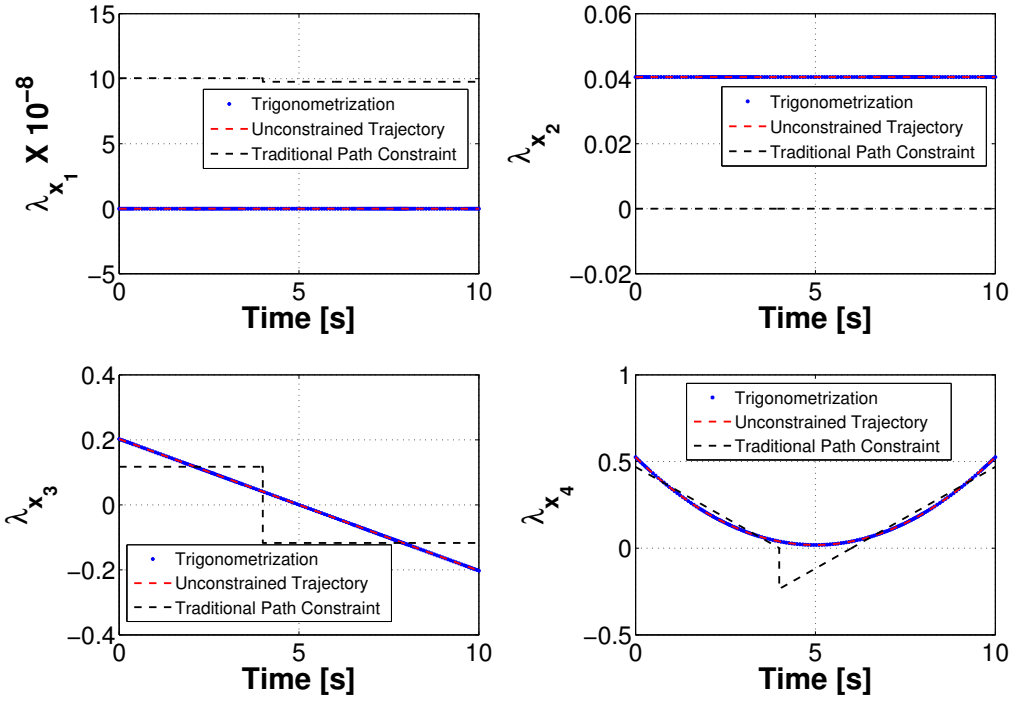

Figure 4.21.: Costates time-history comparison plots for the fourth order problem.

4.6.2 Benefit 2: Avoid Solving a Multi-Point Boundary Value Problem

To demonstrate this benefit, this subsection uses a second order path constraint problem, popularly known as the Bryson Denham problem. [50] This subsection consists of two sub-subsections: first describing the traditional approach and second describing the Trigonometrization approach to solve this problem.

4.6.2.1 Traditional Approach for Bryson Denham Problem

The Bryson Denham problem was set up as shown in Eq. (4.39). Eq. (4.39a) shows the objective functional and Eq. (4.39b) and Eq. (4.39c) describe the state EOMs for this problem. Eq. (4.39d)and Eq. (4.39e) specify the boundary conditions for the states. Eq. (4.39f) shows the constraint on the state x_1.

$$\text{Minimize: } J = \int_0^1 \frac{u^2}{2} \mathrm{d}t \tag{4.39a}$$

$$\text{Subject to: } \dot{x_1} = x_2 \tag{4.39b}$$

$$\dot{x_2} = u \tag{4.39c}$$

$$x_1(0) = 0 = x_1(1) \tag{4.39d}$$

$$x_2(0) = 1 = -x_2(1) \tag{4.39e}$$

$$S = x_1(t) - x_{1_{\text{MAX}}} \leq 0 \quad \text{for} t \in [0, 1] \tag{4.39f}$$

The Hamiltonian for this problem is shown in Eq. (4.40). Using this Hamiltonian, Eq. (1.19) evaluates the EOMs for the costates equations as shown in Eq. (4.41).

$$H = \frac{u^2}{2} + \lambda_{x_1} x_2 + \lambda_{x_2} u + \mu u \tag{4.40}$$

$$\dot{\lambda}_{x_1} = 0 \tag{4.41a}$$

$$\dot{\lambda}_{x_2} = -\lambda_{x_1} \tag{4.41b}$$

Eq. (1.7) uses the Hamiltonian to obtain the optimal control for the unconstrained arcs of the solution as shown in Eq. (4.42a). The Lagrange parameter corresponding to the constraint on state x_1, μ, is shown in Eq. (4.42b).

$$u^* = -\lambda_{x_2} \tag{4.42a}$$

$$\mu = 0 \tag{4.42b}$$

When the path constraint is active the EOMs for the states vanish as shown in Eq. (4.43a) and Eq. (4.43b). The control and the Lagrange parameter, μ, are shown in Eq. (4.43c) and Eq. (4.43d), respectively.

$$\dot{x_1} = 0 \tag{4.43a}$$

$$\dot{x_2} = 0 \tag{4.43b}$$

$$u = 0 \tag{4.43c}$$

$$\mu = -\lambda_{x_2} - u \tag{4.43d}$$

The EOMs for the costates happen to be independent of the Lagrange parameter, μ, when the state constraint is active. Therefore, the EOMs for the costates remain unmodified. Eq. (4.44) determines the tangency constraint matrix, N. Eq. (4.45) then calculates the jumps in the costates at the entry to the constraint.

$$\boldsymbol{N}(\boldsymbol{x}, t) = \begin{bmatrix} x_1 - x_{1_{\text{MAX}}} \\ x_2 \end{bmatrix} \tag{4.44}$$

$$\pi_1 = \lambda_{x_1}({t_{\text{ENTRY}}}^+) - \lambda_{x_1}({t_{\text{ENTRY}}}^-) \tag{4.45a}$$

$$\pi_2 = \lambda_{x_2}({t_{\text{ENTRY}}}^+) - \lambda_{x_2}({t_{\text{ENTRY}}}^-) \tag{4.45b}$$

Using the additional necessary conditions specified in the enhanced method in Sec. 1.2.2.4, the jumps in the costates were found to match with Eq. (4.45). These jump conditions are shown in terms of the Lagrange parameter, μ, in Eq. (4.46).

$$\pi_1 + \dot{\mu}({t_{\text{ENTRY}}}^+) \geq 0 \tag{4.46a}$$

$$\pi_2 = \mu({t_{\text{ENTRY}}}^+) = -\lambda_{x_2}({t_{\text{ENTRY}}}^+) \tag{4.46b}$$

Fig. 4.22 draws a comparison between these two cases. The states and costates time-history plots match exactly for both the traditional method and the enhanced method devised by Jacobson et al.

For this OCP, the value of $\frac{\partial \phi}{\partial t_f}$ and the terminal value of the Hamiltonian, $H(t_f)$, are found to be 0 units based on Eq. (1.12). The Hamiltonian has a constant value for the entire trajectory as it is not an explicit function of time. The Hamiltonian time-history plot for the enhanced and traditional methods, shown in Fig. 4.22, is in excellent agreement with the result obtained using the transversality condition and has an accuracy of 10^{-4}.

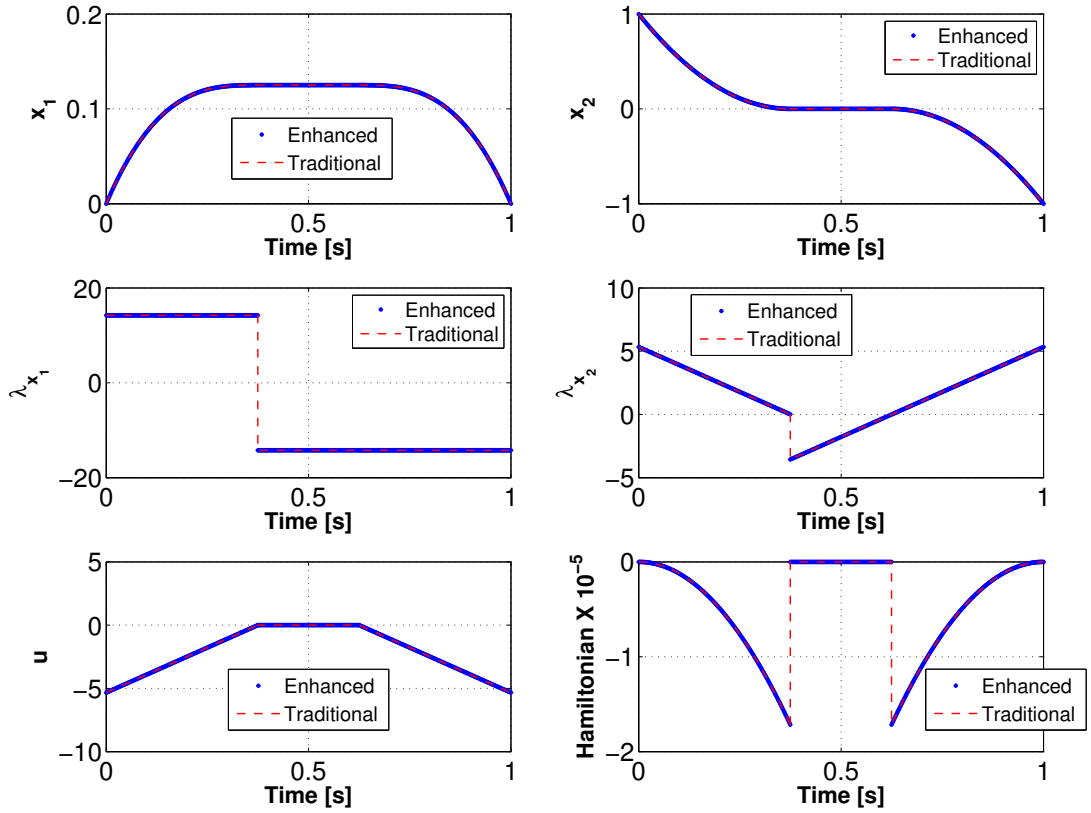

Figure 4.22.: Results comparison between the traditional and enhanced methods for the Bryson Denham problem.

Once the Trigonometrization technique is developed to address OCPs with active pure state constraints, the complicated and tedious traditional approach to solve such OCPs can be avoided. The current effort is to solve certain benchmark OCPs such as the Bryson Denham problem and problems specified in Ref. 179. The ideas to develop the Trigonometrization technique for such OCPs are described in the next chapter as a part of future work.

4.7 Conclusions

This chapter proposed and tested the use of trigonometry in reformulating control expressions in an OCP with mixed state and control constraints. Trigonometrizing the control kept the OCP as a TPBVP, which leads to simpler problem formulation and faster computation of results. This chapter used the Rayleigh problem with a mixed constraint for verification and validation. An aerospace application of the Trigonometrization technique for OCPs with mixed constraints was made through a complicated space shuttle reentry problem. This problem included a very complicated heating constraint comprising of both states and controls for a realistic and safe trajectory. Trigonometrization was able to quickly and simply solve this problem. A weighting factor and a scaling process generated a good initial guess and well-conditioned form for this problem. The results obtained using Trigonometrization for the space shuttle reentry mixed constraint problem were found to be in excellent agreement with the results from the literature.

This chapter then presented the development of Trigonometrization approach for OCPs with mixed state-control constraints, in which the controls appeared in a non-linear form in the constraint. Two different g-load constraint scenarios for an impactor were chosen to showcase the effectiveness of the Trigonometrization technique in solving such complicated OCPs. In the first scenario, the mixed constraint was active in between the boundary points of the trajectory. On the other hand, in the second sce-

nario, the mixed constraint was active at the entire terminal phase of the trajectory. These results were validated through GPOPS-II.

This chapter then proposed further development of the Trigonometrization technique for OCPs with pure state constraints to obtain two benefits. The first benefit is to avoid spurious results as obtained for the fourth order problem, where the traditional OCT methods obtained an optimal solution with an active path constraint when the unconstrained solution was actually more optimal. The Trigonometrization technique was able to avoid the additional necessary conditions specified by Jacobson et al. to solve the fourth order problem. The second benefit of the Trigonometrization technique for OCPs with pure state constraints is to avoid solving a MPBVP. The development of the Trigonometrization technique to reap benefit 2 for such OCPs is an ongoing effort and a part of the future work, which is discussed in the next chapter.

5. Summary and Future Work

5.1 Summary of Contributions

Since the dawn of modern computing, the design community preferred direct methods over indirect methods of optimization. Among various direct methods, pseudospectral methods have been predominantly used in the state-of-the-art optimization software like GPOPS-II. Pseudospectral methods generate solutions based on approximations that do not employ necessary and sufficient conditions of optimality. The quality of such solutions can suffer resulting in many jitters. Moreover, pseudospectral methods are hard to parallelize for on-board real-time applications based on GPU computing. Recent advancements in OCT have enabled indirect methods to overcome these drawbacks of direct methods.

Although many advancements have been made in OCT, this study identified certain areas of improvement. The smoothing regularization method developed to solve bang-bang control problems had certain issues with dimensional consistency. Additionally, this smoothing method generated unrealistic results for OCPs with path constraints. A powerful regularization method developed at RDSL to solve OCPs with path constraints, ICRM, utilized saturation functions to bound controls and states of the OCP. Certain issues were found with ICRM, including more complicated problem formulation and problem solving processes.

Chapters 2-4 of this thesis advance the OCT and compliment ICRM by proposing a new unified approach based on trigonometry. This new approach utilizes implicit bounding property of periodic trigonometric functions in bounding the controls for various class of OCPs. Chapter 2 proposed and developed a new regularization technique, Epsilon-Trig method, to address first class of OCPs, popularly known as bang-bang and singular control problems. Inspired from the Epsilon-Trig regulariza-

tion method, Chapter 3 proposed a new method called Trigonometrization for second class of OCPs. In this second class of OCPs, the control appears in a non-linear form in the Hamiltonian. Chapter 4 extended Trigonometrization to two other classes of OCPs: one with mixed state-control constraints and the other with pure state constraints. The future work section of this thesis includes ideas to further develop the Trigonometrization technique for the OCPs with pure state constraints. The unified theory of Trigonometrization can then be complete. The subsections below summarize the advancements made by this thesis in the field of OCT.

5.1.1 Solving Bang-Bang and Singular Control Problems

To address numerical issues with bang-bang and singular control problems, Silva and Trélat devised a smoothing regularization method. This powerful smoothing method includes error controls and error parameters while solving a new problem that is very close to the original bang-bang problem. However, this method was unable to impose the bounds on the error controls while solving OCPs with path constraints, leading to highly unrealistic results. This thesis devised the Epsilon-Trig regularization method based on the traditional smoothing method, which revealed a trigonometric relationship between the main control and error controls. It was also found that the error parameter, ϵ, introduced by the traditional smoothing method in all the state equations leads to dimensional inconsistency. The Epsilon-Trig method was able to resolve this dimensional consistency issue by using ϵ in only one state equation. Moreover, the Epsilon-Trig method was able to solve for a singular control in a very simple manner. Instead of solving for multiple controls (including error controls) using the traditional smoothing method in an OCP, the Epsilon-Trig method solved for only one control. The sine and cosine components of this single control then generates the smooth and error controls, respectively.

Certain benchmark problems including the boat problem, the Van der pol problem, and the Goddard rocket problem were used in the verification and validation of

the Epsilon-Trig method. This verification and validation process compared the results obtained from the Epsilon-Trig method and GPOPS-II. The results comparison showed an excellent agreement between the Epsilon-Trig method and GPOPS-II for all the benchmark problems. After verification and validation, this study used the Epsilon-Trig method to solve a very complicated aerospace problem in a simple and effective manner. This aerospace problem involved a scramjet missile with an objective to minimize its time of flight. The thrust model for the scramjet missile is very complicated. Moreover, this complex OCP involves five states, two bounded controls and highly non-linear, coupled EOMs for the states. The Epsilon-Trig method was able to solve this complicated aerospace OCP simply and quickly while maintaining dimensional consistency of the error parameters involved.

The Epsilon-Trig method formed the motivation for the Trigonometrization technique used in the other class of OCPs with bounded controls. The Trigonometrization technique forms the basis for the following two contributions.

5.1.2 Solving Optimal Control Problems with Pure Control Constraints and Non-Linear Controls

This study developed a new technique, termed as Trigonometrization, to implicitly bound the controls using periodic trigonometric functions while solving OCPs with pure control constraints. Unlike bang-bang control problems, the control appears in a non-linear form in the Hamiltonian of this new class of OCPs. The Trigonometrization technique solved the OCP as a TPBVP as against the traditional method that converted it into a MPBVP, which becomes more complicated to solve. Moreover, Trigonometrization solved certain OCPs where the control law becomes transcendental in form. This study presented an example of an aerocapture problem on Mars, where the solution obtained was a maximum for a minimization problem and the optimal solution was actually at -∞. Trigonometrization placed realistic bounds on this problem to resolve this issue.

For verification and validation, Trigonometrization used Rayleigh's problem with a pure control constraint. An excellent agreement was found between the results obtained using the Trigonometrization approach, GPOPS-II, and the results from literature studies. Trigonometrization was found to significantly impact the problem formulation and problem solving processes.

After verification and validation process, Chapter 3 used the Trigonometrization method to solve a very complicated general aviation OCP. The objective of this OCP is to determine the minimal-noise trajectory for aircraft to enable night flight operations. This OCP is already very complicated as it involves six states, three controls with constraints upon them, and a highly non-linear objective function. This objective function became further complicated upon multiplication with a non-linear population model to account for a variable population around an airport, which the existing literature did not explore. Trigonometrization was able to simply and quickly solve this complicated aerospace OCP with pure control constraints.

5.1.3 Solving Optimal Control Problems with State Constraints

The ability of the Trigonometrization technique to handle OCPs with pure control constraints motivated the author to look into third class of OCPs involving zeroth order path constraints. In this class of OCPs, called mixed state-control problems, the constraints on states depend directly on the controls. This study extended Trigonometrization to the OCPs with mixed type constraints by reposing the controls in a trigonometric form with bounds depending on the states.

Traditional OCT poses the OCPs with mixed state-control constraints as a complicated and hard-to-formulate MPBVP. The additional necessary conditions further complicate the problem formulation and problem solving processes for OCPs with path constraints. Moreover, the traditional approach requires determination of the order and the number of constrained and unconstrained arcs a priori to solving such OCPs. Trigonometrization keeps the OCP as a TPBVP and significantly impacts

the problem formulation and solving processes. The verification and validation of the Trigonometrization technique utilized Rayleigh's problem with a mixed state-control constraint. The traditional approach involved solving a seven-point BVP with a very complicated control structure. The results obtained using Trigonometrization matched well with the results obtained from this traditional approach and from GPOPS-II.

After the verification and validation, the Trigonometrization technique solved a very complicated aerospace OCP with a mixed state-control constraint. This aerospace OCP involved maximization of the crossrange capability of a space shuttle type vehicle. The trajectory of this vehicle had a highly non-linear re-radiative heating constraint comprising of 21 terms. The coefficient of lift of the vehicle was dependent on its altitude and its velocity. Since this OCP is very ill-conditioned and sensitive to the initial guess, the solution process employed a weighting-based continuation strategy. In this continuation, the OCP was first solved for a pure control constraint. The solution for the OCP with pure control constraint serves as a guess for the OCP with mixed state-control constraint. The weights change between 0 and 1 from the former to the latter in a stepwise manner. For different values of an important heating parameter, the results obtained using Trigonometrization technique matched very well with literature. Thus, the Trigonometrization technique was able to successfully solve OCPs with mixed state-control constraints containing linear controls.

The Trigonometrization technique was further developed to solve OCPs with mixed state-control constraints containing non-linear controls. A particular problem from this class of OCPs was solved in this thesis, where the terminal velocity of an impactor was to be maximized and a g-load constraint was imposed on this impactor. After eliminating certain mathematical inequalities that are always true while solving the g-load problem, the lower and upper bounds of the control were found. Thus, the control was modified to a trigonometric form based on the g-load constraint. It was further shown that the Trigonometrization technique was able

to solve OCPs where the mixed state-control constraints are active on the terminal point. Trigonometrization was found to be a simple yet powerful technique to solve a wide variety of OCPs as a result.

The success of the Trigonometrization technique in solving OCPs with pure control constraints and mixed state-control constraints further motivated its development for OCPs with pure state constraints. The method specified by Bryson et al. for solving OCPs with pure state constraints obtained spurious results for a fourth order problem. Jacobson et al. introduced additional necessary conditions needed to obtain correct results for the fourth order problem. The Trigonometrization technique was able to solve the fourth order problem in a simple and an efficient manner without introducing any new necessary conditions. However, the success of the Trigonometrization technique was obtained for the OCPs with pure state constraints only when the state constraints were not active.

Although the Trigonometrization technique is able to solve several OCPs of different classes, it can be further improved upon. Furthermore, OCPs with pure state constraints can employ Trigonometrization to obtain converged solutions even with an active state constraint. The following section entails future work for this thesis.

5.2 Future Work

5.2.1 Improving the Epsilon-Trig Regularization Method

The future work for the Epsilon-Trig method involves determining a mathematical basis for the placement of the error into the system of state EOMs. Future work also involves determining the approximate value of ϵ in an automated manner while ensuring quick convergence. At the moment, a trial and error process determines the location and magnitude of the error in the system of equations.

5.2.2 Improving the Trigonometrization Technique for Optimal Control Problems with Pure Control Constraints

The Trigonometrization technique is able to handle all OCPs with pure control constraints. However, future work is required for developing and solving a more complicated version of the aircraft landing trajectory noise minimization problem. In this complicated version, the population around real world airports is included in the problem statement. One such airport is Hartsfield-Jackson international airport in Atlanta and the population distribution around this airport is shown in Fig. 5.1.

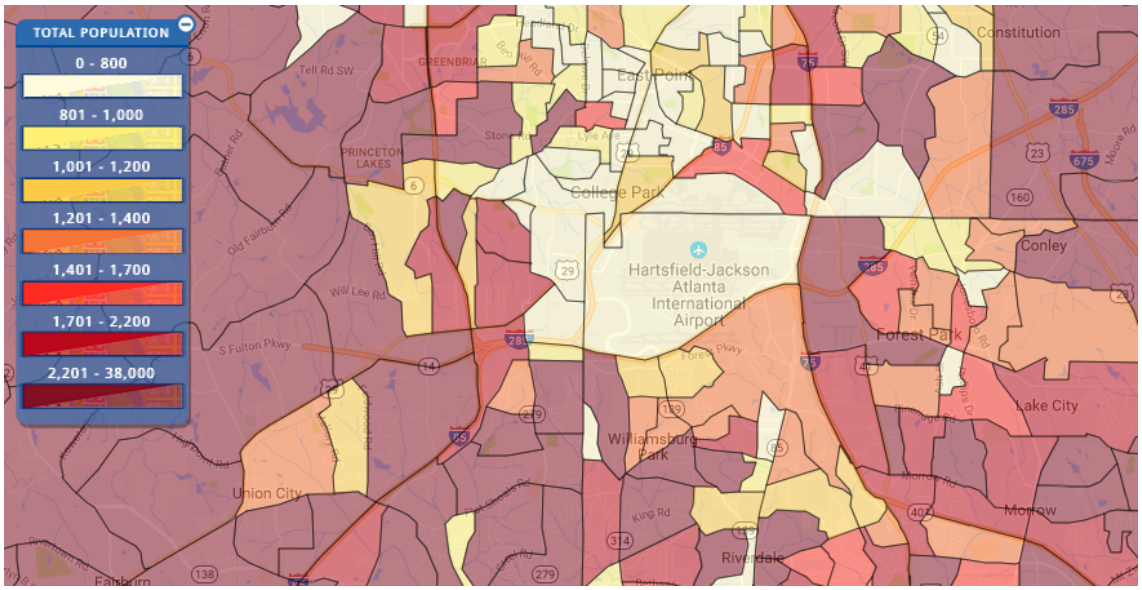

Figure 5.1.: Population distribution model for the Hartsfield-Jackson airport, Atlanta.

Ref. 180 has the population data based on 2010 census. [181] Additionally, a more realistic aircraft needs to be considered. The optimal solutions for this problem might consist of interesting flight trajectories circumnavigating high population zones. These optimal solutions would be useful in planning and enabling night flights around busy airports with varied density of population.

5.2.3 Improving the Trigonometrization Technique for Optimal Control Problems with Mixed State-Control Constraints

This thesis showed that the Trigonometrization technique is able to handle some OCPs with mixed state-control constraints. However, Trigonometrization cannot handle some other OCPs in this class, where a high order polynomial form of the control, u, is constrained by the states, x, as shown in Eq. (5.1). Here C_0 to C_n are n number of constants or state-dependent expressions.

$$f(x) \leq C_0 u^n + C_1 u^{n-1} + ... + C_{n-1} u + C_n \leq g(x) \tag{5.1}$$

The difficulty with Eq. (5.1) is to obtain explicit expressions for the bounds on the control. The Trigonometrization technique requires unique upper and lower bounds on the control, which may not be possible to obtain for complicated mixed control-state constraint expressions.

5.2.4 Improving the Trigonometrization Technique for Optimal Control Problems with Pure State Constraints

The Trigonometrization technique was able to solve OCPs with pure state constraints only when these constraints were not active. Some ideas to use the Trigonometrization technique in order to solve such OCPs when the pure state constraints became active are discussed as follows.

5.2.4.1 Top Down Trigonometrization Approach

The Top Down Trigonometrization approach involves trigonometrizing the state with constraints. The state EOMs are then determined based on the new trigonometrized state. The new Hamiltonian is evaluated based on the transformed state EOMs, which is then used to compute the new control law and the EOMs for the costates. Please note that in indirect methods, the controls are determined based on the costates and

the states depend on the controls. Therefore, this method is named as the Top Down Trigonometrization approach as the effect of trigonometric bounding trickles down from the state to the controls and finally to the costates. The process flow for this approach is shown in Fig. 5.2.

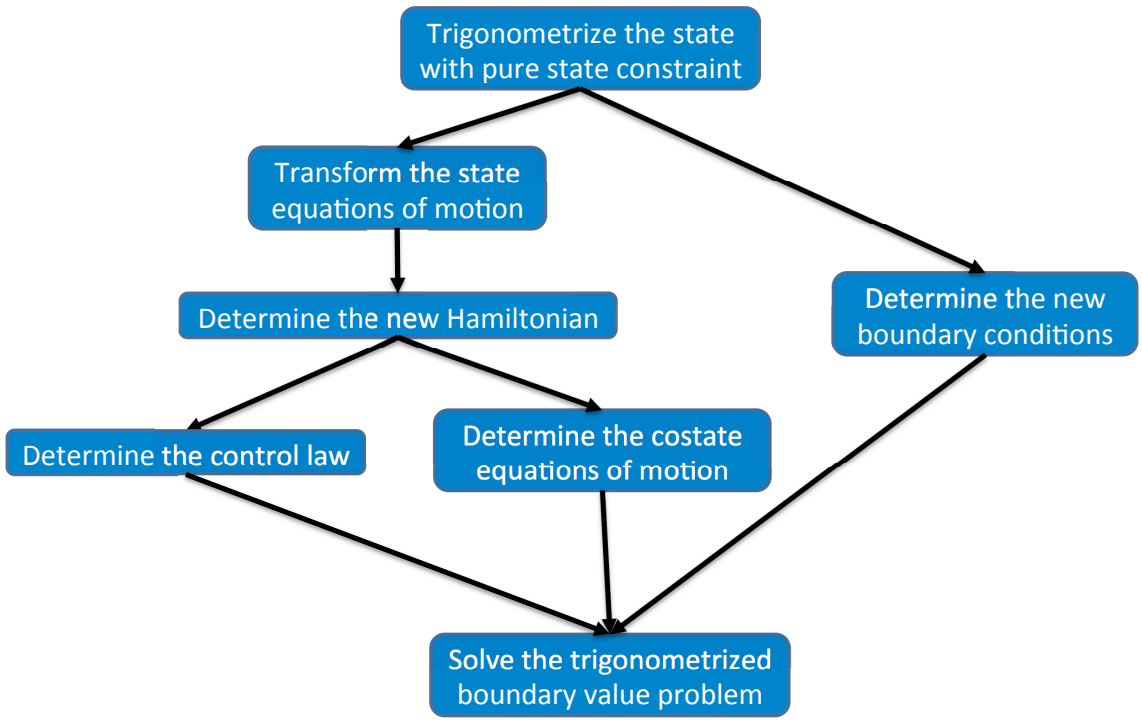

Figure 5.2.: Process flowchart of the Top Down Trigonometrization approach.

The Top Down Trigonometrization approach was found to have some issues, which are demonstrated using the Bryson Denham problem (shown in Eq. (4.39) and discussed in subsection 4.6.2). In this problem, λ_1 affects λ_2 and u, which then affect x_2. Finally, x_2 affects x_1. Upon converting the state, x_1, to a trigonometric form, the changes to the Bryson Denham problem are found to be very similar to Eq. (4.36) for the fourth order problem (discussed in subsection 4.6.1) and are shown in Eq. (5.2). Eq. (5.2a) is the trigonometrized form for the state x_1, which introduces a new state, $x_{1_{\text{TRIG}}}$. Eq. (5.2b) is the transformed EOM corresponding to $x_{1_{\text{TRIG}}}$ and Eq. (5.2c) specifies the new boundary conditions upon this new state. The major difference be-

tween the solutions to the fourth order and Bryson Denham problem is that the state constraint is active only for the latter. This leads to a singularity issue discussed as follows.

$$x_1 = x_{1_{\text{MAX}}} \sin x_{1_{\text{TRIG}}} \tag{5.2a}$$

$$\dot{x}_{1_{\text{TRIG}}} = \frac{x_2}{x_{1_{\text{MAX}}} \cos x_{1_{\text{TRIG}}}} \tag{5.2b}$$

$$x_{1_{\text{TRIG}}}(0) = 0 = x_{1_{\text{TRIG}}}(1) \tag{5.2c}$$

The Hamiltonian for the trigonometrized problem is shown in Eq. (5.3). The EOMs for the costates of this problem are shown in Eq. (5.4) and were found to be similar to Eq. (4.38a) and Eq. (4.38b) of the fourth order problem.

$$H = \frac{u^2}{2} + \frac{\lambda_{x_{1_{\text{TRIG}}}} x_2}{x_{1_{\text{MAX}}} \cos x_{1_{\text{TRIG}}}} + \lambda_{x_{2_{\text{TRIG}}}} u \tag{5.3}$$

$$\dot{\lambda}_{x_{1_{\text{TRIG}}}} = \frac{-\lambda_{x_{1_{\text{TRIG}}}} \sin x_{1_{\text{TRIG}}} x_2}{x_{1_{\text{MAX}}} \cos x_{1_{\text{TRIG}}}^2} \tag{5.4a}$$

$$\dot{\lambda}_{x_{2_{\text{TRIG}}}} = \frac{-\lambda_{x_{1_{\text{TRIG}}}}}{x_{1_{\text{MAX}}} \cos x_{1_{\text{TRIG}}}} \tag{5.4b}$$

The optimal control law for the Top Down Trigonometrization approach for the Bryson Denham problem is shown in Eq. (5.5). Please note that Eq. (5.5) is very similar to Eq. (4.42a) of the traditional approach for the Bryson Denham problem.

$$u^* = -\lambda_{x_{2_{\text{TRIG}}}} \tag{5.5}$$

When the path constraint becomes active, the optimal control attains a non-unique form as the EOMs assume a 0/0 form. To resolve this issue, Table 5.1 includes the EOMs and controls for the path constraint part, where the states, controls and costates are found to stay constant during the path constraint segment of the solution.

Table 5.1.: Constraint conditions for the Bryson Denham problem.

Parameter	x_1	$x_{1_{\text{TRIG}}}$	$\dot{x}_{1_{\text{TRIG}}}$	$\dot{x}_2$	u	$\dot{\lambda}_{x_{1_{\text{TRIG}}}}$	$\dot{\lambda}_{x_{2_{\text{TRIG}}}}$
Value	$x_{1_{\text{MAX}}}$	$\pi/2$	0	0	0	0	0

Even after specifying unique values for the EOMs to resolve the 0/0 issue, bvp4c crashed due to sharp changes in the part of the trajectory just before and after the state constraint becomes active. An alternative approach to resolve this issue is proposed as follows.

5.2.4.2 Epsilon-Trig Approach

In order to avoid issues present in the Top Down Trigonometrization approach, the OCP can be regularized by introducing an error into the state with constraints, x_1. Thus, Eqs. (5.2)–(5.4) of the Top Down Trigonometrization approach are converted into Eq. (5.6) for the Epsilon-Trig approach. The optimal control using the Epsilon-Trig approach for the Bryson Denham problem stays the same as Eq. (5.5).

$$x_1 = x_{1_{\text{MAX}}}(\sin x_{1_{\text{TRIG}}} + \epsilon \cos x_{1_{\text{TRIG}}}) \tag{5.6a}$$

$$\dot{x}_{1_{\text{TRIG}}} = \frac{x_2}{x_{1_{\text{MAX}}}(\cos x_{1_{\text{TRIG}}} - \epsilon \sin x_{1_{\text{TRIG}}})} \tag{5.6b}$$

$$x_{1_{\text{TRIG}}}(0) = -\arctan(\epsilon) = \mathrm{x}_{1_{\text{TRIG}}}(1) \tag{5.6c}$$

$$H = \frac{u^2}{2} + \frac{\lambda_{x_{1_{\text{TRIG}}}} x_2}{x_{1_{\text{MAX}}}(\cos x_{1_{\text{TRIG}}} - \epsilon \sin x_{1_{\text{TRIG}}})} + \lambda_{x_{2_{\text{TRIG}}}} u \tag{5.6d}$$

$$\dot{\lambda}_{x_{1_{\text{TRIG}}}} = \frac{-\lambda_{x_{1_{\text{TRIG}}}}(\sin x_{1_{\text{TRIG}}} + \epsilon \cos x_{1_{\text{TRIG}}}) x_2}{x_{1_{\text{MAX}}}(\cos x_{1_{\text{TRIG}}} - \epsilon \sin x_{1_{\text{TRIG}}})^2} \tag{5.6e}$$

$$\dot{\lambda}_{x_{2_{\text{TRIG}}}} = \frac{-\lambda_{x_{1_{\text{TRIG}}}}}{x_{1_{\text{MAX}}}(\cos x_{1_{\text{TRIG}}} - \epsilon \sin x_{1_{\text{TRIG}}})} \tag{5.6f}$$

Since there are sharp changes in the area where the path constraint on x_1 becomes active, Trigonometrization was expected to benefit from the use of error controls.

However, adding error controls to the Hamiltonian could not resolve issues with the trigonometrized Bryson Denham problem thus far. An alternative approach to the Epsilon-Trig approach is discussed as follows.

5.2.4.3 Auxiliary Approach

Just like ICRM, the Top Down Trigonometrization approach can be converted into an Auxiliary approach by introducing not just new states but also new controls. The Auxiliary approach for the Bryson Denham problem is shown in Eq. (5.7), where $x_{1_{\text{TRIG}}}$ and $x_{2_{\text{TRIG}}}$ are the new states and u_{NEW} is the new control.

$$\dot{x}_1 = x_{1_{\text{MAX}}} \cos x_{1_{\text{TRIG}}} x_{2_{\text{TRIG}}} \tag{5.7a}$$

$$\dot{x}_2 = x_{1_{\text{MAX}}} [\cos x_{1_{\text{TRIG}}} u_{\text{NEW}} - \sin x_{1_{\text{TRIG}}} (x_{2_{\text{TRIG}}})^2] \tag{5.7b}$$

$$\dot{x}_{1_{\text{TRIG}}} = x_{2_{\text{TRIG}}} \tag{5.7c}$$

$$\dot{x}_{2_{\text{TRIG}}} = u_{\text{NEW}} \tag{5.7d}$$

Table 5.1 shows the boundary conditions on the states of the Bryson Denham problem using the Auxiliary approach. This approach is still under development and is a part of the future work.

Table 5.2.: New boundary conditions for the Bryson Denham problem based on the Auxiliary approach.

Parameter	x_1	x_2	$x_{1_{\text{TRIG}}}$	$x_{2_{\text{TRIG}}}$
Initial Value	0	1	0	$1/x_{1_{\text{MAX}}}$
Final Value	0	-1	0	$-1/x_{1_{\text{MAX}}}$

The high mass Mars problem described in Sec. 1.2.2.9 motivated this thesis originally. In addition to the g-load and surface path constraints, the high mass Mars

problem has a heat rate constraint. This heat rate constraint, popularly known as the Sutton Graves equation, is shown in Eq. (5.8) and is a second order path constraint ($q = 2$). [182–185] In Eq. (5.8), q is the convective heating, k is the heat rate constant, and r_n is the nose radius of the entry vehicle.

$$\dot{q} = k\sqrt{\frac{\rho}{r_n}}v^3 \tag{5.8}$$

Trigonometrization is unable to handle such path constraints with $q > 0$ at the moment. The design community needs to look into the development of a unified Trigonometrization approach, which can also solve complicated aerospace OCPs with pure state constraints in a simpler manner. ICRM devised at RDSL can possibly combine with Trigonometrization to solve OCPs like the high mass Mars problem. Such a new hybrid regularization technique to solve all classes of OCPs can possibly utilize the advantages of both these regularization methods. Only further research and investigation can answer the questions pertaining to the limits of the Trigonometrization approach.

REFERENCES

REFERENCES

[1] Roger Fletcher. *Practical Methods of Optimization*. John Wiley & Sons, 2013.

[2] Singiresu S Rao. *Engineering optimization: Theory and Practice*. John Wiley & Sons, 2009.

[3] John T Betts. Survey of numerical methods for trajectory optimization. *Journal of Guidance, Control, and Dynamics*, 21(2):193–207, 1998.

[4] Oskar Von Stryk and Roland Bulirsch. Direct and indirect methods for trajectory optimization. *Annals of Operations Research*, 37(1):357–373, 1992.

[5] Michael J Grant. *Rapid Simultaneous Hypersonic Aerodynamic and Trajectory Optimization for Conceptual Design*. PhD thesis, Georgia Institute of Technology, 2012.

[6] Charles R Hargraves and Stephen W Paris. Direct trajectory optimization using nonlinear programming and collocation. *Journal of Guidance, Control, and Dynamics*, 10(4):338–342, 1987.

[7] Albert L Herman and Bruce A Conway. Direct optimization using collocation based on high-order gauss-lobatto quadrature rules. *Journal of Guidance, Control, and Dynamics*, 19(3):592–599, 1996.

[8] Robert Bibeau and David Rubinstein. Trajectory optimization for a fixed-trim reentry vehicle using direct collocation and nonlinear programming. In *18th Applied Aerodynamics Conference*, page 4262, 2000.

[9] Michael Grant and Gavin Mendeck. Mars science laboratory entry optimization using particle swarm methodology. In *AIAA Atmospheric Flight Mechanics Conference and Exhibit*, page 6393, 2007.

[10] JT Betts and I Kolmanovsky. Practical methods for optimal control using nonlinear programming. *Applied Mechanics Reviews*, 55:B68, 2002.

[11] Michael A Patterson and Anil V Rao. Gpops-ii: A matlab software for solving multiple-phase optimal control problems using hp-adaptive gaussian quadrature collocation methods and sparse nonlinear programming. *ACM Transactions on Mathematical Software (TOMS)*, 41(1):1, 2014.

[12] Fariba Fahroo and I Michael Ross. Dido (optimal control).

[13] I Michael Ross. User's manual for dido: A matlab application package for solving optimal control problems. *Tomlab Optimization, Sweden*, page 65, 2004.

[14] I Michael Ross and Fariba Fahroo. Legendre pseudospectral approximations of optimal control problems. In *New Trends in Nonlinear Dynamics and Control and Their Applications*, pages 327–342. Springer, 2003.

[15] Fariba Fahroo and I Michael Ross. Direct trajectory optimization by a chebyshev pseudospectral method. *Journal of Guidance, Control, and Dynamics*, 25(1):160–166, 2002.

[16] Divya Garg, Michael A Patterson, Camila Francolin, Christopher L Darby, Geoffrey T Huntington, William W Hager, and Anil V Rao. Direct trajectory optimization and costate estimation of finite-horizon and infinite-horizon optimal control problems using a radau pseudospectral method. *Computational Optimization and Applications*, 49(2):335–358, 2011.

[17] David A Benson, Geoffrey T Huntington, Tom P Thorvaldsen, and Anil V Rao. Direct trajectory optimization and costate estimation via an orthogonal collocation method. *Journal of Guidance, Control, and Dynamics*, 29(6):1435–1440, 2006.

[18] Fariba Fahroo and I Michael Ross. Costate estimation by a legendre pseudospectral method. *Journal of Guidance, Control, and Dynamics*, 24(2):270–277, 2001.

[19] Christopher L Darby, William W Hager, and Anil V Rao. Direct trajectory optimization using a variable low-order adaptive pseudospectral method. *Journal of Spacecraft and Rockets*, 48(3):433–445, 2011.

[20] Divya Garg, Michael Patterson, William W Hager, Anil V Rao, David A Benson, and Geoffrey T Huntington. A unified framework for the numerical solution of optimal control problems using pseudospectral methods. *Automatica*, 46(11):1843–1851, 2010.

[21] I Michael Ross and Fariba Fahroo. Pseudospectral methods for optimal motion planning of differentially flat systems. *IEEE Transactions on Automatic Control*, 49(8):1410–1413, 2004.

[22] Cornelius Lanczos. *The Variational Principles of Mechanics*. Courier Corporation, 2012.

[23] Donald E Kirk. *Optimal Control Theory: An Introduction*. Courier Corporation, 2012.

[24] James M Longuski, José J Guzmán, and John E Prussing. *Optimal Control with Aerospace Applications*. Springer, 2016.

[25] Thomas Antony and Michael J Grant. Rapid indirect trajectory optimization on highly parallel computing architectures. *Journal of Spacecraft and Rockets*, pages 1–11, 2017.

[26] Michael J Grant and Thomas Antony. Rapid indirect trajectory optimization of a hypothetical long range weapon system. In *AIAA Atmospheric Flight Mechanics Conference*, page 0276, 2016.

[27] David D Morrison, James D Riley, and John F Zancanaro. Multiple shooting method for two-point boundary value problems. *Communications of the ACM*, 5(12):613–614, 1962.

[28] Josef Stoer and Roland Bulirsch. *Introduction to Numerical Analysis*, volume 12. Springer Science & Business Media, 2013.

[29] Chris McClanahan. History and evolution of gpu architecture. *A Survey Paper*, page 9, 2010.

[30] Enhua Wu and Youquan Liu. Emerging technology about gpgpu. In *Circuits and Systems, 2008. APCCAS 2008. IEEE Asia Pacific Conference on*, pages 618–622. IEEE, 2008.

[31] Stephan Soller. Gpgpu origins and gpu hardware architecture. 2011.

[32] John D Owens, David Luebke, Naga Govindaraju, Mark Harris, Jens Krüger, Aaron E Lefohn, and Timothy J Purcell. A survey of general-purpose computation on graphics hardware. In *Computer Graphics Forum*, volume 26, pages 80–113. Wiley Online Library, 2007.

[33] David Luebke and M Harris. General-purpose computation on graphics hardware. In *Workshop, SIGGRAPH*, 2004.

[34] Michael J Sparapany. *Towards the Real-Time Application of Indirect Methods for Hypersonic Missions*. PhD thesis, Purdue University, 2015.

[35] Kevin P Bollino. High-fidelity real-time trajectory optimization for reusable launch vehicles. 2006.

[36] Helen Oleynikova, Michael Burri, Zachary Taylor, Juan Nieto, Roland Siegwart, and Enric Galceran. Continuous-time trajectory optimization for online uav replanning. In *Intelligent Robots and Systems (IROS), 2016 IEEE/RSJ International Conference on*, pages 5332–5339. IEEE, 2016.

[37] Feng-Li Lian and Richard Murray. Real-time trajectory generation for the cooperative path planning of multi-vehicle systems. In *Decision and Control, 2002, Proceedings of the 41st IEEE Conference on*, volume 4, pages 3766–3769. IEEE, 2002.

[38] Erik P Anderson, Randal W Beard, and Timothy W McLain. Real-time dynamic trajectory smoothing for unmanned air vehicles. *IEEE Transactions on Control Systems Technology*, 13(3):471–477, 2005.

[39] Timothy McLain and Randal Beard. Trajectory planning for coordinated rendezvous of unmanned air vehicles. In *AIAA Guidance, navigation, and control conference and exhibit*, page 4369, 2000.

[40] Alessandro Gardi, Roberto Sabatini, Subramanian Ramasamy, and Trevor Kistan. Real-time trajectory optimisation models for next generation air traffic management systems. In *Applied Mechanics and Materials*, volume 629, pages 327–332. Trans Tech Publ, 2014.

[41] Tamás Kalmár-Nagy, Pritam Ganguly, and Raffaello D'Andrea. Real-time trajectory generation for omnidirectional vehicles. In *American Control Conference, 2002. Proceedings of the 2002*, volume 1, pages 286–291. IEEE, 2002.

[42] Meir Pachter and Phil R Chandler. Challenges of autonomous control. *IEEE Control Systems*, 18(4):92–97, 1998.

[43] Randal W Beard, Timothy W McLain, Michael A Goodrich, and Erik P Anderson. Coordinated target assignment and intercept for unmanned air vehicles. *IEEE Transactions on Robotics and Automation*, 18(6):911–922, 2002.

[44] Ping Lu. Trajectory optimization and guidance for a hypersonic vehicle. In *3rd International Aerospace Planes Conference*, page 5068, 1991.

[45] Richard Bellman, Irving Glicksberg, and Oliver Gross. On the "bang-bang" control problem. *Quarterly of Applied Mathematics*, 14(1):11–18, 1956.

[46] Vladimir Grigorevich Boltyanskii, KN Trirogoff, Ivin Tarnove, and George Leitmann. Mathematical methods of optimal control, 1971.

[47] Régis Bertrand and Richard Epenoy. New smoothing techniques for solving bang–bang optimal control problems—numerical results and statistical interpretation. *Optimal Control Applications and Methods*, 23(4):171–197, 2002.

[48] Cristiana Silva and Emmanuel Trélat. Smooth regularization of bang-bang optimal control problems. *IEEE Transactions on Automatic Control*, 55(11):2488–2499, 2010.

[49] Michael J Grant and Michael A Bolender. Minimum terminal energy optimizations of hypersonic vehicles using indirect methods. In *AIAA Atmospheric Flight Mechanics Conference*, page 2402, 2015.

[50] Arthur E Bryson, Walter F Denham, and Stewart E Dreyfus. Optimal programming problems with inequality constraints. *AIAA Journal*, 1(11):2544–2550, 1963.

[51] David H Jacobson, Milind M Lele, and Jason L Speyer. New necessary conditions of optimality for control problems with state-variable inequality constraints. *Journal of Mathematical Analysis and Applications*, 35(2):255–284, 1971.

[52] Dimitri P Bertsekas. *Nonlinear Programming*. Athena scientific Belmont, 1999.

[53] Jiamin Zhu, Emmanuel Trélat, and Max Cerf. Geometric optimal control and applications to aerospace. *Pacific Journal of Mathematics for Industry*, 9(1):8, 2017.

[54] Philip E Gill, Walter Murray, and Michael A Saunders. Snopt: An sqp algorithm for large-scale constrained optimization. *SIAM Review*, 47(1):99–131, 2005.

[55] A Wächter and L Biegler. Ipopt-an interior point optimizer, 2009.

[56] Andreas Waechter, Carl Laird, F Margot, and Y Kawajir. Introduction to ipopt: A tutorial for downloading, installing, and using ipopt. *Revision*, 2009.

[57] A Wächter, LT Biegler, YD Lang, and A Raghunathan. Ipopt: An interior point algorithm for large-scale nonlinear optimization, 2002.

[58] Andreas Wächter. Short tutorial: Getting started with ipopt in 90 minutes. In *Dagstuhl Seminar Proceedings*. Schloss Dagstuhl-Leibniz-Zentrum für Informatik, 2009.

[59] Jorge Nocedal and Stephen J Wright. *Sequential Quadratic Programming*. Springer, 2006.

[60] Paul T Boggs and Jon W Tolle. Sequential quadratic programming. *Acta Numerica*, 4:1–51, 1995.

[61] Paul T Boggs and Jon W Tolle. Sequential quadratic programming for large-scale nonlinear optimization. *Journal of Computational and Applied Mathematics*, 124(1-2):123–137, 2000.

[62] Oskar Von Stryk. Numerical solution of optimal control problems by direct collocation. In *Optimal Control*, pages 129–143. Springer, 1993.

[63] Kenneth Wright. Some relationships between implicit runge-kutta, collocation and lanczosτ methods, and their stability properties. *BIT Numerical Mathematics*, 10(2):217–227, 1970.

[64] I Michael Ross and Mark Karpenko. A review of pseudospectral optimal control: From theory to flight. *Annual Reviews in Control*, 36(2):182–197, 2012.

[65] Qi Gong, I Michael Ross, Wei Kang, and Fariba Fahroo. On the pseudospectral covector mapping theorem for nonlinear optimal control. In *Decision and Control, 2006 45th IEEE Conference on*, pages 2679–2686. IEEE, 2006.

[66] Qi Gong, I Michael Ross, Wei Kang, and Fariba Fahroo. Connections between the covector mapping theorem and convergence of pseudospectral methods for optimal control. *Computational Optimization and Applications*, 41(3):307–335, 2008.

[67] Jane Cullum. Finite-dimensional approximations of state-constrained continuous optimal control problems. *SIAM Journal on Control*, 10(4):649–670, 1972.

[68] Bengt Fornberg. *A Practical Guide to Pseudospectral Methods*, volume 1. Cambridge University Press, 1998.

[69] Gamal Elnagar, Mohammad A Kazemi, and Mohsen Razzaghi. The pseudospectral legendre method for discretizing optimal control problems. *IEEE transactions on Automatic Control*, 40(10):1793–1796, 1995.

[70] Divya Garg, Michael Patterson, Christopher Darby, Camila Francolin, Geoffrey Huntington, William Hager, and Anil Rao. Direct trajectory optimization and costate estimation of general optimal control problems using a radau pseudospectral method. In *AIAA Guidance, Navigation, and Control Conference*, page 5989, 2009.

[71] Gene H Golub. Some modified matrix eigenvalue problems. *Siam Review*, 15(2):318–334, 1973.

[72] Helmut Maurer. Tutorial on control and state constrained optimal control problems. In *SADCO Summer School 2011-Optimal Control*, 2011.

[73] E Kreindler. Additional necessary conditions for optimal control with state-variable inequality constraints. *Journal of Optimization Theory and Applications*, 38(2):241–250, 1982.

[74] Lawrence F Shampine, Jacek Kierzenka, and Mark W Reichelt. Solving boundary value problems for ordinary differential equations in matlab with bvp4c. *Tutorial Notes*, 2000:1–27, 2000.

[75] Lawrence F Shampine, Ian Gladwell, and Skip Thompson. *Solving ODEs with MATLAB*. Cambridge University Press, 2003.

[76] Jacek Kierzenka. *Studies in the Numerical Solution of Ordinary Differential Equations*. PhD thesis, Southern Methodist University, 1998.

[77] Emmanuel Trélat. *Contrôle Optimal: Théorie & Applications*, volume 865. Vuibert Paris, 2008.

[78] Emmanuel Trélat. Optimal control and applications to aerospace: Some results and challenges. *Journal of Optimization Theory and Applications*, 154(3):713–758, 2012.

[79] Thomas Antony and Michael J Grant. Path constraint regularization in optimal control problems using saturation functions. In *2018 AIAA Atmospheric Flight Mechanics Conference*, page 0018, 2018.

[80] Wolfram Mathematica. Wolfram research. *Inc., Champaign, Illinois*, 2009.

[81] Michael J Grant and Robert D Braun. Rapid indirect trajectory optimization for conceptual design of hypersonic missions. *Journal of Spacecraft and Rockets*, 52(1):177–182, 2014.

[82] Justin R Mansell. *Adaptive Continuation Strategies for Indirect Trajectory Optimization*. PhD thesis, Purdue University, 2017.

[83] Shubham Singh and Michael J Grant. The use of homotopy analysis method for indirect trajectory optimization. In *2018 AIAA Guidance, Navigation, and Control Conference*, page 0864, 2018.

[84] Shubham Singh. *Applications of the Homotopy Analysis Method to Optimal Control Problems*. PhD thesis, Purdue University, 2016.

[85] Robert D Braun and Robert M Manning. Mars exploration entry, descent, and landing challenges. *Journal of Spacecraft and Rockets*, 44(2):310–323, 2007.

[86] John A Christian, Grant Wells, Jarret M Lafleur, Amanda Verges, and Robert D Braun. Extension of traditional entry, descent, and landing technologies for human mars exploration. *Journal of Spacecraft and Rockets*, 45(1):130–141, 2008.

[87] Bradley Steinfeldt, John Theisinger, Ashley Korzun, Ian Clark, Michael Grant, and Robert Braun. High mass mars entry, descent, and landing architecture assessment. In *AIAA SPACE 2009 Conference & Exposition*, page 6684, 2009.

[88] Ronald Sostaric. The challenge of mars edl (entry, descent, and landing). 2010.

[89] Alicia M DwyerCianciolo, Jody L Davis, David R Komar, Michelle M Munk, Jamshid A Samareh, Richard W Powell, Jeremy D Shidner, Douglas O Stanley, Alan W Wilhite, David J Kinney, et al. Entry, descent and landing systems analysis study: Phase 1 report. 2010.

[90] Thomas Zang, Alicia Dwyer-Cianciolo, Mark Ivanov, Ronald Sostaric, and David Kinney. Overview of the nasa entry, descent and landing systems analysis studies for large robotic-class missions. In *AIAA SPACE 2011 Conference & Exposition*, page 7294, 2011.

[91] Ethiraj Venkatapathy, Kenneth Hamm, Ian Fernandez, James Arnold, David Kinney, Bernard Laub, Alberto Makino, Mary McGuire, Keith Peterson, Dinesh Prabhu, et al. Adaptive deployable entry and placement technology (adept): A feasibility study for human missions to mars. In *21st AIAA Aerodynamic Decelerator Systems Technology Conference and Seminar*, page 2608, 2011.

[92] Alicia D Cianciolo and Tara T Polsgrove. Human mars entry, descent, and landing architecture study overview. 2016.

[93] Tara Polsgrove and Alicia M Dwyer-Cianciolo. Human mars entry, descent and landing architecture study overview. In *AIAA SPACE 2016*, page 5494. 2016.

[94] Elon Musk. Making humans a multi-planetary species. *New Space*, 5(2):46–61, 2017.

[95] Brandon Sforzo and Robert D Braun. Feasibility of supersonic retropropulsion based on assessment of mars-relevant flight data. In *AIAA SPACE and Astronautics Forum and Exposition*, page 5295, 2017.

[96] Alicia Dwyer Cianciolo, Thomas A Zang, Ronald R Sostaric, and M Kathy McGuire. Overview of the nasa entry, descent and landing systems analysis exploration feed-forward study. In *International Planetary Probe Workshop*, 2011.

[97] Jarret M Lafleur and Christopher J Cerimele. Mars entry bank profile design for terminal state optimization. *Journal of Spacecraft and Rockets*, 48(6):1012–1024, 2011.

[98] Geethu Lisba Jacob, Geethu Neeler, and RV Ramanan. Mars entry mission bank profile optimization. *Journal of Guidance, Control, and Dynamics*, 37(4):1305–1316, 2014.

[99] Jarret Lafleur and Chris Cerimele. Angle of attack modulation for mars entry terminal state optimization. In *AIAA Atmospheric Flight Mechanics Conference*, page 5611, 2009.

[100] Christopher J Cerimele, Edward A Robertson, Ronald R Sostaric, Charles H Campbell, Phil Robinson, Daniel A Matz, Breanna J Johnson, Susan J Stachowiak, Joseph A Garcia, Jeffrey V Bowles, et al. A rigid mid-lift-to-drag ratio approach to human mars entry, descent, and landing. 2017.

[101] Juan G Cruz-Ayoroa and Robert D Braun. Evaluation of deployable aerosurface systems for mars entry. 2012.

[102] Kshitij Mall and Michael J Grant. High mass mars exploration using slender entry vehicles. In *AIAA Atmospheric Flight Mechanics Conference*, page 0019, 2016.

[103] Elon Musk. Making life multi-planetary. *New Space*, 6(1):2–11, 2018.

[104] Vladimir Alekseevich Morozov and Michael Stessin. *Regularization Methods for Ill-Posed Problems*. CRC Press Boca Raton, FL:, 1993.

[105] Peter J Bickel, Bo Li, Alexandre B Tsybakov, Sara A van de Geer, Bin Yu, Teófilo Valdés, Carlos Rivero, Jianqing Fan, and Aad van der Vaart. Regularization in statistics. *Test*, 15(2):271–344, 2006.

[106] AN Tikhonov. On the solution of ill-posed problems and the method of regularization. In *Dokl. Akad. Nauk SSSR*, volume 151, pages 501–504, 1963.

[107] Vladimir Alekseevich Morozov. On the solution of functional equations by the method of regularization. In *Soviet Math. Dokl*, volume 7, pages 414–417, 1966.

[108] Patricia K Lamm. A survey of regularization methods for first-kind volterra equations. In *Surveys on Solution Methods for Inverse Problems*, pages 53–82. Springer, 2000.

[109] R Plato and G Vainikko. On the regularization of projection methods for solving ill-posed problems. *Numerische Mathematik*, 57(1):63–79, 1990.

[110] Demetri Terzopoulos. Regularization of inverse visual problems involving discontinuities. *IEEE Transactions on pattern analysis and Machine Intelligence*, (4):413–424, 1986.

[111] Yanfei Wang, Anatoly G Yagola, Changchun Yang, et al. *Optimization and Regularization for Computational Inverse Problems and Applications*. Springer, 2011.

[112] Lars Eldén. Algorithms for the regularization of ill-conditioned least squares problems. *BIT Numerical Mathematics*, 17(2):134–145, 1977.

[113] Andrei Nikolaevich Tikhonov. Regularization of incorrectly posed problems. Soviet Mathematics Doklady, 1963.

[114] Heinz Werner Engl, Martin Hanke, and Andreas Neubauer. *Regularization of Inverse Problems*, volume 375. Springer Science & Business Media, 1996.

[115] Thomas Antony. *Large Scale Constrained Trajectory Optimization Using Indirect Methods*. PhD thesis, Purdue University, 2018.

[116] Knut Graichen, Andreas Kugi, Nicolas Petit, and Francois Chaplais. Handling constraints in optimal control with saturation functions and system extension. *Systems & Control Letters*, 59(11):671–679, 2010.

[117] SA Dadebo and KB McAuley. On the computation of optimal singular controls. In *Control Applications, 1995., Proceedings of the 4th IEEE Conference on*, pages 150–155. IEEE, 1995.

[118] D Jacobson, S Gershwin, and M Lele. Computation of optimal singular controls. *IEEE Transactions on Automatic Control*, 15(1):67–73, 1970.

[119] TF Edgar and L Lapidus. The computation of optimal singular bang-bang control ii. nonlinear systems. *AIChE Journal*, 18(4):780–785, 1972.

[120] Yaobin Chen and Jian Huang. A continuation method for singular optimal control synthesis. In *American Control Conference, 1993*, pages 1256–1260. IEEE, 1993.

[121] J Gergaud and J Noailles. Application of simplicial algorithm to a spacecraft trajectory optimization problem. In *Seventh IFAC Workshop on Control Applications of Nonlinear Programming and Optimization*, 1988.

[122] Thomas Haberkorn, Pierre Martinon, and Joseph Gergaud. Low thrust minimum-fuel orbital transfer: A homotopic approach. *Journal of Guidance, Control, and Dynamics*, 27(6):1046–1060, 2004.

[123] Ehsan Taheri, Ilya Kolmanovsky, and Ella Atkins. Enhanced smoothing technique for indirect optimization of minimum-fuel low-thrust trajectories. *Journal of Guidance, Control, and Dynamics*, pages 2500–2511, 2016.

[124] Tieding Guo, Fanghua Jiang, and Junfeng Li. Homotopic approach and pseudospectral method applied jointly to low thrust trajectory optimization. *Acta Astronautica*, 71:38–50, 2012.

[125] Jing Li and Xiao-ning Xi. Fuel-optimal low-thrust reconfiguration of formation-flying satellites via homotopic approach. *Journal of Guidance, Control, and Dynamics*, 35(6):1709–1717, 2012.

[126] Fanghua Jiang, Hexi Baoyin, and Junfeng Li. Practical techniques for low-thrust trajectory optimization with homotopic approach. *Journal of Guidance, Control, and Dynamics*, 35(1):245–258, 2012.

[127] Mischa Kim. *Continuous Low-Thrust Trajectory Optimization: Techniques and Applications*. PhD thesis, Virginia Tech, 2005.

[128] Thomas Paine. *The Age of Reason*. Xist Publishing, 2016.

[129] Gilbert Strang. Linear algebra and its applications, academic, new york, 1976. *Google Scholar*.

[130] Shurong Li, Ruiyan Zhao, and Qiang Zhang. Optimization method for solving bang-bang and singular control problems. *Journal of Control Theory and Applications*, 10(4):559–564, 2012.

[131] Amy F Woolf. Conventional prompt global strike and long range ballistic missiles: Background and issues. Technical report, Congressional Research Service Washington United States, 2017.

[132] Matt Bille and Rusty Lorenz. Requirements for a conventional prompt global strike capability. Technical report, Anser Arlington VA, 2001.

[133] Peter Ouzts. The joint technology office on hypersonics. In *15th AIAA International Space Planes and Hypersonic Systems and Technologies Conference*, page 2576, 2008.

[134] Joseph Williams, Kshitij Mall, and Michael J Grant. Trajectory optimization using indirect methods and parametric scramjet cycle analysis. In *55th AIAA Aerospace Sciences Meeting*, page 1384, 2017.

[135] Joseph Williams. Trajectory optimization using indirect methods and parametric scramjet cycle analysis. 2016.

[136] Rahman Tawfiqur, Hao Zhou, Yong Zhi Sheng, Ya Min Younis, and Ke Nan Zhang. Trajectory optimization of hypersonic vehicle using gauss pseudospectral method. In *Applied Mechanics and Materials*, volume 110, pages 5232–5239. Trans Tech Publ, 2012.

[137] Hitoshi Morimoto and Jason Chuang. Minimum-fuel trajectory along entire flight profile for a hypersonic vehicle with constraint. In *Guidance, Navigation, and Control Conference and Exhibit*, page 4122, 1998.

[138] Ping Lu. Inverse dynamics approach to trajectory optimization for an aerospace plane. *Journal of Guidance, Control, and Dynamics*, 16(4):726–732, 1993.

[139] Oscar Murillo and Ping Lu. Fast ascent trajectory optimization for hypersonic air-breathing vehicles. In *AIAA Guidance, Navigation, and Control Conference*, page 8173, 2010.

[140] H Prasanna, D Ghose, M Bhat, C Bhattacharyya, and J Umakant. Interpolation-aware trajectory optimization for a hypersonic vehicle using non-linear programming. In *AIAA Guidance, Navigation, and Control Conference and Exhibit*, page 6063, 2005.

[141] Thomas A Jackson. Power for a space plane. *Scientific American*, 295(2):56–63, 2006.

[142] TA Jackson, DR Eklund, and AJ Fink. High speed propulsion: Performance advantage of advanced materials. *Journal of Materials Science*, 39(19):5905–5913, 2004.

[143] Stephen Corda, Timothy R Moes, Masashi Mizukami, Neal E Hass, Daniel Jones, Richard C Monaghan, Ronald J Ray, Michele L Jarvis, and Nathan Palumbo. The sr-71 test bed aircraft: A facility for high-speed flight research. *NASA TP-209023*, 2000.

[144] Joel Schmitigal and Jill Tebbe. Jp-8 and other military fuels. Technical report, Army Tank Automotive Research Development and Engineering Center Warren MI, 2011.

[145] Tara M Lovestead and Thomas J Bruno. A comparison of the hypersonic vehicle fuel jp-7 to the rocket propellants rp-1 and rp-2 with the advanced distillation curve method. *Energy & Fuels*, 23(7):3637–3644, 2009.

[146] Lourdes Q Maurice, H Lander, T Edwards, and WE Harrison Iii. Advanced aviation fuels: A look ahead via a historical perspective. *Fuel*, 80(5):747–756, 2001.

[147] Tim Edwards. Usaf supercritical hydrocarbon fuels interests. In *31st Aerospace Sciences Meeting*, page 807, 1993.

[148] H Lander and AC Nixon. Endothermic fuels for hypersonic vehicles. *Journal of Aircraft*, 8(4):200–207, 1971.

[149] Michael K Smart, Neal E Hass, and Allan Paull. Flight data analysis of the hyshot 2 scramjet flight experiment. *AIAA Journal*, 44(10):2366–2375, 2006.

[150] Kshitij Mall and Michael James Grant. Epsilon-trig regularization method for bang-bang optimal control problems. *Journal of Optimization Theory and Applications*, 174(2):500–517, 2017.

[151] Nguyen X Vinh. Integrals of the motion for optimal trajectories in atmospheric flight. *AIAA Journal*, 11(5):700–703, 1973.

[152] Hui Yu and J Mulder. Arrival trajectory optimization on noise impact using interval analysis. In *10th AIAA Aviation Technology, Integration, and Operations (ATIO) Conference*, page 9288, 2010.

[153] Kshitij Mall and Michael J Grant. Trigonomerization of optimal control problems with bounded controls. In *AIAA Atmospheric Flight Mechanics Conference*, page 3244, 2016.

[154] Helmut Maurer. Tutorial on control and state constrained optimal control problems–part i: Examples.

[155] JA Roux. Parametric ideal scramjet cycle analysis. *Journal of Thermophysics and Heat Transfer*, 25(4):581–585, 2011.

[156] H Ohta. Analysis of minimum noise landing approach trajectory. *Journal of Guidance, Control, and Dynamics*, 5(3):263–269, 1982.

[157] Lina Abdallah. Optimal flight paths reducing the aircraft noise during landing. In *Modelling, Computation and Optimization in Information Systems and Management Sciences*, pages 1–10. Springer, 2008.

[158] BAA Heathrow. Flight evaluation report 2007. *British Airports Authority*, 2007.

[159] Worldwide Air Transport Conference (ATCONF). Night flight restrictions. http://www.icao.int/Meetings/atconf6/Documents/WorkingPapers/, 2010. Accessed: 13 Dec. 2016.

[160] Bernd Kugelmann. Minimizing the noise of an aircraft during landing approach. In *Variational Calculus, Optimal Control and Applications*, pages 271–280. Springer, 1998.

[161] Nguyen X Vinh, Adolf Busemann, and Robert D Culp. Hypersonic and planetary entry flight mechanics. *NASA STI/Recon Technical Report A*, 81, 1980.

[162] Lina Abdallah, Mounir Haddou, and Salah Khardi. Optimization of operational aircraft parameters reducing noise emission. *arXiv preprint arXiv:0804.4135*, 2008.

[163] Janav P Udani, Kshitij Mall, Michael J Grant, and Dengfeng Sun. Optimal flight trajectory to minimize noise during landing. In *55th AIAA Aerospace Sciences Meeting*, page 1180, 2017.

[164] Tom Reynolds, Liling Ren, John-Paul Clarke, Andrew Burke, and Mark Green. History, development and analysis of noise abatement arrival procedures for uk airports. In *AIAA 5th ATIO and 16th Lighter-Than-Air Sys Tech. and Balloon Systems Conferences*, page 7395, 2005.

[165] S Alam, MH Nguyen, HA Abbass, C Lokan, M Ellejmi, and S Kirby. A dynamic continuous descent approach methodology for low noise and emission. In *Digital Avionics Systems Conference (DASC), 2010 IEEE/AIAA 29th*, pages 1–E. IEEE, 2010.

[166] Helmut Maurer and Nikolai Osmolovskii. Second-order conditions for optimal control problems with mixed control-state constraints and control appearing linearly. In *Decision and Control (CDC), 2013 IEEE 52nd Annual Conference on*, pages 514–519. IEEE, 2013.

[167] Roland Bulirsch. Die mehrzielmethode zur numerischen lösung von nichtlinearen randwertproblemen und aufgaben der optimalen steuerung. *Report der Carl-Cranz-Gesellschaft*, 251, 1971.

[168] Hans Josef Pesch. Optimal re-entry guidance of space vehicles under control and state variable inequality constraints. 1989.

[169] Bernd Kugelmann and Hans Josef Pesch. New general guidance method in constrained optimal control, part 2: Application to space shuttle guidance. *Journal of Optimization Theory and Applications*, 67(3):437–446, 1990.

[170] Hans Josef Pesch. A practical guide to the solution of real-life optimal control problems. *Control and Cybernetics*, 23(1):2, 1994.

[171] Michael H Breitner and H Joseph Pesch. Reentry trajectory optimization under atmospheric uncertainty as a differential game. In *Advances in Dynamic Games and Applications*, pages 70–86. Springer, 1994.

[172] Hermann Kreim, Bernd Kugelmann, Hans Josef Pesch, and Michael H Breitner. Minimizing the maximum heating of a re-entering space shuttle: An optimal control problem with multiple control constraints. *Optimal Control Applications and Methods*, 17(1):45–69, 1996.

[173] Angelo Miele and Attilio Salvetti. *Applied Mathematics in Aerospace Science and Engineering*, volume 44. Springer Science & Business Media, 2013.

[174] Ernst Dieter Dickmanns. Maximum range three-dimensional lifting planetary entry. 1972.

[175] Thomas Antony, Michael J Grant, and Michael A Bolender. Optimization of interior point cost functions using indirect methods. In *AIAA Atmospheric Flight Mechanics Conference*, page 2399, 2015.

[176] En-mi Yong, Guo-jin Tang, and Lei Chen. Rapid trajectory optimization for hypersonic reentry vehicle via gauss pseudospectral method. *Journal of Astronautics*, 29(6):1766–1772, 2008.

[177] En-mi Yong, Guo-jin Tang, and Lei Chen. Rapid trajectory planning for hypersonic unpowered long-range reentry vehicles with multi-constraints. *Journal of Astronautics*, 29(1):46–52, 2008.

[178] Timothy R Jorris and Richard G Cobb. Three-dimensional trajectory optimization satisfying waypoint and no-fly zone constraints. *Journal of Guidance, Control, and Dynamics*, 32(2):551–572, 2009.

[179] Helmut Maurer. Tutorial on control and state constrained optimal control problems and applications – part 3 : Pure state constraints.

[180] US Census Bureau. 2010 census interactive population map. http://www.census.gov/2010census/popmap/, 2010. Accessed: 13 Dec. 2016.

[181] John-Paul Barrington Clarke. Systems analysis of noise abatement procedures enabled by advanced flight guidance technology. *Journal of Aircraft*, 37(2):266–273, 2000.

[182] Kenneth Sutton and Randolph A Graves Jr. A general stagnation-point convective heating equation for arbitrary gas mixtures. 1971.

[183] Bernard Bonnard, Ludovic Faubourg, Geneviève Launay, and Emmanuel Trélat. Optimal control with state constraints and the space shuttle re-entry problem. *Journal of Dynamical and Control Systems*, 9(2):155–199, 2003.

[184] Karl Edquist, Derek S Liechty, Brian R Hollis, Stephen J Alter, and Mark P Loomis. Aeroheating environments for a mars smart lander. *Journal of Spacecraft and Rockets*, 43(2):330–339, 2006.

[185] Devin M Kipp, John A Dec, Grant William Wells, and Robert D Braun. Development of a planetary entry system synthesis tool for conceptual design and analysis. 2005.

[186] Heinrich G Jacob. An engineering optimization method with application to stol-aircraft approach and landing trajectories. 1972.

[187] J Farrell, G Henry, R Lee, and A Lowe. Procedures for estimating the effects of design and operational characteristics of jet aircraft on ground noise. 1968.

[188] Heinz Erzberger and Homer Q Lee. Technique for calculating optimum takeoff and climb out trajectories for noise abatement. 1969.

[189] G Schadt. Aerodynamic heating problems and their influence on earth orbit lifting entry spacecraft. In *5th Annual Meeting and Technical Display*, page 1126, 1968.

APPENDICES

A. The Analytical Model of an Air-Breathing Engine

Traditionally, trajectory optimization of air-breathing vehicles has been based on tabulated engine models. OCT relies upon continuous derivatives and cannot obtain higher quality solutions for complex problems involving such discrete models. Ref. 134 introduces an analytical model for the scramjet propulsion system to resolve this issue. The analytical relationships may also help in determining better performing operating ranges for scramjets. This analytical model uses a parametric ideal scramjet cycle analysis, developed in Ref. 155 and based on the Brayton cycle. The major assumptions included in this analysis are:

1. an isentropic inlet,
2. a constant pressure combustion,
3. an isentropic nozzle,
4. a constant pressure heat rejection,
5. and the static pressures at nozzle's exit and the ambient freestream are the same.

Following discussion describes the relation of the freestream Mach number and freestream temperature to the operational parameters of scramjet engine like fuel-air ratio and specific thrust. An adiabatic inlet for the scramjet engine leads to an inlet temperature ratio, τ_r, shown in Eq. (A.1), where M_0 is the freestream Mach number.

$$\tau_r = 1 + \left(\frac{\gamma - 1}{2} M_0^2\right) \tag{A.1}$$

Eq. (A.2) determines the total temperature at the nozzle exit, T'_{MAX}, where T_{MAX} is the upper limit of combustor material's temperature. Please note that combustion occurs at supersonic speeds in a scramjet engine. A more compact evaluation of the specific thrust and fuel-air ratio results in creation of another ratio, τ_λ, as shown in Eq. (A.3), where T_0 is the freestream temperature.

$$T'_{\mathrm{MAX}} = T_{\mathrm{MAX}} \left(1 + \frac{\gamma - 1}{2} M_c^2\right) \tag{A.2}$$

$$\tau_\lambda = \frac{T'_{\mathrm{MAX}}}{T_0} \tag{A.3}$$

The ratios τ_r and τ_λ help in the evaluation of two performance variables of the analytical model. The ratio of mass flow rates of fuel injected into the burner to that of the air passing through the engine, f, is the first performance variable and is calculated as shown in Eq. (A.4). Here c_{p} is a specific heat at a constant pressure and h_{pr} is the fuel heating value.

$$\mathrm{f} = \frac{\mathrm{c_p T_0}}{\mathrm{h_{pr}}} (\tau_\lambda - \tau_{\mathrm{r}}) \tag{A.4}$$

The other performance variable, specific thrust, is shown in Eq. (A.5). Varying $\dot{m}_0$, as shown in Eq. (A.6), scales both specific thrust and fuel-air ratio. Finally, specific thrust multiplies with $\dot{m}_0$ to obtain thrust.

$$\frac{F}{\dot{m}_0} = \frac{V_0}{g_{\mathrm{c}}} \left(\sqrt{\frac{\tau_\lambda}{\tau_r}} - 1\right) \tag{A.5}$$

$$\dot{m}_0 = \rho A_{\mathrm{c}} V_0 \tag{A.6}$$

These two performance parameters indicate the scramjet engine's efficiency. For example, a smaller value of f means lesser fuel burnt for a given mass flow rate. Additionally, for a larger specific thrust, same mass flow rate generates more thrust. The expressions obtained for f, $\dot{m}_0$, and thrust feed back into the EOMs, thereby completing the coupled nature of the flight dynamics and propulsion system.

B. The Objective Functional for the Aircraft Landing Noise Minimization Problem

An appropriate performance index requires an estimation of the amount of noise inconvenience for people living in the vicinity of an airport including its runway. Eq. (B.1) defines the maximum perceived noise level of an aircraft. [186, 187] PN dB_0 in Eq. (B.1) is the perceived noise level at a distance R_{REF} (152 m) from the aircraft with its maximum thrust. The second and third terms in Eq. (B.1) account for the impacts of the distance from the aircraft and its thrust on noise levels, respectively.

$$\mathrm{PN\ dB} = \mathrm{PN\ dB}_0 + 25 \log\left(\frac{R_{\mathrm{REF}}}{R}\right) + 52 \log\left(\frac{T}{T_{\mathrm{MAX}}}\right) \tag{B.1}$$

The derivation of Eq. (B.1) uses the following assumptions.

1. The noise field is spherically symmetrical.
2. The compressor noise is small as compared to the jet noise.
3. The community surrounds the area before a point 472 m horizontally distant from the touchdown point, and outside a line 61 m laterally away from the centerline of the runway. [186]

Assumption 3 results in Eq. (B.2) for R, where d is the horizontal distance from the touchdown point.

$$R = \begin{cases} h & \text{if} \quad \mathrm{d} \geq 472\ \mathrm{m} \\ \sqrt{h^2 + 61^2} & \text{if} \quad \mathrm{d} < 472\ \mathrm{m} \end{cases} \tag{B.2}$$

To avoid complicated analysis, $h + 50$ forms approximation for R. The effect of the noise duration adds to PN dB from Eq. (B.1) to calculate the maximum EPNL as shown in Eq. (B.3). [188]

$$\mathrm{EPN\ dB} = \mathrm{PN\ dB} + 20 \log\left(\frac{V_{\mathrm{REF}}}{V}\right) \tag{B.3}$$

Substitution of Eq. (B.1) into Eq. (B.3) leads to a performance index for the maximum IEPNL, J_0, as shown in Eq. (B.4). In this equation ln represents natural logarithm and K_i's (i=1,..., 4) are positive constants.

$$J_0 = \int_{x_0}^{x_f} (K_1 - K_2 \ln(h + 50) + K_3 \ln T - K_4 \ln V) \mathrm{d}x \tag{B.4}$$

Division of the performance index, J_0, by the total horizontal flight distance results in the average value of the performance index, as shown in Eq. (B.5).

$$\overline{\text{EPN dB}} = \frac{1}{x_f - x_0} \int_{x_0}^{x_f} (\text{EPN dB}) \mathrm{d}x \tag{B.5}$$

However, J_0 was found to be deficient due to the use of the logarithmic form and failed to capture coupled effects of thrust and altitude on the noise level. A new performance index, 10^{EPNL}, resolved this issue by incorporating an effective penalty for the use of high thrust at low altitudes. Thus, Eq. (B.6) expresses this new performance index, where C_N is a constant given by Eq. (B.7).

$$J = \int_{x_0}^{x_f} \left(\frac{C_N T^{5.2}}{V^2 (h + 50)^{2.5}} \right) \mathrm{d}x \tag{B.6}$$

$$C_\text{N} = 10^{\text{PN dB}_0} \left(\frac{{R_\text{REF}}^{2.5} {V_\text{REF}}^2}{{T_\text{MAX}}^{5.2}} \right) \tag{B.7}$$

C. The Re-radiative Heating Constraint for the Space Shuttle Reentry Problem

C.1 Background

Medium and high lifting vehicles have a thermal protection system (TPS) comprising of re-radiative and ablative elements at different parts of the vehicle. [189] The L/D of such lifting entry vehicles determines the amount of re-radiation of the TPS. A quasi-steady approximation leads to the formulation of heating constraint on the outer skin of an entry vehicle as shown in Eq. (C.1), where v is the aerodynamic velocity, h is the altitude, and α is the angle of attack of the vehicle. [174]

$$\phi(h,\ v,\ \alpha) = 0 \tag{C.1}$$

$C_{\mathrm{L}}(\alpha, h, v)$ eliminates α in order to reduce the computational effort. As a result, Ref. 174 obtains the expression for C_{LH} based on intuition and trial. C_{LH} actually determines different levels of limit skin temperature, T, for the entry vehicle as shown in Eq. (C.2).

$$T = 1093 + 3704\ C_{\mathrm{LH}}\ (\mathrm{C}). \tag{C.2}$$

ΔC_{LH} is an adjustment parameter for C_{LH}. $\overline{h}$ and b are the scaling parameters for altitude and velocity, respectively. These parameters keep the values in the coefficient matrix, g, closer to 1.

The partial derivatives of C_{L} with respect to the altitude and the velocity are shown in Eq. (C.3a) and Eq. (C.3b), respectively. Here i ranges between 1 and 5, and Eq. (C.3c) gives the expression for C_{i}.

$$\frac{\partial C_{\mathrm{LH}}}{\partial h} = C_{\mathrm{i}} H_{\mathrm{i}} + B_{\mathrm{i}}\ \frac{\partial H}{\partial h} \tag{C.3a}$$

$$\frac{\partial C_{\mathrm{LH}}}{\partial v} = B_{\mathrm{i}}\ \frac{\partial H}{\partial v} \tag{C.3b}$$

$$C_{\mathrm{i}} = \sum_{j=1}^{4} (j-1)\; g_{\mathrm{ij}} \overline{h}^{(j-2)} \tag{C.3c}$$

Eq. (C.3a) and Eq. (C.3b) then lead to Eq. (C.4) as shown below.

$$\frac{\partial h}{\partial v}\Big|_{C_{\mathrm{LH}}} = -\left(\frac{\dfrac{\partial C_{\mathrm{LH}}}{\partial v}}{\dfrac{\partial C_{\mathrm{LH}}}{\partial h}}\right) \tag{C.4}$$

The approximation for C_{LH} was found to be in excellent agreement with the original input data as shown in Fig. C.1. Ref. 174 supplied the input data for a limit temperature of 2000^0 F. For maximum range trajectories, the lift coefficients stay around maximum L/D, thereby eliminating the need for the 70 km curve.

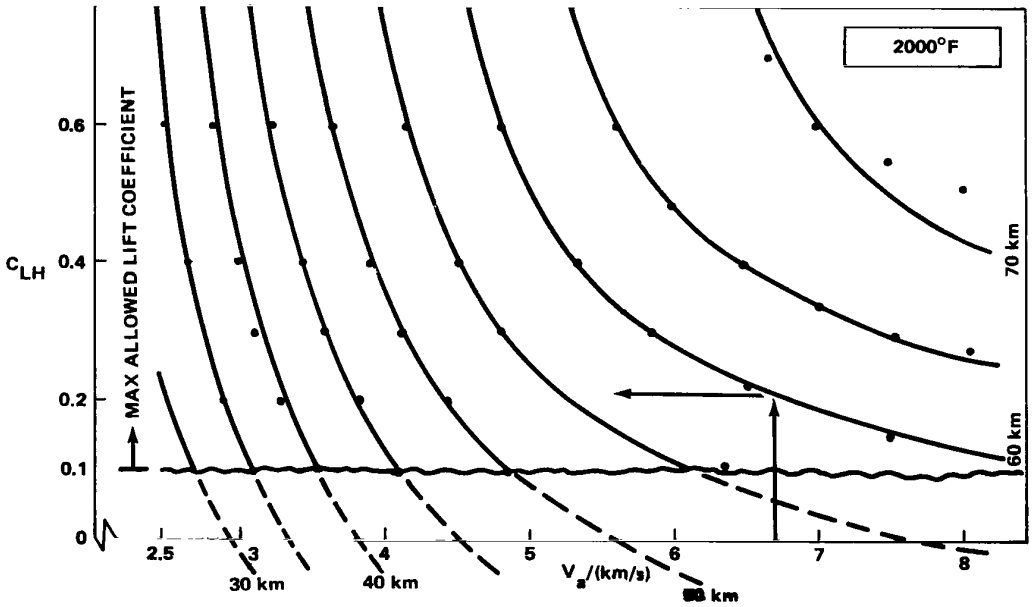

Figure C.1.: Comparison between the approximate values and original data for the re-radiative heating constraint of a space shuttle. [174]

C.2 Equations of Motion for the Costates

This section includes the complicated and lengthy EOMs for the costates, which previous studies in the literature omitted. The first lengthy costate EOM is corresponding to the altitude.

$$\dot{\lambda_h} = \lambda_\gamma((v\cos(\gamma))/(h+r_E)^2-(2mu\cos(\gamma))/(v(h+r_E)^3)-\mathrm{SA}v\cos((\pi(\sin(\sigma_{\mathrm{TRIG}})+1))/4)\exp(-h/H)(0.5w((v/(bh^2)-(3b)/v+(2b^2h)/v^2)(40.4855(h/h_s-1)^2+57.83333(h/h_s-1)^3+(13.62131h)/h_s-10.470043)-((80.971(h/h_s-1))/h_s+(173.49999(h/h_s-1)^2)/h_s+13.62131/h_s)(v/(bh)-(b^2h^2)/v^2+(3bh)/v-3)+((b^2h^2)/v^2-(2bh)/v+1)((20.63256(h/h_s-1))/h_s+(68.92458(h/h_s-1)^2)/h_s+2.337815/h_s)-((2b)/v-(2b^2h)/v^2)(10.31628(h/h_s-1)^2+22.97486(h/h_s-1)^3+(2.337815h)/h_s-1.525574)+((139.7381(h/h_s-1))/h_s+(383.333334(h/h_s-1)^2)/h_s+19.0734/h_s)(v^2/(b^2h^2)-(4v)/(bh)+(b^2h^2)/v^2-(4bh)/v+6)-(b/v-(2b^2h)/v^2)(0.864369(h/h_s-1)^2+12.1(h/h_s-1)^3-(2.73417h)/h_s+3.406847)-(69.86905(h/h_s-1)^2+127.777778(h/h_s-1)^3+(19.0734h)/h_s-16.705305)((4b)/v-(4v)/(bh^2)-(2b^2h)/v^2+(2v^2)/(b^2h^3))+((b^2h^2)/v^2-(bh)/v)((1.728738(h/h_s-1))/h_s+(36.3(h/h_s-1)^2)/h_s-2.73417/h_s)+(b^2h^2((2.427358(h/h_s-1))/h_s-(3.182499(h/h_s-1)^2)/h_s+0.834519/h_s))/v^2+(2b^2h(1.213679(h/h_s-1)^2-1.060833(h/h_s-1)^3+(0.834519h)/h_s-0.723802))/v^2)+0.5w\sin(C_{\mathrm{Lw}})((v/(bh^2)-(3b)/v+(2b^2h)/v^2)(40.4855(h/h_s-1)^2+57.83333(h/h_s-1)^3+(13.62131h)/h_s-10.470043)-((80.971(h/h_s-1))/h_s+(173.49999(h/h_s-1)^2)/h_s+13.62131/h_s)(v/(bh)-(b^2h^2)/v^2+(3bh)/v-3)+((b^2h^2)/v^2-(2bh)/v+1)((20.63256(h/h_s-1))/h_s+(68.92458(h/h_s-1)^2)/h_s+2.337815/h_s)-((2b)/v-(2b^2h)/v^2)(10.31628(h/h_s-1)^2+22.97486(h/h_s-1)^3+(2.337815h)/h_s-1.525574)+((139.7381(h/h_s-1))/h_s+(383.333334(h/h_s-1)^2)/h_s+19.0734/h_s)(v^2/(b^2h^2)-(4v)/(bh)+(b^2h^2)/v^2-(4bh)/v+6)-(b/v-(2b^2h)/v^2)(0.864369(h/h_s-1)^2+12.1(h/h_s-1)^3-(2.73417h)/h_s+3.406847)-(69.86905(h/h_s-1)^2+127.777778(h/h_s-1)^3+(19.0734h)/h_s-16.705305)((4b)/v-(4v)/(bh^2)-(2b^2h)/v^2+(2v^2)/(b^2h^3))+((b^2h^2)/v^2-(bh)/v)((1.728738(h/h_s-1))/h_s+(36.3(h/h_s-1)^2)/h_s-2.73417/h_s)+(b^2h^2((2.427358(h/h_s-1))/h_s-(3.182499(h/h_s-1)^2)/h_s+0.834519/h_s))/v^2+(2b^2h(1.213679(h/h_s-$$

$$1)^2-1.060833(h/h_s-1)^3+(0.834519h)/h_s-0.723802))/v^2))+(SAv\cos((\pi(\sin(\sigma_{\mathrm{TRIG}})+1))/4)\exp(-h/H)(0.5C_{\mathrm{LLB}}+0.5w(\Delta C_{\mathrm{LH}}-(40.4855(h/h_s-1)^2+57.83333(h/h_s-1)^3+(13.62131h)/h_s-10.470043)(v/(bh)-(b^2h^2)/v^2+(3bh)/v-3)+((b^2h^2)/v^2-(2bh)/v+1)(10.31628(h/h_s-1)^2+22.97486(h/h_s-1)^3+(2.337815h)/h_s-1.525574)+((b^2h^2)/v^2-(bh)/v)(0.864369(h/h_s-1)^2+12.1(h/h_s-1)^3-(2.73417h)/h_s+3.406847)+(69.86905(h/h_s-1)^2+127.777778(h/h_s-1)^3+(19.0734h)/h_s-16.705305)(v^2/(b^2h^2)-(4v)/(bh)+(b^2h^2)/v^2-(4bh)/v+6)+(b^2h^2(1.213679(h/h_s-1)^2-1.060833(h/h_s-1)^3+(0.834519h)/h_s-0.723802))/v^2)-0.5C_{\mathrm{LUB}}(w-1)-0.5\sin(C_{\mathrm{Lw}})(C_{\mathrm{LLB}}-w(\Delta C_{\mathrm{LH}}-(40.4855(h/h_s-1)^2+57.83333(h/h_s-1)^3+(13.62131h)/h_s-10.470043)(v/(bh)-(b^2h^2)/v^2+(3bh)/v-3)+((b^2h^2)/v^2-(2bh)/v+1)(10.31628(h/h_s-1)^2+22.97486(h/h_s-1)^3+(2.337815h)/h_s-1.525574)+((b^2h^2)/v^2-(bh)/v)(0.864369(h/h_s-1)^2+12.1(h/h_s-1)^3-(2.73417h)/h_s+3.406847)+(69.86905(h/h_s-1)^2+127.777778(h/h_s-1)^3+(19.0734h)/h_s-16.705305)(v^2/(b^2h^2)-(4v)/(bh)+(b^2h^2)/v^2-(4bh)/v+6)+(b^2h^2(1.213679(h/h_s-1)^2-1.060833(h/h_s-1)^3+(0.834519h)/h_s-0.723802))/v^2)+C_{\mathrm{LUB}}(w-1))))/H)-\lambda_\psi((v\cos(\gamma)\cos(\psi)tan(\phi))/(h+r_E)^2+(\mathrm{SA}v\sin((\pi(\sin(\sigma_{\mathrm{TRIG}})+1))/4)\exp(-h/H)(0.5w((v/(bh^2)-(3b)/v+(2b^2h)/v^2)(40.4855(h/h_s-1)^2+57.83333(h/h_s-1)^3+(13.62131h)/h_s-10.470043)-((80.971(h/h_s-1))/h_s+(173.49999(h/h_s-1)^2)/h_s+13.62131/h_s)(v/(bh)-(b^2h^2)/v^2+(3bh)/v-3)+((b^2h^2)/v^2-(2bh)/v+1)((20.63256(h/h_s-1))/h_s+(68.92458(h/h_s-1)^2)/h_s+2.337815/h_s)-((2b)/v-(2b^2h)/v^2)(10.31628(h/h_s-1)^2+22.97486(h/h_s-1)^3+(2.337815h)/h_s-1.525574)+((139.7381(h/h_s-1))/h_s+(383.333334(h/h_s-1)^2)/h_s+19.0734/h_s)(v^2/(b^2h^2)-(4v)/(bh)+(b^2h^2)/v^2-(4bh)/v+6)-(b/v-(2b^2h)/v^2)(0.864369(h/h_s-1)^2+12.1(h/h_s-1)^3-(2.73417h)/h_s+3.406847)-(69.86905(h/h_s-1)^2+127.777778(h/h_s-1)^3+(19.0734h)/h_s-16.705305)((4b)/v-(4v)/(bh^2)-(2b^2h)/v^2+(2v^2)/(b^2h^3))+((b^2h^2)/v^2-(bh)/v)((1.728738(h/h_s-1))/h_s+(36.3(h/h_s-1)^2)/h_s-2.73417/h_s)+(b^2h^2((2.427358(h/h_s-1))/h_s-(3.182499(h/h_s-1)^2)/h_s+0.834519/h_s))/v^2+(2b^2h(1.213679(h/h_s-1)^2-1.060833(h/h_s-1)^3+(0.834519h)/h_s-0.723802))/v^2)+0.5w\sin(C_{\mathrm{Lw}})((v/(bh^2)-(3b)/v+(2b^2h)/v^2)(40.4855(h/h_s-1)^2+57.83333(h/h_s-1)^3+(13.62131h)/h_s-10.470043)-((80.971(h/h_s-1))/h_s+(173.49999(h/h_s-$$

$$1)^2)/h_s + 13.62131/h_s)(v/(bh) - (b^2h^2)/v^2 + (3bh)/v - 3) + ((b^2h^2)/v^2 - (2bh)/v + 1)((20.63256(h/h_s - 1))/h_s + (68.92458(h/h_s - 1)^2)/h_s + 2.337815/h_s) - ((2b)/v - (2b^2h)/v^2)(10.31628(h/h_s-1)^2+22.97486(h/h_s-1)^3+(2.337815h)/h_s-1.525574)+((139.7381(h/h_s - 1))/h_s + (383.333334(h/h_s - 1)^2)/h_s + 19.0734/h_s)(v^2/(b^2h^2) - (4v)/(bh)+(b^2h^2)/v^2-(4bh)/v+6)-(b/v-(2b^2h)/v^2)(0.864369(h/h_s-1)^2+12.1(h/h_s-1)^3 - (2.73417h)/h_s + 3.406847) - (69.86905(h/h_s - 1)^2 + 127.777778(h/h_s - 1)^3 + (19.0734h)/h_s-16.705305)((4b)/v-(4v)/(bh^2)-(2b^2h)/v^2+(2v^2)/(b^2h^3))+((b^2h^2)/v^2-(bh)/v)((1.728738(h/h_s-1))/h_s+(36.3(h/h_s-1)^2)/h_s-2.73417/h_s)+(b^2h^2((2.427358(h/h_s-1))/h_s-(3.182499(h/h_s-1)^2)/h_s+0.834519/h_s))/v^2+(2b^2h(1.213679(h/h_s-1)^2 - 1.060833(h/h_s - 1)^3 + (0.834519h)/h_s - 0.723802))/v^2)))/\cos(\gamma) - (\mathrm{SA}v\sin((\pi(\sin(\sigma_{\mathrm{TRIG}})+1))/4)\exp(-h/H)(0.5C_{\mathrm{LLB}}+0.5w(\Delta C_{\mathrm{LH}}-(40.4855(h/h_s-1)^2+57.83333(h/h_s-1)^3+(13.62131h)/h_s-10.470043)(v/(bh)-(b^2h^2)/v^2+(3bh)/v-3)+((b^2h^2)/v^2-(2bh)/v+1)(10.31628(h/h_s-1)^2+22.97486(h/h_s-1)^3+(2.337815h)/h_s-1.525574)+((b^2h^2)/v^2-(bh)/v)(0.864369(h/h_s-1)^2+12.1(h/h_s-1)^3-(2.73417h)/h_s+3.406847)+(69.86905(h/h_s-1)^2+127.777778(h/h_s-1)^3+(19.0734h)/h_s-16.705305)(v^2/(b^2h^2)-(4v)/(bh)+(b^2h^2)/v^2-(4bh)/v+6)+(b^2h^2(1.213679(h/h_s-1)^2-1.060833(h/h_s-1)^3+(0.834519h)/h_s-0.723802))/v^2)-0.5C_{\mathrm{LUB}}(w-1)-0.5\sin(C_{\mathrm{Lw}})(C_{\mathrm{LLB}}-w(\Delta C_{\mathrm{LH}}-(40.4855(h/h_s-1)^2+57.83333(h/h_s-1)^3+(13.62131h)/h_s-10.470043)(v/(bh)-(b^2h^2)/v^2+(3bh)/v-3)+((b^2h^2)/v^2-(2bh)/v+1)(10.31628(h/h_s-1)^2+22.97486(h/h_s-1)^3+(2.337815h)/h_s-1.525574)+((b^2h^2)/v^2-(bh)/v)(0.864369(h/h_s-1)^2+12.1(h/h_s-1)^3 - (2.73417h)/h_s + 3.406847) + (69.86905(h/h_s - 1)^2 + 127.777778(h/h_s - 1)^3 + (19.0734h)/h_s - 16.705305)(v^2/(b^2h^2) - (4v)/(bh) + (b^2h^2)/v^2 - (4bh)/v + 6) + (b^2h^2(1.213679(h/h_s - 1)^2 - 1.060833(h/h_s - 1)^3 + (0.834519h)/h_s - 0.723802))/v^2) + C_{\mathrm{LUB}}(w-1))))/(H\cos(\gamma)))-\lambda_v((2mu\sin(\gamma))/(h+r_E)^3+(SAv^2\exp(-h/H)((0.5C_{\mathrm{LLB}}+0.5w(\Delta C_{\mathrm{LH}}-(40.4855(h/h_s-1)^2+57.83333(h/h_s-1)^3+(13.62131h)/h_s-10.470043)(v/(bh) - (b^2h^2)/v^2 + (3bh)/v - 3) + ((b^2h^2)/v^2 - (2bh)/v + 1)(10.31628(h/h_s - 1)^2 + 22.97486(h/h_s-1)^3+(2.337815h)/h_s-1.525574)+((b^2h^2)/v^2-(bh)/v)(0.864369(h/h_s-1)^2+12.1(h/h_s-1)^3-(2.73417h)/h_s+3.406847)+(69.86905(h/h_s-1)^2+127.777778(h/h_s-1)^3+(19.0734h)/h_s-16.705305)(v^2/(b^2h^2)-(4v)/(bh)+(b^2h^2)/v^2-(4bh)/v+$$

$$6)+(b^2h^2(1.213679(h/h_s-1)^2-1.060833(h/h_s-1)^3+(0.834519h)/h_s-0.723802))/v^2)-0.5C_{\mathrm{LUB}}(w-1)-0.5\sin(C_{\mathrm{Lw}})(C_{\mathrm{LLB}}-w(\Delta C_{\mathrm{LH}}-(40.4855(h/h_s-1)^2+57.83333(h/h_s-1)^3+(13.62131h)/h_s-10.470043)(v/(bh)-(b^2h^2)/v^2+(3bh)/v-3)+((b^2h^2)/v^2-(2bh)/v+1)(10.31628(h/h_s-1)^2+22.97486(h/h_s-1)^3+(2.337815h)/h_s-1.525574)+((b^2h^2)/v^2-(bh)/v)(0.864369(h/h_s-1)^2+12.1(h/h_s-1)^3-(2.73417h)/h_s+3.406847)+(69.86905(h/h_s-1)^2+127.777778(h/h_s-1)^3+(19.0734h)/h_s-16.705305)(v^2/(b^2h^2)-(4v)/(bh)+(b^2h^2)/v^2-(4bh)/v+6)+(b^2h^2(1.213679(h/h_s-1)^2-1.060833(h/h_s-1)^3+(0.834519h)/h_s-0.723802))/v^2)+C_{\mathrm{LUB}}(w-1)))^{1.86}+0.04))/H-1.86\mathrm{SA}v^2\exp(-h/H)(0.5w((v/(bh^2)-(3b)/v+(2b^2h)/v^2)(40.4855(h/h_s-1)^2+57.83333(h/h_s-1)^3+(13.62131h)/h_s-10.470043)-((80.971(h/h_s-1))/h_s+(173.49999(h/h_s-1)^2)/h_s+13.62131/h_s)(v/(bh)-(b^2h^2)/v^2+(3bh)/v-3)+((b^2h^2)/v^2-(2bh)/v+1)((20.63256(h/h_s-1))/h_s+(68.92458(h/h_s-1)^2)/h_s+2.337815/h_s)-((2b)/v-(2b^2h)/v^2)(10.31628(h/h_s-1)^2+22.97486(h/h_s-1)^3+(2.337815h)/h_s-1.525574)+((139.7381(h/h_s-1))/h_s+(383.333334(h/h_s-1)^2)/h_s+19.0734/h_s)(v^2/(b^2h^2)-(4v)/(bh)+(b^2h^2)/v^2-(4bh)/v+6)-(b/v-(2b^2h)/v^2)(0.864369(h/h_s-1)^2+12.1(h/h_s-1)^3-(2.73417h)/h_s+3.406847)-(69.86905(h/h_s-1)^2+127.777778(h/h_s-1)^3+(19.0734h)/h_s-16.705305)((4b)/v-(4v)/(bh^2)-(2b^2h)/v^2+(2v^2)/(b^2h^3))+((b^2h^2)/v^2-(bh)/v)((1.728738(h/h_s-1))/h_s+(36.3(h/h_s-1)^2)/h_s-2.73417/h_s)+(b^2h^2((2.427358(h/h_s-1))/h_s-(3.182499(h/h_s-1)^2)/h_s+0.834519/h_s))/v^2+(2b^2h(1.213679(h/h_s-1)^2-1.060833(h/h_s-1)^3+(0.834519h)/h_s-0.723802))/v^2)+0.5w\sin(C_{\mathrm{Lw}})((v/(bh^2)-(3b)/v+(2b^2h)/v^2)(40.4855(h/h_s-1)^2+57.83333(h/h_s-1)^3+(13.62131h)/h_s-10.470043)-((80.971(h/h_s-1))/h_s+(173.49999(h/h_s-1)^2)/h_s+13.62131/h_s)(v/(bh)-(b^2h^2)/v^2+(3bh)/v-3)+((b^2h^2)/v^2-(2bh)/v+1)((20.63256(h/h_s-1))/h_s+(68.92458(h/h_s-1)^2)/h_s+2.337815/h_s)-((2b)/v-(2b^2h)/v^2)(10.31628(h/h_s-1)^2+22.97486(h/h_s-1)^3+(2.337815h)/h_s-1.525574)+((139.7381(h/h_s-1))/h_s+(383.333334(h/h_s-1)^2)/h_s+19.0734/h_s)(v^2/(b^2h^2)-(4v)/(bh)+(b^2h^2)/v^2-(4bh)/v+6)-(b/v-(2b^2h)/v^2)(0.864369(h/h_s-1)^2+12.1(h/h_s-1)^3-(2.73417h)/h_s+3.406847)-(69.86905(h/h_s-1)^2+127.777778(h/h_s-1)^3+(19.0734h)/h_s-16.705305)((4b)/v-(4v)/(bh^2)-(2b^2h)/v^2+(2v^2)/(b^2h^3))+((b^2h^2)/v^2-(bh)/v)((1.728738(h/h_s-1))/h_s+(36.3(h/h_s-1)^2)/h_s-$$

$2.73417/h_s)+(b^2h^2((2.427358(h/h_s-1))/h_s-(3.182499(h/h_s-1)^2)/h_s+0.834519/h_s))/v^2+(2b^2h(1.213679(h/h_s-1)^2-1.060833(h/h_s-1)^3+(0.834519h)/h_s-0.723802))/v^2))(0.5C_{\mathrm{LLB}}+0.5w(\Delta C_{\mathrm{LH}}-(40.4855(h/h_s-1)^2+57.83333(h/h_s-1)^3+(13.62131h)/h_s-10.470043)(v/(bh)-(b^2h^2)/v^2+(3bh)/v-3)+((b^2h^2)/v^2-(2bh)/v+1)(10.31628(h/h_s-1)^2+22.97486(h/h_s-1)^3+(2.337815h)/h_s-1.525574)+((b^2h^2)/v^2-(bh)/v)(0.864369(h/h_s-1)^2+12.1(h/h_s-1)^3-(2.73417h)/h_s+3.406847)+(69.86905(h/h_s-1)^2+127.777778(h/h_s-1)^3+(19.0734h)/h_s-16.705305)(v^2/(b^2h^2)-(4v)/(bh)+(b^2h^2)/v^2-(4bh)/v+6)+(b^2h^2(1.213679(h/h_s-1)^2-1.060833(h/h_s-1)^3+(0.834519h)/h_s-0.723802))/v^2)-0.5C_{\mathrm{LUB}}(w-1)-0.5\sin(C_{\mathrm{Lw}})(C_{\mathrm{LLB}}-w(\Delta C_{\mathrm{LH}}-(40.4855(h/h_s-1)^2+57.83333(h/h_s-1)^3+(13.62131h)/h_s-10.470043)(v/(bh)-(b^2h^2)/v^2+(3bh)/v-3)+((b^2h^2)/v^2-(2bh)/v+1)(10.31628(h/h_s-1)^2+22.97486(h/h_s-1)^3+(2.337815h)/h_s-1.525574)+((b^2h^2)/v^2-(bh)/v)(0.864369(h/h_s-1)^2+12.1(h/h_s-1)^3-(2.73417h)/h_s+3.406847)+(69.86905(h/h_s-1)^2+127.777778(h/h_s-1)^3+(19.0734h)/h_s-16.705305)(v^2/(b^2h^2)-(4v)/(bh)+(b^2h^2)/v^2-(4bh)/v+6)+(b^2h^2(1.213679(h/h_s-1)^2-1.060833(h/h_s-1)^3+(0.834519h)/h_s-0.723802))/v^2)+C_{\mathrm{LUB}}(w-1)))^{0.86})+(\lambda_\phi v\cos(\gamma)\sin(\psi))/(h+r_E)^2$

The costate EOM corresponding to the crossrange angle, ϕ, is relatively very small.

$\dot{\lambda_\phi} = (\lambda_\psi v\cos(\gamma)\cos(\psi)(tan(\phi)^2+1))/(h+r_E)$

The second lengthy costate EOM is corresponding to the velocity.

$\dot{\lambda_v} = \lambda_v(2\mathrm{SA}v\exp(-h/H)((0.5C_{\mathrm{LLB}}+0.5w(\Delta C_{\mathrm{LH}}-(40.4855(h/h_s-1)^2+57.83333(h/h_s-1)^3+(13.62131h)/h_s-10.470043)(v/(bh)-(b^2h^2)/v^2+(3bh)/v-3)+((b^2h^2)/v^2-(2bh)/v+1)(10.31628(h/h_s-1)^2+22.97486(h/h_s-1)^3+(2.337815h)/h_s-1.525574)+((b^2h^2)/v^2-(bh)/v)(0.864369(h/h_s-1)^2+12.1(h/h_s-1)^3-(2.73417h)/h_s+3.406847)+(69.86905(h/h_s-1)^2+127.777778(h/h_s-1)^3+(19.0734h)/h_s-16.705305)(v^2/(b^2h^2)-(4v)/(bh)+(b^2h^2)/v^2-(4bh)/v+6)+(b^2h^2(1.213679(h/h_s-1)^2-1.060833(h/h_s-1)^3+(0.834519h)/h_s-0.723802))/v^2)-0.5C_{\mathrm{LUB}}(w-1)-0.5\sin(C_{\mathrm{Lw}})(C_{\mathrm{LLB}}-w(\Delta C_{\mathrm{LH}}-(40.4855(h/h_s-1)^2+57.83333(h/h_s-1)^3+(13.62131h)/h_s-10.470043)(v/(bh)-(b^2h^2)/v^2+(3bh)/v-3)+((b^2h^2)/v^2-(2bh)/v+1)(10.31628(h/h_s-1)^2+22.97486(h/h_s-$

$$1)^3+(2.337815h)/h_s-1.525574)+((b^2h^2)/v^2-(bh)/v)(0.864369(h/h_s-1)^2+12.1(h/h_s-1)^3-(2.73417h)/h_s+3.406847)+(69.86905(h/h_s-1)^2+127.777778(h/h_s-1)^3+(19.0734h)/h_s-16.705305)(v^2/(b^2h^2)-(4v)/(bh)+(b^2h^2)/v^2-(4bh)/v+6)+(b^2h^2(1.213679(h/h_s-1)^2-1.060833(h/h_s-1)^3+(0.834519h)/h_s-0.723802))/v^2)+C_{\mathrm{LUB}}(w-1)))^1.86+0.04)-1.86\mathrm{SA}v^2\exp(-h/H)(0.5w(((2b^2h^2)/v^3-(2bh)/v^2)(10.31628(h/h_s-1)^2+22.97486(h/h_s-1)^3+(2.337815h)/h_s-1.525574)+(1/(bh)+(2b^2h^2)/v^3-(3bh)/v^2)(40.4855(h/h_s-1)^2+57.83333(h/h_s-1)^3+(13.62131h)/h_s-10.470043)+((2b^2h^2)/v^3-(bh)/v^2)(0.864369(h/h_s-1)^2+12.1(h/h_s-1)^3-(2.73417h)/h_s+3.406847)+(69.86905(h/h_s-1)^2+127.777778(h/h_s-1)^3+(19.0734h)/h_s-16.705305)(4/(bh)-(2v)/(b^2h^2)+(2b^2h^2)/v^3-(4bh)/v^2)+(2b^2h^2(1.213679(h/h_s-1)^2-1.060833(h/h_s-1)^3+(0.834519h)/h_s-0.723802))/v^3)+0.5w\sin(C_{\mathrm{Lw}})(((2b^2h^2)/v^3-(2bh)/v^2)(10.31628(h/h_s-1)^2+22.97486(h/h_s-1)^3+(2.337815h)/h_s-1.525574)+(1/(bh)+(2b^2h^2)/v^3-(3bh)/v^2)(40.4855(h/h_s-1)^2+57.83333(h/h_s-1)^3+(13.62131h)/h_s-10.470043)+((2b^2h^2)/v^3-(bh)/v^2)(0.864369(h/h_s-1)^2+12.1(h/h_s-1)^3-(2.73417h)/h_s+3.406847)+(69.86905(h/h_s-1)^2+127.777778(h/h_s-1)^3+(19.0734h)/h_s-16.705305)(4/(bh)-(2v)/(b^2h^2)+(2b^2h^2)/v^3-(4bh)/v^2)+(2b^2h^2(1.213679(h/h_s-1)^2-1.060833(h/h_s-1)^3+(0.834519h)/h_s-0.723802))/v^3))(0.5C_{\mathrm{LLB}}+0.5w(\Delta C_{\mathrm{LH}}-(40.4855(h/h_s-1)^2+57.83333(h/h_s-1)^3+(13.62131h)/h_s-10.470043)(v/(bh)-(b^2h^2)/v^2+(3bh)/v-3)+((b^2h^2)/v^2-(2bh)/v+1)(10.31628(h/h_s-1)^2+22.97486(h/h_s-1)^3+(2.337815h)/h_s-1.525574)+((b^2h^2)/v^2-(bh)/v)(0.864369(h/h_s-1)^2+12.1(h/h_s-1)^3-(2.73417h)/h_s+3.406847)+(69.86905(h/h_s-1)^2+127.777778(h/h_s-1)^3+(19.0734h)/h_s-16.705305)(v^2/(b^2h^2)-(4v)/(bh)+(b^2h^2)/v^2-(4bh)/v+6)+(b^2h^2(1.213679(h/h_s-1)^2-1.060833(h/h_s-1)^3+(0.834519h)/h_s-0.723802))/v^2)-0.5C_{\mathrm{LUB}}(w-1)-0.5\sin(C_{\mathrm{Lw}})(C_{\mathrm{LLB}}-w(\Delta C_{\mathrm{LH}}-(40.4855(h/h_s-1)^2+57.83333(h/h_s-1)^3+(13.62131h)/h_s-10.470043)(v/(bh)-(b^2h^2)/v^2+(3bh)/v-3)+((b^2h^2)/v^2-(2bh)/v+1)(10.31628(h/h_s-1)^2+22.97486(h/h_s-1)^3+(2.337815h)/h_s-1.525574)+((b^2h^2)/v^2-(bh)/v)(0.864369(h/h_s-1)^2+12.1(h/h_s-1)^3-(2.73417h)/h_s+3.406847)+(69.86905(h/h_s-1)^2+127.777778(h/h_s-1)^3+(19.0734h)/h_s-16.705305)(v^2/(b^2h^2)-(4v)/(bh)+(b^2h^2)/v^2-(4bh)/v+6)+(b^2h^2(1.213679(h/h_s-1)^2-1.060833(h/h_s-1)^3+(0.834519h)/h_s-0.723802))/v^2)+$$

$$C_{\mathrm{LUB}}(w-1)))^{0}.86)-\lambda_h\sin(\gamma)-\lambda_\gamma(\cos(\gamma)/(h+r_E)+(mu\cos(\gamma))/(v^2(h+r_E)^2)+\mathrm{SA}\cos((\pi(\sin(\sigma_{\mathrm{TRIG}})+1))/4)\exp(-h/H)(0.5C_{\mathrm{LLB}}+0.5w(\Delta C_{\mathrm{LH}}-(40.4855(h/h_s-1)^2+57.83333(h/h_s-1)^3+(13.62131h)/h_s-10.470043)(v/(bh)-(b^2h^2)/v^2+(3bh)/v-3)+((b^2h^2)/v^2-(2bh)/v+1)(10.31628(h/h_s-1)^2+22.97486(h/h_s-1)^3+(2.337815h)/h_s-1.525574)+((b^2h^2)/v^2-(bh)/v)(0.864369(h/h_s-1)^2+12.1(h/h_s-1)^3-(2.73417h)/h_s+3.406847)+(69.86905(h/h_s-1)^2+127.777778(h/h_s-1)^3+(19.0734h)/h_s-16.705305)(v^2/(b^2h^2)-(4v)/(bh)+(b^2h^2)/v^2-(4bh)/v+6)+(b^2h^2(1.213679(h/h_s-1)^2-1.060833(h/h_s-1)^3+(0.834519h)/h_s-0.723802))/v^2)-0.5C_{\mathrm{LUB}}(w-1)-0.5\sin(C_{\mathrm{Lw}})(C_{\mathrm{LLB}}-w(\Delta C_{\mathrm{LH}}-(40.4855(h/h_s-1)^2+57.83333(h/h_s-1)^3+(13.62131h)/h_s-10.470043)(v/(bh)-(b^2h^2)/v^2+(3bh)/v-3)+((b^2h^2)/v^2-(2bh)/v+1)(10.31628(h/h_s-1)^2+22.97486(h/h_s-1)^3+(2.337815h)/h_s-1.525574)+((b^2h^2)/v^2-(bh)/v)(0.864369(h/h_s-1)^2+12.1(h/h_s-1)^3-(2.73417h)/h_s+3.406847)+(69.86905(h/h_s-1)^2+127.777778(h/h_s-1)^3+(19.0734h)/h_s-16.705305)(v^2/(b^2h^2)-(4v)/(bh)+(b^2h^2)/v^2-(4bh)/v+6)+(b^2h^2(1.213679(h/h_s-1)^2-1.060833(h/h_s-1)^3+(0.834519h)/h_s-0.723802))/v^2)+C_{\mathrm{LUB}}(w-1)))-\mathrm{SA}v\cos((\pi(\sin(\sigma_{\mathrm{TRIG}})+1))/4)\exp(-h/H)(0.5w(((2b^2h^2)/v^3-(2bh)/v^2)(10.31628(h/h_s-1)^2+22.97486(h/h_s-1)^3+(2.337815h)/h_s-1.525574)+(1/(bh)+(2b^2h^2)/v^3-(3bh)/v^2)(40.4855(h/h_s-1)^2+57.83333(h/h_s-1)^3+(13.62131h)/h_s-10.470043)+((2b^2h^2)/v^3-(bh)/v^2)(0.864369(h/h_s-1)^2+12.1(h/h_s-1)^3-(2.73417h)/h_s+3.406847)+(69.86905(h/h_s-1)^2+127.777778(h/h_s-1)^3+(19.0734h)/h_s-16.705305)(4/(bh)-(2v)/(b^2h^2)+(2b^2h^2)/v^3-(4bh)/v^2)+(2b^2h^2(1.213679(h/h_s-1)^2-1.060833(h/h_s-1)^3+(0.834519h)/h_s-0.723802))/v^3)+0.5w\sin(C_{\mathrm{Lw}})(((2b^2h^2)/v^3-(2bh)/v^2)(10.31628(h/h_s-1)^2+22.97486(h/h_s-1)^3+(2.337815h)/h_s-1.525574)+(1/(bh)+(2b^2h^2)/v^3-(3bh)/v^2)(40.4855(h/h_s-1)^2+57.83333(h/h_s-1)^3+(13.62131h)/h_s-10.470043)+((2b^2h^2)/v^3-(bh)/v^2)(0.864369(h/h_s-1)^2+12.1(h/h_s-1)^3-(2.73417h)/h_s+3.406847)+(69.86905(h/h_s-1)^2+127.777778(h/h_s-1)^3+(19.0734h)/h_s-16.705305)(4/(bh)-(2v)/(b^2h^2)+(2b^2h^2)/v^3-(4bh)/v^2)+(2b^2h^2(1.213679(h/h_s-1)^2-1.060833(h/h_s-1)^3+(0.834519h)/h_s-0.723802))/v^3)))+\lambda_\psi((\cos(\gamma)\cos(\psi)\tan(\phi))/(h+r_E)-(\mathrm{SA}\sin((\pi(\sin(\sigma_{\mathrm{TRIG}})+1))/4)\exp(-h/H)(0.5C_{\mathrm{LLB}}+0.5w(\Delta C_{\mathrm{LH}}-(40.4855(h/h_s-1)^2+57.83333(h/h_s-1)^3+$$

$$(13.62131h)/h_s-10.470043)(v/(bh)-(b^2h^2)/v^2+(3bh)/v-3)+((b^2h^2)/v^2-(2bh)/v+1)(10.31628(h/h_s-1)^2+22.97486(h/h_s-1)^3+(2.337815h)/h_s-1.525574)+((b^2h^2)/v^2-(bh)/v)(0.864369(h/h_s-1)^2+12.1(h/h_s-1)^3-(2.73417h)/h_s+3.406847)+(69.86905(h/h_s-1)^2+127.777778(h/h_s-1)^3+(19.0734h)/h_s-16.705305)(v^2/(b^2h^2)-(4v)/(bh)+(b^2h^2)/v^2-(4bh)/v+6)+(b^2h^2(1.213679(h/h_s-1)^2-1.060833(h/h_s-1)^3+(0.834519h)/h_s-0.723802))/v^2)-0.5C_{\mathrm{LUB}}(w-1)-0.5\sin(C_{\mathrm{Lw}})(C_{\mathrm{LLB}}-w(\Delta C_{\mathrm{LH}}-(40.4855(h/h_s-1)^2+57.83333(h/h_s-1)^3+(13.62131h)/h_s-10.470043)(v/(bh)-(b^2h^2)/v^2+(3bh)/v-3)+((b^2h^2)/v^2-(2bh)/v+1)(10.31628(h/h_s-1)^2+22.97486(h/h_s-1)^3+(2.337815h)/h_s-1.525574)+((b^2h^2)/v^2-(bh)/v)(0.864369(h/h_s-1)^2+12.1(h/h_s-1)^3-(2.73417h)/h_s+3.406847)+(69.86905(h/h_s-1)^2+127.777778(h/h_s-1)^3+(19.0734h)/h_s-16.705305)(v^2/(b^2h^2)-(4v)/(bh)+(b^2h^2)/v^2-(4bh)/v+6)+(b^2h^2(1.213679(h/h_s-1)^2-1.060833(h/h_s-1)^3+(0.834519h)/h_s-0.723802))/v^2)+C_{\mathrm{LUB}}(w-1))))/\cos(\gamma)+(\mathrm{SA}v\sin((\pi(\sin(\sigma_{\mathrm{TRIG}})+1))/4)\exp(-h/H)(0.5w(((2b^2h^2)/v^3-(2bh)/v^2)(10.31628(h/h_s-1)^2+22.97486(h/h_s-1)^3+(2.337815h)/h_s-1.525574)+(1/(bh)+(2b^2h^2)/v^3-(3bh)/v^2)(40.4855(h/h_s-1)^2+57.83333(h/h_s-1)^3+(13.62131h)/h_s-10.470043)+((2b^2h^2)/v^3-(bh)/v^2)(0.864369(h/h_s-1)^2+12.1(h/h_s-1)^3-(2.73417h)/h_s+3.406847)+(69.86905(h/h_s-1)^2+127.777778(h/h_s-1)^3+(19.0734h)/h_s-16.705305)(4/(bh)-(2v)/(b^2h^2)+(2b^2h^2)/v^3-(4bh)/v^2)+(2b^2h^2(1.213679(h/h_s-1)^2-1.060833(h/h_s-1)^3+(0.834519h)/h_s-0.723802))/v^3)+0.5w\sin(C_{\mathrm{Lw}})(((2b^2h^2)/v^3-(2bh)/v^2)(10.31628(h/h_s-1)^2+22.97486(h/h_s-1)^3+(2.337815h)/h_s-1.525574)+(1/(bh)+(2b^2h^2)/v^3-(3bh)/v^2)(40.4855(h/h_s-1)^2+57.83333(h/h_s-1)^3+(13.62131h)/h_s-10.470043)+((2b^2h^2)/v^3-(bh)/v^2)(0.864369(h/h_s-1)^2+12.1(h/h_s-1)^3-(2.73417h)/h_s+3.406847)+(69.86905(h/h_s-1)^2+127.777778(h/h_s-1)^3+(19.0734h)/h_s-16.705305)(4/(bh)-(2v)/(b^2h^2)+(2b^2h^2)/v^3-(4bh)/v^2)+(2b^2h^2(1.213679(h/h_s-1)^2-1.060833(h/h_s-1)^3+(0.834519h)/h_s-0.723802))/v^3))))/\cos(\gamma))-(\lambda_\phi\cos(\gamma)\sin(\psi))/(h+r_E)$$

The third lengthy costate EOM is corresponding to the flight path angle, γ.

$$\dot{\lambda_\gamma}=\lambda_\gamma((v\sin(\gamma))/(h+r_E)-(mu\sin(\gamma))/(v(h+r_E)^2))-\lambda_\psi((v\cos(\psi)\sin(\gamma)tan(\phi))/(h+r_E)+(\mathrm{SA}v\sin((\pi(\sin(\sigma_{\mathrm{TRIG}})+1))/4)\exp(-h/H)\sin(\gamma)(0.5C_{\mathrm{LLB}}+0.5w(\Delta C_{\mathrm{LH}}-(40.4855(h/h_s-1)^2+57.83333(h/h_s-1)^3+(13.62131h)/h_s-10.470043)(v/(bh)-$$

$(b^2h^2)/v^2+(3bh)/v-3)+((b^2h^2)/v^2-(2bh)/v+1)(10.31628(h/h_s-1)^2+22.97486(h/h_s-1)^3+(2.337815h)/h_s-1.525574)+((b^2h^2)/v^2-(bh)/v)(0.864369(h/h_s-1)^2+12.1(h/h_s-1)^3-(2.73417h)/h_s+3.406847)+(69.86905(h/h_s-1)^2+127.777778(h/h_s-1)^3+(19.0734h)/h_s-16.705305)(v^2/(b^2h^2)-(4v)/(bh)+(b^2h^2)/v^2-(4bh)/v+6)+(b^2h^2(1.213679(h/h_s-1)^2-1.060833(h/h_s-1)^3+(0.834519h)/h_s-0.723802))/v^2)-0.5C_{\mathrm{LUB}}(w-1)-0.5\sin(C_{\mathrm{Lw}})(C_{\mathrm{LLB}}-w(\Delta C_{\mathrm{LH}}-(40.4855(h/h_s-1)^2+57.83333(h/h_s-1)^3+(13.62131h)/h_s-10.470043)(v/(bh)-(b^2h^2)/v^2+(3bh)/v-3)+((b^2h^2)/v^2-(2bh)/v+1)(10.31628(h/h_s-1)^2+22.97486(h/h_s-1)^3+(2.337815h)/h_s-1.525574)+((b^2h^2)/v^2-(bh)/v)(0.864369(h/h_s-1)^2+12.1(h/h_s-1)^3-(2.73417h)/h_s+3.406847)+(69.86905(h/h_s-1)^2+127.777778(h/h_s-1)^3+(19.0734h)/h_s-16.705305)(v^2/(b^2h^2)-(4v)/(bh)+(b^2h^2)/v^2-(4bh)/v+6)+(b^2h^2(1.213679(h/h_s-1)^2-1.060833(h/h_s-1)^3+(0.834519h)/h_s-0.723802))/v^2)+C_{\mathrm{LUB}}(w-1))))/\cos(\gamma)^2)-\lambda_h v\cos(\gamma)+(\lambda_v mu\cos(\gamma))/(h+r_E)^2+(\lambda_\phi v\sin(\gamma)\sin(\psi))/(h+r_E)$

The last costate EOM for the space shuttle mixed heating constraint problem is corresponding to the heading angle, ψ.

$\dot{\lambda_\psi} = -(\lambda_\phi v\cos(\gamma)\cos(\psi))/(h+r_E)-(\lambda_\psi v\cos(\gamma)\sin(\psi)tan(\phi))/(h+r_E)$

D. Papers Status

D.1 A Relevant Journal Publication

1. Mall, K. and Grant, M. J., "Epsilon-Trig Regularization Method for Bang-Bang Optimal Control Problems," *Journal of Optimization Theory and Applications*, Vol. 174, No. 2, 2017, pp. 500-517.

D.2 Relevant Conference Publications

1. Williams, J., Mall, K., and Grant, M. J., "Trajectory Optimization using Indirect Methods and Parametric Scramjet Cycle Analysis," AIAA 2017-1180, AIAA SciTech Forum, Grapevine, TX, 9-13 Jan. 2017.
2. Udani, J.P., Mall, K., Grant, M. J., and Sun, D., "Optimal Flight Trajectory to Minimize Noise During Landing," AIAA 2017-1384, AIAA SciTech Forum, Grapevine, TX, 9-13 Jan. 2017.
3. Mall, K. and Grant, M. J., "Trigonomerization of Optimal Control Problems with Bounded Controls," AIAA 2016-3244, AIAA Atmospheric Flight Mechanics Conference, Washington, D.C., 13-17 Jun. 2016.
4. Mall, K. and Grant, M. J., "Epsilon-Trig Regularization Method for Bang-Bang Optimal Control Problems," AIAA 2016-3238, AIAA Atmospheric Flight Mechanics Conference, Washington, D.C., 13-17 Jun. 2016.
5. Mall, K. and Grant, M. J., "High Mass Mars Exploration using Slender Entry Vehicles," AIAA 2016-0019, AIAA Aerospace Sciences Meeting, San Diego, CA, 4-8 Jan. 2016.

D.3 Relevant Forthcoming Publications

1. Article submission to the AIAA SciTech 2019 regarding solving OCPs with mixed state-control constraints and linear controls using Trigonometrization.
2. Article submission to the Journal of Spacecraft and Rockets regarding solving OCPs with mixed state-control constraints using Trigonometrization.
3. Journal submission to Acta Astronautica regarding solving OCPs with pure control constraints using Trigonometrization.

D.4 An Additional Publication

Iino, S., Mall, K., Ono, A., Stuart, J., Das, A., Moriyama, E., Ohgi, T., Gillin, N., Tanaka, K., Aida, Y., and Fagin, M., "International Student Design Competition for Inspiration Mars Mission Report Summary (Team Kanau)," 17th Annual International Mars Society Convention, League City, TX, 2014.

VITA

VITA

Kshitij Mall was born in Barkuhi, India in May 1987. He received his B.Tech. degree in Mechanical Engineering in India in 2010. He then worked as a Computer Systems Engineer at Infosys Technologies Ltd. in India till May 2011. In August 2011, he joined the School of Aeronautics & Astronautics at Purdue University. In July 2012, he started working under Professor Grant at Rapid Design of Systems Laboratory (RDSL). His primary research focus at RDSL included trajectory optimization for various aerospace missions and developing the Optimal Control Theory. He received his master's degree in Aerospace Engineering at Purdue University in 2013.

Kshitij has been the co-project manager of an international collaborative team from Purdue University and Keio University, named Team Kanau, which won first prize globally in August 2014 in a Mars flyby student competition organized by The Mars Society and Inspiration Mars. At University of Tokyo and Keio University, he studied about a Vietnamese satellite called MicroDragon in 2017. He has also been a part of a Purdue-NASA MSFC project on human-class Mars missions in 2017. As the co-founder and ex-president of the Mars Society Purdue Chapter, he initiated Purdue's debut team to the Mars Desert Research Station in 2017 and was its executive officer. As hobbies, he enjoys flying aircraft and playing different sports including tennis and cricket.